All Plastic UAV

Design of a high altitude observation platform

B. de Heij, M.k. Jeliazkov, M.A.P. Kerssemakers
B. van den Kieboom, K. Mooi, M.N. Roelofs, J. Seelen
R. van Stralen, P.R. Vendrig, C.K. Verhoeff

Tutors Prof. dr. ir. T. Dingemans
Ir. J. Melkert
Coaches Ir. R. Bos
M.Sc. H. Udluft

Final Report
Design Synthesis Excercise

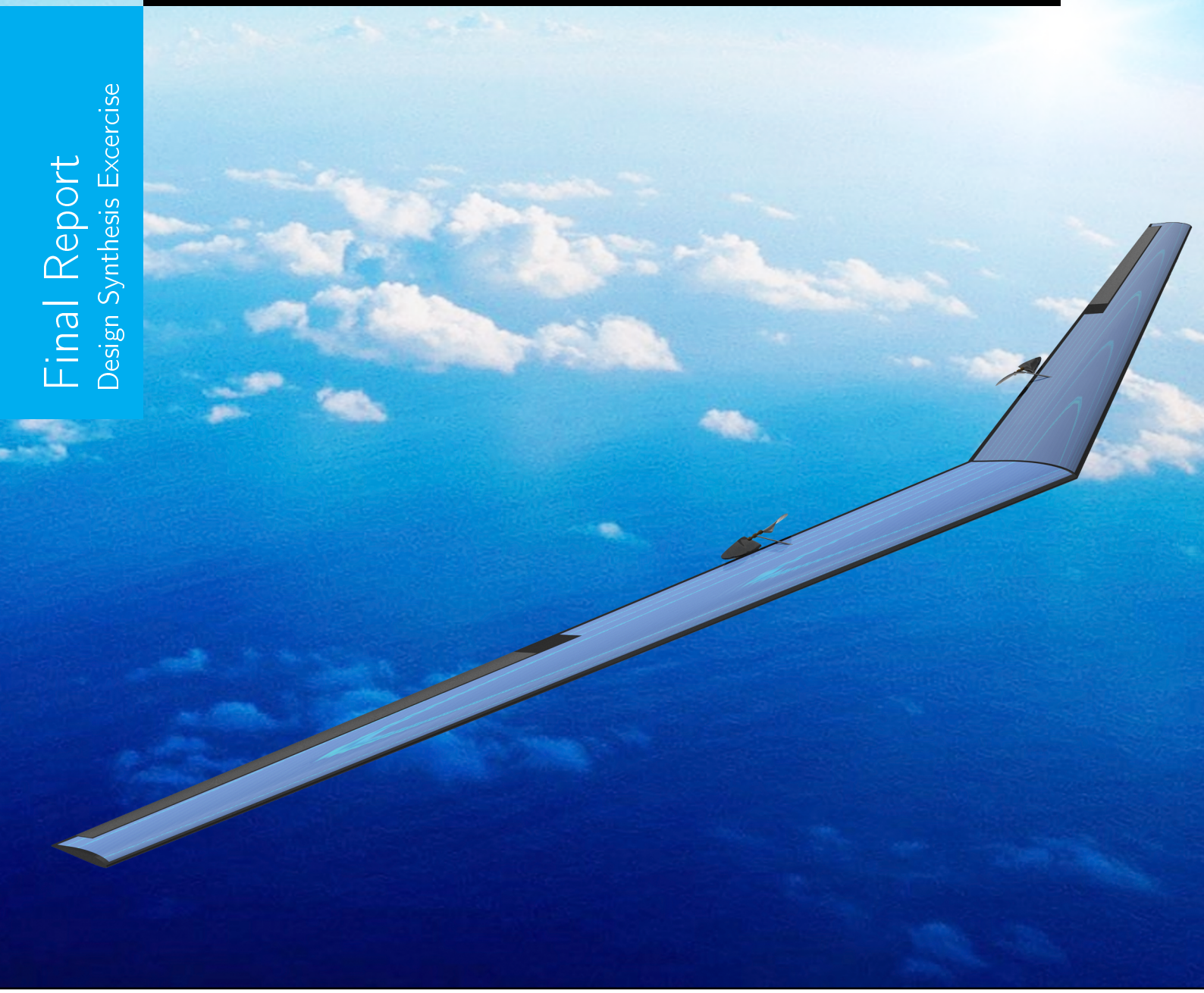

TU Delft Delft University of Technology

Aerospace Engineering

July 2, 2013

Final Report

DSE group 7, All plastic UAV

July 2, 2013

Tutors

Prof. dr. ir. T. Dingemans	TU Delft
Ir. J. Melkert	TU Delft

Coaches

Ir. R. Bos.	TU Delft
M.Sc. H. Udluft	TU Delft

Group members

B. de Heij	1507095
M.K. Jeliazkov	4105826
M.A.P. Kerssemakers	4005880
B. Van Den Kieboom	4114752
K. Mooi	4020367
M.N. Roelofs	4077407
J. Seelen	1317547
R. van Stralen	4019342
P.R. Vendrig	4023838
C.K. Verhoeff	1114344

Change record

Version	Date	Chapter	Section	Editor
1.0	10/6/2013	Subsystem Design	Battery	Martijn
1.1	10/6/2013	Final Design	Performance	Martijn
1.2	14/6/2013	Mission Requirements	Problem Statement	Ties
1.3	19/6/2013	Subsystem Design	Propulsion	Martijn
1.4	19/6/2013	Environmental Analysis	Solar Characteristics	Carel
1.5	19/6/2013	Introduction	Introduction	Rick & Ties
1.6	19/6/2013	Design Feasibility	Cost	Jannick
1.7	19/6/2013	Design Feasibility	Compliance Matrix	Ties
1.8	20/6/2013	Subsystem Design	Solar Panel & MPPT	Carel
1.9	20/6/2013	Subsystem Design	Heat Management	Martijn
1.10	20/6/2013	Environmental Analysis	Wind	Jannick
1.11	20/6/2013	Subsystem Design	Structures	Ties
1.12	20/6/2013	Design feasibility	Technical Risk	Kevin & Ties
1.13	20/6/2013	Subsystem Design	Aerodynamics	Kevin & Rick
1.14	20/6/2013	Subsystem Design	Mission Profile	Rick
1.15	20/6/2013	Subsystem Design	Communication	Bas
1.16	20/6/2013	Subsystem Design	Payload	Bas
1.17	20/6/2013	Design Feasibility	Sustainability	Martijn
1.18	20/6/2013	Design Feasibility	Sensitivity	Rick
1.19	20/6/2013	Subsystem Design	Structures	Momchil
1.20	20/6/2013	Mission requirements	Market analysis	Bas
1.21	20/6/2013	Subsystem Design	Propulsion	Perrin
1.22	20/6/2013	Future Activities	Gantt chart and Project design& logic	Boudewijn
1.23	20/6/2013	Design Integration	Summary	Kevin
1.24	21/6/2013	Acknowledgements	-	Boudewijn
1.25	21/6/2013	Conclusion	-	Rick & Kevin
1.26	21/6/2013	Summary	-	Carel
1.27	21/6/2013	Abstract	-	Boudewijn
1.28	24/6/2013	Final Design Analysis	Compliance Matrix; Feasibility Analysis	Kevin & Ties
1.29	24/6/2013	Systems Integration	Design Integration; Technical Budgets	Kevin
2.0	25/6/2013	Bibliography	Fixed references	Jannick
3.0	26/6/2013	Control Surface actuation	Added	Boudewijn
3.1	28/6/2013	Subsystem Design, Final Design	CATIA drawings	Martijn

Abstract

Polymer materials are currently rapidly being developed with their applications continuously being increased. However, new materials need more than 15 years of development and testing before they can be used in manned applications such as cars and aircraft. Since Unmanned Aerial Vehicles (UAVs) can be developed a lot faster, novel materials can be introduced rapidly during the development of these UAVs. The research question for this Design Synthesis Exercise was to what extent such a HALE UAV, designed to perform a year long high resolution Earth observation mission, can be made from polymer materials.

In response to this research question a flying wing has been designed. Atmospheric conditions have been analyzed. Furthermore tools for structural components, payload, performance and aerodynamics have been created and used to find and calculate solutions and make the design as optimal as possible. Finding novel ways of applying polymers has been a continuous focus of research throughout the project.

To perform the observation mission a light weight, low power camera and communication system has been designed, consisting almost exclusively of polymers. Conventional type systems are used for propulsion and control actuation. Using conducting polymers instead of their metal equivalents would result in a 37 times higher specific weight. Photovoltaic polymers could not convert solar energy to electricity with enough efficiency, thus thin film Gallium-Arsenide cells have to used.

This has resulted in a design of an aircraft containing 85% polymers by weight. Within two years the production of the UAV can start and with hundred units produced the cost would be less than a million euro per mission.

Acknowledgements

Special gratitude goes to prof. dr. ir. Theo Dingemans and ir. Joris Melkert for their guidance and supervision throughout the Design Synthesis Excercise. We also want to express our appreciation to our coaches ir. René Bos and Heiko Udluft M.sc. whom gave us their unlimited support for the duration of the project.

We would also like to thank the other staff members and PhD. Students of TU Delft that helped us with our enquiries on various matters. Special thanks go to dr. Sergio Turteltaub for his help in space systems, Steven Engelen and dr. ir. Ben Gorte for helping us with the optics, dr. ir. Roeland de Breuker, ir. Freek Sluis and dr. ir. Otto Bergsma for providing us with information about structural components, composites, piezoelectric polymers and shape memory alloys, dr. ir. Geurt Jongbloed for helping us in statistical data handling and dr. ir. Leo Veldhuis, dr. Steven Hulshoff, ir. Lars Bernhammer and ir. Nando Timmer for their help in aerodynamics and propulsion. Without their knowledge and efforts we would not be able to produce a result of the same level for our excersice.

Contents

Nomenclature

List of Abbreviations

AM	Air Mass
AOI	Angle of Incidence
BOL	Begin of Life
CCD	Charge Coupled Device
CDF	Cumulative Density Function
CF	Carbon fiber
CMOS	Complementary Metal Oxide Semiconductor
CPU	Computer Processing Unit
DC	Direct Current
DoD	Depth of Discharge
DSE	Design Synthesis Exercise
EOL	End of Life
FB	Functional Breakdown
FEM	Finite Element Method
FF	Fill Factor
FFD	Functional Flow Diagram
FIR	Far Infra Red
GaAs	Gallium Arsenide
GPS	Global Positioning System
HALE	High Altitude Long Endurance
HM	High modulus
ISA	International Standard Atmosphere
ISR	Intelligence, Surveillance an Reconnaissance
LCP	Liquid crystal polymer
LED	Light Emitting Diodes
LSB	Laminar Separation Bubble
MIMO	Multiple Inputs Multiple Outputs
MNS	Mission Need Statement
MPPT	Maximum Power Point Tracker
PAI	Polyamide-imide

PBO	Polybenzobisoxazole
PCB	Printed Circuit Board
PDF	Probability Density Function
PEA	Piezo Electric Actuator
PEEK	Polyetheretherketone
PEI	Polyetherimide
PES	Polyethersulfone
PO	Project Objective
PV	Photovoltaics
RAM	Random Acces Memory
RMA	Rubber Muscle Actuator
ROYGBIV	Visible spectrum (Red Orange Yellow Green Blue Indigo Violet)
RPM	Revolutions Per Minute
SAR	Synthetic Aperture Radar
Si	Silicon
SMA	Shape Memory Alloy
SNR	Signal to Noise Ratio
SSD	Solid State Drive
STC	Standard Test Conditions
TMA	Three-mirror anastigmat
UAV	Unmanned Aerial Vehicle
UD	Unidirectional
UHF	Ultra High Frequency
UHMWPE	Ultra-high-molecular-weight polyethylene
US	United States
UTS	Ultimate Tensile Strength
UV	Ultraviolet

List of Constants

σ	Stephan-Boltzmann constant	5.6704 e -8 [J/s/m^2/K^4]
c	Speed of light	299 792 458 [m/s]
k	Boltzmann constant	1.676 e -16 [J/K/kg]

List of Symbols

#pixels	Number of pixels in one picture	[-]
$\bar{U}$	Mean wind speed	[m/s]
β^*_{req}	Standard required twist angle	[°]
β_{c_m}	Additional twist angle	[°]
$\beta^*_{c_m}$	Standard additional twist angle	[°]
β_{req}	Required twist angle	[°]
Γ	Dihedral	[°]
Λ	Aspect ratio	[-]
λ	Operating wavelength of imaging sensor	[m]
λ	Taper ratio	[-]
μ	Mean in normal distribution	[-]
ϕ	Phase angle	[hr]
ϕ	Sweep	[°]
ρ	Density	[kg/m^3]
σ	Stability margin	[-]
σ	Standard deviation in normal distribution	[-]
σ^*	Standard stability margin	[-]
$\sigma_{\bar{U}}$	Wind speed standard deviation	[m/s]
τ	Overwatch	[J/m^3/kg]
f	Frequency	[Hz]
A	Amplitude	[m/s]
a	Speed of sound	[m/s]
b	Number of bits in one pixel	[-]
b	Span	[m]
c	Scale factor in Weibull distribution	[-]
C_D	Drag coefficient wing	[-]
C_d	Drag coefficient airfoil	[-]
C_L	Lift coefficient wing	[-]
C_l	Lift coeffiicent airfoil	[-]
C^*_L	Standard lift coefficient wing	[-]
C_r	Root chord lenght	[m]
C_t	Tip chord length	[m]
d	Cell size	[m]
d_{33}	coupling coefficient	[pm/V]

DR	Data rate	[bps]
f	Bandwidth frequency	[Hz]
f	Focal length	[m]
fps	Frames per second	[-]
G_r	Gain receiver	[dB]
G_t	Gain transmitter	[dB]
H	Altitude	[km]
h	Height	[m]
I	Irradiance	[W/m^2]
k	Shape factor in Weibull distribution	[-]
L_s	Free space loss	[dB]
P	Pressure	[N/m^2]
P	Transmitting power	[dB]
P_{avg}	Average incoming solar power	[W/m^2]
Q	Picture quality	[-]
r	Distance between transmitter and receiver	[m]
SNR	Signal to noise ratio	[dB]
T_s	System temperature	[K]
U(t)	Wind speed as a function of time	[m/s]
V_{des}	Design airspeed during cruise	[m/s]
V_{max}	Maximum airspeed	[m/s]
X	Ground Resolution	[m]

List of Figures

List of Tables

Summary

The objective of this project is to design a multi-functional, polymer, high altitude observation platform for a mission duration of one year at moderate latitudes. The cruise altitude must be above 15 km in order to avoid other air traffic. Furthermore 90% of the time station keeping must be guaranteed. The payload must be able to observe people on the ground and follow them if necessary.

An Unmanned Aerial Vehicle (UAV) powered by solar cells is designed for the most critical conditions it can encounter during this mission. These conditions occur at the 21^st of December at 55° north latitude. This is the shortest day of the year and the angle of incidence (AOI) with the sun is the largest, resulting in low irradiance (I) and relatively low efficiency of the solar cells, making energy collection more difficult. Also the wind speeds at 55° north latitude are relatively high in the winter, requiring a relatively high cruise speed to maintain station keeping.

From approximately the 10^th of November to 31^st of January at the highest latitude the 'banana' flight profile is flown during the day to collect enough energy. In this flight profile the solar panels are oriented more towards the sun to increase the incoming energy. The energy collected during the day is partly stored in batteries, which provide the UAV with power during the night.

The payload carried by the UAV is a camera placed at the bottom center of the structure pointing at the Earth's surface. It is capable of tracking and following an individual, with a field of view of 115 x 173 m and a pixel size of 2.6 cm during day. Imaging during night time is possible with a far infra-red sensor and gives a ground resolution of 8.05 cm with a field of view of 82 x 61 m. It weights 1.5 kg and requires 21.8 W of power.

Communication is done via satellites and two ground stations. S-band is used for data transfer and L-band is used for navigation. During the day data is send on a regular basis and during night the data is stored and send the following morning. The UAV has a back-up system in case of signal loss. The communications system requires about 100 W of power.

The take-off and landing are performed at an asphalted airfield with the assistance of trucks. The take-off length is 30 m and the landing distance is 69 m, the airfield length is therefore not a problem. During operation, one mission control ground station can be used to monitor multiple UAVs by a couple of operators, thereby reducing the overall operating costs.

The UAV has been designed for 8 years of operational life, where some parts need to be replaced regularly. The structure is mainly build from carbon fibre components, which last for the entire operational life and almost 90% is recyclable. The lightweight design requires little material and most parts that need replacement can be recycled or re-used. This makes the design quite sustainable.

Most parts of the UAV are made of polymers. The solar panels consist of 50% polymer, due to the cells being made of Gallium Arsenide (GaAs). This is the largest none polymer contribution of the UAV. The overall polymer content of the design is 85%.

The total lifetime of the aircraft is estimated at 8 years. The costs for the subsystems and their lifetime are taken into account. Some parts need to be replaced regularly within the the lifetime. The total estimated cost for one mission is about €980,000.

Chapter 1
Introduction

The aerospace industry is increasingly using lightweight (fibre reinforced) polymers as structural components. This results in fast and fuel-efficient aircraft, like the Boeing 787 Dreamliner, which is composed of around 50% composite materials (by weight) [1]. Besides uses in structural components, polymers are being developed to be used as flexible and light weight electronics, such as Light Emitting Diodes (LEDs), solar cells and batteries. Polymer based actuators are also being developed, such as shape memory polymers [2, 3] and electro-active polymers [4, 5].

The possibilities to use polymers seem to be growing rapidly, however introducing them in the existing market of passenger aircraft can take up to fifteen years. To keep pace with the rapid development of polymers it is convenient to reduce the introduction time of new materials on the market. This is done by turning toward other markets in the aerospace sector.

One of these markets in the aerospace sector is the development of Unmanned Aerial Vehicles (UAV) [6]. According to this study investments in the UAV market in Europe and the Asia-Pacific region are expected to be doubled by 2016. In this context the UAV market could be used as a test bed for new materials, being able to introduce new materials more rapidly compared to introduction in passenger aircraft.

One specific UAV to be designed in the context given above is a high altitude, long endurance observation platform constructed from mostly polymers. This UAV must remain airborne for one full year in a stationary position between 0° and 55° latitude at an altitude above 15 km. It should carry a payload which is able to observe Earth with enough accuracy to distinguish individuals. The design of this UAV is the task of the Design Synthesis Exercise (DSE) group 7 during the spring semester of 2013.

Important aspects to investigate for this mission are atmospheric conditions (wind speeds, gusts), energy collection and storage, payload design, communication, materials, aerodynamics and much more. Since there were not any design constraints on the layout, the team is free to design any type of vehicle (zeppelin, flying wing, multi-fuselage glider e.g.) and choose any type of energy collection/storage.

In the preliminary design phases, first the functions and requirements of the aircraft and the mission have been determined. A market analysis was performed and several mission aspects have been analysed including costs, risks, information flow and logistics. Several concepts have been generated and analyzed after which a trade-off between these concepts was done. In conclusion, a flying wing concept has been selected to fulfill the mission requirements.

This is the final report, as a result of the preliminary design phase which followed after the concept choice. In the final design phase the conceptual analysis on the flying wing was the starting point. In chapter 2 the mission description is given, this includes the top level requirements, the problem and mission need statements and the market analysis. The mission environment analysis is finalized, this is subdivided into wind and solar conditions and are together with the mission profile part of chapter 3. With the details of the mission and surroundings known, the subsystem design can be done, as described in chapter 4. This is split up into payload & communications, aerodynamics, performance & propulsion, batteries, solar panels & power point trackers, heat management and wing structure. An overview of the final design is given in chapter 5. In chapter 6 an analysis on the final design is given with operation and logistics, a cost breakdown and sensitivity analysis. A compliance matrix can be found here as well, along with the technical risks and sustainability analysis. Further development and recommendations are topics of chapter 7. The conclusions can be found in chapter 8.

Chapter 2
Mission Requirements

In this chapter the mission requirements are given. This is done in several steps, starting with the top level requirements in section 2.1. From these requirements and the objectives given in chapter 1, a Project Objective (PO) and Mission Need Statement (MNS) are derived. For the operation of the vehicle a Functional Breakdown (FB) structure and Functional Flow Diagram (FFD) are shown. Finally, the market analysis is given in section 2.4.

2.1 Top Level Requirements

The observation platform should comply with a number of requirements, these are formulated as the top level requirements and are listed below:

- Take-off and landing must be possible in wind force 3 conditions
- Maximum cross wind during take-off and landing of at least 5 kts
- Cruise altitude above all traffic, 15 km or above
- Cruise will take place between 0° and 55° latitude
- At cruise altitude, 90% station keeping must be guaranteed
- Able to fly non-stop for one full year
- Payload mass is limited to a maximum of 3 kg
- Payload should operate using less than 25 W
- The payload should be able to track individuals on the ground from cruise altitude, night vision is a plus
- On board energy storage is allowed
- Communication and data handling must be designed
- The costs of one mission should be less than 1 million euro based on a series of 100 units.

Apart from these top level requirements use of as many polymers in the vehicle as possible. Design elements should be multi-functional where possible. Although the design is not limited by size, it should be practical in use. Furthermore, sustainability is addressed during the entire design.

2.2 Project Objective and Mission Need Statement

From the top level requirements and the objectives given in chapter 1 the following project objective is formulated:

"*Design a multi-functional, polymer high altitude observation platform for a mission of one year at moderate latitudes by ten students in eleven weeks.*"

To identify the exact mission of the vehicle, a MNS is formulated. It is deducted from the top level requirements and PO and reads as follows:

"*Observe the Earth with sufficient accuracy to spot individuals from a stationary position above all air traffic for one year.*"

2.3 Functional Breakdown Structure and Functional Flow Diagram

The Functional Breakdown (FB) is a diagram showing the functions the (sub)systems should perform. It is a time-independent hierarchical tree where the main functions of the UAV are categorized by overall mission objective. The FB is shown in Figure 2.1.

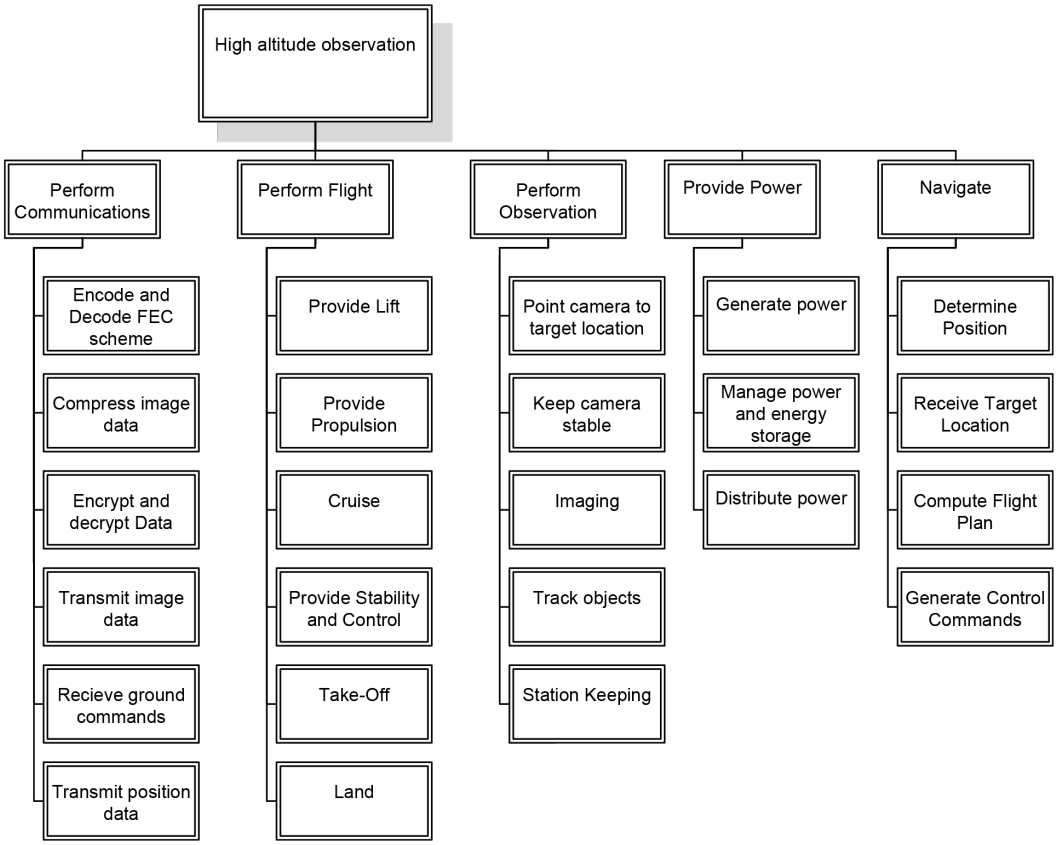

Figure 2.1: FB for the all plastic high altitude observation platform

In addition to the FB a Functional Flow Diagram (FFD) has been made to show the time-dependent structure of the different functions performed during the mission. Figure 2.2 shows the top level functional flow on top. These functions combine lower-level functions which are shown beneath the top level functional flow.

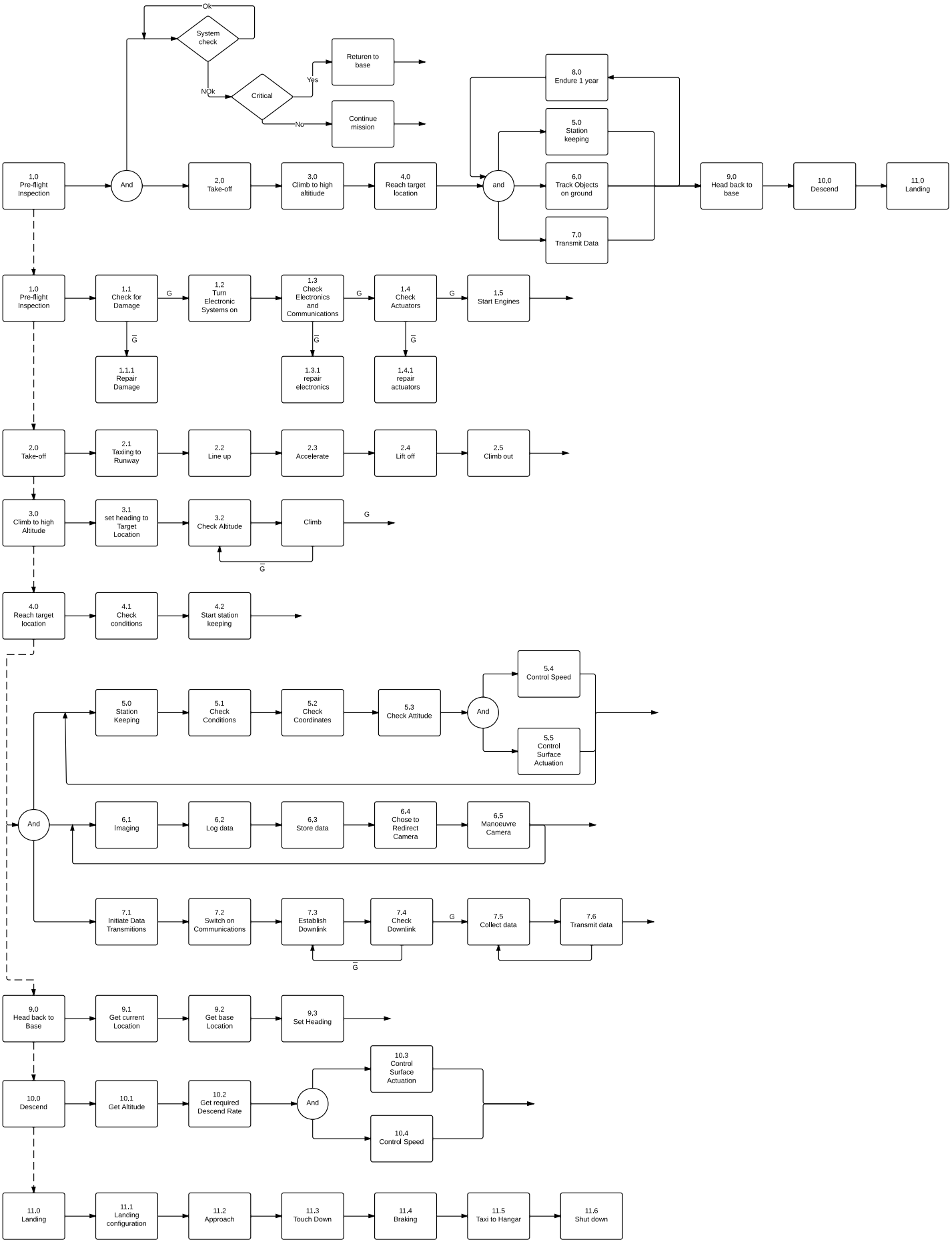

Figure 2.2: FFD for the all plastic high altitude observation platform

2.4 Market Analysis

Before a project initializes, the markets in which it can be used should be analyzed. During this project a UAV is designed, therefore an analysis of the global UAV market is performed. Recent trends, potential customers and their specific needs are investigated and discussed in this section.

2.4.1 The UAV Market

From a study performed by Lucintel [6] it is concluded that the market for UAVs is growing. The world spending on UAVs in 2010 was five billion dollars and expected to grow to 11.4 billion dollars in 2021. In the 2010 budget roughly 1/3 of the spendings on UAVs was from the High Altitude, Long Endurance (HALE) type, which is closely related to the UAV to be designed. Especially the United States invested extensively, producing 75% of the HALE type UAVs.

The type of mission for the UAV is best described as an Intelligence, Surveillance and Reconnaissance (ISR) mission. This type of mission is often used for military purposes but could also be used in civil markets [7]. Different customers put different requirements on the vehicle in terms of station keeping, resolution and update time.

2.4.2 Competitors

Observation missions can be carried out in a variety of ways. Competing options are satellites, manned flights and low endurance and/or low altitude UAVs. There are advantages and disadvantages to use a HALE UAV over the competitors which are listed in Table 2.1.

2.4.3 Customers

It is important for any design project to define the possible customers. Therefore a customer analysis is performed. This is done by looking at what HALE UAVs can do, and then looking at what would be interesting for a possible market. After this research four main groups are defined:

- Military
- Civil
- Science
- Mapping

The military group would be interested in observation and surveillance mission. The UAV could be useful for the civil market as well because they can spot fires, observe traffic etc. The science group could track animals down to a size of 2.6 cm during the day (section 4.1), they could observe coastal lines, image ocean population. What would also be possible is to change the sensor for other scientific uses as long the payload has a lower weight then 3 kg and a lower power consumption then 25 W. Another application is the possibility of mapping for one whole year. This could be useful to create high resolution Earth maps, as there is a possibility for image storing without communication. In Table 2.2 further possibilities and who could be interested in them are discussed.

For a lot of private companies and commercial purposes, purchasing and utilising the UAV for several years (system purchase includes several mission, section 6.2) may not be necessary or could be a risky investment. The military might, but the number of (private) companies that are able to do so and may find use for it during that whole period are limited. Providing lease and rent services should bring an outcome to those who would like to make use of the UAVs capabilities to a lesser extent. A company could lease the UAV for less than eight year-long missions and then switch users through the same lease-system or be sold for a lower unit cost. In regard to renting, hours, days, weeks or months could be reserved through the year by different companies to make use of the UAV for their purposes. This option should be especially interesting to those who require use for the system only for one (short and) specific purpose. This whole concept however, requires deeper analysis of, for example, investment costs and interest rates which will not be treated any further in this report.

Table 2.1: Advantages and disadvantages of HALE UAVs compared to other methods

Advantage	**Remarks**
	Satellite
No ground track for UAV.	A satellite can not provide constant surveillance due to the type of orbit flown. The UAV can provide this.
A UAV is more flexible for mission changes.	A satellite must change its orbit if a different area is to be surveyed and lose valuable fuel, whereas the UAV will simply fly to the new destination.
A satellite needs to be launched.	Bringing a satellite into orbit is expensive due to the launcher needed. A UAV can take-off from almost every airfield at any time.
Repairs are not possible in space.	If for example the camera breaks down, the UAV can land where the satellite is rendered useless.
	Manned flight
Higher endurance for the UAV.	A manned flight can not be airborne for one full year
No equipment for pilot in UAV.	Since there is no pilot, weight can be saved by eliminating the need to pressurize and hold and protect the pilot.
Hazardous areas can be observed.	The absence of a pilot allows the UAV to operate in dangerous areas, war zones or extreme weather conditions.
	Low endurance and/or altitude UAV's
More time on target with HALE	With a low endurance UAV the surveillance time is less
Less ground operation	Due to long endurance, a HALE UAV spends less time on the ground, reducing the use of airfields
Longer range for HALE UAV	Because it can fly one full year, the range is indefinite during this year, eliminating the need to take-off or land in dangerous areas.
Less exposure from ground.	Due to high cruise altitude, a HALE is more difficult to spot and reach compared to a low altitude UAV.
Disadvantage	**Explanation**
	Satellite
Lower field of view for UAV.	A satellite operates at a higher altitude so a larger field of view is possible.
	Manned flight
The controllability is harder for a UAV	The algorithm for an UAV is complicator then that for a manned flight.
	Low endurance and/or altitude UAV's
Damage can be seen earlier with a low endurance UAV	A low endurance UAV must land more often then a HALE UAV, during this landing a check up can be performed.

Table 2.2: Possible interests of different markets

	Military	Science	Civil	Mapping
Different payload	✓	✓	✓	✓
Faster cruise speed	✓	✓	✓	
Bigger loiter radius	✓	✓	✓	
Laser pointer	✓	✓		
Bigger field of view	✓	✓	✓	✓
Smaller ground pixel size	✓	✓		
Flying different patterns	✓	✓	✓	✓
Stealth	✓			

Chapter 3

Environmental Analysis

In this chapter the overall mission and its environmental conditions are discussed. In section 3.1 the atmospheric conditions concerning the wind and gusts are explained. Then, in section 3.2 the solar conditions and solar panel performance are elaborated upon. Finally, in section 3.3 the mission and flight profiles are explained. This chapter is the basis for the design of the subsystems, the topic of the following chapter.

3.1 Wind Analysis

The purpose of the wind analysis is to gain insight into wind speeds and their variation through latitude, height and time. The wind speeds directly correlate to design constraints on station keeping, engine power required, solar array size, aerodynamics and many more. The first objective of the analysis is to provide an estimate on design wind speed and altitude or in other words the cruise condition analysis. The second objective is to give a seasonal analysis on the wind speed to determine when and where the worst day with respect to power required and solar incidence angle occurs. The last objective is to give insight into gusts for take-off landing climb and cruise conditions followed by a final conclusion on the occurring wind conditions for this design.

3.1.1 Cruise Condition Analysis

First a three dimensional dataset is created. This data set with wind speeds versus altitude, latitude and time is then used together with reference standard deviations to create a Weibull distribution of every coordinate in three dimensions (height, latitude and time). Finally an estimate on design wind speed is made from the cumulative distribution with respect to the station keeping requirements.

Fourier Approximation

Altitude and design wind speed are determined with the use of the data sets from *Global atmospheric circulation statistics*, A.H.Oort [8]. Earlier analysis of that data is provided from "Monthly Mean Global Climatology of Temperature, Wind, Geopotential Height and Pressure for 0-120 km" al [9]. In this analysis it is explained that the data sets are made with a Fourier approximation and Gaussian in order to extrapolate and smoothen. The paper *The contribution of small - scale wind and photovoltaic renewable energy sources to the scottish energy mix* Fowler [10] and webpage Java applet *Java Applet on signals* Crutchfield [11] were used as reference in the approximation of the Fourier signal. Equation 3.1 shows the Fourier approximation used.

$$U(t) = \bar{U} + (A_1 cos\,(f_1 \cdot t + \phi_1) + A_2 cos\,(f_2 \cdot t + \phi_2) + A_3 cos\,(f_3 \cdot t + \phi_3)) \qquad [\mathrm{m/s}]$$

$$\text{Where; } f_1 = \tfrac{2\pi}{8550}, f_2 = \tfrac{4\pi}{8550}, f_3 = \tfrac{6\pi}{8550} \qquad [\mathrm{Hz}] \tag{3.1}$$

$$0 < t \leq 8766(365.25 \cdot 24) \qquad [\mathrm{hr}]$$

Where $U(t)$ is the wind speed signal, subscript 1 denotes the annual cycle, subscript 2 denotes the semi-annual cycle, subscript 3 denotes the three-annual cycle, $\bar{U}$ is the yearly mean wind speed, $A_{1,2,3}$ are the various amplitudes of the cycles, $f_{1,2,3}$ are the various frequencies of the cycles, $\phi_{1,2,3}$ are the various phase angles of the cycles or in other words the time where the maximum occurs and t is the time in hours over a duration of one year.

The amplitudes, phase angles and yearly means are provided by the data set A.H.Oort 1958-1973 [8]. For every altitude at every latitude a signal is created. This signal approximates the mean μ at various values for t in hours.

Table 3.1: Standard deviations [12] averaged per month

Month	$\sigma_{\bar{U}}$
Januari	4.75
Februari	6.10
March	4.10
April	2.50
May	2.50
June	2.50
July	2.35
August	2.40
September	2.45
October	2.25
November	4.20
December	7.05

Standard Deviation

The variation of the means is estimated with data from "Statistical wind analysis for near-space applications" Roney by [12] and averaged over the two measurement points taken in the paper. Their averaged values are presented in Table 3.1.

Weibull Distributions

Every coordinate in latitude, altitude and time now also includes it's standard deviation. From that data the Weibull parameters are calculated for every coordinate, resulting in a 3D matrix with a k (shape) and c (scale) parameter for every coordinate.

$$\begin{aligned} k &= \left(\frac{\sigma_{\bar{U}}}{\bar{U}}\right)^{-1.086} \quad [\text{-}] \\ c &= \frac{\bar{U}}{\Gamma\left(1+\frac{1}{k}\right)} \quad [\text{-}] \end{aligned} \tag{3.2}$$

Equation 3.2 from Roney 2007 [12] are used to calculate Weibull parameters k (shape) and c (scale) where $k > 0$, $c > 0$ by definition. The parameter limits are estimated from reference data [12] $1 < k < 10$ and $0.1 < c < 20$ to exclude the cases where $k \to \infty$ for $\bar{U} \to 0$ and $c \to \infty$ for $k \to 0$. With those parameters a Weibull probability distribution and a Weibull cumulative density distribution are made (Figure 3.1).

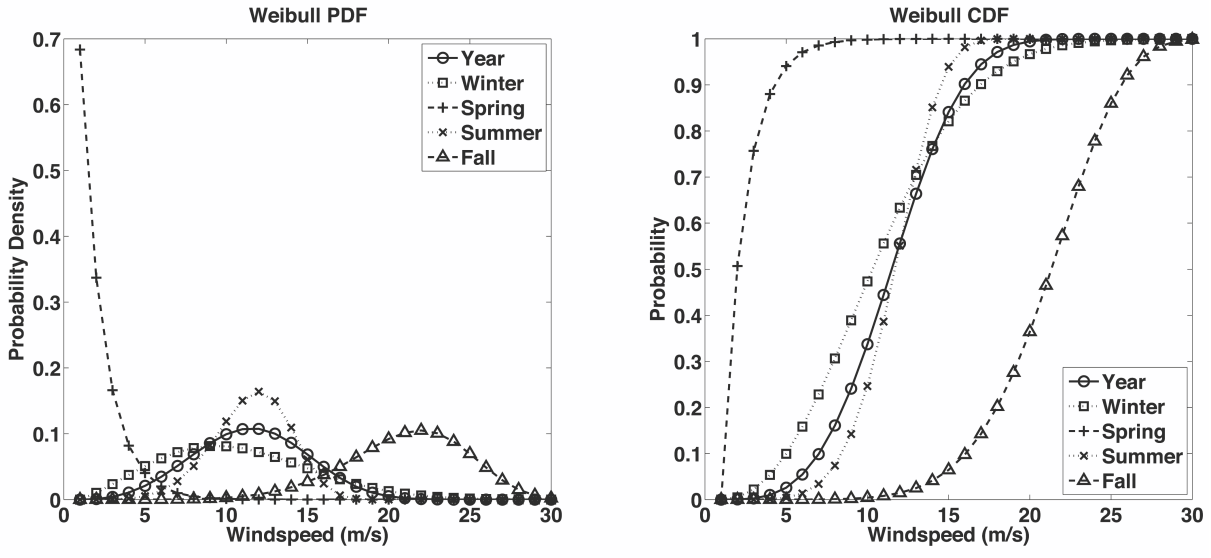

Figure 3.1: Preliminary Weibull distribution at 55° latitude and 18 km altitude Northern Hemisphere.

Conclusion

From the Weibull distribution an engineering estimate is made taking into account that this coordinate is one of the worst conditions. Therefore the design wind speed preliminary estimate was 25 m/s with an altitude of 18 km with a 90% probability on the Weibull cumulative distribution. The preliminary maximum design wind speed was set at 30 m/s which is the right tail of the fall PDF. The spring PDF is odd since the mean values for the spring are lower then the other seasons. Since these are lower values they are not do not have to be further analyzed. This distribution does not give a total picture on global wind speed expectance since only one coordinate is plotted. Therefore further analysis is required with plots including every coordinate for comparison.

3.1.2 Seasonal Analysis

Further analysis on wind speeds is done by taking a look at the seasonal variations. With the 3D data matrices described in subsection 3.1.1 contour plots is made. From these plots a final design wind speed and altitude are estimated. Finally a conclusion is drawn on the various wind conditions the design encounters.

Seasonal Plots

Plots are made for every season and for the entire year. Per season and for the entire year four plots are generated. The seasonal plots are shown in Appendix A. The yearly plots are presented within this section.

The first plot gives the failure volume which is the times counted that the wind speed exceeds the maximum design wind speed of 30 m/s. These area's are therefore the no fly zones as station keeping and/or structural integrity can not be guaranteed. The failure volume in times of occurrence counted is plotted in the out of plane direction with respect to the altitude in km on the vertical axis and the latitude in degrees on the horizontal axis.
Although failure volumes can be higher than 20 times per year, a 20 times failure was considered to be the plot upper limit as the goal is to let failure never occur in an entire year, hence the failure volume should be zero. Values higher than 20 are therefore outside the scope of this analysis.

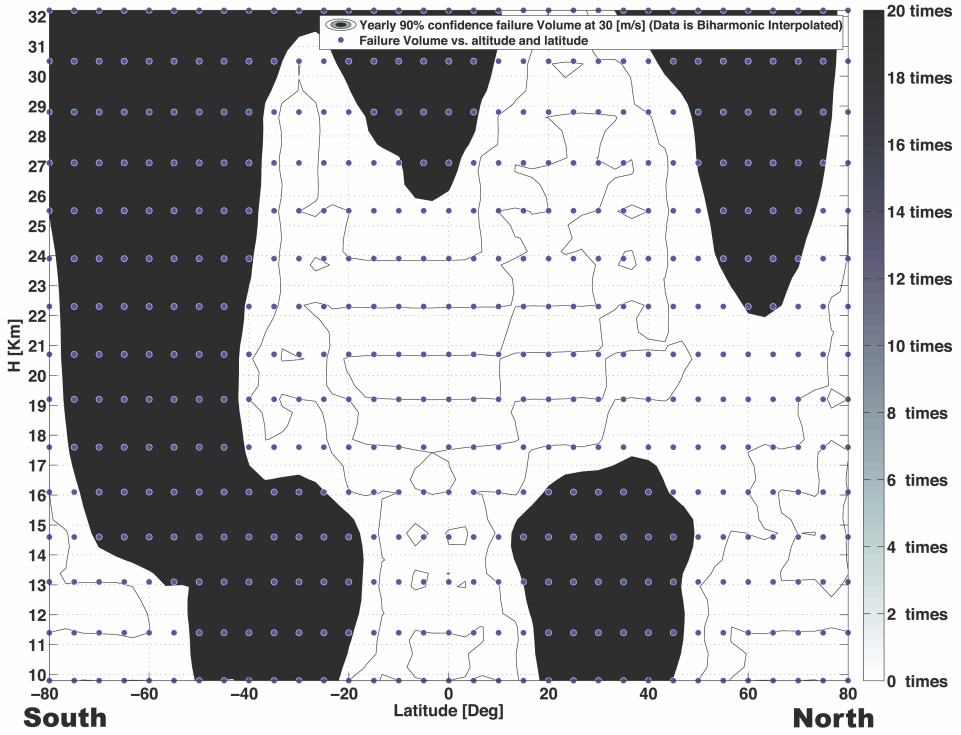

Figure 3.2: Yearly failure volume (Times wind speed exceeds max design wind speed)

The second plot (Figure 3.3 gives the average wind speeds from which the operation field (Alti-

tude, latitude and time of year) can be chosen in order to minimise propulsion power required. The average wind speed in m/s is plotted in the out of plane direction with respect to the altitude in km on the vertical axis and the latitude in degrees on the horizontal axis. Although maximum Weibull 90% confidence wind speed is set on 30 m/s actual wind speeds can be much higher. Since 30 m/s is the maximum design windspeed higher values for wind speed are outside of the scope of this analysis.

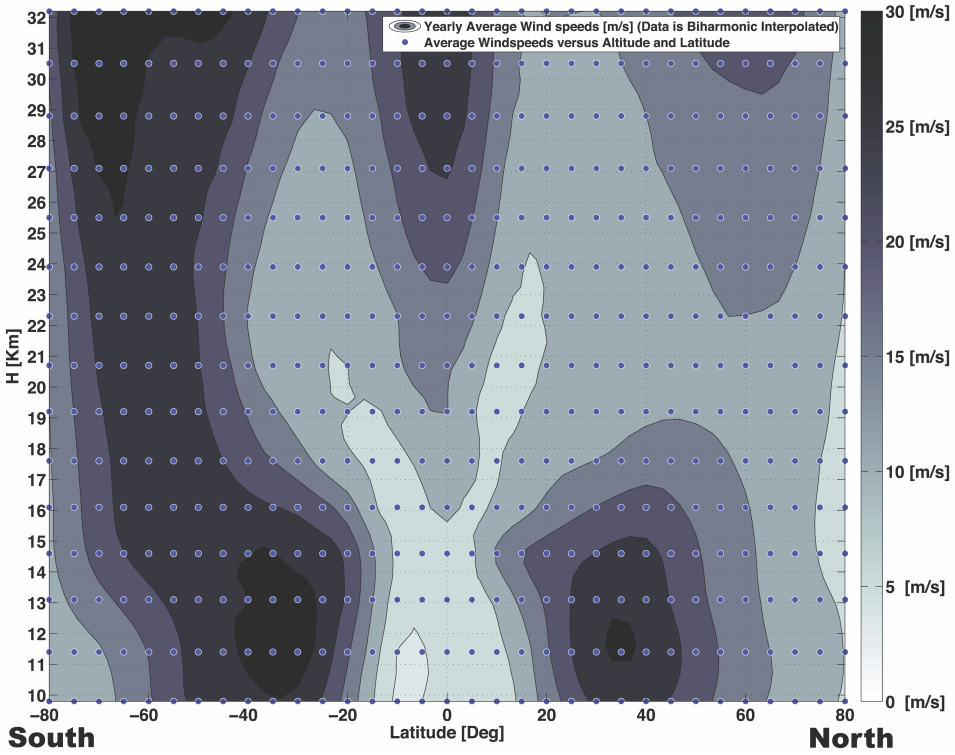

Figure 3.3: Yearly average wind speeds

The third (Figure 3.4) and fourth plot (Figure 3.5) give the minimum and maximum wind speeds respectively, which influence the minimum and maximum airspeed requirements discussed further in (section 4.3). The minimum and maximum wind speeds in m/s are plotted in the out of plane direction with respect to the altitude in km on the vertical axis and the latitude in degrees on the horizontal axis.

First the yearly winds speeds are plotted. After that, the data for seasonal plots is plotted and can be found in Appendix A. Summer is set to July, August and September, fall to October, November and December, winter to January, February and March and spring to April, May and June due to data constraints (per month blocks). Please note that the shortest day (21^{st} of December) hence occurs in the fall. Also note that wind speeds may vary along longitude but are outside of the scope of this analysis.

Conclusion and Notes on Wind Data

All mentioned seasons with the plots are on the Northern Hemisphere unless explicitly stated otherwise. Note that the plots made are the 90% confidence Weibull values. This means that if the wind speed notated can be flown, the station keeping requirement is met (see section 4.3. Also note that in the plots no difference between easterlies and westerlies or other directions was made since only absolute values of windspeed are used.

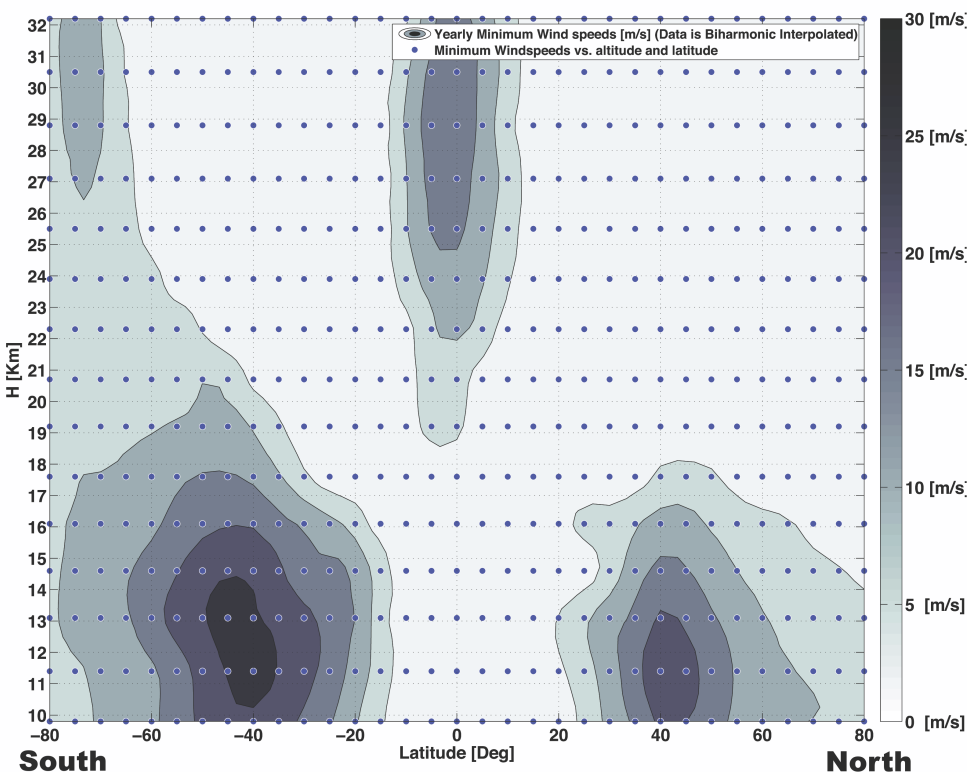

Figure 3.4: Yearly minimum wind speeds

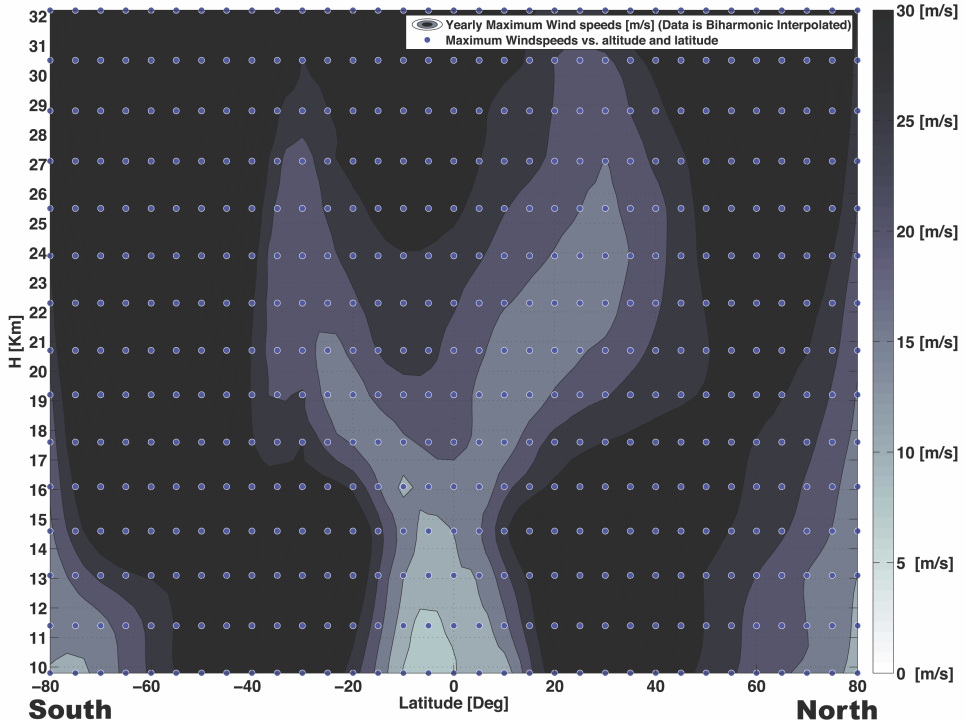

Figure 3.5: Yearly maximum wind speeds

Yearly Wind Data

From Figure 3.2 the field of operation is recommended between $-40° \leq \phi \leq 80°$ latitude for 18 km $\leq H \leq$ 22 km altitude. This is solely based on the avoidance of the no fly zones where wind speeds exceed the maximum design wind speed of 30 m/s.
Those no fly zones consist of the two subtropical jet streams (black circles) at roughly $\phi = \pm 35°$ latitude for 11 km $\leq H \leq$ 13 km altitude and the two polar jet streams at roughly $\phi = 60°$ latitude for $H \geq$ 22 km altitude with variations to $\phi = 0°$ latitude for $H \geq$ 26 km altitude on the Northern Hemisphere and at roughly $H \geq$ 16 km altitude and $\phi = \pm 60°$ latitude for the Southern Hemisphere. The northern polar jet stream oscillates between latitudes as where the southern polar jet stream can vary in altitude and is much more powerful then the northern one. These jet streams occur due to global movement of air at high windspeed due to the earth's rotation and atmospheric heating. Information on Earth's meteorology was used from *Meteorology for Scientists and Engineers* by R.B.Stull [13].

Figure 3.3 confirms the recommendation for the field of operation of 18 km $\leq H \leq$ 22 km altitude for $-40° \leq \phi \leq 80°$ latitude since this is also the area where there is a low average wind speed (20 m/s and below) which results in a low propulsion power requirement.

Figure 3.4 and Figure 3.5 show that there is great variation between minimum and maximum wind speeds. From Figure 3.5 a field between 18 km $\leq H \leq$ 22 km altitude for $-40° \leq \phi \leq 40°$ latitude can be concluded where the mission will not be affected by wind speed with a certainty of at least 90% (Weibull CDF limit).
The question then remains where and when these minimum and maximum wind conditions occur and how they influence the mission on latitudes higher than $\phi = \pm 40°$.

Summer Wind Data

From Figure A.1 it can be concluded that for the earlier stated altitude there are no limitations on latitude for the field of operations as long as the power available due to lower incidence angles at high latitudes allows this (See also section 3.2. It can also be concluded that almost all global wind speeds don't exceed the maximum design wind speed of 30 m/s.
From Figure A.2 it can be concluded that the summer winds are fairly stable and that there are no big differences between the Northern (Summer) and Southern (Winter) Hemisphere even though the Southern Hemisphere is in its winter season. Also the wind speeds are relatively low compared to the other seasonal plots on both Hemispheres.

Fall Wind Data

From Figure A.3 it can be concluded that during fall wind speeds on the Northern Hemisphere drastically increase and that the field of operations is thereby limited to $-40° \leq \phi \leq 55°$ latitude for 18 km $\leq H \leq$ 22 km altitude. Also the number of sun hours on the Northern Hemisphere is getting less due to an incidence angle which is decreasing furthermore the average wind speeds increase thereby increasing the propulsion power required whilst decreasing the amount of available power. It is noted that this season is the best candidate for the worst conditions possible because of it's relative high average wind speeds and low incidence angle at high latitudes on the Northern Hemisphere.
From Figure A.4 it can be concluded that wind speeds vary slightly but are most of all relatively high compared to the other seasons.

Winter Wind Data

From Figure A.5 it can be concluded that during this season the wind speeds on the Southern Hemisphere reach their yearly maximum value and the wind speeds on the Northern Hemisphere are relatively low compared to the Fall. This results in a field of operations of $-40° \leq \phi \leq 80°$ latitude for 18 km $\leq H \leq$ 22 km altitude. It is noted that this field of operation is most likely limited by it's solar conditions at high altitude for this season.
From Figure A.6 it can be concluded that the wind speeds during winter do not vary much. The minimum and maximum are reasonably close together.

Spring Wind Data

From Figure A.7 it can be concluded that during spring wind speeds on the Southern Hemisphere increase and that the field of operations is thereby limited to 18 km $\leq H \leq$ 22 km altitude for $-35° \leq \phi \leq 80°$ latitude. Also during spring wind speeds on the Northern Hemisphere are relatively low compared to the other seasons.

From Figure A.8 it can be concluded that there is almost no variation in the wind speeds as the minima and maxima are fairly close to each other.

Wind Data Summary

Operating latitudes are limited on the Southern Hemisphere in Spring to $\phi = -35°$ with wind speeds of 25 m/s average with peaks up to almost 30 m/s. However since there is enough power available due to a relative slightly higher incidence angle compared to the Northern Hemisphere this is expected to only limit operations to $\phi = -40°$. There is more solar power available hence there can be more propulsion power required.
Operating latitudes are limited on the Northern Hemisphere in Fall to $\phi = 55°$ with wind speeds of 25 m/s average with peaks over 30 m/s at $H = 18$ km. Since December (included in Fall) has the shortest day this becomes really critical as there is also the lowest yearly value of solar power available. It is recommended that operational altitude in Fall is limited to 18 km $\leq H \leq$ 22 km with an operational latitude of $-40° \leq \phi \leq 55°$. Slightly increasing the altitude for this coordinate ($H = 18$ km, $\phi = 55°$) with ≈ 500 m would slightly decrease the average wind speed but most of all will avoid the maximum wind speeds of up to 30 m/s and above (Figure A.3a)
As long as there is enough power available extreme latitudes are manageable. Problems are expected on the Northern Hemisphere especially on the shortest day of the year ($\approx$ 21 December). It is noticed that the more extreme wind speeds occur at the Southern Hemisphere around Antartica. It may be assumed that the extreme low ground temperatures together with a big white ice land mass results in thermal circulation locally in the atmosphere due to solar reflectance. Next to that it is also noted that the Northern Hemisphere has calmer atmosphere which is assumed to be caused by a better land to water ratio then the south.

3.1.3 Gusts

During the mission, gusts can influence the speed and stability of the vehicle. Three gust requirements are used. During take-off and landing the given requirement of 5 kts indicates wind or gust speeds up to 2.6 m/s. This affects the take-off and landing yaw control which is discussed in section 4.3. In flight, up to an altitude of 20,000 ft (6096 m) possible gusts of 50 ft/s (15.2 m/s) have to be taken into account as stated in the CS-23 airworthiness requirements *Certification Specifications for Normal, Utility, Aerobatic, and Commuter Category Aeroplanes CS-23* by (EASA2012) [14]. From 20,000 ft up to 50,000 ft (15,240 m) the gusts decrease linearly to 25 ft/s (7.6 m/s). Longitudinal stability depends on these vertical gusts. A stability analysis based on vertical gusts is performed in "Stability" included in section 4.3.
Furthermore, gust speeds at cruise altitude are taken into account based on the effective gust velocity [15].

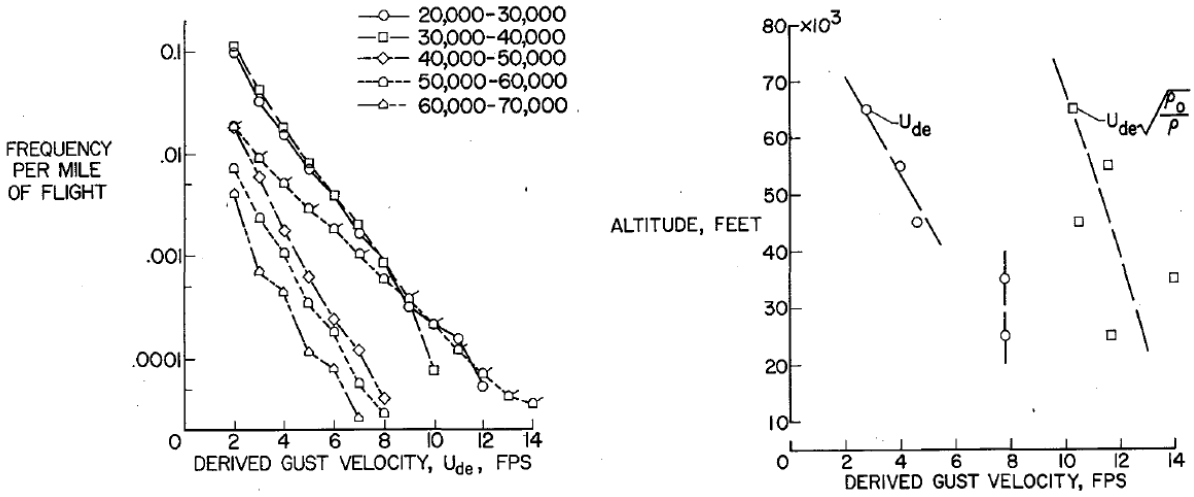

Figure 3.6: Probability U_{de} per mile & average U_{de} against altitude [15]

The graphs on the left hand side in Figure 3.6 show the frequency per nautical mile of gust speeds for different altitudes. With a cruise speed of 22 m/s, the total distance flown during a mission length of one year is approximately 375,000 Nautical mile. At altitudes of 60,000 ft and higher the maximum gust velocity (U_{de}) that is designed for should occur a few times during the mission and will have a frequency in the order of $1 \cdot 10^{-5}$ per mile (3-4 times a year) from the

corresponding graph, this velocity is estimated around 8 ft/s. In the graph on the right hand side of Figure 3.6 the mean true derived gust velocity (U^*_{de}) is compared to the mean derived gust velocity. At an altitude of 18 km, a factor of 3.2 should therefore be applied to obtain this true derived gust velocity, resulting in 25.6 ft/s as the maximum true derived gust velocity. This is still a derived gust velocity and should be converted to the effective gust velocity. A method using the conversion factor k'/k_g has been used "A revised gust-load formula and a re-evaluation of v-g data taken on civil transport airplanes from 1933 to 1950" by Walker [16]. Using formulas (4), (9) and (14) in this method a conversion factor of 0.3 has been obtained. Multiplying this with true maximum derived gust velocity, the true maximum effective gust velocity of 7.5 ft/s, 2.3 m/s, is found.

3.2 Solar Incidence Angle

The mission is designed for the worst possible conditions. During mid winter at 55° north latitude the amount of sun hours is only 6.9 and the average Angle of Incidence (AOI) with the sun is about 82°. Because of this large AOI the average irradiance (I) is only 190 W/m^2 [17]. The AOI is defined as in Figure 3.7 [18].

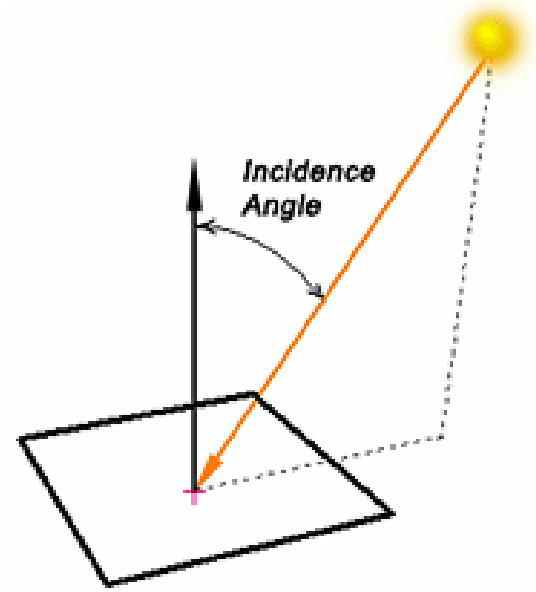

Figure 3.7: Angle of Incidence

The incidence angle is the 3-dimensional angle between the surface normal and the current position of the Sun. The smaller the AOI the higher the energy density per unit area will be. This effect can be calculated using the cosine law, where the irradiance from the sun is simply multiplied by the cosine of the AOI. The estimated solar irradiance at cruise altitude all year round is given in Figure 3.8.

Also with increasing AOI the performance of the solar cells becomes less efficient. The angular performance is given in Figure 3.9.

At an AOI of 82.2°, the relative efficiency is about 49%. This means only 49% of normal power output is available, resulting in too little power. Therefore the AOI needs to be decreased during flight with special manoeuvres. These manoeuvres are explained in section 3.3. If the AOI could be decreased with 10° to 72.2° for instance, the relative efficiency of the solar cells becomes 78.6% already.

Good performance of the solar cells with high efficiencies is very important for the design, since the incoming energy in winter time is very limited.

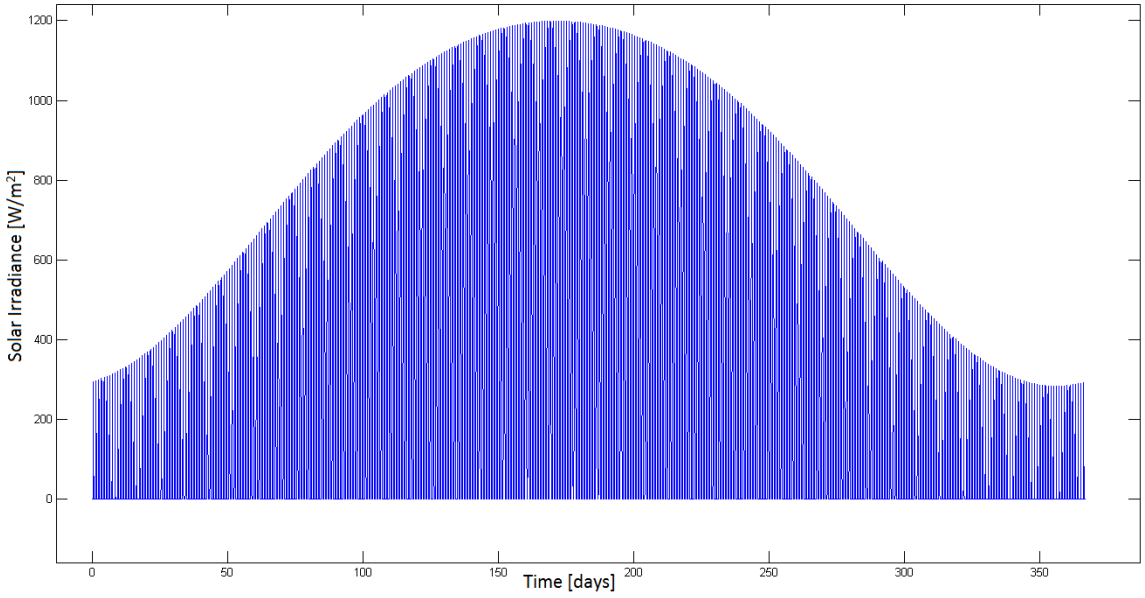

Figure 3.8: Solar Irradiance for one year

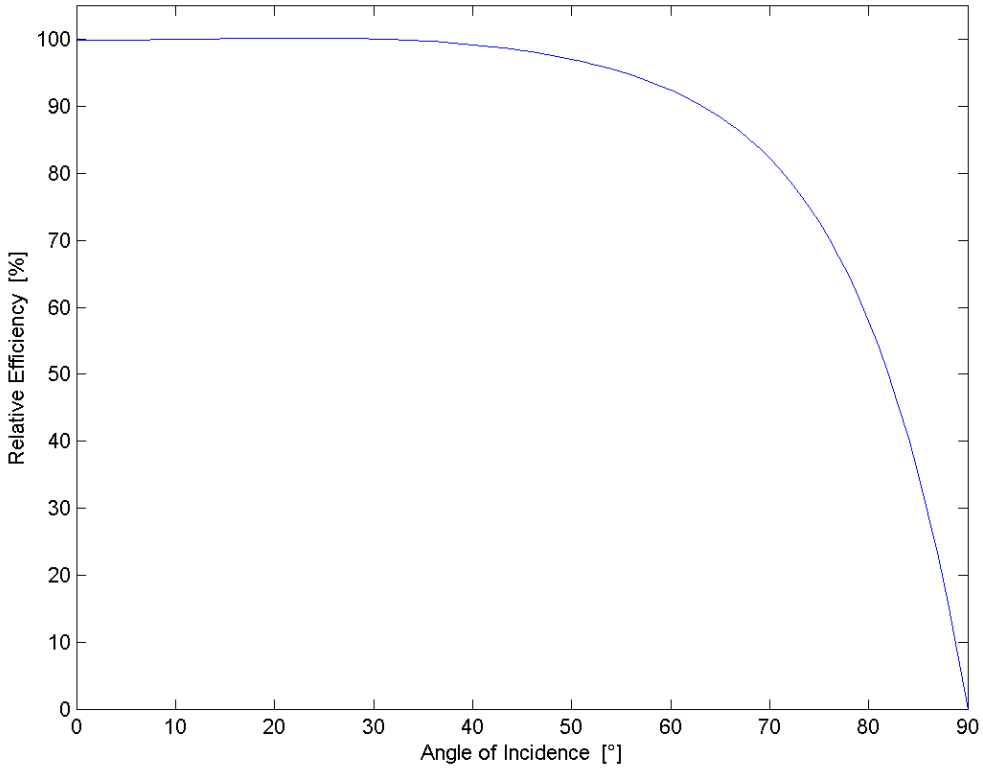

Figure 3.9: Angular performance of solar panels

3.3 Mission Profile

In this section the mission profile is given (subsection 3.3.1), critical conditions of the mission are stated (subsection 3.3.2 and several flight profiles will be discussed (subsection 3.3.3).

3.3.1 Mission Profile

The observation mission is based on a one year mission duration while keeping station at high altitude. Stationary in this context means that the payload can observe its target. At an altitude of 18 km and directly above target, the payload needs to stay within 1 km of that point. This implies that the space in which the UAV has to perform its mission consists of a circle with a 2 km diameter. The mission starts with a take-off followed by a climb to the cruise altitude (18 km) within 24 hours. At cruise altitude the UAV will fly to a specified target area for observation where the payload is switched on. During the mission, the UAV might have to fly to different locations depending on the customers needs. During these periods the payload will be switched off to enable faster cruise. After one full year or in case of emergency the UAV will fly back to a landing site, descend and land. To maintain a stationary position at cruise altitude, the flight profile has to be determined, which will be discussed in subsection 3.3.3.

3.3.2 Critical Conditions

From section 3.2 it is clear the AOI on the solar panels is very high during the winter at high latitudes. Since these high angles are both detrimental for the incoming energy and the operating efficiency of the solar panels, these conditions are critical for the design. The most critical conditions during the mission therefore occur when this incoming energy is lowest; 21^{st} of December, on the highest latitude; 55° north. In section 3.1 the wind conditions for 90% station keeping during these critical conditions require the aircraft to fly at speeds of 22 m/s. Maximum wind speeds that can occur are 30 m/s.

3.3.3 Flight Profiles

Several flight profiles are considered. One flight profile considered performs a climb during the day from 18 km to 21.5 km arriving at the highest altitude at sunset, a gliding circular turn back to 18 km afterwards and circling the rest of the night at cruise altitude. In theory this profile should require less batteries since during the gliding part of the night the engines are switched off. In practice the problem is the extra required energy required to climb. Therefore this profile is not implemented during the design.

For minimizing power required while still guaranteeing station keeping a continuous coordinated turn at 18 km altitude can be flown with a bank angle of 4.5°. In this profile, high solar incidence angles are critical for the design. Moreover, the circular path in combination with a bank angle decreases the solar influx, because during a part of the circle the solar panels will face away from the sun. This profile is used on days without energy shortage (31^{st} of January to the 10^{th} of November at 55° north latitude) and during the night. When the wind speeds increase this circle becomes more elliptical and once the wind speed is equal to or higher than the airspeed, the UAV will fly a straight path. Since 90% station keeping is guaranteed with the current velocity of 22 m/s, 10% of the time the UAV will drift off while flying into the direction of the wind.

A different profile was designed to increase the AOI and thus the available power. The principle of this profile is to have a shallow, 10° banking turn with the wings inclined towards the sun as much as possible. Once the flight direction starts facing the sun (and the AOI increases), a sharp, low speed and high bank angle turn of 180° is performed after which the same shallow bank is performed in opposite direction. An example of this profile in zero wind conditions can be seen in Figure 3.10. The next three subsections will describe the different phases of this profile in further detail.

Turn-around

To optimize the energy gained by performing aforementioned maneuver, the turn-around time needs to be minimized, since during this bank the wings become tangential with the sun and thus receive very little to no energy. This is done by increasing the bank angle to 40° and by flying at the minimum turning speed for this bank angle of 17 m/s to minimize the turn. The turn-around also includes two rolls during which the bank angle changes. One roll changes the bank angle from 10° to 40°, this takes approximately 2.7 s. Then the aircraft has to turn back another 50° in order to have the wings facing the sun again, taking 4.5 s. During these maneuvers

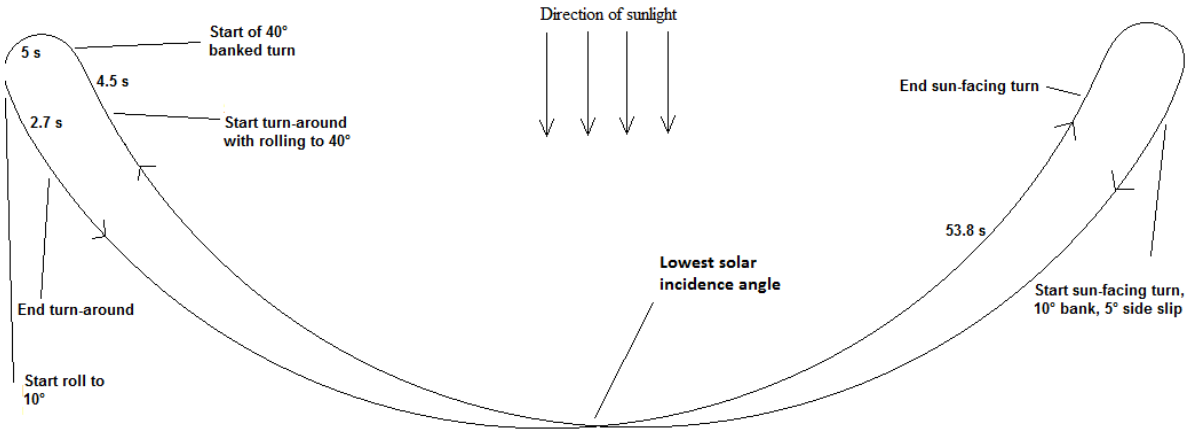

Figure 3.10: Top view of the flight during zero wind conditions

the UAV rotates about 40° of the total required 180°, this leaves 140° in high-bank turning. The high-bank turn has a radius of 35.1 m and takes about 5 s to perform. The time of the total turn-around will then equal 12.2 s. Only one third of this time the solar panels are able to gather energy from the sun.

Sun-facing turn

To determine the optimal sun-facing turn, the net energy gain of the full profile should be considered. Flying at 22 m/s with a 10° bank angle will result in a turn-radius of 280 m. However, flying with side slip of 5° increases the effective radius by decreasing the effective turn angle, the resulting drag penalty is explained in subsection 4.3.2. The radius with side slip becomes 563.9 m. In case the sun-facing turn is 180°, the UAV will fly towards the sun at the ends of the turn. The corresponding AOI will be less than the incidence angle without banking. During the worst conditions this AOI is equal to 82.2° with the corresponding relative efficiency of the solar panels of 49%. In the center of the turn the AOI will be 72.2° with a relative efficiency of the solar panels of 78.6%. A relation has been established between the position on the circle, the AOI and the relative solar panel efficiency. For different fractions of the 180° turn, the average efficiency and duration have been determined. Combining this duration and the turn-around time in which 2/3 of the turn is spent without energy gain, the average efficiency of the whole flight path is determined. The highest average efficiency followed at a circular fraction of 0.66 (118.8°). The duration of this sun-facing turn is 53.8 s, with a total flight path duration of 130 s. Without wind, the length of the flight profile is approximately 1,040 m, well within the maximum of 2 km.

Wind effects

In the previous section the sun-facing flight profile has been described without wind. In this section wind effects on this profile are considered. In the region where this flight profile is used; northern latitudes between 49° to 55°, the wind predominantly comes from the west, referred to as the westerlies [19]. Since the direction of the sunlight relative to the UAV comes from the south [20], the sun-facing turn in combination with the westerlies leads to turns that are mainly flown with either headwind or tailwind. During headwind the sun-facing turn is repeatedly flown in the same direction until the UAV has reached its ground-track limits (2 km). A turn-around is performed followed by a sun-facing turn with tailwind. This turn can only be fully performed when the wind does not exceed 18 m/s as this will drift the UAV 960 m during the turn resulting in a total ground track of 2 km. Higher wind speeds imply that the turn-around has to be performed before the whole 118.8° turn has been flown. It can be concluded that easterly and westerly winds can be combined with this profile and can be flown most of the time.

Northern and southern winds will change the profile, as the UAV will drift off during the sun-facing turns. This can be compensated by flying into the wind direction between these turns which will increase the AOI. However, northern winds can be somewhat beneficial as the angle of attack increases the AOI slightly. Southern winds are worst and will require either more power to fly faster and decrease the flying time in the southern direction or longer periods without solar influx. The exact implications depend on the day of the year, but might become critical near the worst conditions.

Table 3.2: Design Parameters

Parameter	Value	Unit
Design Cruise speed V_{Design}	22	[m/s]
Maximum Flight Speed V_{max}	30	[m/s]
Sun angle of incidence	72.2	[°]
Relative solar panel efficiency	78.6%	[-]
Ratio of time in beneficial turns and total time	0.88	[-]
Critical day	December 21^{st}	[-]
Amount of sunlight hours on critical day	6.9	[hr]
Average power (P_{avg}) critical day	370	[W/m^2]

3.3.4 Conclusion

The mission profile includes a day of take-off and climbing, cruising to the required location and a long endurance loiter with payload active, a descent and landing to finish the mission. Circles or ellipses are flown depending on the wind speed and the AOI. On days and locations where the AOI and resulting solar energy becomes critical, sun-facing turns are flown during the day while circles or ellipses are flown during the night. The exact shape of the sun-facing turns largely depends on wind direction, wind speed, the exact AOI during the turn-arounds, the day and location. The UAV will need software on board to optimise the flight path taking all these conditions into account. The details of the software however, are beyond the scope of this project.

3.4 Design Conclusions

A summary of the design parameters, derived from the analysis of the environment which the aircraft must operate in, is given in Table 3.2. These values will be used as a basis for the subsystem design in chapter 4. The design cruise speed (V_{cruise}) is chosen on the basis of the wind analysis performed in section 3.1. While it could be observed that the average speed required for 90% station keeping during fall (the dataset in which the critical day is included) was equal to 25 m/s, a lower design speed was chosen. It can be observed the critical day December 21^{st} is at the very edge of the fall dataset. Furthermore, the adjacent dataset for the winter has an average wind speed for 90% station keeping of 15 m/s. Thus it was chosen to choose a point in between these two extreme values, with some margin added. Thus the design V_{design} of 22 m/s is reached.

Chapter 4
Subsystem Design

With the mission objectives and environmental analysis finished, the designing of the vehicle starts. The designing of each subsystem is presented in this chapter. In section 4.1 the payload used for observations is presented. The communication systems are then discussed in section 4.2. Next, the details on the aerodynamics and stability of the UAV are explained in section 4.3. Control surface sizing is done in section 4.4. The propulsion system is designed in section 4.5. The sizing of the batteries, solar cells and maximum power point trackers is done in section 4.6, section 4.7 and subsection 4.7.6 respectively. The heat system is then explained section 4.8. This chapter finishes with the design of the structures, presented in section 4.9.

4.1 Payload

One of the mission criteria is to be able to observe an individual with a sufficient ground resolution to be discerned. It is found that a pixel size of at most 10 x 10 cm for good tracking [30]. This observation is done with imaging, for which the payload is used. Further requirements on the payload are a total mass below 3 kg and a power consumption below 25 W. There are different kinds of imaging processes which will be discussed in the upcoming sections. Lenses and mirrors to increase the pixel resolution will be discussed. At the end of this section a complete lay out of the payload is presented.

4.1.1 Imaging Sensor

There are various types of imaging sensors. There are sensors using the visible spectrum, the far infra-red spectrum and another imaging technique is the synthetic aperture radar (SAR). It is of great advantage for the customers to have observation capabilities both day and night. Therefore, two sensors are used, one uses the visible spectrum and operates during the day, the second is used during the night and operates in the far infra-red spectrum. Because of the mass and power constraints the SAR imager is not an option. The nano SAR is currently the smallest possible solution, but the power consumption of these systems is over the maximum power consumption of 25 W and the resolution is too low to recognize individuals.

Daytime Sensor

Here, the sensor used during daylight that operates in the optic spectrum is discussed. To stay within total costs budget, the costs of the sensor is taken into account. A CCD or CMOS sensor will be used, these are currently the cheapest with a good quality.
The sensor must have small cell size. This will decrease the focal length of the lens or decrease the ground pixel size in case of a fixed focal length. The 25 W maximum power requirement includes both the image sensors and the stabilizer. It is also necessary that the sensor resolution is as high as possible so that a large field of view can be obtained.
The possible sensors that have been found can be seen in Table 4.1.

In Table 4.1 two cameras are considered good. The first one is the IMX081PQ sensor and the second one is the KAI-29050 sensor. The IMX081PQ can give sharp images but the KAI has a bigger field of view. For the mission it is important to have a ground pixel size of 10 cm or less and to have a high field of view. These two sensors can achieve a ground pixel size lower than 10 cm but the KAI sensor has a bigger field of view. Therefore, the KAI-29050 sensor is chosen for daytime imagery.

Table 4.1: Types of sensors during the day

Name Sensor	**Type**	**Cell Size [μm]**	**Resolution**	**Power consumption [W]**	**Mass [g]**
CMOS Board-level Camera [21]	CMOS	6.5	2048 x 2048	8.4	215
1/2-Inch Megapixel CMOS Digital Image Sensor [22]	CMOS	5.2	1280 x 1024	0.363	206
IMX081PQ [23]	CMOS	1.75	4672 x 3552	0.3	256
Truesense KAI-16000 [24]	CCD	7.4	4872 x 3248	6	391
KAI-29050 sensor [25]	CCD	5.5	6644 x 4452	0.5	454

Night Time Sensor

To take pictures during the night a sensor that operate in the far infra-red spectrum has to be chosen. Typically, far infra-red spectrum sensors have a bigger cell size than the sensors that operate in the visual spectrum. The far infra-red spectrum is chosen such that it is possible to look through clouds during the night and if necessary during the day. The possible far infra-red sensors are shown in Table 4.2.

Table 4.2: Night time sensor

Name Sensor	**Type**	**Cell Size [μm]**	**Resolution**	**Power consumption [W]**	**Mass [g]**
Pico1024E [26]	CMOS	17	1024 x 768	0.130	30
U8000 [27]	CMOS	17	1024 x 768	0.450	18
U8000 LCC [28]	CMOS	17	1024 x 768	0.450	9
ASP-LWIR-640-480 [29]	CMOS	17	640 x 480	3	50

As can be seen from Table 4.2, all the sensors have the same cell size and resolution (except the ASP sensor). The only differences are found in the mass and the power consumption. Since power consumption is a critical design parameter, the option with the least power consumption is chosen. So the sensor that will provide pictures during the night is the Pico1024E.

4.1.2 Basic Lens Characteristics

Before we can start sizing the lens all its basic characteristics have to be calculated. These characteristic are the focal length, aperture diameter and picture quality. Because the far infra-red sensor has the highest cell size (17 μm) it would need a higher focal length than the daytime sensor, so this means that the lens will be designed for the night time sensor. The focal length of the lens can be calculated with Equation 4.1. The focal length is determined with a ground resolution of 8 x 8 cm which is somewhat smaller than the required 10 x 10 cm [30].

$$f = \frac{d \cdot h}{X} = \frac{17 \cdot 10^{-6} \cdot 18 \cdot 10^{3}}{8 \cdot 10^{-2}} = 3.8 \qquad [\text{m}] \tag{4.1}$$

With d the cell size, h the distance to the object and X the ground pixel size. This means that the maximum focal length of the lens will be 3.8 m.
Because the size of the flying wing and the limited space for the lens, an aperture of 1 m is taken. This affects the image quality and this effect can be calculated with Equation 4.2 [30].

$$Q = \frac{D \cdot d}{2.44 \cdot \lambda \cdot f} \qquad [\text{-}] \tag{4.2}$$

With D the aperture diameter, λ the operating wavelength and f the focal length. Table 4.3 can be constructed by using Equation 4.1 and Equation 4.2.

Table 4.3: Basic lens characteristics

Parameter	**Day Time Sensor**	**Night Time Sensor**
focal length [m]	3.8	3.8
height [km]	18	18
Cell Size [μm]	5.5	17
Ground Pixel Size [cm]	2.6	8.05
Aperture Diameter [m]	1	1
Operating Wavelength [m]	500-700 [nm]	8-14 [μm]
Picture Quality	0.84	0.23
Field of View [m]	115.98 x 173.09	82.43 x 61.824

It can be seen that a lens with a focal length of 3.8 m is needed to have a sharp image. This focal length can not be achieved with a normal lens. In the following section possible lens configurations will be discussed.

Lens

Because a high focal length is needed there are a few possible solutions: Cassegrain telescope, Three-mirror anastigmatic (TMA), Gregorian telescope and compact Gregorian telescope. Each of these solutions will decrease the size of the lens but keep the 3.8 m focal length. In Figure 4.1 all the possible configurations can be seen. The length of the telescope can be decreased by 1/2 of the focal length for the Gregorian telescope, 2/3 for the Cassegrain telescope and 1/7 for the compact Gregorian telescope [31]. A TMA lens could decrease the length of the lens but would increase the width to stack al the mirrors. For now the best solution would be the compact Gregorian lens but the lens would still be 54 cm high and this is not possible due to the drag that would increase, because the lens must be mounted outside of the wing to have enough light. This problem is resolved by combining the compact Gregorian lens and TMA lens in one system. In Figure 4.2 this solution is shown. For the payload the compact lens will have a focal length of 2.75 m and the mirrors will do the rest of the 3.8 m focal length. This gives us the dimension of a lens with a height of 39.2 cm and a mirror with a height of 26 cm. The total length of the system is 65.2 cm. The 39.2 cm Gregorian lens will be mounted on the outside of the wing and the 26 cm mirror will be mounted in the wing body.

Polymer lens One of the design objectives is to use polymers where possible. Therefore a small study was performed to look if it is possible to make the mirrors from the lenses of polymers. These polymers must have a low thermal expansion and must be very stiff so the image will not shift. It is possible in the near future to make big polymer lenses. These will be made out of carbon fibre with a resin, and also a resin on top of the carbon fibre sheet. The top resin layer is needed to smoothen the surface of the lens. Because polymers have poor reflective characteristics, a coating must be applied. This coating will be the only non polymer layer of the lens. The coating will be an aluminium coating and it will be applied by the use of magnetron sputtering. The only problems with these lenses is that they are hard to produce due to resin shrinking and achieving a good surface roughness. In conclusion it is possible to make a polymer lens with a polymer content of at least 95%.

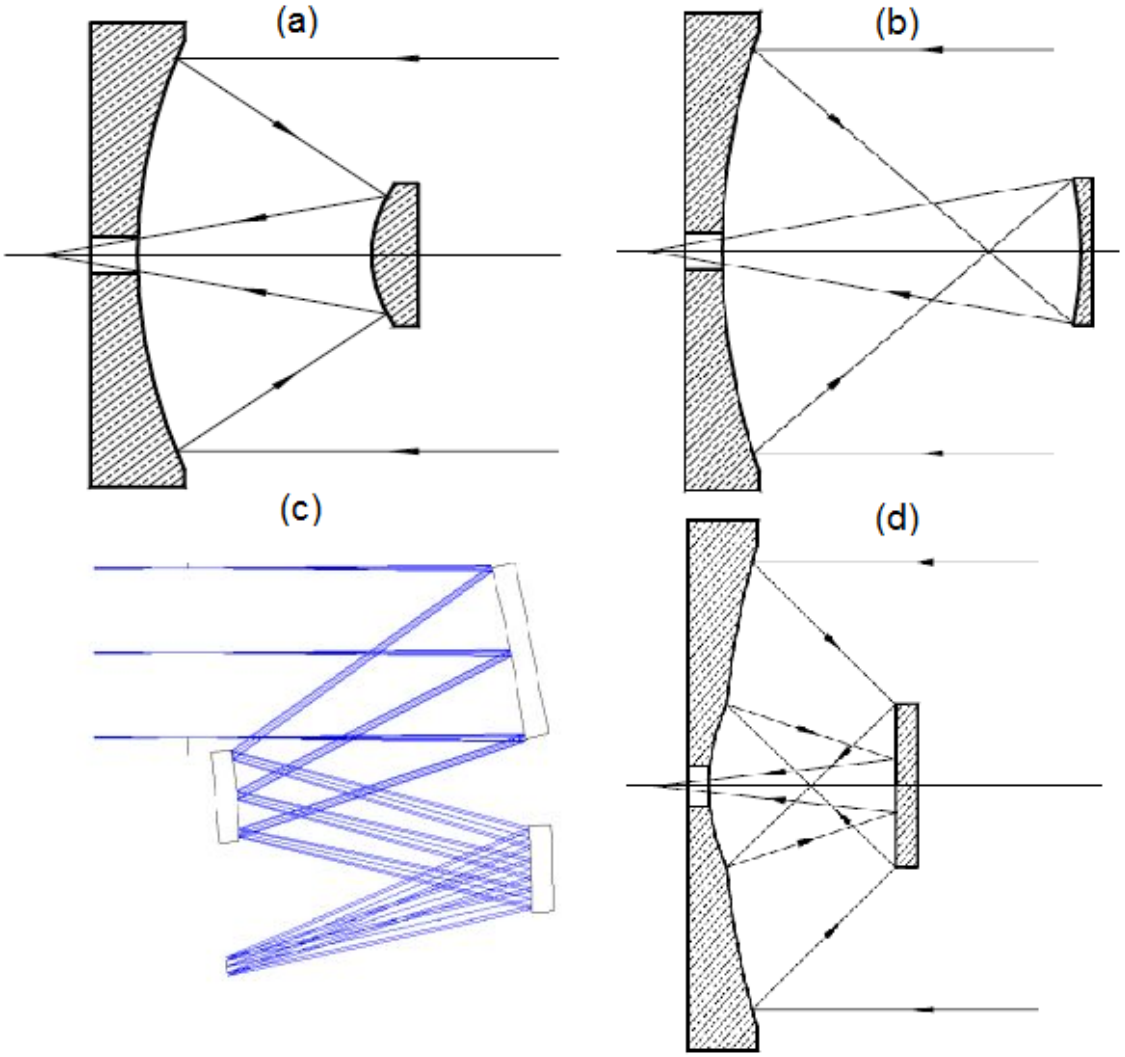

Figure 4.1: Lens configurations: Cassegrain telescope(a), Gregorian telescope(b), Three-mirror anastigmatic(c) and compact Gregorian telescope(d)[31]

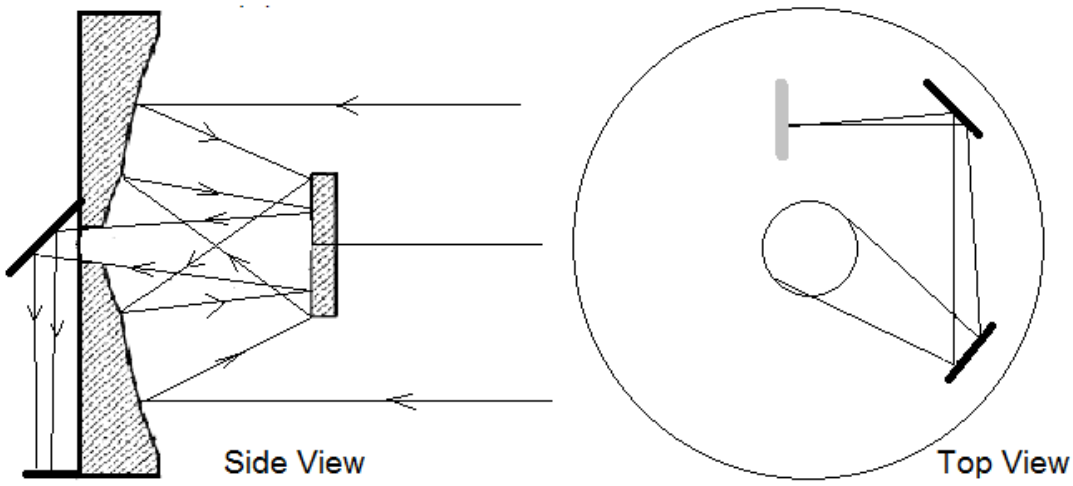

Figure 4.2: Compact Gregorian Telescope combined with TMA telescope

4.1.3 Stabilizer

To point the camera, a stabilizer has to be designed. During coverage, the bank angle is 10° and the max angle with the target of observation is 3°, the minimum angle must therefore be 13° to have a good line of sight. To achieve this angle two servos are placed so the camera can pitch. The problem when the dome pitches is that a lot of light is lost due to the wing. To deal with this problem, the camera must move down and up, which is done by using two linear actuators. Lastly, the dome must turn 360°. This will be done by the use of two servos connected to a O-ring gear. In Figure 4.3 a complete setup can be seen on how everything moves. The servos and actuators that will be used can be seen in Table 4.4.

Table 4.4: Data from the servos

Type	**Torque [Nm]**	**Velocity**	**Power [W]**	**Purpose**	**Number used**
PD3237 ∅32 mm carbon brushes 4 W [32]	1.177	16.9 [RPM]	4	360°	2
PD3237 ∅32 mm carbon brushes 4 W [32]	1.177	16.9 [RPM]	4	pitching of the dome	2
S12-17A16-xx [33]		1.4 [cm/s]	2.4	moving dome up and down	2
Total	N/A	N/A	20.8	N/A	N/A

4.1.4 Conclusion

To perform observations during the mission 2 CMOS sensors are used, one during night and one during the day. These 2 sensors will be shifted by the use of a small servo that will spin a disk where the sensor are mounted on. A compact Gregorian telescope combined with TMA telescope will be used as lens. The focal length of this lens will be 3.8 m and have a diameter of 1 m with a height of 65.2 cm. The lens will have a polymer level of atleast 95% and will have a mass of 1.2 kg. The lens will be mounted into the wing and can handle angles up to 15°, achieved by the use of 2 servos for pitching. Two servos are used to turn the dome 360° and 2 linear actuators will let the dome go down 15 cm to assure enough light on the mirrors. The total mass of the payload will be 1,786 gram, without the stabilizer this will have a mass of 1.5 kg. The power consumption of the complete system will be 21.23 W, complying with the requirements. The total configuration can be seen in Figure 4.3 and the specific components are shown in Figure 4.4.

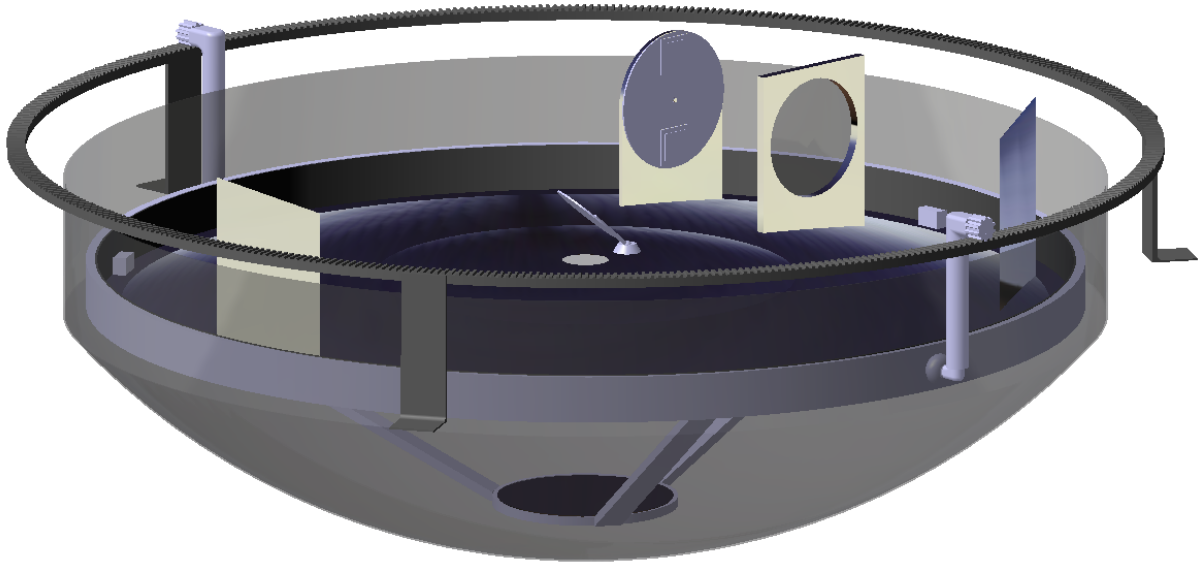

Figure 4.3: The total camera set-up

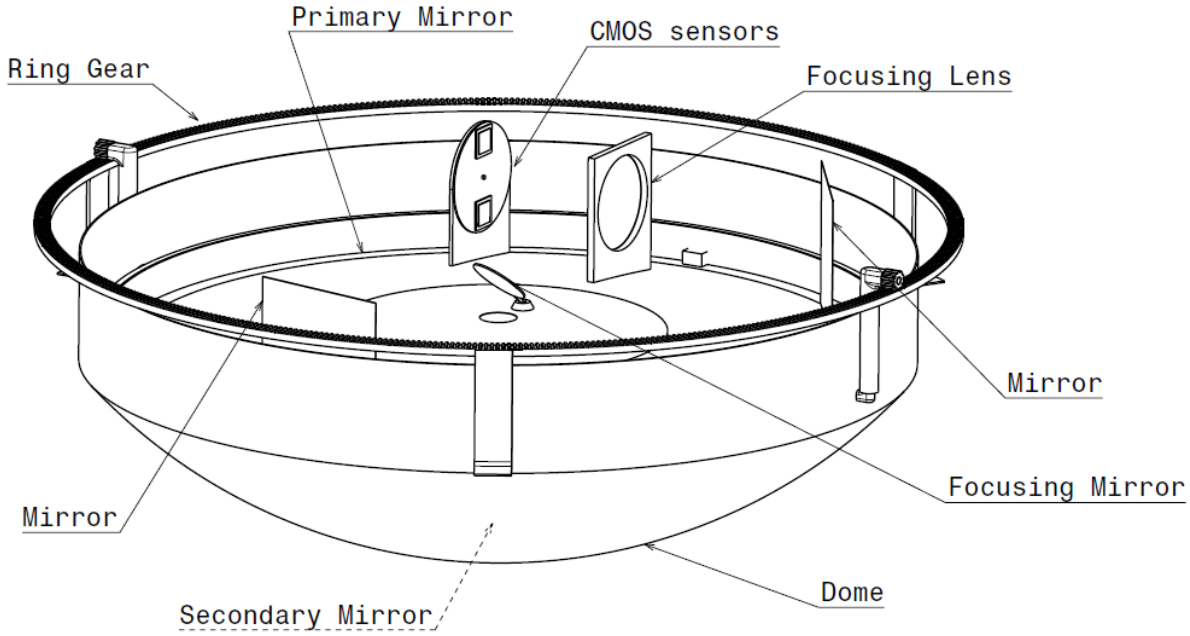

Figure 4.4: Components of the camera

4.2 Communication

Like every other aircraft the UAV will have a communication system and a data handling system that will receive, send a data signal. the data signal will consist out navigation data and pictures taken during the observation. In this section compression techniques, receivers and transmitters, Signal to noise ratio and ground station will be discussed.

4.2.1 Data Compression

If no compression is used on the pictures the data rate (DR) would be to high such that it is not possible to send everything down in a reasonable time. The DR without compression would be:

$$DR = \#pixels \cdot b \cdot fps = 29.6 \cdot 8 \cdot 1 = 236 \qquad [\text{Mbit/s}] \tag{4.3}$$

With # pixels is the number of pixel in one picture, b is the number of bits in one pixel and fps is the number of pictures taken in one second. As can be seen the uncompressed data would be 236 Mbit/s only for picture data stream. This means that a compression technique must be applied. The compression technique that will be used is H.264 [34]. H.264 is based on making one picture and this will be the reference picture, and for all the next pictures that will be stored or send only the changed pixels will be used. The only moving part that will be seen in the observation is the individual. An average human size from above is 1 x 1.5 m, The pixel resolution needed during the day would be 143 x 215 pixels. The number of pixels needed is 1820, this means that one picture will have a size of 14.56 kbit if one pixels consist out 8 bits. And the frame rate is 1 frame per second, the new data rate would become 14.56 kbit/s. This is a huge improvement compared to the 236 Mbit/s. So the first picture will have a size of 236 Mbit and the rest of the pictures have a size of 14.56 kbit.
The compression will be done by the use of a custom build computer. The computer will also be used for data handling. This can be seen in Table 4.5 out what the computer consist. Because there is a total storage room 5.64 TB there is also a possibility of not sending pictures at all but store them on the 5.64 TB hard disk, this can be handy for scientific purposes or for detailed mapping. However on these pictures a compression technique must be used, the compression techniques that is used JPEG-2000 [38]. JPEG-2000 can make the file with a factor of 33.5 smaller.

Table 4.5: Computer

Name	Number Needed	Total Power [W]	Total mass [g]
AMD Opteron 4256 EE Tray (8-core CPU 32 avgP 35 TDP)[35]	1	32	10
Supermicro H8SCM-F (Motherboard)	1	1	200
Kingston ValueRAM KVR13LR9D4K4/64 (4xRAM LoV 1.35V) [36]	1	1	40
Crucial M500 SSD (6 drives of 940GB) [37]	6	0.9	420

4.2.2 Stations

There is one head base station that will have a antenna and transmitters and receivers that will provide communication with three stations. These three stations will be sending and receiving data to the the HALE UAV. The head quarter will be powered by a 2 MW windmill and will also be grid connected so that in the case there is not enough wind there is still enough power, but in the case there is to much wind the power can be sold to the grid. The main head quarter will send all the commands to the UAV but also analyse its data. The three substations are a satellite network, a ground station that is closer to the UAV and there is a possibility to have a mobile ground station.

4.2.3 Transmitting Pictures

Data will be send to a ground station or to satellites by the use of a transmitter, this data will consist out of pictures. Data will be received for making pictures like the target location that need to be observed, so that the camera can be pointed to right location to give an optimal observation mission.
The requirements for the transmitter are low power consumption and a low mass, a minimum data rate of 20 Mbit/s and a low as possible bandwidth to minimize the power. The 20 Mbit/s is necessary to send the reference pictures within the first minute. The bandwidth of the transmitter can not operate in the L-band because the GPS signal operates at this band. The transmitter that will be used is ST-5000S S-Band transmitter with the following specification:[39]

- Bandwidth: S-Band
- Data rate: 40 Mbit/s
- Power: 10 W
- Mass: 226.8 gram

The Receiver requirements are again low power and mass and operating at the S-band like the transmitter. The receiver that is chosen is MFT733A-PCI. The specification are:[40]

- Bandwidt: S-band
- Data rate: 15 Mbit/s
- Power: 4.8 W
- Mass: 260 gram

The data received will come from three stations one mobile ground station, a fixed ground station and from a satellite all operating on a S-Band. Because of these configuration a maximum of 3 signals will be received, there for the error that is send from one signal can be reduced by two other signals from two other station. Because the data error is reduced a more accurate control can be guaranteed. The communication block diagram can be seen in Figure 4.5 During the night there is less sunlight so there is a power shortage, this means it is not possible to send pictures during the night to the ground station. But they will be stored on the SSD and send to the ground station during the day or within short time intervals in the night.
There are three stations that receive and send data, the antennas will use these station for communication. Two antennas need to be used, one for satellite communication and one on the lower side of the wing to receive from the ground stations. Two ground stations are available, one

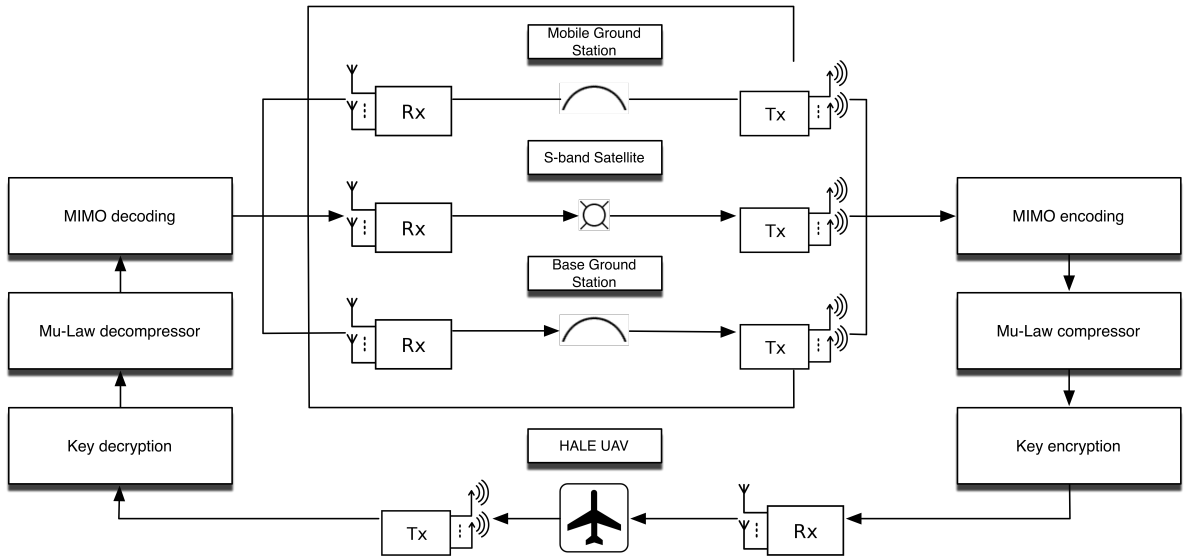

Figure 4.5: Communication block diagram showing the three station MIMO(Multiple inputs Multiple Outputs)

mobile station and one fixed station. The mobile station will send the data to the base station. These antenna must operate on the S-band because the transmitter and receiver operate on this bandwidth. One of the requirements is that the antenna is as aerodynamics as possible, because the antenna will be mounted outside the wing. The antenna chosen is S-Band Patch Antenna, this is an antenna that is used in space mission [41]. The advantage of this antenna is that it is flat so it can be integrated in the skin so that it has a minimal contribution to the drag. The mass of the antenna is less than 80 gram. The antennas will be connected to a custom made combiner, there is a switch build in to the system so there can be chosen when to send data and when to receive because these two options can't be done at the same time. The switch that is used is custom build. Because there are 3 signals coming in at the same time a splitter is needed to split the three signals. The splitter will be custom made.

4.2.4 Navigation

The navigation will be an off the shelf system. The system that will be used is flightTEK® Geneva [42]. This is a complete system a receiver and transmitter are built in and this only need to be connected to a separate antenna This antenna will operate on the L-band . The antenna that is used is a Multi-band Antenna for Mini UAV's, this antenna operate at a bandwidth between UHF an C band. What this system can do is pre-programmed loiter route, in case the signal is lost the UAV will be send back to base and auto landing and take-of. A separate Solid state drive is attached to do data logging during the year.

4.2.5 Back up system

In case of system failure an back up system is provided that will take the UAV back safely to the base for repair. This system will consist only out a navigation box and an antenna. The system will start working as soon as the main navigation box is damaged or when any other important subsystem is broken. The back up system will have the same configuration as the navigation system, so it consist out a solid state drive with a storage capacity of 940 GB and a flightTEK® Geneva box. The location of this back up system will be placed at the and of the wing far away from all other subsystems.

4.2.6 SNR

The last part of this section is to calculate the Signal to Noise ratio (SNR). SNR is the amount of desired signal compared to the background the noise. The SNR can be calculated with Equation 4.4 [30].

$$SNR = P + G_t + G_r + L_s + 228.6 - 10\log(T_s) - 10\log(DR) \qquad \text{[dB]} \tag{4.4}$$

With P the transmitted signal in dB, G_r is the receiver gain, G_t is the transmitter gain, L_s is the path loss, T_s is the system temperature and DR is the data rate. L_s can be calculated with Equation 4.5.

$$L_s = 10 \cdot \log\left(\left(\frac{c}{4 \cdot \pi \cdot f \cdot r}\right)^2\right) \qquad \text{[dB]} \tag{4.5}$$

With c is the speed of light, r is the distance between the receiver and transmitter and f is the frequency of the signal (2.2 Ghz). From the data sheet it can be seen that the antenna gain of the receiver and transmitter is 7 dB [41] the transmitted power P is 10 W this is also equal to 10 dB. There are two cases that must be analysed, the first one is when there will be communication with the ground station and the second one is during communication with the satellite. Filling in all the values in Equation 4.5 and Equation 4.4 the SNR will be 15.25 dB. This 15.25 dB is a favourable because the signal has a higher power then the noise.

Lets look what the SNR will be if there is communicated with the satellites. the satellites and UAV are separate by each other with a distance of 1,982 km. This means that the SNR will be -9.25 dB. This is unacceptable as the signal has a less power than noise. This can be fixed by adding an amplifier, the amplifier should have a gain of atleast 10 dB. After some research the chosen amplifier is BGA2865, this amplifier has a gain of 28.1 dB and an extra noise of -3.6 dB. The new SNR will be 15.25 dB and this is a favourable value. The amplifier will use 163 mW of power.

4.2.7 Patch antenna verification

Before the antenna is used a recheck is performed to check if it could provide the promised gain at the operating wavelength. This can be checked by the use of Equation 4.6 [43].

$$G = \frac{4 \cdot \pi \cdot A_{eff}}{\lambda^2} = \frac{4 \cdot \pi \cdot A_{eff} \cdot f^2}{c^2} \qquad \text{[dB]} \tag{4.6}$$

A_{eff} is the effective antenna area, which is equal to 0.00528 m^2. Filling in all data the antenna gain is 3.6 dB.

4.2.8 Overall Layout

In Figure 4.6 the total lay out can be seen for the main communication group without the amplifier because it is a small component. It can be seen that the communication box is a long vertical beam with at both ends the antennas. This is done to shorten the wiring length and here by decreasing the mass of the communication block. Also it is mounted vertical to decrease radar visibility for increasing stealth properties.

From Figure 4.8 it can be seen how all the hardware is connected. It can be seen that the navigation has a separate antenna, and that the main navigation box is connected to the CPU to control the payload.

4.3 Aerodynamics, Stability and Control

Aerodynamics is an integral part of aircraft design. It is one of the major drivers of the performance of the aircraft and directly influences critical components such as battery weight, required solar cell area and payload stabilization. First the airfoil will be chosen, starting from a two-dimensional situation and extending to a three dimensional situation. The results will be compared to reference wind tunnel data. Once the airfoil selection is complete, a planform design is made using inputs from various components such as the wing, battery and solar cells. Once the planform design is complete and finalized, the control and stability of the aircraft is first designed in a number of iterations and afterwards evaluated.

4.3.1 Airfoil Selection

This section will provide information on the selection of the airfoils for the aircraft. Several airfoils were evaluated, after which the appropriate one was chosen trying to fulfill as many requirements as possible imposed by the various sub departments such as aerodynamics and structures. Finally, these results and tools were validated using reference data from a wind tunnel.

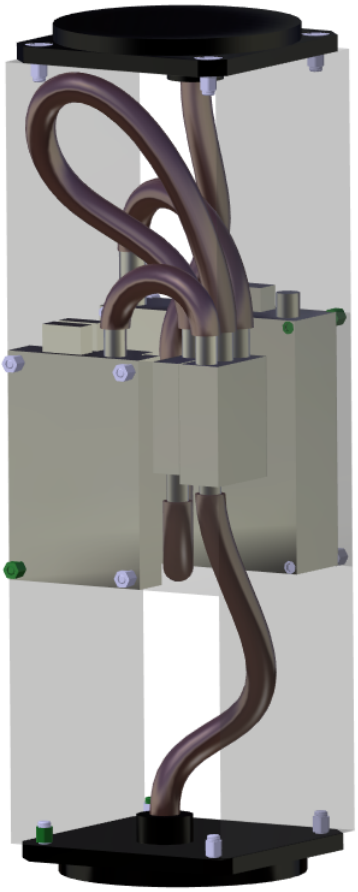

Figure 4.6: The total communication set-up without amplifier

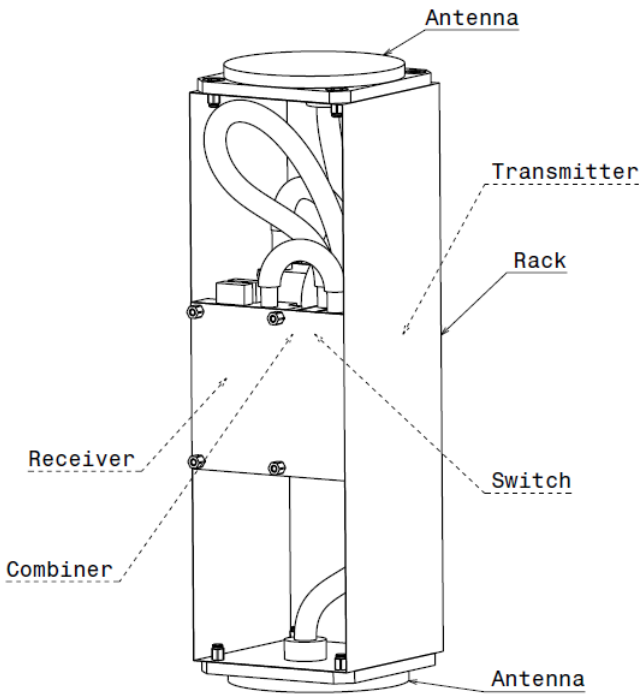

Figure 4.7: Subcomponents of communications subsystem

The main goal while selecting airfoils was optimizing for loiter conditions, since the majority of the mission is spent in this condition as stated in chapter 3. Therefore $C_L^{(3/2)}/C_D$ needs to be maximized at the cruise speed of 22 m/s during the critical conditions. The maximum speed the aircraft has to fly depends on the maximum wind conditions, which are 30 m/s. Since the aircraft is a flying wing without a horizontal stabilizer, the moment C_m of the airfoil should ideally be minimized during cruise conditions to reduce trim drag. This would also allow a reduction in wing twist, which is beneficial for the aerodynamic performance. An additional design consideration from a structural point of view is that a thicker airfoil will lead to a lower wing weight. However, very generally it can be said that a thicker wing leads to worse aerodynamic efficiency. An optimum between these two conflicting requirements must therefore be determined. Summarizing the requirements are as follows:

- Maximize $C_L^{(3/2)}/C_D$ at cruise speed
- Have acceptable performance at 30 m/s
- Minimize C_m at cruise conditions
- Optimize t/c ratio without compromising the performance

With these requirements in mind, airfoils from five different designers were chosen to be evaluated. Two of those airfoils, designed by Fauvel and Marske were dismissed after a short evaluation, because it was immediately obvious these airfoils had far lower performance compared to the other three. The other airfoils, designed by Eppler, Martin Hepperle and Wortmann, were evaluated in more detail. The strengths and weaknesses of each design will be briefly discussed in the next couple of paragraphs.

Each airfoil was evaluated using the aerodynamics simulation program XFLR5 [44]. A reference aircraft design (with a sweep of 10°, a span of 44.44 m, wing area of 80 m^2 and a weight of 119

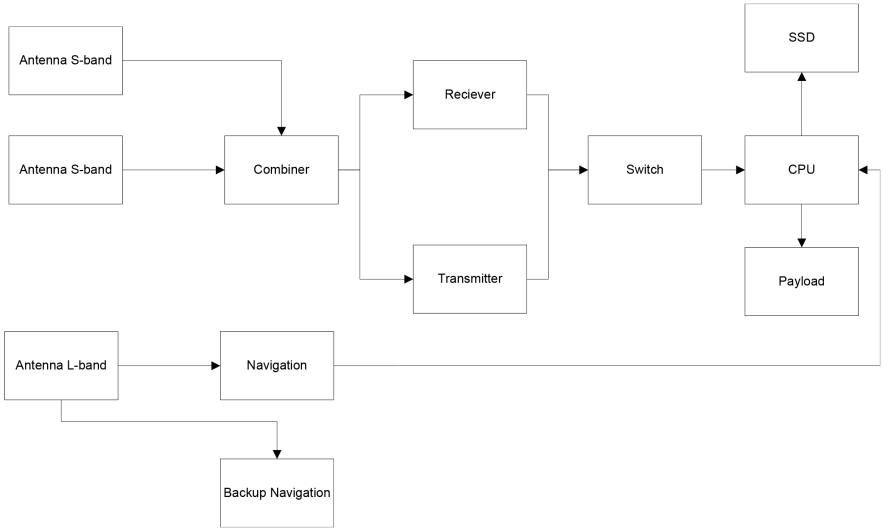

Figure 4.8: Hardware block diagram

kg) was used to check the performance of each airfoil. This specific reference aircraft was chosen because it was a feasible aircraft during preliminary calculations.

Eppler Series Airfoil Prof. Dr. Richard Eppler has designed a whole series of reflexed airfoils specially for flying wings. Out of the series of airfoils designed by Eppler, the one with the highest $C_L^{(3/2)}/C_D$ was chosen for further evaluation. This is the Eppler 329 airfoil. Also, in an attempt to minimize induced drag the Eppler 330 was also chosen for evaluation, being the thinnest of the series. Both airfoils were designed with Reynolds numbers of 700,000 in mind [45] and were retrieved from the University of Illinois airfoil database [46].

The thickness of the Eppler 329 airfoil is 13.54%, while the Eppler 330 airfoil has a thickness of 11.03%. Figure 4.9 shows the value of $C_L^{(3/2)}/C_D$ against velocity for the Eppler 329 airfoil. The maximum $C_L^{(3/2)}/C_D$ is roughly 5% higher for the 329 airfoil, however the Eppler 330 has a far broader range of operating speeds, which is beneficial when the aircraft needs to cruise at a higher speed of approximately 30 m/s. The Eppler 329 has typical C_m values of around -0.05, while the C_m values of the Eppler 330 are around 0.

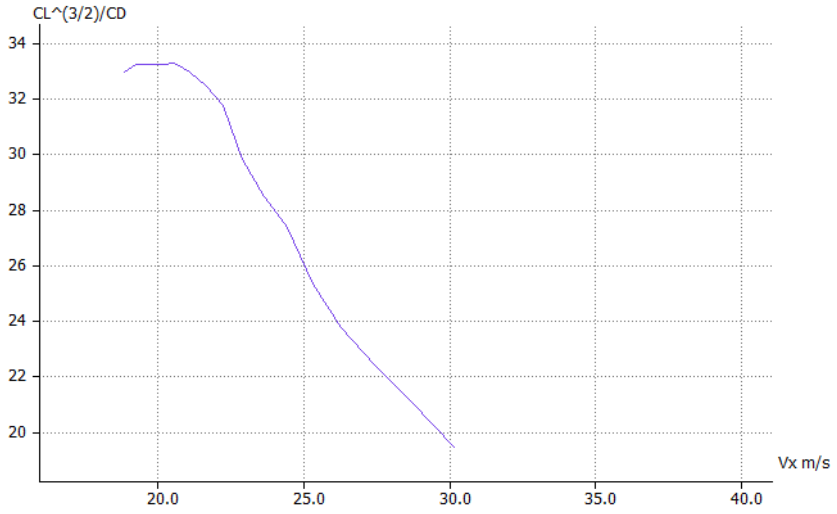

Figure 4.9: $C_L^{(3/2)}/C_D$ against velocity for the Eppler 329 airfoil

MH Airfoils Dr. Martin Hepperle has designed a series of airfoils specifically for flying wings. Unlike the Eppler airfoils, these are not fully reflexed but have been designed to generate low negative C_m values of typically -0.01. Which is beneficial for the design as relatively little sweep and twist are needed to make the aircraft controllable.
The $C_L^{(3/2)}/C_D$ against airspeed for the MH70 airfoil is shown in Figure 4.10. The thickness is 11.06%. Compared to the Eppler airfoils, a clear performance improvement in terms of maximum $C_L^{(3/2)}/C_D$ can be observed. Furthermore, good $C_L^{(3/2)}/C_D$ ratios can be observed at a broader speed range, giving the aircraft a higher operating flexibility. All of the MH airfoils display similar characteristics. The main difference between them is the thickness, which varies from 9% to 13% and the speed range at which the given maximum C_L/C_D occurs.

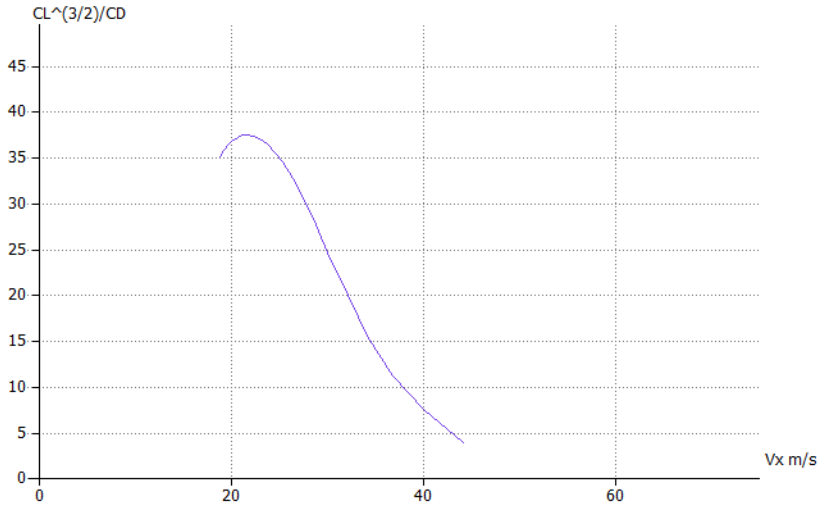

Figure 4.10: $C_L^{(3/2)}/C_D$ against velocity for the MH70 airfoil

Wortmann Airfoils Franz Xaver Wortmann was a professor at the Technical University of Stuttgart and has designed a large series of laminar airfoils. These airfoils were designed for conventional gliders and small general aviation aircraft and therefore have a far higher (negative) value of C_m compared to the airfoils discussed previously. However, several Wortmann profiles showed significant higher two dimensional aerodynamic performance compared to the Eppler and MH airfoil series. Thus it was decided to investigate several of these airfoils with XFLR5 to see if any benefits could be achieved.

Two airfoils, both of which boasted large $C_L^{(3/2)}/C_D$ values in two dimensional cases were chosen for further evaluation. The FX63-137 airfoil has a thickness of 13.7%, while the FX 60-100 has a thickness of 10%. Figure 4.11 shows the $C_L^{(3/2)}/C_D$ against velocity for the FX60 airfoil. It can be seen that the FX60 clearly has a better performance at speeds closer to the desired range. The drawback of both airfoils is the relatively high C_m value, with the FX63-137 airfoil having values of -0.2 and the FX60-100 has C_m values of -0.11.

Validation of XFLR5

The aircraft is designed for operation at low Reynolds numbers, between 100,000-700,000 Re. This range is part of the transitional range of Reynolds numbers where the flow switches from being fully laminar to fully turbulent[47]. This is also the point at which the critical Reynolds range occurs. Above this critical Reynolds range the L/D will sharply increase as the flow starts to switch from laminar to turbulent flow. While designing the aircraft, it is essential to stay above this critical range. One of the most commonly cited reasons for the transition is the Laminar Separation Bubble (LSB). Yet predicting the exact number at which the transition occurs can be complex. The aim of this section is therefore to validate the performance of XFLR5, particularly at the lowest Reynolds numbers encountered during the aircraft design.
Much wind tunnel research has been performed on the Eppler 387 airfoil. This airfoil has a very comparable performance with the previously discussed airfoils but has not been considered for this aircraft because of the lower thickness compared to other airfoils, which can lead to structural problems . Therefore this airfoil was chosen for validation purposes only. Figure 4.12

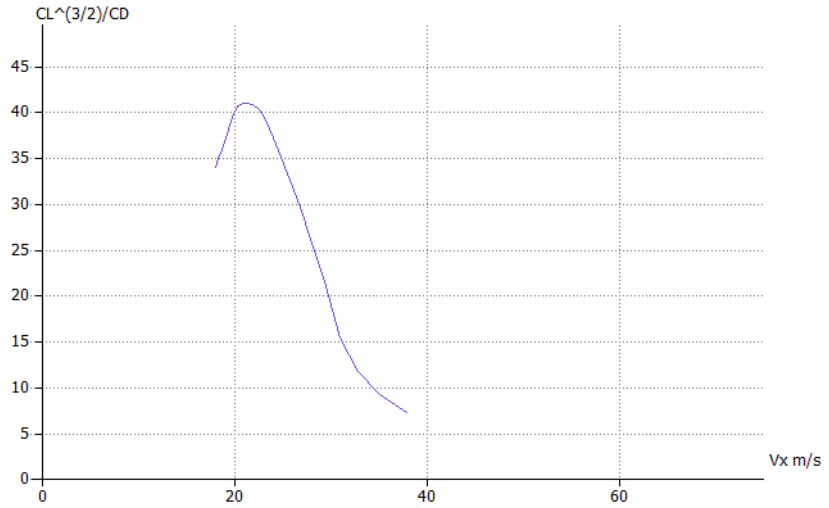

Figure 4.11: $C_L^{(3/2)}/C_D$ against velocity for the Wortmann FX60-100 airfoil

shows the drag polar for the Eppler 387 airfoil as measured by various institutions around the world, which can be compared with Figure 4.13 showing the drag polar of the same airfoil, calculated by XFLR5. Starting with Re=60,000, it can be seen that the measured data graphs show a big range of C_d values, particularly around C_l=0.7. This is caused by the laminar separation bubbles, forming at these low Reynolds numbers. The calculated airfoil shows similar erratic behavior around that range of C_l and the values fall within the extreme measured values. The C_d at zero C_l is equal to the extreme measured value and the C_d at maximum C_l is also equal to the most pessimistic measurements. This behavior is mimicked at the other two Re values. It can be concluded XFLR5 gives an accurate calculation for this type of airfoil for the Reynolds numbers under consideration.
McArthur [47] has performed measurements at various Reynolds numbers on a three dimensional model of an Eppler 387 airfoil with an aspect ratio of 6. Figure 4.14 shows the result which will be compared to XFLR5. An identical wing was modeled in XFLR5 at Reynolds numbers of 60,000. Only the linear part of the polar could be calculated by XFLR5. Compared to the wind tunnel data in Figure 4.14, the XFLR5 data gives very similar, but overall slightly lower values for C_L. For example, the maximum value at $\alpha = 11$ is 1.047, compared to 1.08 for the measured value.
Comparing the values of C_D, it is clear that the measured values are actually lower compared to the calculated values. For example, the maximum calculated value of C_D in the angle of attack range between 0 and 12 is 0.1, while the measured value never exceeds 0.07. This can also be seen when evaluating C_L/C_D. The measured values go up to 25, while the calculated C_L/C_D is never above 11. However, the values obtained with XFLR5 will be used as this relatively large difference can be caused by the difference in aspect ratio. To be on the safe side, the lower value is preferable, but this might allow for better aerodynamic performance and make the design more feasible.
Concluding, it can be said XFLR5 is accurate when evaluating two dimensional situations. When evaluating very low Reynolds numbers of 60,000 in a three dimensional situation, the lift calculation is still accurate. However, the calculated drag is too high compared to measured data. When designing the aircraft, this deficiency is not a huge issue because it results in a more conservative design. An attempt was made to further focus the investigation on comparing the three dimensional situation at higher aspect ratios and slightly higher Reynolds numbers of 100,000-200,000. However, all of the current research is focused on low aspect ratio wings with very low Reynolds number of between 10,000 and 100,000. Finding more data was therefore not possible within the limited time available for this project.

Non-Linear effects

From the requirements of a light weight structure and high aerodynamic performance, almost automatically a slender, high aspect ratio wing ensues. One of the dangers of this type of wing is the high flexibility, leading to high tip deflections. This will have two effects:

1. The lift vector will be tilted inwards towards the root. As a result the effective lift will be reduced, but simultaneously the tip deflection will be increased due to the vector tilt. In

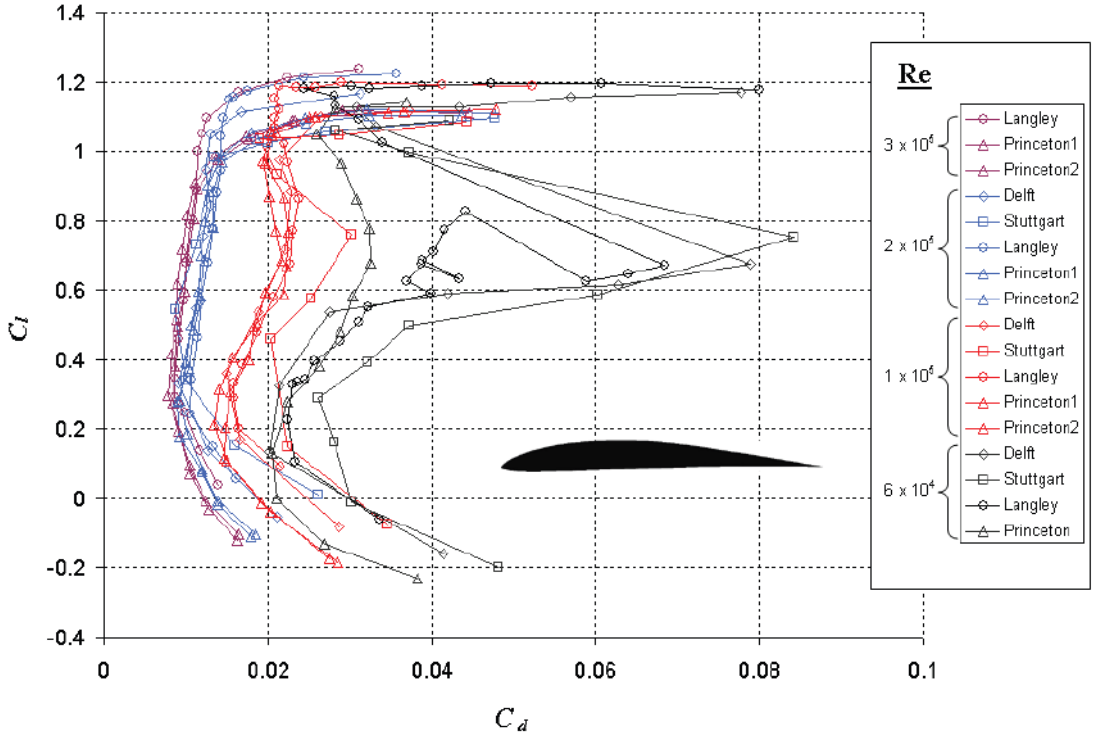

Figure 4.12: Drag polar of the Eppler 387 airfoil at various Re as measured by different institutions [47, 48, 49, 50, 51, 52]

Table 4.6: Technical data MH70 airfoil

MH70 Airfoil	
C_L/C_D	46.11
$C_L^{3/2}/C_D$	37.06
$C_{L_{design}}$	0.6317
α_{design}	5.50

extreme cases this can lead to structural failure. [53]

2. Due to the high deflection, the airflow will not encounter a flat horizontal wing but a curved beam. When tip deflections become to high, the approximations and methods used to analyze the aerodynamic performance in this section are invalid.

The analysis of these type of effects are outside the scope of this project. After consultation with an expert on high aspect ratio planforms Ir. L.O. Bernhammer, it was decided to avoid these effects by limiting the tip deflection to 10% of the halfspan at maximum load factors. This will now be a requirement while designing the structural part of the wing.

Final Airfoil Selection

The final choice of the airfoil was dependent on the exact sizing, flying speed and weight of the aircraft. During later iterations, the wing loading increased. This allowed the MH70 airfoil to be selected, which has the best performance but previously could not meet the speed requirements due to the lower wing loading values. An additional benefit is the fact the MH70 airfoil was one of the thickest airfoils under consideration, with benefits in terms of increased available space for the payload and a lighter design of the wingbox. This airfoil is shown in Figure 4.16. The data for this airfoil can be seen in Table 4.6.

4.3.2 Planform Design

Now the airfoil has been selected, this will be used as the basis to design the wing. First the various inputs will be discussed. At the end, a sketch of the planform with control surfaces,

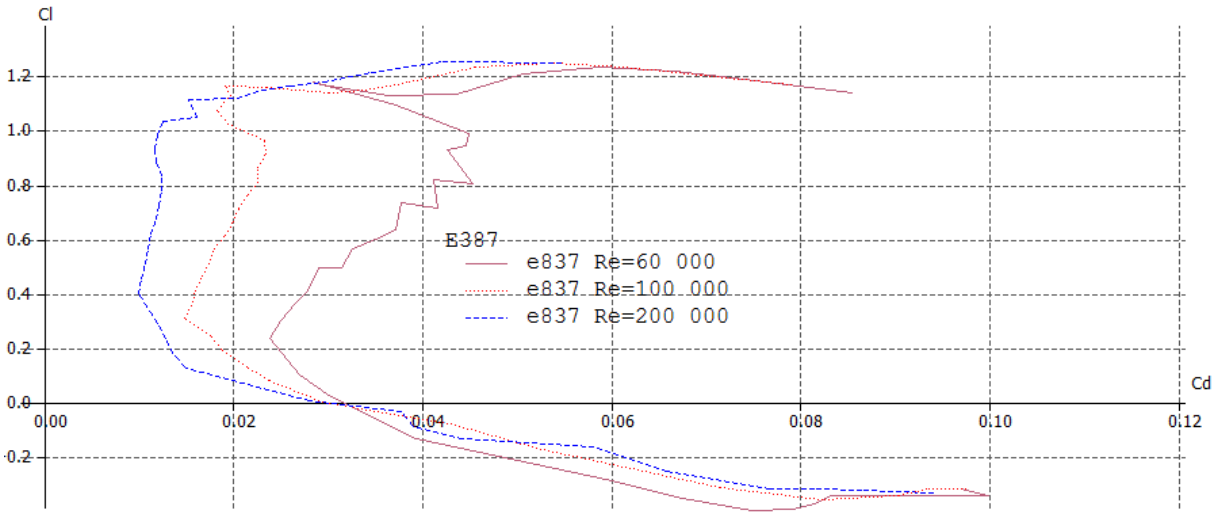

Figure 4.13: Drag polar of the Eppler 387 airfoil at various Re as calculated by XFLR5

center of gravity location as well as the dimensions of the planform will be shown.

Generation of the Planform layout

A MATLAB function was written in order to quickly be able to generate various planform designs. A number of input parameters were used such as battery density, solar panel density and the semi-fixed weight of the different subsystems, such as the payload, communications and power point trackers. Finally some slack weight for contingencies was included.

A separate function was written by the specialist structures group which estimates the wing weight based on the wing loading, aspect ratio and the load reducing weights such as battery and solar panel weight. This wing weight in turn changed parameters such as battery weight and wing loading, which are inputs for the same function. Several iteration are therefore performed until the wing weight converges.

Another function was written to calculate the energy available from the sun as a function of latitude. Finally, manual aerodynamic data from XFLR5 was used as an input for the aerodynamic and performance calculations. The work flow logic can be seen in Figure 4.17. The program starts with a certain wing area. Parameters which are a function of this area are calculated, after which the wing weight is iterated. Now a check is performed if the incoming solar power at the selected day exceeds the power required by the entire aircraft. If this condition is not met, the area is increased and the entire process starts again until the conditions are fulfilled. When this condition holds, the program is terminated and the design is envelope is determined.

The end result is a weight budget, which can be seen in Table 5.5. Furthermore, a wing planform size of 110 m^2 was calculated with an aspect ratio of 23. This leads to a wingspan of 50.3 m. From a structural point of view it is favorable to have as much taper as possible (limited to 0.25)[54] for bending stress relief. However a lower local cord leads to lower Reynolds numbers. Therefore it was chosen to limit the taper ratio to 0.52, which leads to a Reynolds number of roughly 100,000 at the wingtip at stall speed. The planform design and layout can be seen in Figure 4.18. Finally, it was decided to have 0° dihedral. The aircraft already has positive sweep, which has the same stabilizing effect as dihedral [54]. Adding dihedral would make the aircraft too stable to perform the required roll rate. The final aerodynamic values for this wing in a three dimensional setting for the chosen cruise speed can be seen in Table 4.6.

Additional Drag

Additional drag is introduced from two separate sources. Firstly, drag will increase due to the fact the aircraft is continually banking and side slipping to create optimum solar exposure. Secondly, the dome containing the payload at the bottom of the aircraft will also cause a drag increase. Investigation will start from the baseline case with the above mentioned wing parameters and additional 15° of sweep with $-4.50°$ of twist, the design of which will be discussed in subsection 4.3.3. In this configuration, the aircraft has a value of C_D equal to 0.01305 while flying 22 m/s. This leads to a drag of 41.69 N. In this section the amount of additional drag will be

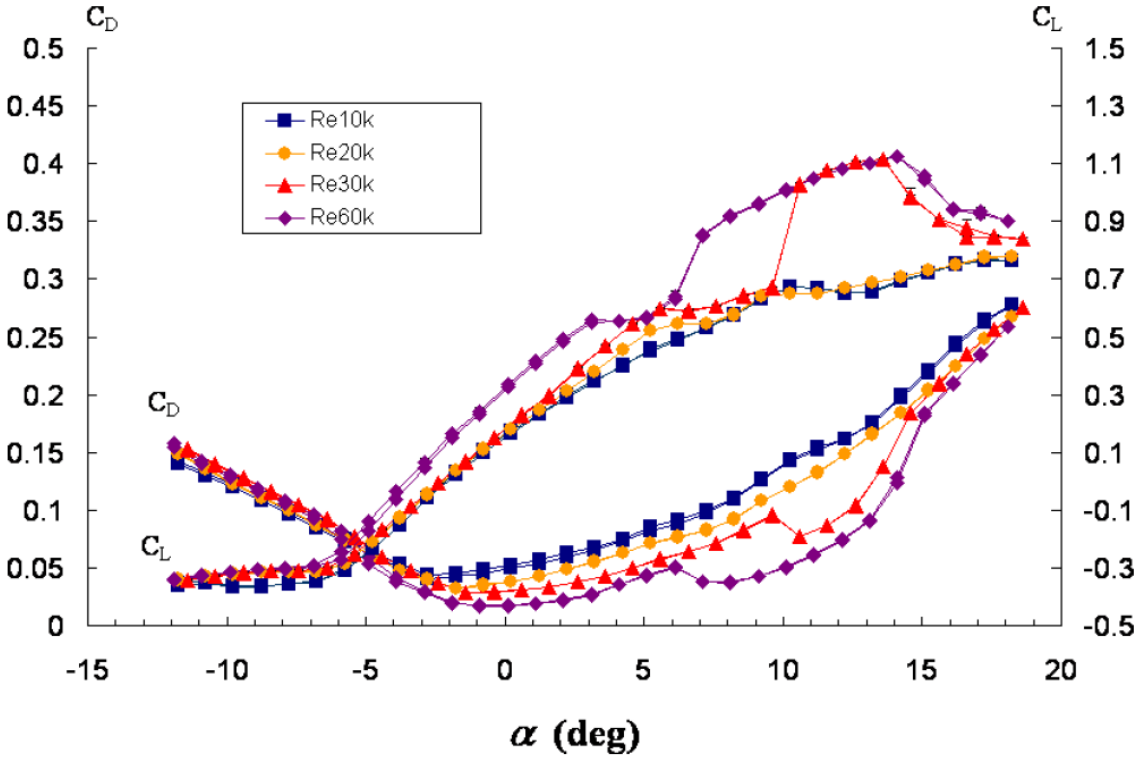

Figure 4.14: C_L and C_D of a wing with an Eppler 387 airfoil with an aspect ratio of 6 as measured in a windtunnel [47]

approximated and added to the original drag to generate a value which can be used while power and performance subsystems of the aircraft.

Three separate cases will be considered as a consequence of flying the maneuver explained in Figure 3.3.3. During the coordinated, banked turn of 10° the load factor n increases to 1.015. Assuming C_L/C_D remains the same while the turn is fully coordinated, this leads to an extra drag of 0.652 N. Second, the case of a 40° will be considered. Using the same assumptions, the load factor increases to 1.305 and the drag increases by 13.25 N. Finally, the case of a side-slipping flight of 5° is considered. In this case, the bank is not coordinated and therefore the previous assumption of constant C_L/C_D is not valid. Evaluating side-slip in XFLR5 shows a decrease of C_L/C_D of 0.55%. Combined with the bank angle of 5°, this leads to a drag increase of 0.770 N.

So there is a significant drag increase when flying the steeply banked turn, while the drag increase as a consequence of the limited bank and side-slip angles is almost negligible. Therefore it is important to optimize the ratio between steep turns and shallow banks/side-slipping flight as much as possible.

Calculating the drag of the payload dome with a diameter of 1.19 m and protruding by 45 cm out of the aircraft, first the Reynolds number must be known. This is equal to 212,270 Re. Using Hoerner [55] and Figure 4.19, the drag coefficient can be estimated. Because of the high Reynolds numbers, line b can be taken with c/t equal to 2.64 (1.19/0.45). This results in an estimated C_D of 0.11, which leads to a drag of 3.55 N as a consequence of the payload dome. This results in a total drag force of 46 N, which will in turn be used to size the propeller and performance in section 4.5.

4.3.3 Stability

This subsection will investigate the stability of the aircraft. First the aircraft will be designed for stability using a handbook approach at the cruise trim point of $\alpha = 6°$. Once that is done, XFLR5 will be used to investigate the dynamic stability in both the longitudinal and lateral

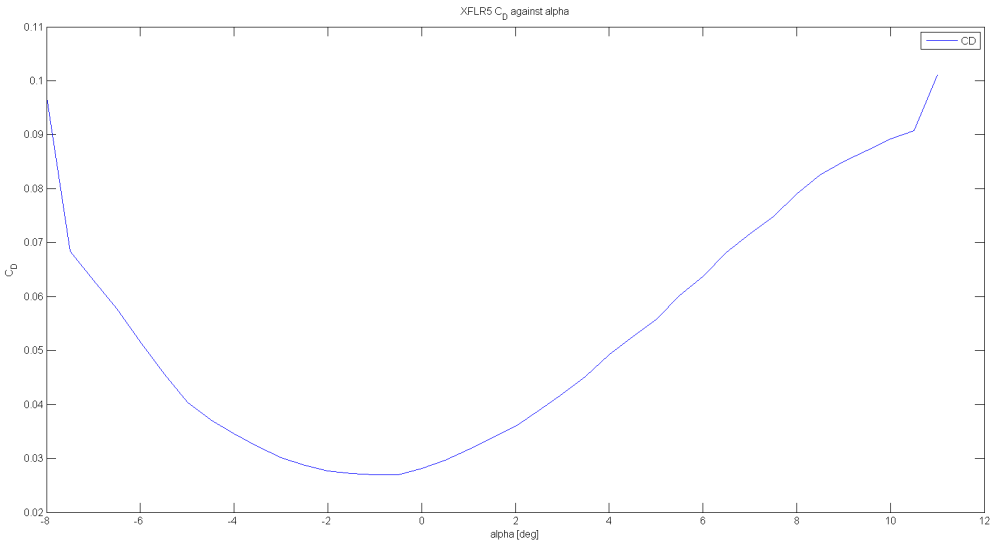

Figure 4.15: C_D of a wing with an Eppler 387 airfoil with an aspect ratio of 6 as calculated by XFLR5

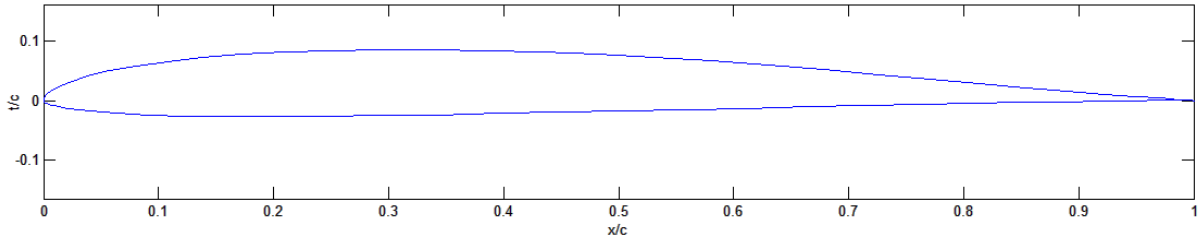

Figure 4.16: MH70 airfoil shape

direction. Output will be given in terms of sweep, twist and a center of gravity location.

Twist and sweep

In this section the wing twist and sweep will be estimated using the Martin Hepperle approach [56] based on the book by Karl Nickel and Michael Wohlfahrt. [57]

In aircraft design, the general rule of thumb is to keep the twist below 5° to avoid drag increase when the wing is not operating at $C_{L_{design}}$. To avoid wing tip stall the twist is usually atleast around -3° [54]. Therefore the aim is design a stable aircraft with a twist between -5° and -3°. By changing the sweep, the twist can be found using the estimation approach as explained in detail below. The sweep will follow as a result of the limitations set on the twist.

Figure 4.20 shows the required twist against the aspect ratio (Λ) for multiple sweep angles. With 15° sweep (ϕ) and an aspect ratio of 23, a standard required twist β^*_{req} of approximately 5.5 can be found. Since a standard stability margin ($\sigma*$) of 0.1 and a standard lift coefficient (C^*_L) of 1 have been used in the given approach, whilst different values of respectively 0.63 and 0.05 are used in the current design, two correction factors are applied over β^*_{req} to arrive at the required twist β_{req}. These are shown in Equation 4.7. This results in a geometric twist angle of 1.74.

$$\beta_{req} = \beta^*_{req} \cdot \frac{C_L}{C^*_L} \cdot \frac{\sigma}{\sigma^*} \qquad [°] \tag{4.7}$$

An additional twist angle (β_{c_m}) due to the moment coefficient has to be used. Shown in Figure 4.21, the standard additional twist angle $\beta^*_{c_m}$ is plotted against aspect ratio for multiple sweep angles. For a sweep of 15° and an aspect ratio of 23 $\beta^*_{c_m}$ becomes 3°. This value must be multiplied by the ratio of the actual value of C_m generated by the airfoil (-0.046) and the

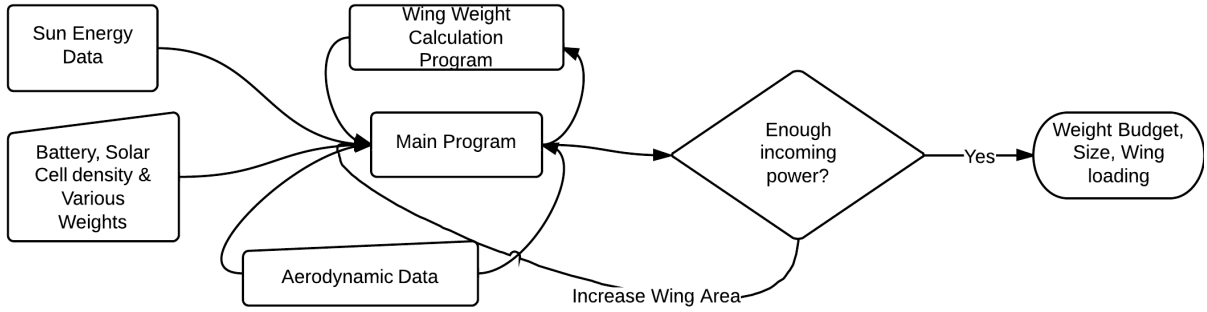

Figure 4.17: Work flow logic used during the wing planform design

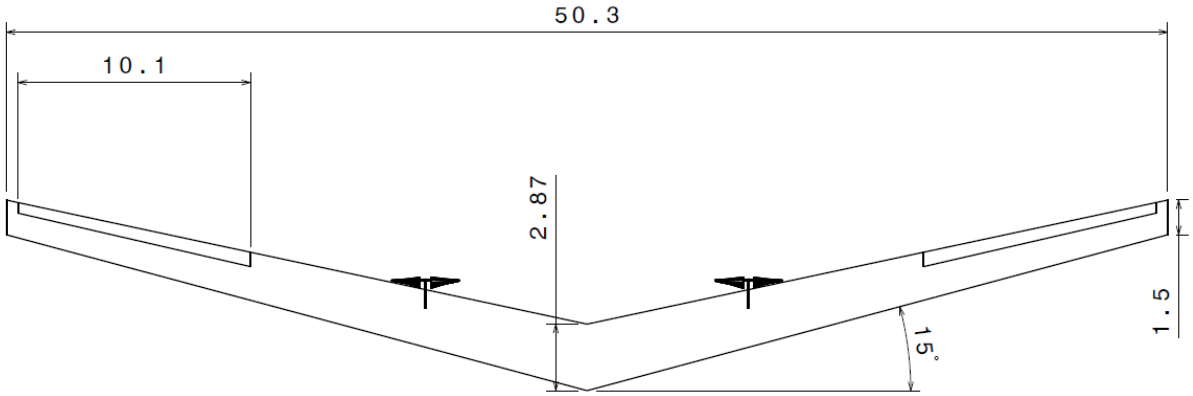

Figure 4.18: Aircraft planform with sizes in meters

standard value which was used while making the graph (0.05). The additional twist angle is then equal to -2.76°.

The total geometric twist angle (β_{geo}) can then now be found by adding these two values and equals -4.5°.

XFLR5 Stability Simulation

Using the values from subsection 4.3.2 and the sweep and twist calculated in the previous section, a three dimensional model is created in XFLR5 to simulate the stability of the aircraft and thus verify the design. First the $C_m - \alpha$ graph is checked and can be seen in Figure 4.22. The slope is negative, in other words $\frac{dC_m}{d\alpha}$ is negative, thus the requirement for static longitudinal stability is met [58]. Static stability has now been demonstrated, which means one of the requirements for dynamic longitudinal stability has been fulfilled. Further proof of longitudinal dynamic stability can be seen in Figure 4.23, where it can be seen that all the eigenvalues are negative on the real axis and mirrored on the imaginary axis. Figure 4.24 shows the eigenvalues for the lateral modes. The most conspicuous aspect is one eigenvalue which is positive. Table 4.7 shows the calculated values for the eigenmotions [58] based on the eigenvalues determined in Figure 4.24. A slightly different approach, based on the stability derivatives given by XFLR5, was used to calculate the eigenvalues for the longitudinal eigenmodes. The phugoid has a low value for the period of 3.73 s. This will have to be actively stabilized for the payload to be able to function. A low damping ratio can be observed, which makes sense because of the very high C_L/C_D values. The short period has a higher damping ratio, within the normal range. The time to half damping and natural frequency however are odd. Further investigation will be needed. Both the short period and the phugoid have been calculated using the simplified equations of motion as explained in chapter 5.3 in [58].

For the aperiodic motions, the time to damp to half amplitude is 0.2549, so this is not a control problem. However, $T_{\frac{1}{2}}$ for the spiral motion is a negative value, indicating instability of the aircraft in this motion. This corresponds to the positive eigenvalue in Figure 4.24. However, the value is high, indicating the motion is only slightly unstable. Furthermore, many aircraft have a slightly unstable spiral motion which is usually acceptable because the time it takes for the

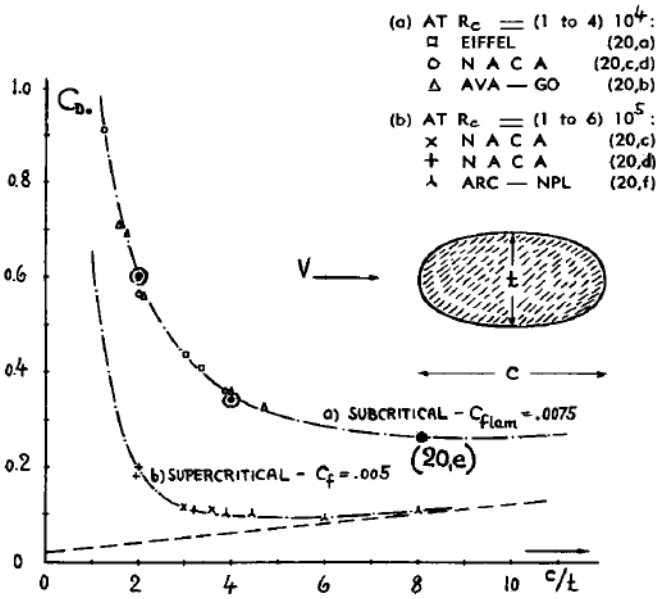

Figure 4.19: Drag of elliptical sections above and below the critical Reynolds numbers [55]

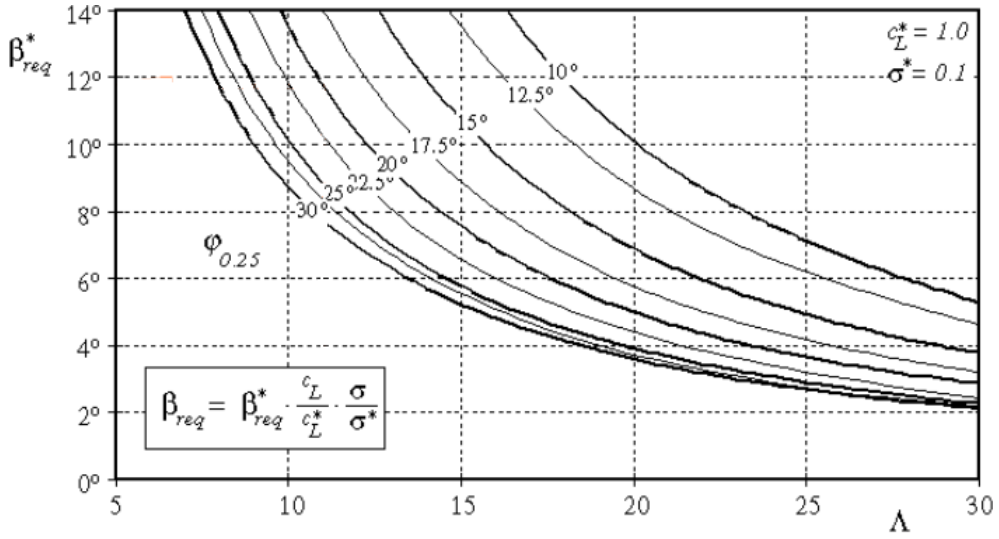

Figure 4.20: Geometric twist against aspect ratio for multiple sweep angles [56]

motion to increase in amplitude is high, giving the pilot or autopilot enough time to correct the aircraft. Finally, the Dutch Roll is also a damped motion. However, the $T_{\frac{1}{2}}$ is rather high, which could be a problem when performing observation, because it could deform the image. Thus some form of yaw damping system in the flight management computer is advisory to increase observation capability.

Center of Gravity Location

This analysis was done by first applying a sweep and twist to the wing in XFLR5. Now the center of gravity was moved around until the point had been reached where $C_m = 0°$ at the trim point of 6°, in order to reduce the trim drag to a minimum. The position on the x-axis of the center of gravity at which this has been achieved, is 3.679 m from the front of the aircraft. In order to fulfill the center of gravity requirement, the batteries will have to be place on the same horizontal line as the propellers. In practice this means they need to be placed at 14 m from the root in spanwise direction.

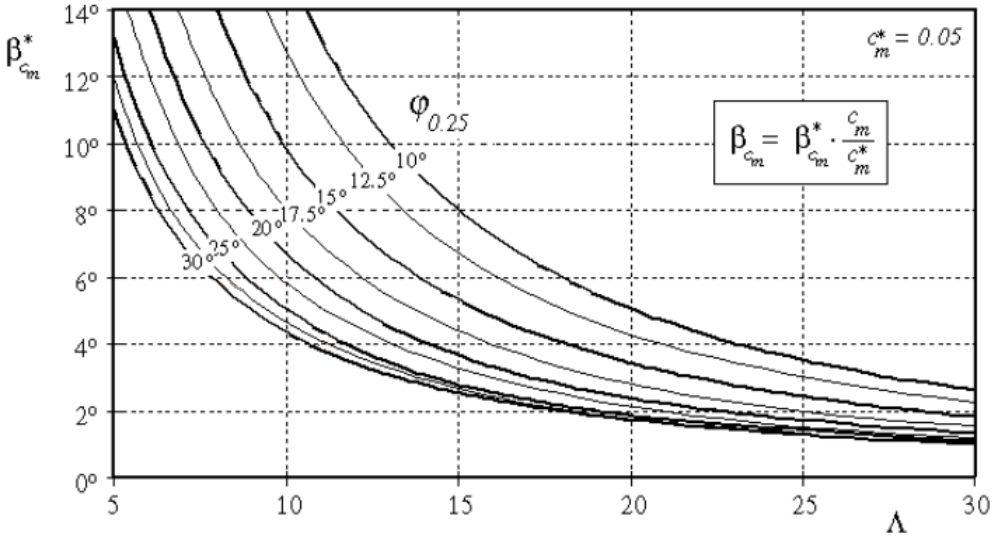

Figure 4.21: Twist due to the airfoil against aspect ratio for multiple sweep angles [56]

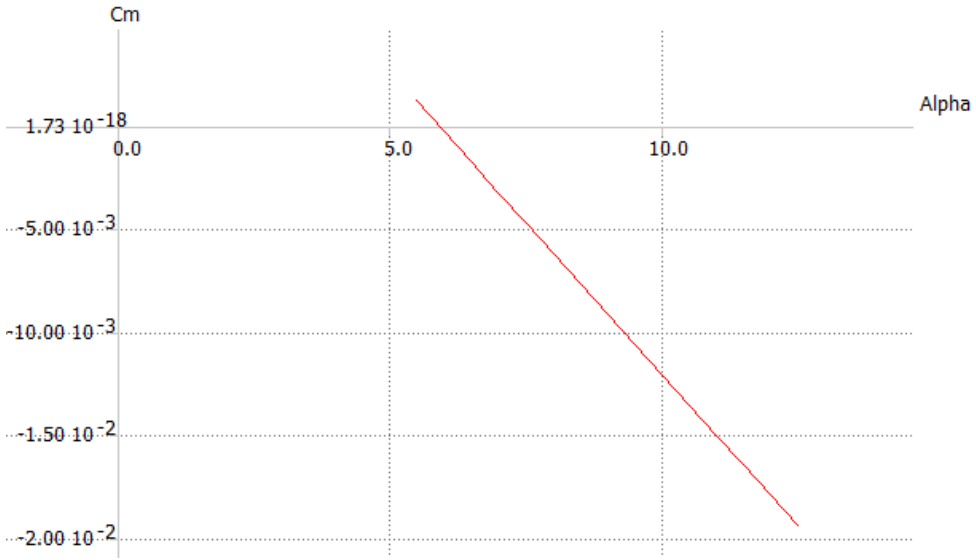

Figure 4.22: $C_m - \alpha$ graph of the full wing with trim point at $\alpha = 6°$

4.3.4 Stability during Vertical Gusts

A potential problem for the aircraft could be a vertical gust. It is possible, if the gust hits one side of the wing, this wing would roll and get out of balance and crash. It is also possible that the aircraft pitches so hard due to the angle of attack increase that it gets into a deep stall and also crashes. Therefore a study is done on what the aircraft response will be during a vertical gust of 10 m/s. There are two cases one is when one wing is hit by a gust and will start to roll, the second one is the one when the aircraft flies straight through a gust and will start pitching.

Roll Response

The wing will be represented by a flat plat with a C_D coefficient of 1.17. The area of one wing will be 55 m^2, the vertical gust will be 10 m/s. The most crucial part of the flight is during take-of and landing, because during these procedures the highest wind gust will be measured. The drag that will be produced can be calculated with Equation 4.8

$$D_{gust} = \frac{1}{2} \cdot \rho \cdot U^2 \cdot A \cdot C_D = \frac{1}{2} \cdot 1.225 \cdot 10^2 \cdot 55 \cdot 1.17 = 3.94 \qquad \text{[kN]} \tag{4.8}$$

This will introduce a rolling moment around the center of gravity, which will introduce then an angular acceleration. Due to this angular acceleration a roll rate will be introduced. Because

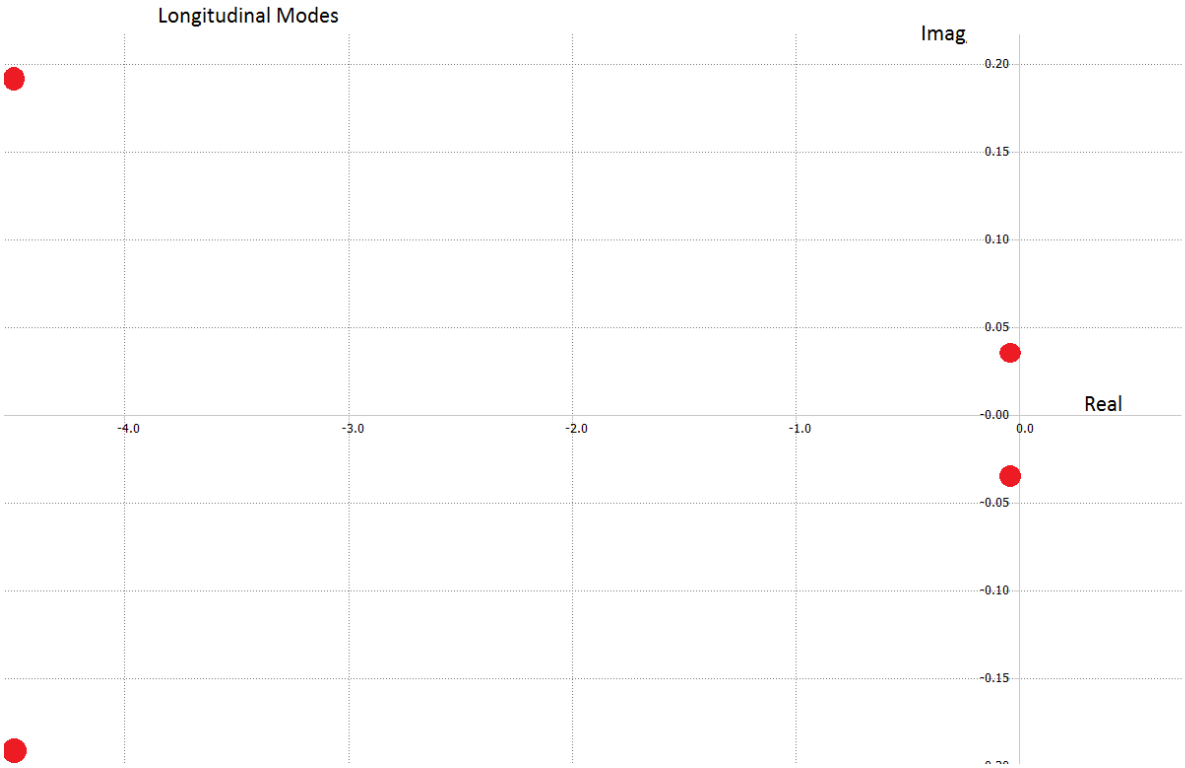

Figure 4.23: Eigenvalues of the longitudinal eigenmodes

Table 4.7: Calculated values for the Longitudinal and Lateral eigenmotions

	Phugoid	**Short period**	**Aperiodic motion**	**Spiral motion**	**Dutch Roll**
eigenvalue	-0.001±0.0662i	-0.6285±0.6043	-6.216	0.03271	-0.1016±.2985i
Period [s]	3.7352	1.068	-	-	48.1261
$T_{\frac{1}{2}}$ [s]	27.016	0.01133	0.2549	43.728	15.59
ω_0 [rad/s]	1.6824	8.487	-	-	3.0695
ζ	0.0152	0.7208	-	-	0.3222

of this roll rate an extra drag will be introduced opposite to the vertical wind drag. This roll drag will also a moment but opposite to the already exciting moment of the vertical gust. If it is assumed the gust continues for 3 sec then the angle that it has turned will be 5°. This is an rather good value and this means that the aircraft can handle a gust of 10 m/s on one wing.

Pitch Response

It is now assumed there is a vertical gust and the aircraft flies right trough it with a speed of 6.9 m/s. It is also assumed that the wing only needs to fly trough the gust until the center of gravity is hit by the gust, since the back part will reduce the pitch angle that is created during the first part of the gust. The area in front of the center of gravity will be 40 m^2 and the C_D is again 1.17.

From the Figure 4.25 There can be seen that the pitch angle is 16° at this angle the wing will start to stall. Further research needs to be performed to check if the aircraft can get out of this stall.

4.3.5 Conclusion

This subchapter has described the development of the aerodynamic properties of the wing in sequential order. Of course this is an iterative process and almost all of decisions and choices were performed in parallel. Input parameters also changed throughout the process, as other specialty groups used the data from aerodynamics to calculate more accurate parameters of their own. This has resulted in a stable, controllable aircraft which fulfills the requirements

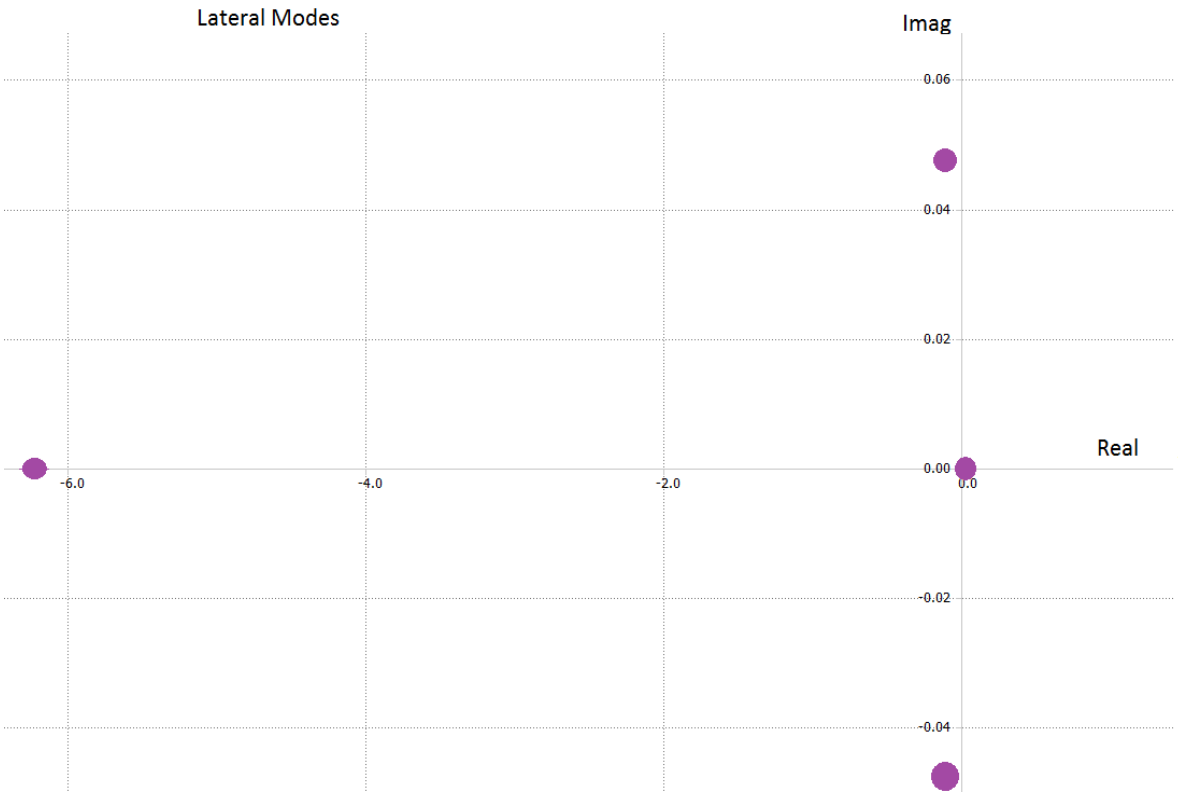

Figure 4.24: Eigenvalues of the lateral eigenmodes

imposed on it from both a structures and performance point of view as well as being able to carry the payload. One point for further research is the fact it is possible for the aircraft to entire a stall as a result of a strong vertical gust. This in itself is not necessarily a problem, but research needs to be performed if the aircraft is able to recover from a stall or if it becomes unstable and enters a unrecoverable deep stall.

4.4 Control Surface Sizing

In this section the control surfaces will be sized. Since the aircraft in question is a flying wing, no horizontal or vertical stabilizers are available for control. Therefore longitudinal control will be merged with the ailerons, thus using elevons. Yaw control will be done by differential pitch on the two engines. First the assumptions used during the sizing and the requirements imposed on the control surfaces will be discussed. Afterwards the elevons will first be sized, followed by the yaw control.

4.4.1 Assumptions and Requirements

Because high roll rates of around 50° within 4.5 seconds are required, while the aircraft is resistant to rolling due to the high aspect ratio, it was assumed the requirements on the aileron are the most critical requirement. Thus if the elevons are sized for roll rate requirements, the longitudinal requirements will automatically be fulfilled.

The requirements for the control subsystem are:

- Take-off and landing must be possible in wind speeds of up to 5.4 m/s
- Handle a crosswind during take-off and landing of 5 kts
- A roll from -10° to 40° must be able to be performed within 4.5 seconds
- Ideally drag must be minimized while performing control corrections

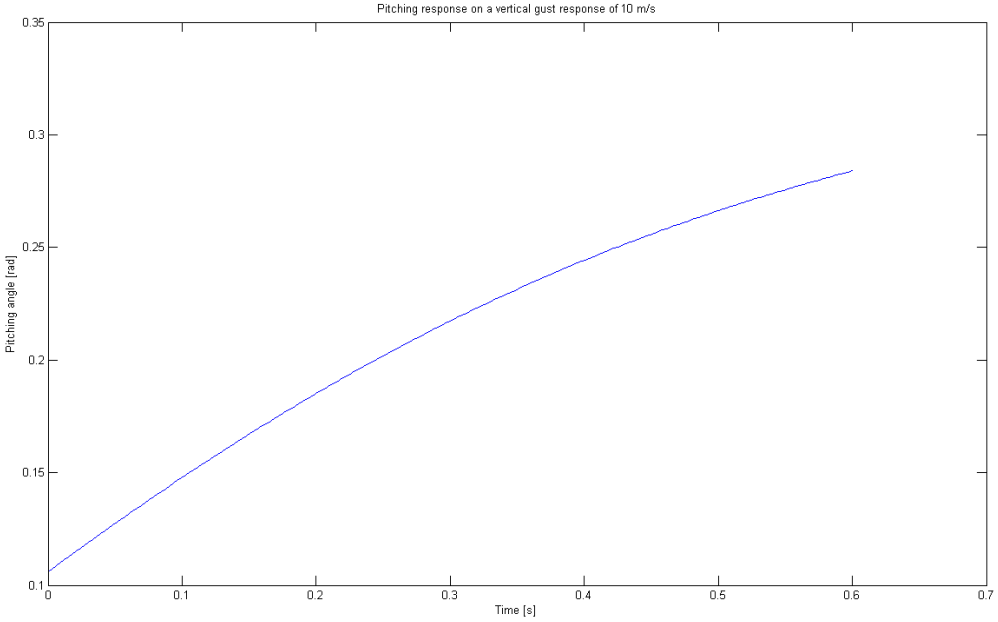

Figure 4.25: Pitch response of a vertical wind gust of 10 m/s

4.4.2 Roll sizing

Using the moment of inertia generated by XFLR5, a dynamic analysis was performed in MATLAB to calculate roll performance. This resulted in a required roll rate p of 0.1939 rad/s. An angular acceleration and roll angle followed. Ruijgrok [59] was used to calculate the turned angle during the roll maneuver. The two different rolls performed during the station keeping maneuver are considered. This results in a required force generated per elevon of 42N. During the roll from -10° to 40°, the aircraft turns 15°. Applying the same force to a 30° roll, from 10° to 40°, results in a roll of 2.65 seconds. During this roll the aircraft turns 25°.

Now the required roll rate is known, the elevons can be sized using Equation 4.9 [58]. All values are already known, except for the two stability derivatives. C_{ℓ_p} was taken from XFLR5 and determined to be -0.68955.

$$\frac{pb}{2V} = -\frac{C_{\ell_{\delta_\alpha}}}{C_{\ell_p}}\delta_\alpha \qquad [\text{-}] \tag{4.9}$$

Using Equation 4.9, the value for $C_{\ell_{\delta_\alpha}}\delta_\alpha$ can be calculated. "Theoretical Stability and Control Characteristics of Wings With Various Amounts of Taper and Twist" was used to calculate the value for $C_{\ell_{\delta_\alpha}}$. The data in this paper assumed maximum elevon deflection of 20°. Furthermore, in order to avoid reducing the L/D too much, it is of interest to reduce the flap deflection as much as possible. Therefore it was decided to design for a elevon deflection of 20°. Taking an elevon of 0.3 chord length, value of k can be taking from figure 18 in [60]. Using this value, figure 16 in Pearson gives the relevant value for the elevons. This results in a elevon with a size of 0.4 times the halfspan and 0.3 chord length.

4.4.3 Yaw sizing

The driving requirement for sizing yaw control was handling cross winds of up to 5 kts. Crosswind requires the aircraft to fly at an angle pointing away from the runway to compensate for wind drift. During the worst case scenario, the aircraft will fly just above the stall speed at sea level (5 m/s) and the wind will be 90° cross. This results in a side slip angle of 24.84°. The requirement is imposed the aircraft must be able to reduce this angle to zero within four seconds to fulfill control requirements. The maximum thrust from the power plant system is given as 141 N. Since a variable pitch system has been chosen for the propellers, negative thrust can be delivered by one engine, it is assumed that this can be done with 50% efficiency. Together with the positive thrust from the other engine, a couple moment is created. A similar model as for aileron sizing was used to calculate the arm (in other words, the distance of the engines from the root) necessary

to meet the requirement. This results in a minimum required distance of 13.56 m between the two engines for yaw control.

4.4.4 Actuator Seizing

To size the actuators the moment and forces need to be known. It is known that the deflection is 20° and the position is 0.5 to 10.17 meters from the tip. The length of the flap is 30% of the local chordlength. The force distribution is approximated using the C_p values found from the plots seen in Figure 4.26b and using Equation 4.10. The pressure coefficient is assumed to be linear between the hinge of the flap and the trailing edge. The presure coefficents of the airfoil without and with the flap deflected are seen in Figure 4.26a and 4.26b respectively. With Equation 4.10 the real pressure is calculated and the resulting forces and moments. The resulting moment on the flap is 32.1 Nm. Including a safety margin of 1.5 a total moment of 48.2 Nm has to be accounted for.

Initially a non-conventional actuation system was desired to comply with the all plastic requirement. Piezoceramics, Electro Active Polymers (PEA), Rubber Muscle Actuators (RMA) and Shape Memory Materials (SMM) where considered. Unfortunatly these techniques were insufficient for the design as they become to heavy, required to much energy or could simply not generate the required deflection and force. As a result the option left over was a conventional actuation.

For the actuator itself an off-the-shelf solution is sought for, as the development of an actuator is a difficult and time consuming operation. Linear and rotary servo actuators were considered and after comparison of several option the MTC ERSA-0311 electrical rotary servo actuator is chosen. The actuator delivers 25 Nm maximum torque and weights 0.875 kg. Two actuators per control surface are needed, resulting in a total weight of 3.5 kg. The total peak power is 448 W, which is only required for 50 Nm for both flaps. Power use without flap deflection is in the sub-Watt range.

$$C_p = \frac{p - p_\infty}{q_\infty} = \frac{p - p_\infty}{\frac{1}{2}\rho_\infty V_\infty^2} \qquad [\text{-}] \tag{4.10}$$

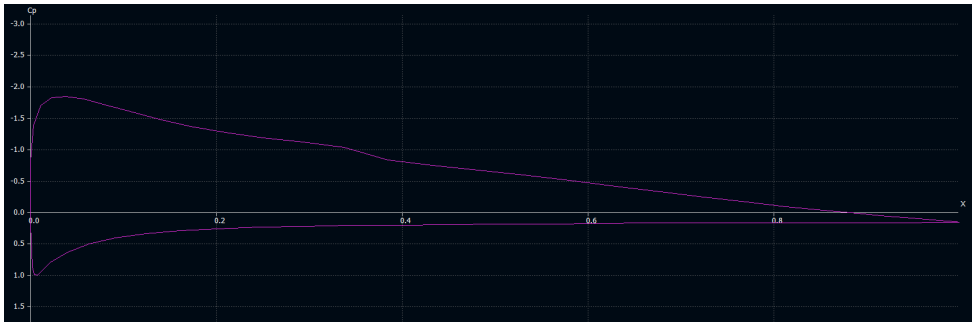

(a) without deflection

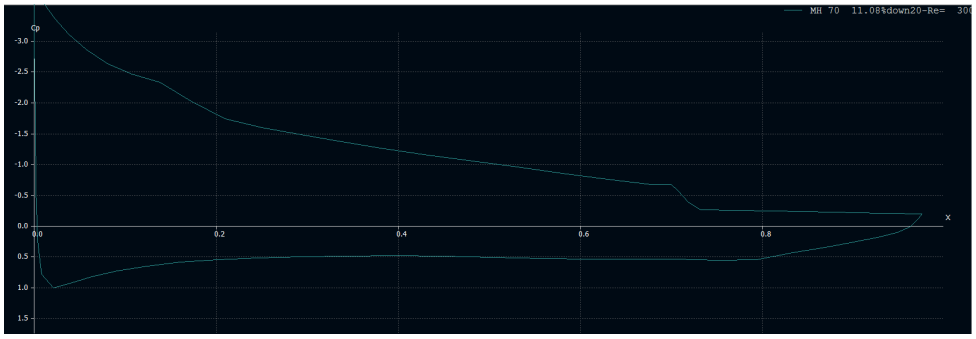

(b) with 20^o deflection

Figure 4.26: pressure distribution over the airfoil in normal and in deflected position

4.5 Propulsion

This section presents the design of the so called 'drivetrain'; the subsystem delivering power to the propeller from the battery. It includes the motor, gearbox, driveshaft, hub and propeller. From section 5.3 the thrust levels required for different flight segments can be obtained by dividing the power delivered by each propeller by the flight velocity. The results are summarized in Table 4.8 which will be used for propeller sizing. This determines the amount of blades, motors and therefore the rest of the drivetrain.

Table 4.8: Thrust levels for different flight segments

Flight Segment	Velocity [m/s]	Thrust [N]
10° Turn	22	46
40° Turn	17	85
Cruise	20.8	44
Climb	22.9	50

4.5.1 Propeller

Xrotor [61] was used for designing and optimising the propeller. Xrotor generates a certain propeller geometry with minimum induced losses for a set of input variables. A potential flow approach was selected within Xrotor for the sizing. The reason to deviate from the commonly used momentum methods was that the momentum formulation in Xrotor is not suitable for advance ratios lower than 0.5 (which is usually the case up until half-span in design flight conditions)[61]. A disadvantage however, of the potential flow method, is that the viscosity is not taken into account, which plays an important role in the low Reynolds regime. For simplicity reasons, the interference of the wing to the airflow ahead of the propeller will not be taken into account during the design process of the propeller. The MH122 is used as a reference airfoil.

Xrotor generates an optimal propeller geometry based on a few input parameters: Number of blades, propeller radius, hub radius, flight velocity, rpm, thrust or power and lift-coefficient. For stability reasons there will be two propellers on either side of the wing and they will be placed at the rear of the wing (whilst their respective motors are placed ahead of the centre of gravity) for relieving the pitch-up moment of the whole configuration. The foremost flight profile requires 46 N of thrust in total or 23 N delivered by each propellerTable 4.8. The other parameters are either determined by literature or flight- and wind conditions.

In Figure 4.27 it becomes evident that 2 bladed propellers are more efficient than 3 bladed propellers. The thrust output however, for 2 bladed propellers, is limited, but this is of no relevance for the aircraft since the required thrust is rather low [62].

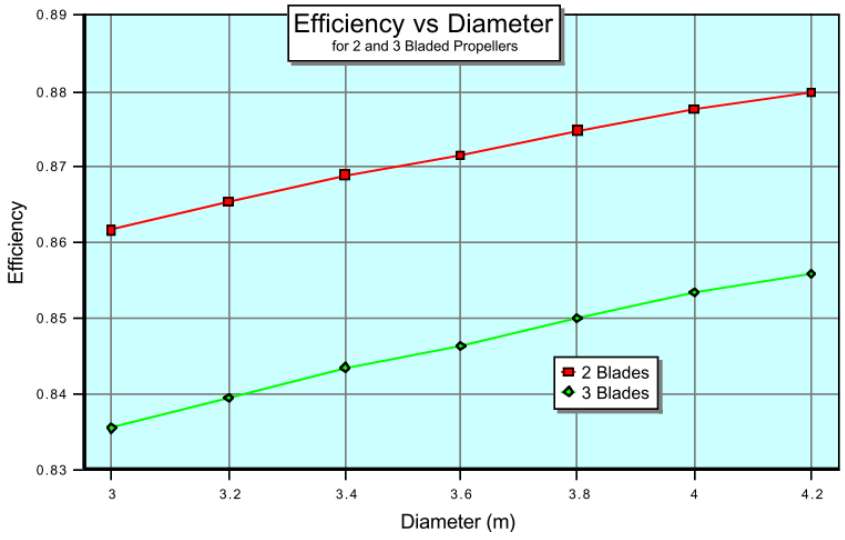

Figure 4.27: Efficiency vs. propeller diameter for two- and three-bladed propellers [62]

From Figure 4.28 in the following and using the single propeller of the NASA Perseus [62] as a reference, the blade radius of the propeller was determined to be 1.47 m. The hub radius usually lies between a tenth and a fifth of the total propeller diameter. A hub radius of 0.23 m appeared to be the most efficient after trial and error.

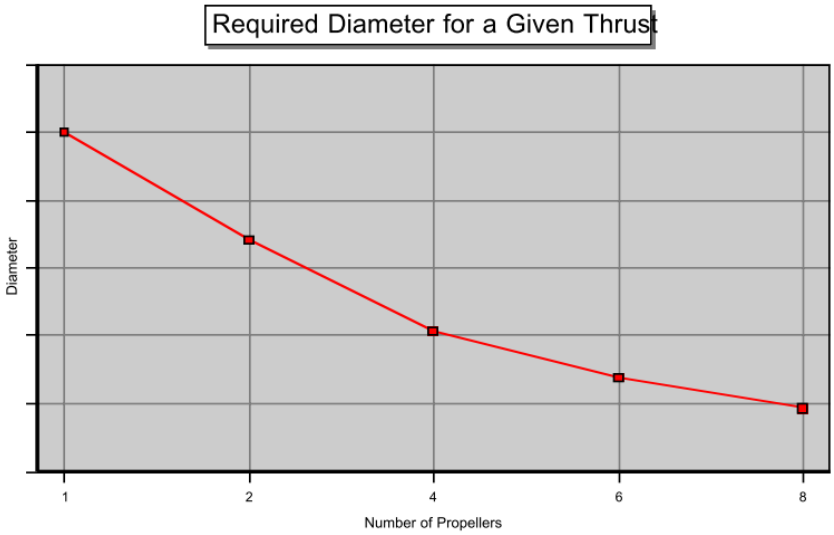

Figure 4.28: Propeller diameter vs. number of propellers [62]

The optimal flight velocity was set at 22 m/s in the previous section and this value will also be used for the optimisation with Xrotor. The propeller will operate at 400 revolutions per minute - Slow revolving propellers appeared to be more efficient while using Xrotor. For the lift coefficient along the span of the propeller blade it is assumed that it will be varying linearly between typical cruise values of 0.5 and 0.3 from root to tip. With these parameters Xrotor gave the following geometry which can be seen in Figure 4.29 This propeller geometry has a efficiency of 85.3 % and a thrust-coefficient of 0.1157. The power and torque required for providing 23 N of thrust would be 593 W and 14.2 Nm respectively. The Mach number under these conditions wouldn't exceed 0.25 and the Reynolds numbers over the blade go down from 120,000 at the root- and mid-section to 20,000 at the tip.

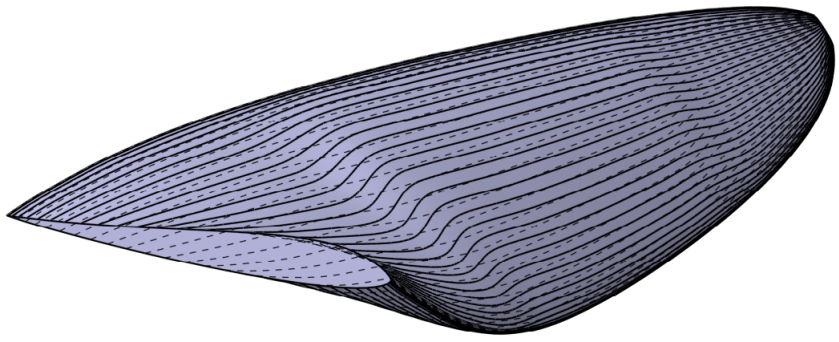

Figure 4.29: Propeller geometry

The propeller geometry in Figure 4.29 has a maximum chord length of 32.82 % and has high blade twist angles varying from 74.2° at the root to 23.5° at the tip with respect to its rotational direction. The angle of attack experienced by the propeller blade can be calculated by deducting the phi-angles, which is the tangent of the rotational velocity and the free-stream velocity, and the induced angle of attacks, which is determined by the method presented in [63], from the blade twist angles for every section found by Xrotor. From root to tip the effective angles of attack vary from 7.8° to 3.8°. At the root, the MH110 airfoil will be used (up until r/R = 0.4) instead of the MH122 as it can handle higher angles of attack and at the tip-section (from r/R = 0.8 on) the MH23-8 is chosen as it handles very low Reynolds numbers better as it is very thin. Both changes from the MH122 reference airfoil were decided upon after an analysis in XFLR5. The airfoils selection for the propeller blade is largely simplified by only taking three different foils over the blade-span. Some important parameters and results per propeller for the design condition and off-design conditions are summarized in the following table:

Table 4.9: Propeller performance in design and off-design conditions

Flight Segment	**Velocity [m/s]**	**Thrust [N]**	**Efficiency [%]**	**Power [W]**	**Torque [Nm]**
10° Turn	22	23	85.3	593	14.2
40° Turn	17	42.5	82.4	877	20.9
Cruise	20.8	22	84.6	541	12.9
Climb	22.9	25	86.0	666	15.9

In Table 4.9 it is assumed that the rotational speed does not change from 400 rpm. The propeller blades however change angle for the different flight segments by using a servo-motor in order to optimise performance. The propeller is able to operate at lower altitudes and at sea-level as well by lowering the rpm of the propeller in addition to changing the blade pitch-angle. Even though the motor would operate below its optimum rpm-range, the power available would never be exceeded as the flight velocities at lower altitudes are much lower than 22 m/s. On top of that, the increased efficiency for the lower rpm partially cancels out the decreased motor efficiency.

Kev 49 with an epoxy matrix [64] is chosen as the material for the propeller as it has relatively low density among other composites - Solid wooden cross-sections proved to be heavier. With an assumed thickness of 0.5 mm for (hollow) propeller, each blade will weigh 690 g.

The low Reynolds number values are the result of the strongly decreased density at higher altitudes, the short chord-length and the low airspeed as well as the low rotational speed. As a result of the low Reynolds numbers, the laminar airflow has more difficulty to stay attached to the airfoil because of adverse pressure gradients after the peak pressure along the chord. The separated laminar flow will eventually turn into a turbulent flow at the transition point where after this turbulent flow reattaches to the airfoil again. The area enclosed by the airfoil, the separated laminar flow and the reattaching turbulent flow makes up the laminar separation bubble. This separation bubble increases the undesired pressure drag considerably. In a pressure distribution, a laminar separation bubble can easily be noticed as the gradient of the pressure decrease along the chord after the pressure peak is rather low, almost horizontal, and at a given location suddenly drops to lower pressure levels.

In order to remove the laminar separation bubble over the airfoil of the propeller blade and therefore gain better performance characteristcs, the boundary layer over the airfoil can be tripped before the separation bubble would start to appear. The laminar air flow will then be converted into a turbulent air flow before the laminar transition bubble. A turbulent air flow contains more energy than a laminar air flow and therefore stays attached to the airfoil. The separation bubble then simply disappears. With the bubble removed, the strong increase in pressure drag from before will also be eliminated. The viscous drag would of course increase because of the turbulent flow over the airfoil, but the total drag will significantly be lower than for when a separation bubble is present nevertheless.

In the remainder of this section, the lift curves and drag polars for the airfoils of the propeller blade in their specific flight regime will be plotted, then the pressure distributions along the chord of the propeller blade for every airfoil will be investigated and so the location of the trips will be determined thereafter (just ahead of where the seperation would initiate). The benefit of the applied trips will be shown by creating the same plots and distributions again.

The following graphs show the drag polars and lift curves of the used airfoils for the different propeller blade-sections in their average Mach- and Reynolds number regime. There are no trips applied yet and it can clearly be seen that the laminar separation bubble is present; the drag coefficient is disproportionally increased for values of the lift coefficient that are still within the laminar region of their respective lift-curve. Besides that, for the corresponding pressure distributions at the average angle of attack that the airfoils will encounter during flight, the flat envelope of the pressure distributions show the presence and location of the bubble. In Figure 4.30, Figure 4.31 and Figure 4.32 the drag polar, lift curve and pressure distribution of the different airfoils can be seen with the presence of laminar separation bubbles.

Optimal trip locations were found with XFLR5 and these were located at 0.19c, 0.57c and 0.61c for the MH110, MH122 and MH23-8 airfoils respectively. The new curves and distributions after tripping the airfoils can be seen in Figure 4.33, Figure 4.34 and Figure 4.35. In these graphs it can be clearly seen that the airfoils have better characteristics after the applied trips.

The figures in the previous are the result of a 2-dimensional flow analyses. In reality, the propeller operates in a 3-dimensional flow and therefore will the envelope of these curves change. There is

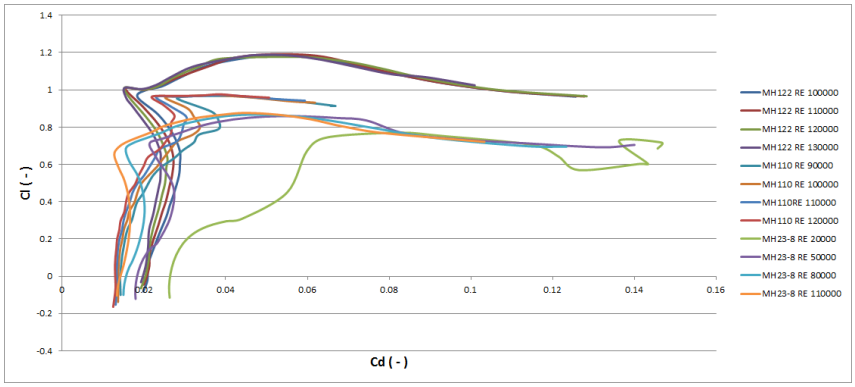

Figure 4.30: Drag polars of the airfoils used for the propeller blade without trips in their Reynolds number regime.

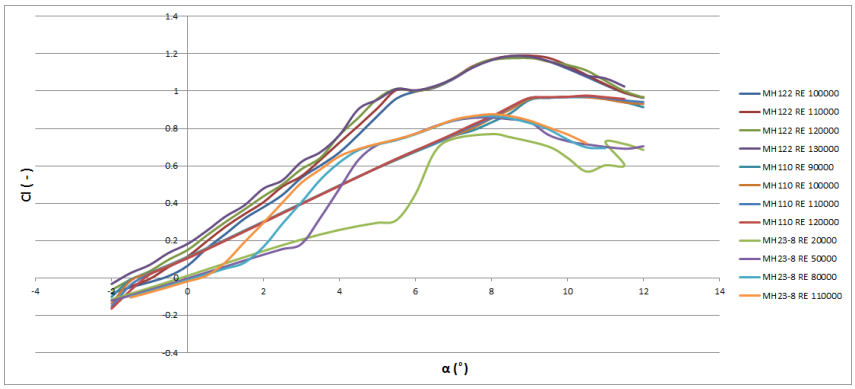

Figure 4.31: Lift curves of the airfoils used for the propeller blade without trips in their Reynolds number regime.

no clear solution for a 3-dimensional correction for rotors [65] and the correction that is usually on wings is not valid because of the rotation. From [65] it can be said that for 3-dimensional conditions the lift slope near the root stays the same compared to a 2-dimensional wing. The maximum lift coefficient increases however, because Coriolis-Forces stabilize the laminar air flow - The best trip location of the airfoil near the root determined earlier may therefore also change. At the outer sections of the propeller blade, the lift slope decreases as well as the maximum angle of attack.

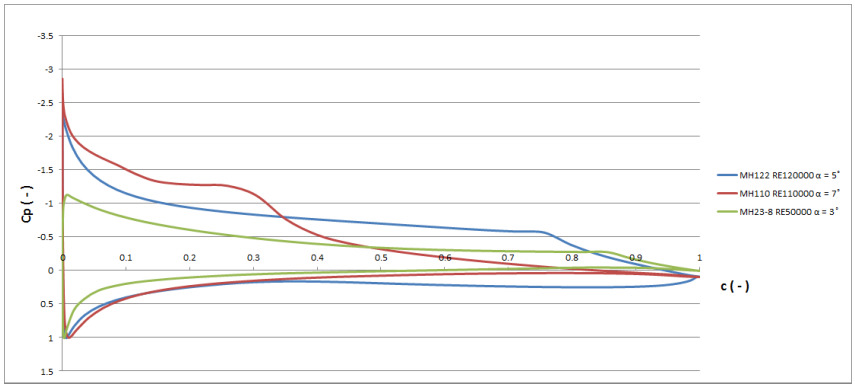

Figure 4.32: Pressure distribution of the airfoils used for the propeller blade without trips at their average Reynolds number and angle of attack over the blade span.

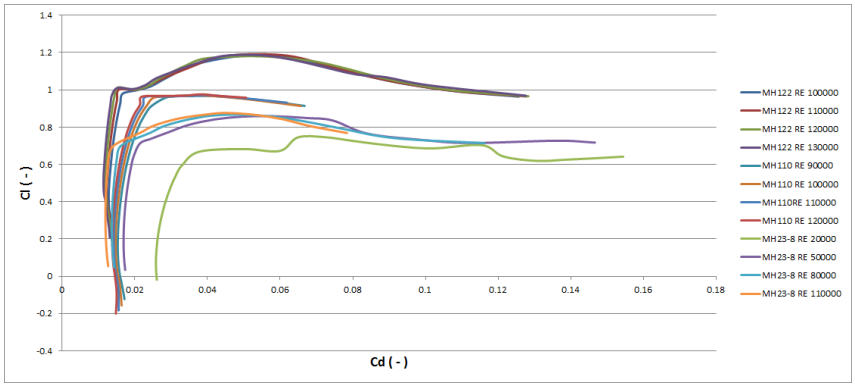

Figure 4.33: Drag polar of the airfoils used for the propeller blade with trips in their Reynolds number regime.

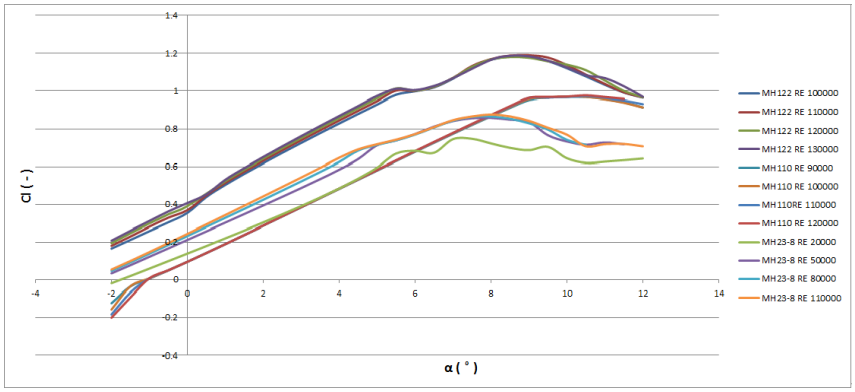

Figure 4.34: Lift curves of the airfoils used for the propeller blade with trips in their Reynolds number regime.

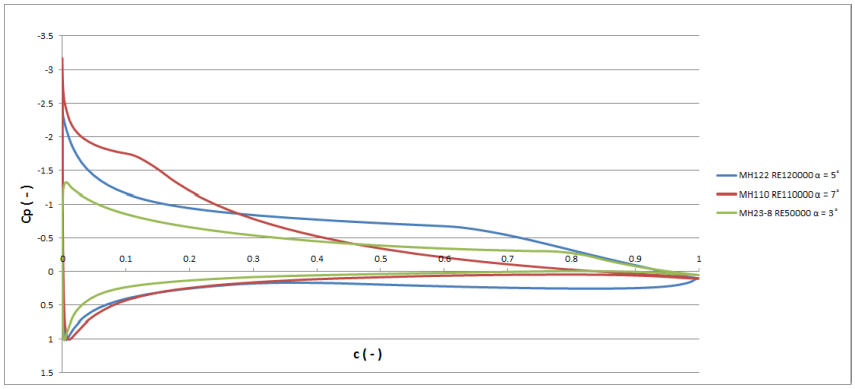

Figure 4.35: Pressure distribution of the airfoils used for the propeller blade with trips at their average Reynolds number and angle of attack over the blade span.

4.5.2 Motor

An off the shelf motor has been selected to fit the required propulsive needs. The CPM90-22-1500-L has specifically been chosen for its high efficiency at low rpm [66]. It would allow the use of only one gear box to transfer the power to the propeller and therefore limit transmission losses. Small and light electro-motors usually reach their best performance at around 7,000 rpm which would require two planetary gear boxes as the transmission-ratio for these is limited to 10:1. The 2.3 kg CPM90-22-1500-L motor can deliver 1.5 kW nominally with an efficiency of 90% at an rpm of 3600. The motors include speed-controllers.

4.5.3 Transmission

A gearbox has been designed to reduce the motor rpm mentioned above to the rpm required by the propeller. A gear ratio of 9:1 is required. The choice for a planetary gear box has been made for its small volume and efficient load transfer due to the relatively small loads induced in each gear. The efficiency for a planetary gearbox is about 97 % [67]. The geometry of the planetary gearing is shown in Figure 4.36, where the ring gear and planet gears are very distinct. The sun gear is hidden behind the structure holding the planet gears in place.

To prevent necessity for lubrication and housing the gearbox will be made of Polyamide 6/66 [68], which also reduces gear mass. Sizing the gearing resulted in a sunwheel with 10 teeth, the three planet gears having 35 and the ring gear 80 [69]. The outer diameter of the entire gearbox is 17 cm and total mass is approximately 300 g.

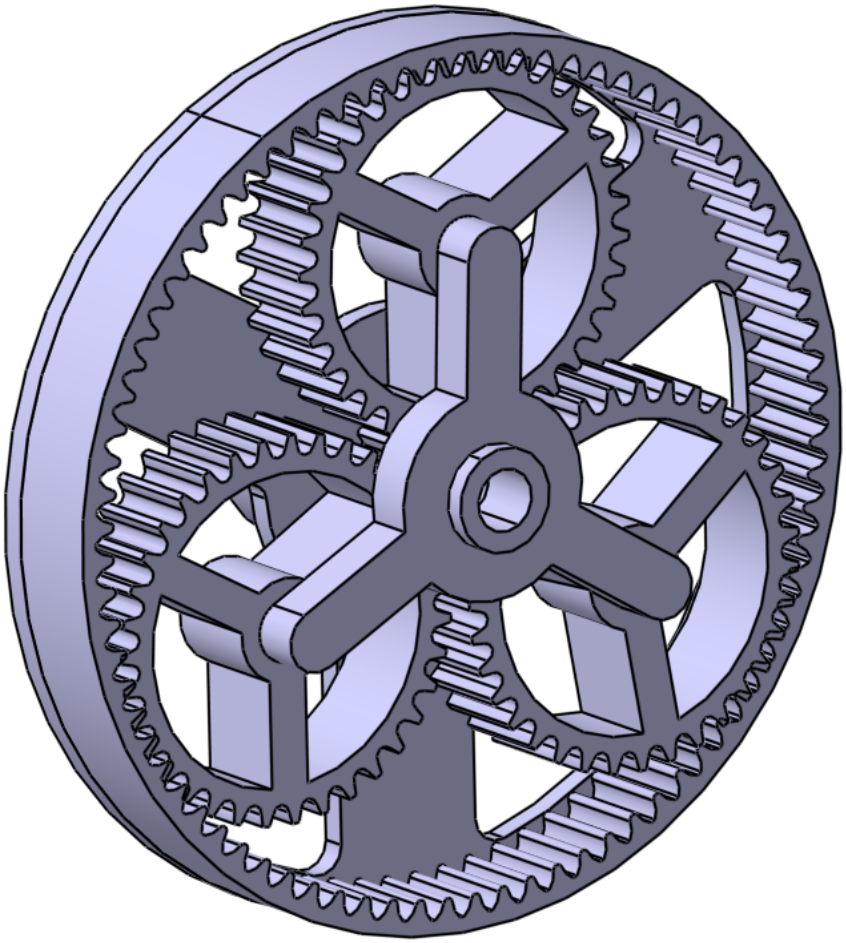

Figure 4.36: Planetary gearing

A carbon fibre driveshaft made of As 4 fibres and a PEEK matrix [64] will transfer the torque to the hub. This material was chosen for its properties in handling shear stress. A diameter of 3.6 cm and thickness of 0.5 mm are sufficient to carry maximum torque and results in a mass of approximately 147 g for one shaft. The dimensions were determined by setting the minimal thickness to 0.5mm and the torque at a maximum of 83.6 N, which is the torque required for

the sharp turn Table 4.8 when failure of one engine is considered and a safety factor of two, and thereafter calculating the enclosed area of the thin-walled closed cross-section [70].

Finally, the load is transferred to the hub, to which both propeller blades are attached. The hub will be made from the same material used for the gearbox. It is a hollow structure to reduce mass as much as possible and to contain a servomotor on each side needed for variable pitch. Bare hub mass is approximately 250 grams.

4.5.4 Design

The entire drivetrain is shown in Figure 4.37. Both the motor and gearbox will be fixed to the rear spar of the wingbox and the driveshaft will run through the upper wing skin and needs a supporting structure up to the hub.

All supportive structures, bearings and cabling are yet to be designed or selected. The blade pitching-system must be designed into detail on top of that.

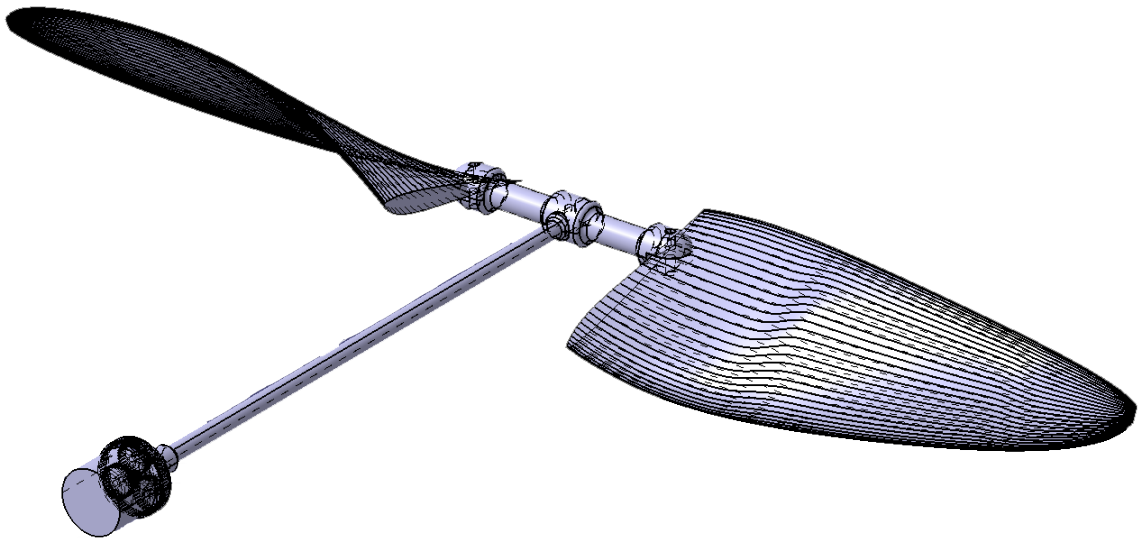

Figure 4.37: Drivetrain assembly

4.6 Battery

The flying wing depends heavily on a battery to store energy for consumption during the night. Especially for a mission duration of one year many situations occur which require more power than cruise flight. The battery needs to store enough energy for these events, while remaining lightweight and small. This chapter discusses the selection of batteries and the sizing and design of the entire battery system.

4.6.1 Requirements

Several requirements have been set which the battery has to comply with, which are listed below. Since a battery can deliver only a certain voltage and a transformer would add unnecessary weight, a separate battery is required for the flight systems and payload. The following requirements apply to both batteries.

- Total mass should not exceed 87 kg (mass budget)
- Supply required power during longest night, i.e. 17.1 hours
- Endure a mission of at least one year

Additionally each battery has a few requirements specifically for its purpose, listed below. The following apply to the propulsion battery.

- Have a voltage of 48 V (motor manufacturer specifications)
- Even number of packs for division in wings

The systems battery only has one extra requirement:

- Have a voltage of 12 V (systems manufacturer specifications)

These voltages are rather low but result in only 0.62% voltage drop over a 7 m (see chapter 5) aluminium cable.

4.6.2 Battery Type Selection

Several battery types have been investigated and the most relevant parameters have been summarized in Table 4.10. Common batteries like NiCd and NiMH are excluded with an eye on sustainability and polymer usage.

Table 4.10: Important parameters of several batteries [71, 72, 73]

	Li-ion	**LiP**	**LiS**	**Li-air**	**Unit**
Specific Energy	400	250	400	1000	[Wh/kg]
Efficiency	98	99.8		81	[%]
Cycle-life	400	500	200	4,000	[-]
Min. Temp.	-20	-20	-20	30	[°C]
Available	2015	Now	Now	2025	[-]

The selection of a battery type has been performed keeping development trends in mind. Lithium-sulfur (LiS) batteries are already available and perform equally well compared to lithium-ion, but with unacceptable cycle-life. Although LiS has the potential for higher specific energy, cycle-life will remain an issue and acceptable values are not expected in the coming 5 years.

Solid-state, thin-film batteries would be the best choice, but are unavailable until 2020 [74]. Cycle-life of thousands of cycles are possible, with specific energies of 1,110 Wh/kg (Li-air) [75]. Moreover, thin-film batteries can be integrated with solar cells or other components, which allows innovative designs.

Li-ion batteries have been selected because of their availability, specific energy and cycle-life.

4.6.3 Sizing

Envia systems produces Li-ion cells with a specific energy of 400 Wh/kg [76]. These cells have been used to size the battery pack of this UAV, with the values presented in Table 4.11. Specific energy and cell capacity are given at EOL.

Table 4.11: Properties of Envia Li-ion cell

Property	**Value**	**Unit**
Specific Energy	325.4	[Wh/kg]
Density	1,981	[kg/m^3]
Efficiency	98	[%]
Cycle-life	400	[cycles]
Min. Temp.	-20	[°C]
Cell Mass	365	[g]
Cell Voltage	3.11	[V]
Cell Capacity	38.2	[Ah]
Cell Width	97	[mm]
Cell Length	190	[mm]
Cell Thickness	10	[mm]

From Figure 4.38 it was estimated that at EOL the cell performance would be 83% of its Begin of Life (BOL). The voltages required determine the amount of cells in series, simply by dividing by the cell voltage. A module is then this amount of cells connected in series.

The entire battery has been sized with a model of the power input and output during December 21 at 55°N. Incoming solar power has been modeled using Equation 4.11 [78] during the day and $I(t) = 0$ during the night, systems power has been defined in section 4.1 and propulsive power in section 4.5. The top graph in Figure 4.39 shows the incoming and outgoing power. Solar

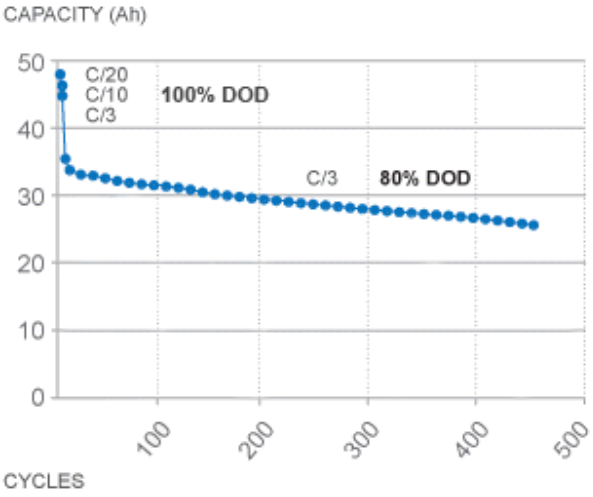

Figure 4.38: Capacity over cycles for Envia li-ion cell [77]

incidence data has been obtained from [**solpos**] and an irradiation of 1,200 W/m^2 has been assumed.

Charge power is simply the net power available ($P_{sun} - P_{system} - P_{propulsion}$) and determines the energy stored in the battery (bottom graph in Figure 4.39). This amount of energy should not drop below 20% of maximum capacity, because of a maximum Depth of Discharge (DoD) of 80% otherwise impairing cycle-life. The energy left in the battery at the end of the 24 hour interval should be higher than the value at the start to ensure enough storage for the entire night. The battery capacity and solar panel area have been changed until this requirements was met. Following is determining the amount of modules in parallel by dividing the power required by the module voltage, which results in a certain final mass and capacity. To finalize, this capacity would be put in the program to size the solar panels such that the battery would just be at maximum capacity at sunset.

$$I(t) = I_{max} \sin\left(\frac{\pi(t - t_{sunrise})}{t_{daylight}}\right) \qquad [\mathrm{W/m^2}] \tag{4.11}$$

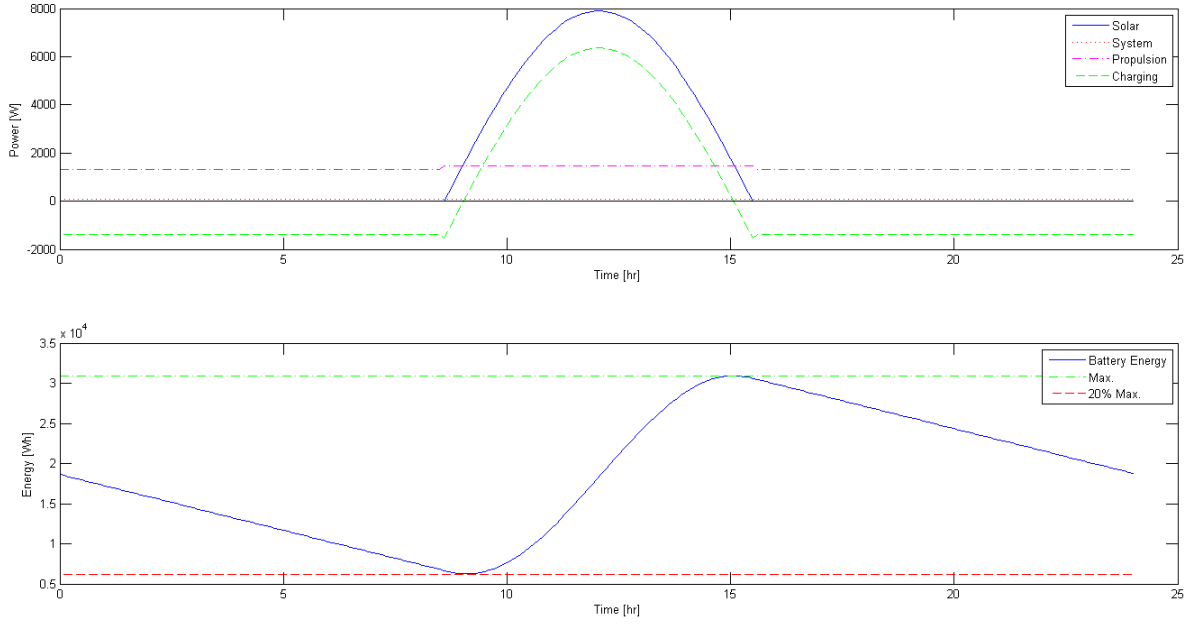

Figure 4.39: Power and battery cycling during Dec. 21, 55°N

Propulsion Battery Pack

The amount of power required is calculated in section 5.3, but the values differ slightly with the outcome of the propeller analysis. The latter have been used for sizing. The configuration is presented in Table 4.12 and the performance in Table 4.13.

Table 4.12: Propulsion battery configuration

Property	Value
Series	15
Parallel	8
Packs	2
Total # cells	240

Table 4.13: Propulsion battery performance

Property	Value	Unit
Voltage	46.7	[V]
Current	17.9	[A]
Power	1,666	[W]
Energy	28.5	[kWh]
Capacity	9,163	[Ah]
Mass	87.6	[kg]

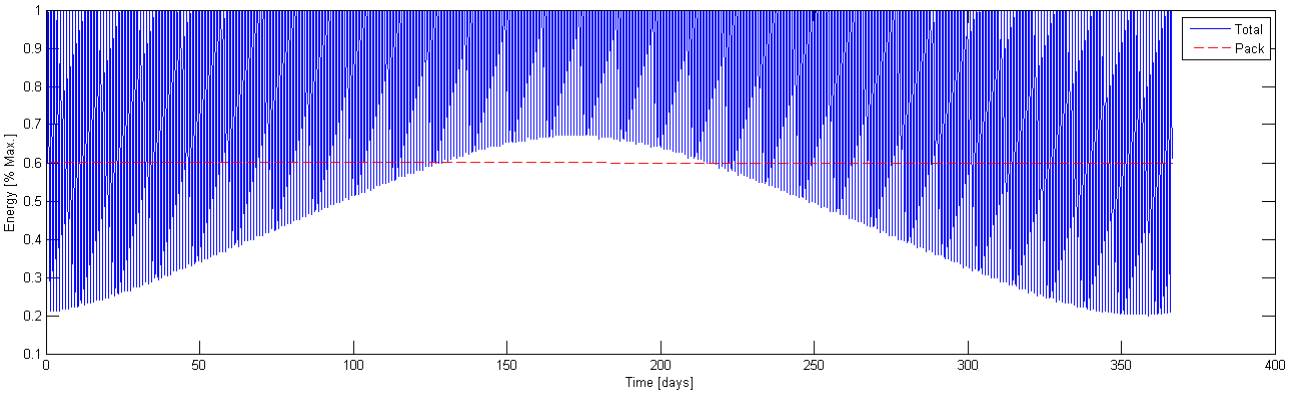

Figure 4.40: Power and battery cycling during 1 year, 55°N

Systems Battery Pack

The systems battery pack should deliver 74 W continuous power. The configuration is presented in Table 4.14 and the performance in Table 4.15.

Table 4.14: Systems battery configuration

Property	Value
Series	4
Parallel	3
Packs	1
Total # cells	12

Table 4.15: Systems battery performance

Property	Value	Unit
Voltage	12.4	[V]
Current	6.7	[A]
Power	83	[W]
Energy	1.4	[kWh]
Capacity	458	[Ah]
Mass	4.4	[kg]

Cycle-life Analysis

Some nights require less energy than what is stored in a battery pack. This is shown in Figure 4.40, where the dashed line indicates the stored capacity of one battery pack. Note that the systems battery has been incorporated in the entire battery for this analysis.

Looking at the minima of the sinusoid, only 1 pack is needed on the days where these minima are above the red line. On these days the battery effectively only makes half a cycle, while on all other days a full cycle is made. Each battery pack then has a total of 323 cycles during the year, but still has to be replaced after each mission (max. 400 cycles). Please note this does not take into account that on many days the battery is not discharged for the maximum DoD. Moreover, when this battery becomes commercially available in 2015, cycle-life will have been improved to compete with current battery technologies. The actual cycle-life will therefore be higher than calculated here, but it is better to assume 2 full years of operation will not be achievable even then.

Conclusions

The total mass adds up to 92 kg, 5 kg heavier than budgeted. The overshoot can be explained by the fact that it is built up of the specified cells, which will most likely not add up to the exact performance required. One could see this as rounding towards a higher integer number. Upside of this is that the battery will therefore perform better in the other requirements because of this. The voltages differ slightly from the values required, but this does not impose a problem. Both batteries can deliver more power than required and for a longer time. Therefore special manoeuvres can even be performed at night.

4.6.4 Design

The geometrical design of the battery was mainly driven by the electrical configuration. Secondary drivers were to minimize radar cross-section and minimize total surface area. The latter is necessary for heat management. All three batteries will be enclosed by a lightweight, fire resistant casing with a reflective coating on the inside. Figure 4.41 shows one of the two propulsion battery packs together with the systems battery.

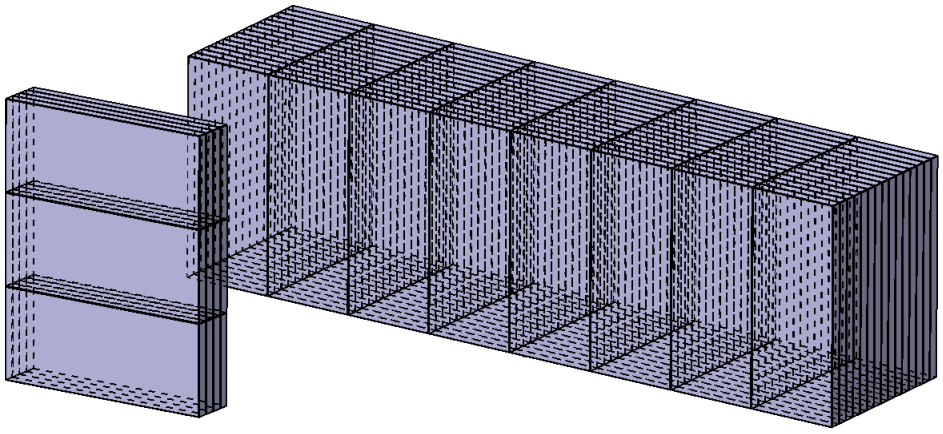

Figure 4.41: Propulsion battery and systems battery

Still to be designed are the connections between cells, a fireproof casing, cabling and the battery management system. The actual battery packs will therefore be slightly larger than shown and most probably each pair of modules will be separated by a fire resistant plate to prevent the entire battery from burning in case of fire. Finally, a backup battery should be incorporated in case the systems battery fails.

4.7 Solar Cells

The mission requires the Unmanned Aerial Vehicle (UAV) to be self sustained for a full year. This aircraft needs very lightweight, high power density solar arrays on top of the wings as the sole power source during the day. The solar arrays power the aircraft and charge batteries to be used at night. This section describes the process of selecting solar cells for the mission and the final arrangement of the solar panels. First the requirements for this mission are discussed and then a solar cell is selected from the available PV technologies. In subsection 4.7.3 the encapsulation for the solar cells is discussed. Also a Maximum Power Point Tracker (MPPT) is selected for this mission in subsection 4.7.6. Finally the arrangement of the PV system is laid out in some detail in subsection 4.7.7.

4.7.1 Requirements

During the selection of suitable solar cells, the following aspects are taken into account: costs, sustainability, polymer content, degradation, efficiency, weight, flexibility and multi-functionality. However first and foremost the solar cells need to have high efficiencies in order to deliver enough power to the UAV. Next to the efficiency the solar cells need to be lightweight, flexible and insensitive to degradation as much as possible. These are the four decisive requirements.

- Efficiency

- Degradation
- Weight
- Flexibility

An End of Life (EOL) efficiency of no less than 25% is required to meet the needs of the design. Furthermore the density of the solar panels should be little as possible to maintain a lightweight structure.

4.7.2 Selection

A sustainable way to generate solar energy is the use of organic solar cells [79, 80]. Organic solar cells use polymers from an organic origin, which makes them biodegradable. During the last couple of years this technology has made a huge progress in cell efficiencies; from 3% in 2004 to a maximum of 11% nowadays. However these organic solar cells aren't stabilized ,which means they degrade rapidly. In fact this degradation can lead to efficiencies of less than 1% within a couple of months. Because the UAV needs to be self sustained for a full year, these type of solar cells are not an option for this mission.

Among all available PV technology today, Gallium Arsenide (GaAs) is known for its performance and reliability. GaAs cells and modules have high efficiencies, but they are very expensive compared to thin film amorphous Silicon (Si) solar cells [81]. However these Si cells have efficiencies less than the required 25% and they degrade faster than GaAs. Therefore also these type of cells are not an option for this mission.

Traditional GaAs cells are usually heavy and brittle, making them inappropriate for use in flexible wing structures. Recent advances in the development of new, thin and flexible GaAs thin-film PV technology have changed this situation. AltaDevices has been able to develop lightweight, flexible and thin-film GaAs solar cells, with extreme environmental endurance and reliability at a fraction of the cost associated with traditional GaAs PV technology [82]. They have a record single junction solar cell efficiency of 28.8%. Furthermore they perform very well under large incidence angles with the sun. "Under real-world operating conditions, mc-Si PV power output degrades 5x more than Alta's mobile power technology under typical field operating temperatures, and degrades 2.5x more under early/late/cloudy sun conditions." [82]

The efficiency of these solar panels is 26%. However due to degradation this efficiency will drop over time. "The expected degradation rate is about 0.8% relative per year." [83] This results in an absolute efficiency drop of 1% in 5 years, according to Equation 4.12.

$$\eta_{(EOL)} = 26 \cdot (1 - 0.008)^5 = 25 \qquad [\%] \tag{4.12}$$

Because they meet the demands of the design, these type of solar cells are selected for the design.

4.7.3 Encapsulation

On top of the solar cells an encapsulation is placed to protect the cells from environmental conditions. The encapsulation is made from polycarbonate. Polycarbonate is a durable material, with high impact-resistance and temperature resistance and is highly transparent to visible light. It has better light transmission than many kinds of glass. Also polycarbonate has excellent compatibility with ozone, meaning no chemical effects from interaction with ozone [84]. Furthermore it is lightweight as opposed to glass; in the order of 1.0 to 1.2 g/cm^3. Only a thin layer of encapsulation is used to keep the structure lightweight. However polycarbonate is sensitive to ultraviolet (UV) radiation from the Sun [85]. The molecular weight of polycarbonate decreases during UV exposure, making it susceptible to embrittlement and surface erosion. Also the optical properties of the polymer are affected, including reduced light transmission. This could eventually decrease the power output of the solar cells. According to [86], the reduction in light transmission after 2000 hours of direct UV exposure is approximately 5%. During a mission of one year, the encapsulation faces about 4383 hours of sunlight. However this sunlight is almost never directly above the material, reducing the amount of degradation due to UV radiation. Furthermore the material can be protected with the use of UV stabilizer additives. UV stabilizers are added to polycarbonate to help protect the material from the effects of exposure to the Sun for a longer period of time. Of course, it is impossible to completely remove the degradation effects due to UV radiation. Therefore after every mission of 1 year the encapsulation is replaced with a new one to maintain good performance of the solar cells.

4.7.4 Cell specifications

The GaAs solar cells from AltaDevices meet the demands of the design. They have an efficiency of 26%, with a small degradation rate of 0.8% relative per year and a panel density of 0.237 kg/m^2. Adding an encapsulation on top of the cells, brings the total solar panel density to 0.4 kg/m^2.

The back contact of the solar cells is a polymer carrier film, and is estimated to be one sixth of the cell mass. Together with the encapsulation about 50% of the solar panel is made of polymers.

The cell specifications during the worst conditions can be found in Table 4.16. Here the average irradiance of 370 W/m^2 is used, during the special manoeuvres that will be performed as explained in section 3.3.

Table 4.16: GaAs Cell Specifications at 370 W/m^2 and -56.5° C.

Parameter	**Value**	**Unit**
I_{mp}	79.3	[mA]
V_{mp}	1.13	[V]
P_{mp}	89.7	[W]
I_{sc}	82.4	[mA]
V_{oc}	1.26	[V]
FF	86.7	[%]
η	26	[%]
Degradation	0.8	[% year]
Length	50	[mm]
Width	19.1	[mm]
Thickness	110	[μm]
Panel density	0.4	[kg/m^2]
Polymer content	50	[%]

4.7.5 Solar Area

The required solar energy depends on the energy needed for propulsion during the day and the required battery energy for the night during the most critical conditions.

$$E_{solar} = E_{prop} + E_{battery} \qquad \text{[Wh]} \tag{4.13}$$

This solar energy depends on the irradiance, the efficiency and the angular performance (η_{rel}) of the cells, the number of sun hours and the total solar area.

$$E_{solar} = \eta_{(EOL)} \cdot \eta_{rel} \cdot [hr]_{sun} \cdot I(t) \cdot A_{solar} \qquad \text{[Wh]} \tag{4.14}$$

Here I(t) is calculated as in Equation 4.11. From Equation 4.14 the solar area can be calculated and is found to be 91.5 m^2. Placing the panels on top of the wing cannot be done without 5% loss of area. Therefore the solar panels require a wing area of about 96.3 m^2. The total wing area is 110 m^2, where 11.4 m^2 is reserved for the ailerons. This leaves 98.6 m^2 for the solar panels, which is enough.

4.7.6 MPPT

A Maximum Power Point Tracker (MPPT) makes sure the process of charging the batteries from the PV panels goes as efficiently as possible. A MPPT can also deliver power directly to other systems of the UAV, like the electric motor for instance. Basically a MPPT is an electronic Direct Current (DC) to DC converter that optimizes the match between the PV panels and the battery or another device. Or simply, they convert a voltage DC output from solar panels up or down to the higher or lower voltage needed to charge batteries, respectively. Drivetek AG produces MPPTs that suit the demands best [87]. The MPPT needs about an inch of clearance for proper heat flow through the heat sink to maintain high efficiencies. It is estimated that

about 20% of the MPPT mass is polymer. The characteristics of the MPPT are given in table Table 4.17.

Table 4.17: MPPT Race V 4.0

Parameter	**Minimum**	**Typical**	**Maximum**	**Unit**
Input Power	5		1250	[W]
Input Current			9	[A]
Peak Efficiency		99		[%]
Input Voltage	36		144	[V]
Output Voltage	40		200	[V]
Transmission Ratio	1.05		4	[-]
Operating Temperature	0		70	[°C]
Mass		650		[g]
Polymer content		20		[%]

4.7.7 Arrangement

The MPPTs are set up to perform best under the most critical conditions, i.e. in winter. The peak efficiency of the MPPTs occurs at 400 W input power. During the shortest day the peak power is about 520 W and the average is about 370 W. The efficiency of the MPPTs doesn't drop below 98.5% around these days [87].

The solar modules have been designed to produce a voltage that suits the demands of the batteries best. The MPPT's optimum transmission ratio is about 1.15 and the battery charge voltage is around 47 V, requiring a panel output voltage of around 41 V. Furthermore due to the varying irradiance during mission, the current output of the cells varies a lot as well. The MPPTs should operate all year round and their maximum current is 9 A. In summer the solar cells produce the largest currents and therefore the modules are designed for these currents. This results in modules of 36 cells connected in series and 35 cells connected in parallel, resulting in an area of about 1.2 m^2.

Next to that a separate battery is installed for the systems. This battery requires much less power from the solar panels and a charging voltage of only about 12 V. Separate modules are set up for this battery, with an area less than 0.1 m^2. This is actually quite useful since these modules can be placed at more difficult positions on the wing, e.g. near the edges, and thus using the wing area more effectively.

In total 8 MPPTs are used to guide the electric circuit of the UAV, with a total mass of 5.2 kg. The total solar panel area is 91.5 m^2, with a total mass of 36.6 kg. This is divided into 74 large modules and 32 smaller modules to provide for the system battery. This is summarized in Table 4.18.

Table 4.18: Arrangement

Parameter	**Number [-]**	**Area [m^2]**	**Mass [kg]**
Solar Panel	-	91.5	36.6
MPPT	8	-	5.2
Main module	74	1.2	0.480
Small module	32	0.086	0.034

4.8 Heat Management

All active components of the aircraft have an operating temperature range which should be guaranteed. Therefore an analysis was performed to compute the incoming and lost heat of several components: the batteries, communication & control subsystems and the motors. This resulted in a determination of the heat management systems that should be in place. A few requirements were set for this system.

- Low total mass

- Low power consumption (preferably passive)
- Maximize use of polymers, minimize metal use
- No harmful chemicals should be present
- All components should be kept in operating temperature range, preferably at optimal temperature

For each component heat generated was computed with its power input and efficiency. It was assumed the wing is a black body, with no convection inside. Therefore each component would only lose heat through radiative heat transfer and the temperature inside the wing would equal ambient temperature. After all calculations explained below this assumption was verified: the inside wing temperature would be 217 K, only 0.35 K above ambient temperature.

The relation between heat emitted and temperature of the object is given in Equation 4.15

$$P = A\sigma\epsilon\left(T_1^4 - T_2^4\right) \qquad [\text{W}] \tag{4.15}$$

where A is the total area encapsulating the object, σ the Stephan-Boltzmann constant, ϵ the emissivity coefficient and T_1 and T_2 are the temperature of the object and the environment, respectively. Some systems have to be cooled beyond what can be reached by radiation, so convection has been modelled as well. Equation 4.16 shows the relation between heat loss by forced convection and object temperature.

$$q = h_C A \Delta T \qquad [\text{W}] \tag{4.16}$$

Here h_C is the convective heat transfer coefficient, which depends on the Reynolds number, A is the area over which convection takes place and ΔT is the temperature difference between the object and the environment.

4.8.1 Design and Sizing

One battery pack delivers 656 W on average which results in 13.12 W of heat (see Table 5.7). The surface area is 0.5 m^2. The battery should have a temperature of around 20°C which requires use of a reflective coating on the inside of the casing. However, covering the entire casing with aluminium foil would make the battery overheat (91°C), so holes should be introduced into the casing with a total area of about 0.03 m^2, which would result in a temperature of 20.5°C. Another option could be to find an optimal area of aluminium foil such that no holes need to be made in the casing.

Each motor receives 656 W and produces 65.6 W of heat. To loose as much as heat as possible it should approach a black body, so an emissivity of 0.98 has been assumed. This would result in the motor becoming 111°C. This can be reduced to 37°C by convection over a surface of 0.01 m^2 with a convective heat transfer coefficient of 25 W/m^2K. How this convection should be implemented in the design is not determined yet, but probably will encompass a cool rib in the wing skin.

Finally, the electronic subsystems generate about 25 W of heat and are contained in a box of 0.1 m^2. With an emissivity of 0.98 the temperature inside would be 13°C which is acceptable. Therefore no special heating or cooling systems are required.

All above values are calculated for an ambient temperature of 216.65 K which will be the nominal temperature for the aircraft. However, during maximum solar irradiation this temperature will increase inside the wing and the systems may not overheat in this situation. Assuming 1200 W/m^2 solar irradiation perpendicular to the solar array generates approximately 98 kW of heat which increases inside temperature to 222 K with an aluminium foil applied to the inside of the upper wing skin. The wing skin itself can lose the heat through the lower half by radiation and convection.

The electronic subsystems now reach 15.5°C, the batteries 22.8°C and the motors 38.6°C. All are well within operational range.

4.8.2 Conclusion

The heat management systems proposed in this section is completely passive and requires no special chemical fluids. It comprises mostly casings around the subsystems with in some cases an aluminium foil. The total mass has not been determined, but all components would have had

a casing in the first place, so the extra mass is expected to be small. The temperature ranges are kept well within and most systems are even kept around optimal operating temperature. Lastly, the bulk of material required for the heat system is some polymer (e.g. carbon fibre or polycarbonate), but unfortunately some metal (aluminium) is required as well. Reflective polymer materials are not available at this moment or incorporate a thin metal film or coating.

4.9 Structures and Materials

This chapter discusses the entire structural design of the UAV. In the first section the possible materials that could be used for the aircraft structure are outlined with the main focus being on composites and sandwich structures. The second section is concerned with calculating the forces acting on the wing structure in the different load cases. After that the structural design and analysis is presented, which contains the configurations considered, the preliminary Matlab optimization of the structure and the explanation of the Finite Element Method (FEM) analysis performed with the following results and design iterations. Finally thermal and mechanical fatigue are analysed. A short conclusion provides the summary of the final design with recommendations on future improvement.

4.9.1 Materials selection

In this section the materials researched for main load bearing structures is presented. The section is split into four main topics. First the available fibres for composite reinforcement are summarized. Then the polymer matrices researched are presented with their corresponding properties. The third subsection gives a short overview of sandwich structures - including foam and honeycomb reinforcements. Finally a trade-off is performed in order to make a selection of the most feasible materials.

Reinforcement fibres

A number of different reinforcement fibres are considered for the use in composite structures in the design. Those fibres can be split into several categories:

- Metallic - mostly aluminum and steel based, not feasible due to no polymer content and low specific properties
- Glass - low mechanical properties, not feasible for primary load bearing structure
- Carbon - large range of options available, usually tailored for either high strength or high modulus, provide very good specific properties
- Organic - high specific properties, usually lighter than carbon but perform worse in compression
  - Ultra-high-molecular-weight polyethylene based (UHMWPE) - commercially available Dyneema and Spectra, very low weight
  - Para-aramid based - Kevlar, Twaron, Technora
  - Liquid crystal polymer (LCP) based - Vectran
  - Polybenzobisoxazole (PBO) based - Zylon
- Specialized
  - Boron
  - Silicon carbide
  - Quartz

Summary of properties of the most feasible fibres are presented in Table 4.19.

Polymer matrices

Here the possible polymer matrices to be reinforced with fibres are presented. Those polymers could be split in two main categories - thermosets and thermoplastics. Thermosets have the following advantages over thermosets:

- Well-established in structural applications, more widely used - more information available
- Lower raw material costs

Table 4.19: Fibre properties, [88, 89, 90, 91, 92]

Fiber	Tensile strength [GPa]	Tensile modulus [GPa]	Elongation at break [%]	Specific gravity [-]	Fiber diameter [μm]	Specific strength [GPa]	Specific modulus [GPa]
Glass							
E-glass	1.5-3	72	1.8-3.2	2.55		1.17	28
S-glass	4.5	86		2.49		1.8	35
Carbon							
AS4	3.7	235		1.81		2.04	130
IM7	5.17	290		1.8		2.87	161
Torayca T1000G	6.37	294	2.2	1.8	5	3.54	163
Torayca M60J	3.92	588	0.7	1.93	5	2.03	305
Hexcel IM10	6.96	303	2.1	1.79	4.4	3.89	169
UHMWPE							
Dyneema SK78	3.3-3.9	109-132	3-4	0.98	12-21	3.97	135
Spectra 900	2.3-2.6	75-79	3.6-3.9	0.97	38	2.68	81
Spectra 1000	2.9-3.7	97-172	2.8-3.5	0.97	27	3.81	100-177
Spectra 3000	3.25-3.42	96-135	3.3	0.97		3.52	139
Aramid							
Kevlar 29	3.6	83	4	1.44	12	2.5	58
Kevlar 49	3.8	131	2.8	1.44	12	2.64	91
Kevlar 149	3.5	186	2	1.47	12	2.38	126
Twaron	2.4-3.6	60-120	2.2-4.4	1.44	12	2.48	83
Technora	3.4	78	4.6	1.39		2.44	56
LCP							
Vectran HT	3.2	75	3.8	1.41		2.27	53
Vectran UM	3	103	2.8	1.4		2.14	74
PBO							
Zylon AS	5.8	180	3.5	1.54		3.77	117
Zylon HM	5.8	270	2.5	1.56		3.72	173
Boron							
Boron	3.45	395		2.5		1.38	158

- Easier processing and impregnating - lower temperatures and pressures required
- More complex shapes possible

On the other hand thermoplastics are better in the following areas:

- Cheaper storage of raw material - does not require refrigeration
- Better chemical resistance and lower water absorption - higher lifetime

- Wider range of manufacturing options and shorter processing times than thermosets
- Improved impact resistance and better fatigue properties
- There is no chemical reaction upon solidification - the process is reversible; therefore reforming, easier repairs and reusing are possible as well as welded joints which could lead to lower overall weight
- High delamination resistance

In Table 4.20 the most widely used matrices are summarized.

Table 4.20: Comparison of different matrix materials, [92, 64, 93]

Matrix	Advantages	Disadvantages
	Thermosets	
Polyester	Low material and manufacturing costs, resistant to acids	Poor bonding with CF and aramid fibres, should not be used in primary structural components unless reinforced with fiberglass
Vinyl ester	Low material costs	Same as polyester
Phenolic	Good insulating properties and moisture resistance	Poor toughness and mechanical properties, mostly used in secondary structures
Polyimides	Excelent thermal capabilities	Difficult handling and processing
Bismaleimide	Good thermal capabilities	Hard to process, brittle
Epoxy	Most widely used - excelent databases, many prepreg options commercially available, good overall properties, low material costs	Low moisture resistance, brittle
Cyanate ester	Very good thermal capabilities, electrical and moisture resistance, used in primary structures	High material costs
	Thermoplastics	
Polyetheretherketone (PEEK)	Large databases available, good mechanical properties as well as chemical, moisture and UV resistance	High processing temperatures, high material costs
Polyetherimide (PEI)	Low processing temperatures, impact resistance	Poor mechanical properties
Polyethersulfone (PES)	Good processing characteristics	Poor UV resistance
Polyphenylene Sulfide	Low processing temperatures	Very low service teperatures
Polyamide-imide (PAI)	Very good thermal capabilities, chemical resistance, excelent mechanical propertes	High material cost, not proven in primary structural use

Sandwich structure panels

The use of sandwich panels as structural component has several advantages over non-sandwich panels. Sandwich panels consist of two stiff skins with a lightweight core in between. This design improves especially bending and buckling performance by increasing the moment of area of the panel by placing the stiff (and heavier) away from the center whilst adding a lightweight material in the midst. This is a similar principle as from an I-beam. An example is shown in Figure 4.42.

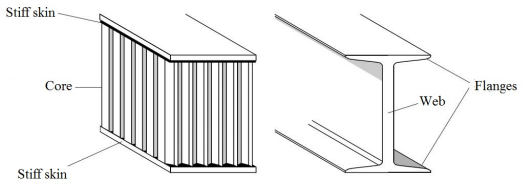

Figure 4.42: Sandwich structure (left) and I-beam (right) (*adapted from [94]*)

There exist a wide variety of sandwich panels because of the wide variety of materials that can be used. Some examples are presented in [95].

Skin panels can be made from all sorts of materials, from metals to wood and polymers. The core can be made of different materials and have different structures. Two are shown in Figure 4.43, the honeycomb (4.43a) and foam (4.43b) core.

(a) Honeycomb core (b) Foam core

Figure 4.43: Different core structures

Trade-off

A trade-off is performed to narrow down the selection of possible materials.

Fibre choice Glass and LCP fibers are directly eliminated due to their comparatively very low specific modulus and rather low specific strength. Boron fibers are not feasible either because of their metal content and properties that do not exceed those of Carbon Fiber (CF). The following parameters are then considered for the other fibers - specific modulus, specific strength and minimum thickness of a layer. Modulus is given a very high weighing factor, since extreme tip deflections have to be remedied in a high aspect ratio design. The minimum layer thickness available matters for the design, because with a low wing loading some parts of the wing have very low stresses. To minimize the weight one has to use the thinnest possible sheets. While the design is generally stiffness critical, there are some parts which would be strength critical (i.e. the root section cutout), therefore specific strength is also considered in the trade-off.

Table 4.21: Fibre trade-off

Property	Weight	CF	UHMWPE	Aramid	PBO
Specific modulus	0.45	5	4	3	5
Specific strength	0.1	4	5	3	5
Layer thickness	0.45	4	3	5	2
Total	1	4.45	3.65	3.9	3.65

Looking at Table 4.21, CF is by far the most feasible solution. This could be attributed to the specific properties - there are different types of CF, which can outperform almost any other fiber. Combined with the extensive property databases available, this makes it the fiber of choice. Coming second are the aramid fibers, especially Kevlar 49, and Kevlar 149. Although they are worse than CF in specific properties, and generally more expensive, they could be used to reduce the weight in low stress parts of the wing - they have lower density, and lower minimum layer thickness. Aramid composites provide better impact resistance as well, which makes them a good material choice for the leading edge. Finally, polymers reinforced with Kevlar are radio-wave transparent - antennas can be incorporated in the wing without the necessity for cutouts and a lower radar cross-sectional area could be achieved.

Matrix choice Epoxy resin and PEEK are the two most feasible material choices. PEEK is chosen due to a number of advantages:

- Much better fatigue resistance
- Better mechanical properties
- Better chemical, UV and ozone resistance

- Lighter bonding between panels

The main disadvantage of PEEK is its significantly higher cost, but this is offset by the higher lifetime, achieved by better fatigue and degradation resistance.

Sandwich reinforcement Two types of honeycomb are chosen, namely Hexcel HexWeb HRH-36 Kevlar/phenolic honeycomb, with densities 0.032 (HRH-36-4.8-32) and 0.072 (HRH-36-4.0-72). Their properties are presented in Table B.1.

4.9.2 Load cases

Four main load cases are considered, resulting in four different load factors. These are:

- cruise conditions - load factor of 1
- steep turn - load factor of 1.5
- limit load - load factor of 3.2; occurs at 6,100 m, maximum gust of 15.5 m/s
- ultimate load - limit load times a 1.2 safety factor - load factor of 3.84

Such a low safety factor is chosen due to several reasons:

- The design is for an unmanned aircraft - a possible structural failure would not endanger a human life
- The gusts at limit load conditions are determined rather conservatively. Also those conditions do not occur at cruise altitude, but at medium altitude during climb - therefore only expected once during a mission. Furthermore, the duration of the mission allows for precise planning of launch, hence avoiding extreme weather conditions.
- The subsequent analysis is performed using data for epoxy matrix composites, while in the final design PEEK matrix is used. A comparison of epoxy and PEEK reinforced with the same type of fibers shows that PEEK composites have slightly better overall mechanical properties and much higher in-plane shear strength (in the order of 50%) [96, 97]. At the same time, the strength critical parts of the construction - the cutout and the section of the front spar closest to the root, are most likely to fail in shear

In conclusion, with the approach taken, a safety factor of 1.2 would result in a sufficiently safe design, since both material properties and limit loads employed in the design are very conservative.

The shear force, bending moment and torque distributions for half a wing are shown in the figures below.

The load calculations account for the weight of the main battery system positioned at around 14 m from the root and acting over 0.6 m width, and a point load for the engine positioned at 7 m from the root.

4.9.3 Structural design and analysis

In this section the structural design and analysis of the wing is presented. First the initial wingbox configuration is discussed. Then a short introduction on composites is given, with simplifications and methods of analysis, as well as a number of different composite plies with their properties. The fourth subsection gives an outline of the Matlab approach to the structural optimization. Finally the FEM analysis is reviewed - the problems of the initial configuration are pointed out, the solution is given, and the following results are summarized.

Wingbox configuration

An initial wingbox configuration was chosen to facilitate further calculation and optimization. The geometry is presented in the figure below. The structure consists of a load carrying leading edge D-wingbox which extends up to 25% of the chord with a spar at this position, and a second conventional rectangular wingbox - extending from 25% to 50% of the chord, and terminating at 60% of the half span, as shown in Figure 4.46.

This configuration was chosen because the low wing loading leads to very low forces and moments in the tip section, which could be carried by a relatively small structure. On the other hand, in the inboard section subsystems and batteries can be stored in the higher volume provided by the conventional wingbox.

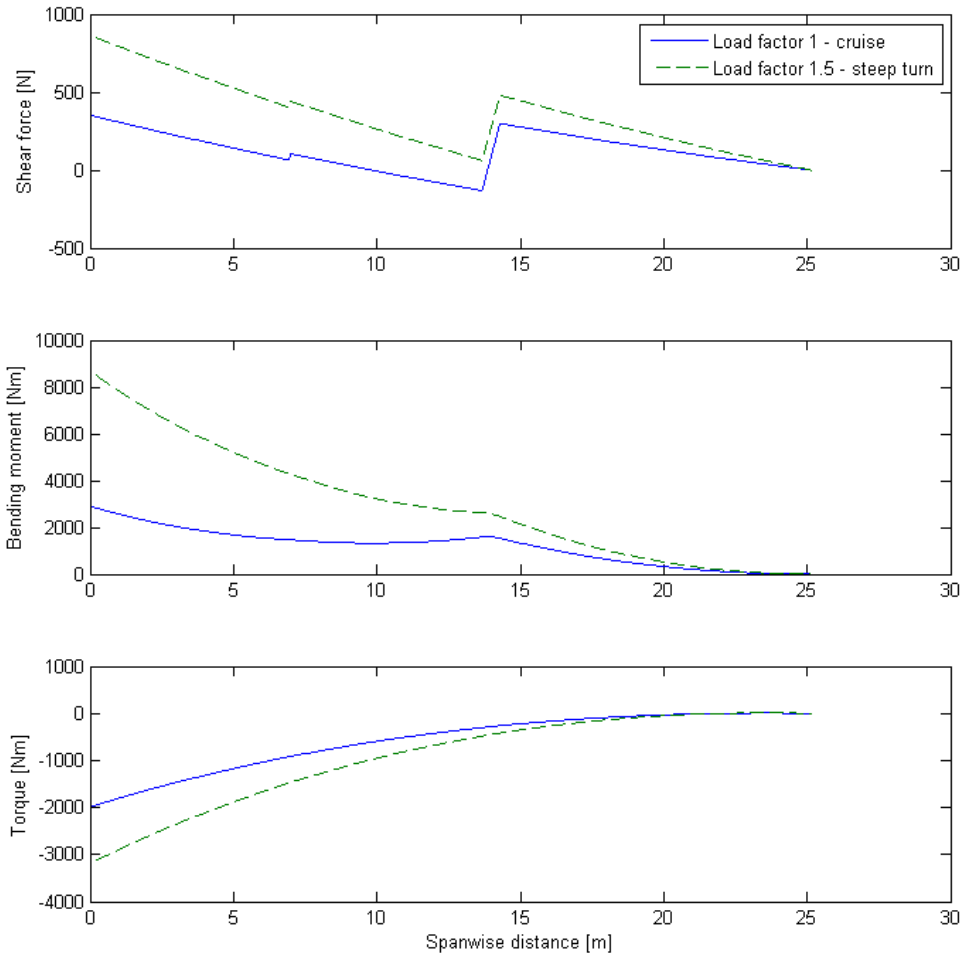

Figure 4.44: Force and moment distributions for cruise and turn

Composite analysis and simplifications

A simplified calculation procedure for composite structures was applied in the analysis. The following approach was used to examine a laminate as explained in [98]:

- Laminate configuration is chosen, by stacking multiple plies with well-known parameters
  - Angles and thicknesses of the laminates are chosen
  - Configuration is kept such that the laminate is symmetric and balanced (i.e. for each X° ply there is a -X° ply)
  - Required parameters are 0°/90° Young's moduli, shear modulus, in-plane Poisson's ratio, 0°/90° tensile and compressive strengths
- The stiffness matrix of each ply is calculated from its engineering constants and then transformed into the coordinate system of the laminate
- The stiffness matrix of the laminate is calculated from the transformed matrices and thicknesses of all the plies
- Engineering constants (i.e. 0°/90° Young's moduli and shear modulus) for the laminate are calculated
- The stresses in the laminate are calculated
- From these stresses and the inverse of the stiffness matrix, the laminate strains are obtained
- Each ply is checked for failure after transforming the strains into the ply's local coordinate system
- Out of plane stresses are assumed to be non-critical

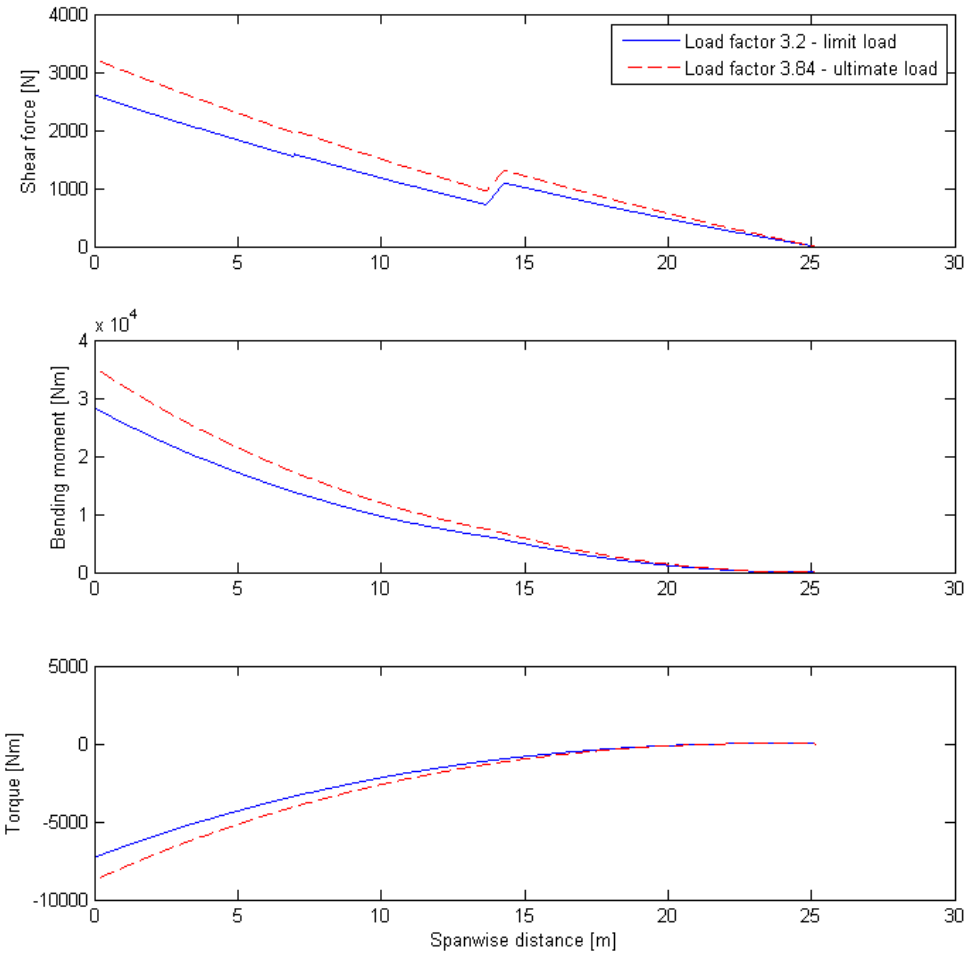

Figure 4.45: Force and moment distributions for limit and ultimate loads

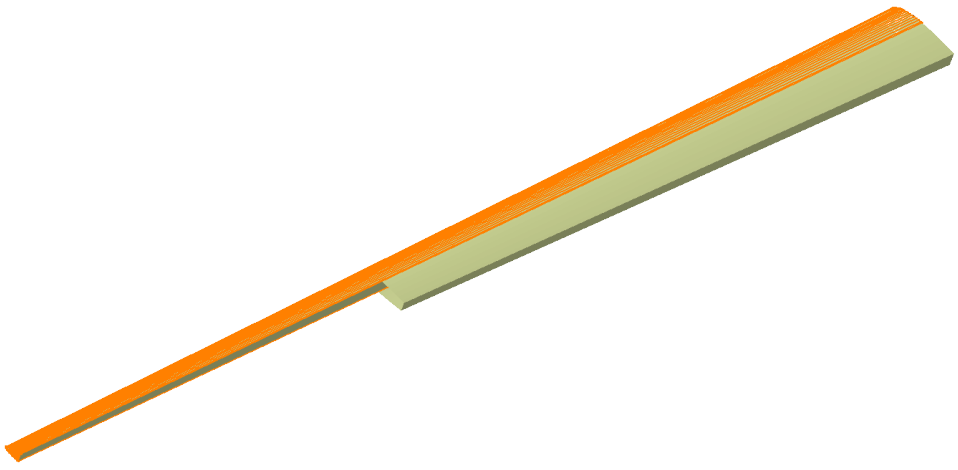

Figure 4.46: Initial wing configuration

Composite plies

A number of composite plies are chosen from reference literature and commercial datasheets for the structural optimization. Their mechanical and elasticity properties are listed in Table B.2. Four of the plies chosen for analysis use epoxy resins and one uses cyanate matrix. The reason is that epoxy matrices are most common and extensive datasheets and property values are widely available. The design would still use PEEK matrix for all the structural composites; PEEK matrix is expected to provide slightly better mechanical properties than epoxy, therefore the design would be slightly conservative.

Matlab structure optimization

A Matlab code was implemented for a preliminary structural design. The algorithm is outlined in Figure 4.47.

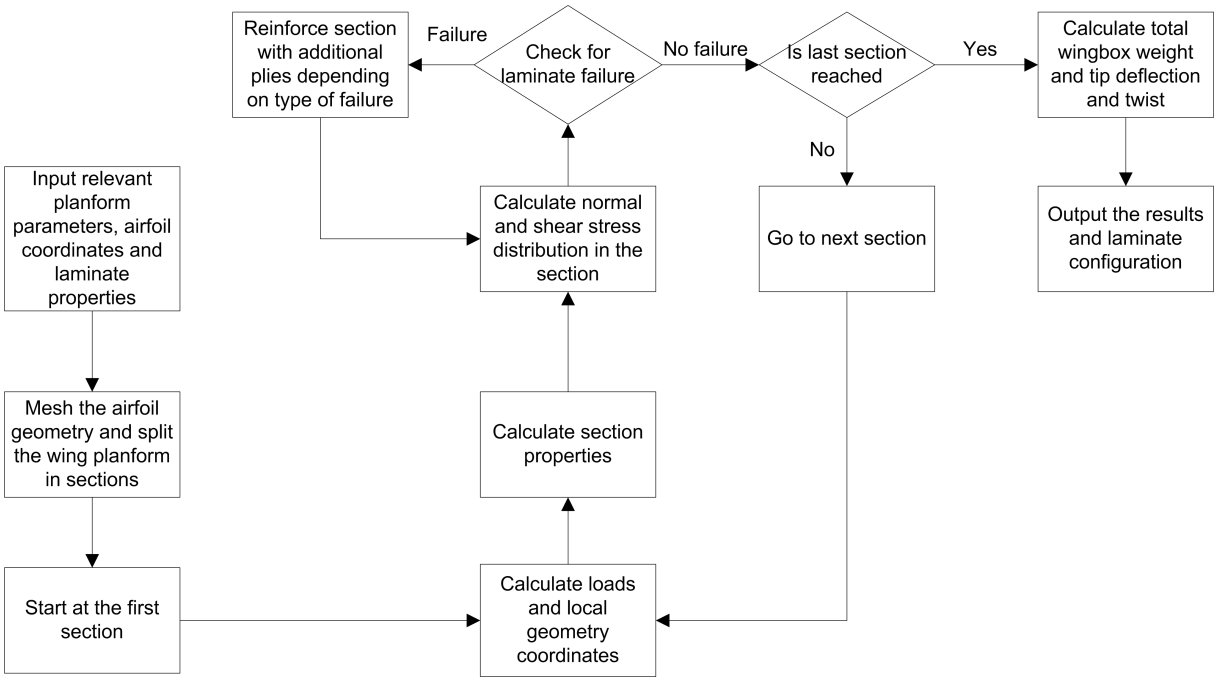

Figure 4.47: Matlab code flowchart

The optimization process only accounts for structural failure. Tip deflection and twist are outputs at this point of the design and they are further considered in the subsequent FEM analysis.

Section reinforcement is performed by adding additional plies of material with the minimum possible weight to prevent failure. They are added either in the 0° direction in case of a tensile or compressive failure or in the ±45 ° direction in case of a shear failure.

To analyze a section containing different materials, the cross sectional areas are weighted by the material's density and the moments of inertia are weighted by the material's Young's modulus as explained in [99]. The failure is calculated by using the maximum stress failure theory as explained previously and in [98].

The results from the Matlab optimization are presented below (all calculations performed for ultimate load factor - 3.84):

- Total weight of the wingbox is 45 kg
- Total tip deflection is 7.3 m, and tip twist is -24°
- The laminates used are:
  - The leading edge contains a single layer of IM6/Epoxy UD laminate
  - The front and back spars contain a single layer of Kevlar/Epoxy ±45° laminate
  - The top and bottom panels contain IM6/Epoxy UD laminates, two layers for the first 20% span and one layer from 20% to 60% span

FEM analysis

A FEM analysis was performed using Abaqus 6.12-1. This subsection outlines the approach taken, the findings of the analysis and how encountered problems are resolved.

Initial configuration analysis The first analysis is performed on the configuration consisting of thin laminates and the second spar terminating at 60% of the half span. An immediate result is that the thin composite sheets are very unstable and give very high deflections and therefore structural failure. The first adjustment to the structure is to add honeycomb core to all the sheets to improve their bending stiffness and lower the deflections. This is highly beneficial for

the design and results in a rather small weight increase. A von Mises stress distribution of this design is presented in Figure 4.48.

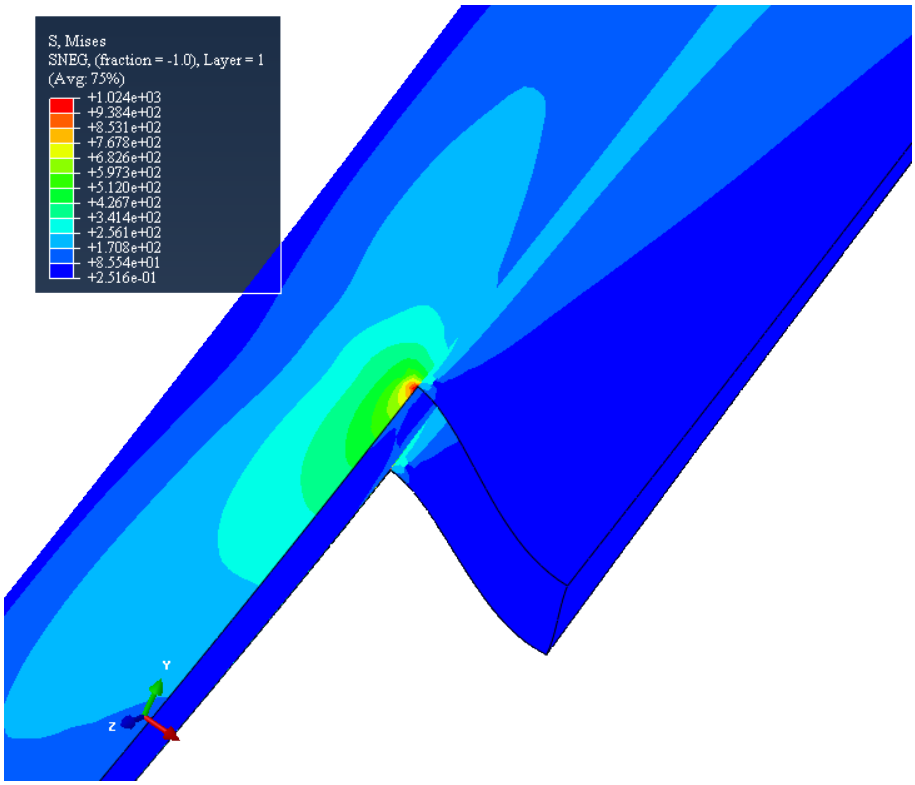

Figure 4.48: Stress distribution of the initial design reinforced with honeycomb

A second problem becomes apparent in this analysis - very high stress concentrations occur at the position where the spar terminates. This is because the stresses of the D-wingbox have to be distributed over the back panels introduced in the inboard section. Reinforcing this transition would give major weight penalties, and decrease the stiffness of the wing. This is because at this point shear strength has to be improved by adding plies in the $\pm 45°$ direction, which in turn would greatly reduce the modulus in the $0°$ direction. Therefore a new design has to be considered.

New design configuration The new design incorporates two spars extending along the whole span of the wing. The front spar is positioned at 25% of the chord. At this point of the design process a cutout for the imaging payload is implemented. Since the circular lens system has to extend 21 cm into the wing from the bottom panel, it has to be positioned in the front part of the airfoil where the thickness can accommodate it. This interferes with the front spar at the root section. Therefore the spar is designed with a curvilinear shape around the cutout. The transition from the straight part is accomplished by ensuring that the curvature of the spar is always tangential, to minimize stress concentrations. A short section perpendicular to the root is positioned at the end, in order to transfer loads to the second half of the wing avoiding geometrical discontinuities. This configuration is presented in Figure 4.49.

The second spar is straight along the whole length of the wing. Its position is determined in such a way that it does not interfere with the elevon which extends from 70% to 100% of the chord in the tip section, or the cut-out. This corresponds to a position at 60% chord length at the tip and 70% chord length at the root.

Optimization strategy An optimization process is performed in Abaqus by changing the materials in different sections up to the point where the requirements are satisfied. Since this process is conducted manually and the FEM analysis is computationally intensive and time consuming, some qualitative guidelines are implemented.

- The spars should contain mostly $\pm 45°$ layers to take shear forces, and a low thickness honeycomb core, since their bending stiffness is not critical

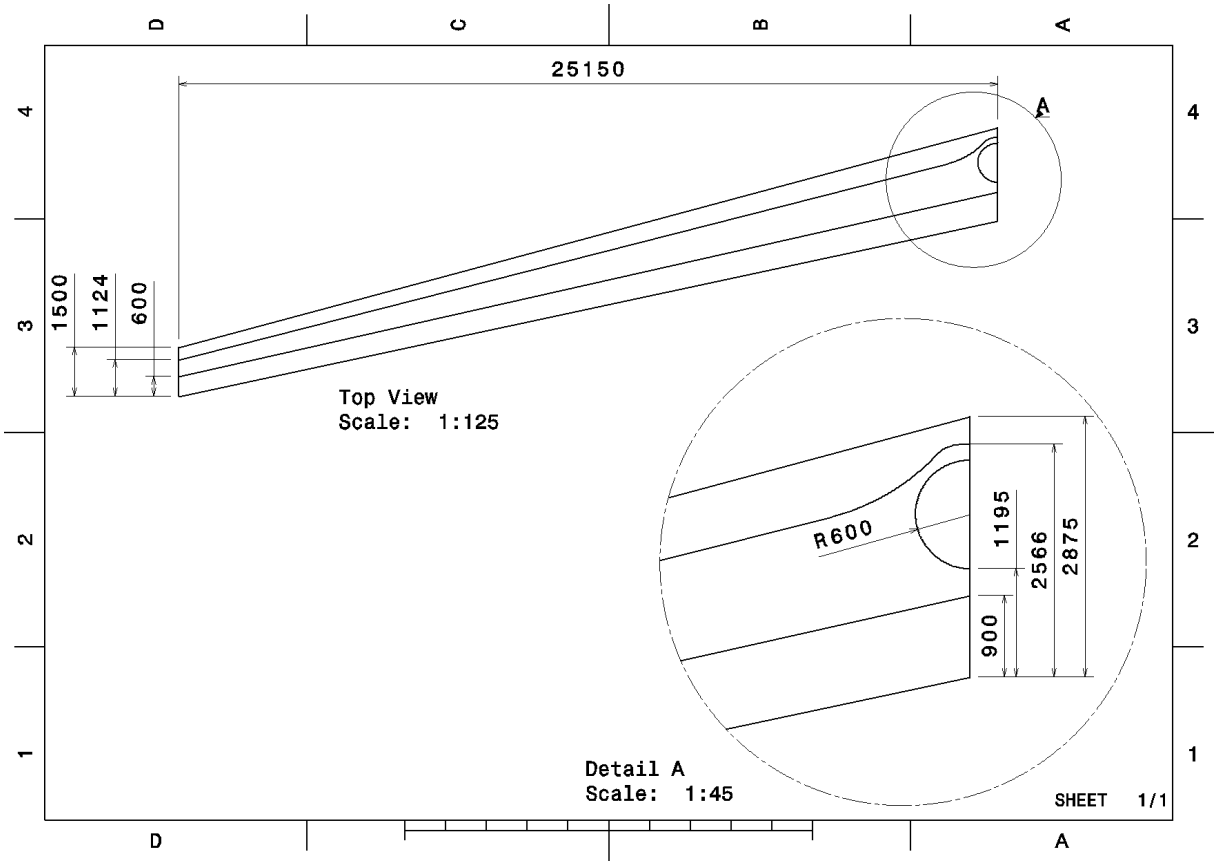

Figure 4.49: New wing configuration

- The top and bottom panels should contain predominantly 0° layers to take bending moments, with honeycomb core used to increase their stiffness
- Sections near the cutout should contain 0°/90°/±45° layers, to give them quasi-isotropic properties, since stress directions are hard to predict near the stress concentrations
- The leading edge should be constructed from the lightest possible material, with less regard for the structural properties, since it is not expected to carry high stresses and it has a relatively low contribution to the overall stiffness
- Sections near the tip should be less stiff than root sections, since they have less contribution to the overall deflection
- Sections with high stresses should have at least one ply in a common direction with neighboring sections
- Neighboring sections which have a very similar material layout might be adjusted to have the same configuration, in order to facilitate easier manufacturing and lower the number of different parts; when doing this the stronger of the two material layouts is chosen for both sections, and the resulting weight penalty is assessed

The sections containing different material layouts are as follows:

- Back spar
- Front spar - straight section
- Front spar - curved section
- Bottom panels, top panels and leading edge - each of them additionally split into five sections - from 0% to 5% span, from 5% to 10% span, from 10% to 30% span, from 30% to 60% span, and from 60% span to the tip; the bottom panel nearest to the root contains the cutout

After each analysis the stresses in critical sections are reviewed. Abaqus allows checking 0°, 90° and in-plane shear stresses; therefore failing sections can be reinforced at the most optimal ply

angle.

A minimum thickness of the honeycomb core of 0.5 mm is used for panels containing only one composite sheet on each side, 1 mm for panels with two sheets and 2 mm for panels with 3 sheets. The thickness is later optimized in steps of 0.25 mm in the top and bottom panels for best bending stiffness to weight penalty ratio.

Final configuration, analysis results, deflections In this subsection the final design is presented with the corresponding results. The laminate configuration is given for the whole wingbox, resulting in the total weight of the wing. The tip deflection and twist are given for the different load cases as well as the stress ratios used for fatigue analysis. First the requirements for the design are summarized.

- Complete wingbox weight less than 52.5 kg
- Wing tip twist of -5° during cruise for optimal aerodynamic properties
- Wing tip deflection of 10% of the half span at the limit load factor, to avoid aeroelastic instabilities
- Stress ratio of less than 0.72 during turns, to account for fatigue damage
- Structural integrity maintained at the ultimate load factor

Seven different laminates are used in the final design:

- Two layers of ±45° Kevlar composite with 0.5 mm thick HRH-36-4.8-32 core are used for the back spar, the straight part of the front spar and the last 90% span of the leading edge
- Six layers of HM CF 0°/90°, six layers of HM CF ±45° and six layers of IM6 UD with 2 mm thick HRH-36-4.0-72 core are used for the bottom panel reinforcing the cutout
- Two layers of 0°/90° Kevlar composite and four layers of HM CF ±45°, with 2 mm thick HRH-36-4.0-72 core are used for the curved part of the front spar
- Two layers of ±45° Kevlar composite and two layers of IM6 UD with 2 mm thick HRH-36-4.0-72 core are used for the bottom panel from 5% to 10% span
- Two layers of M55J UD with 1 mm thick HRH-36-4.8-32 core are used for the bottom panel from 10% to 30% span and for the top panel from 0% to 30% span
- Two layers of T300 UD with 0.75 mm thick HRH-36-4.8-32 core are used for the top and bottom panels from 30% span to the tip
- Two layers of ±45° and two layers of 0°/90° Kevlar composite with 1 mm thick HRH-36-4.0-72 core are used for the first 10% span of the leading edge

Figure 4.50 presents the maximum stress factor distribution in steep turns. This is a weighted sum of the ratios between the stresses that develop in different directions and the strength in these directions - essentially an equivalent of von Mises stress distribution for non-isotropic materials.

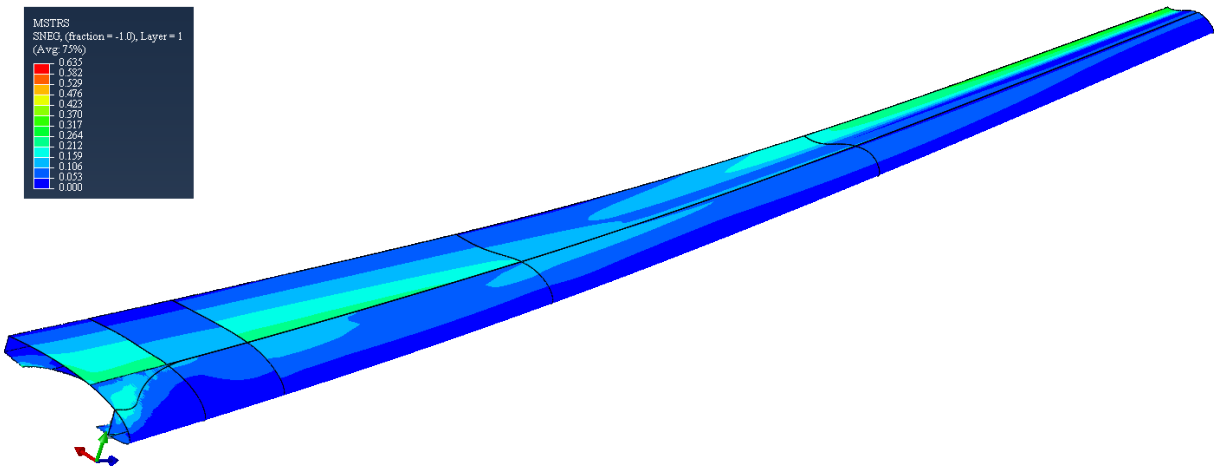

Figure 4.50: Developed stress to failure stress ratio, load factor 1.5

Stresses and deflection are rather low in this condition with most of the structure being very lightly loaded. There are some sections (front spar transition and connection to the leading edge) which have slightly higher stresses, but they are still within reasonable limits.

Figure 4.51 presents the maximum stress factor distribution around the cutout at the ultimate load factor. One can see where the maximum stress concentrations occur - near the edges and at the center of the cutout.

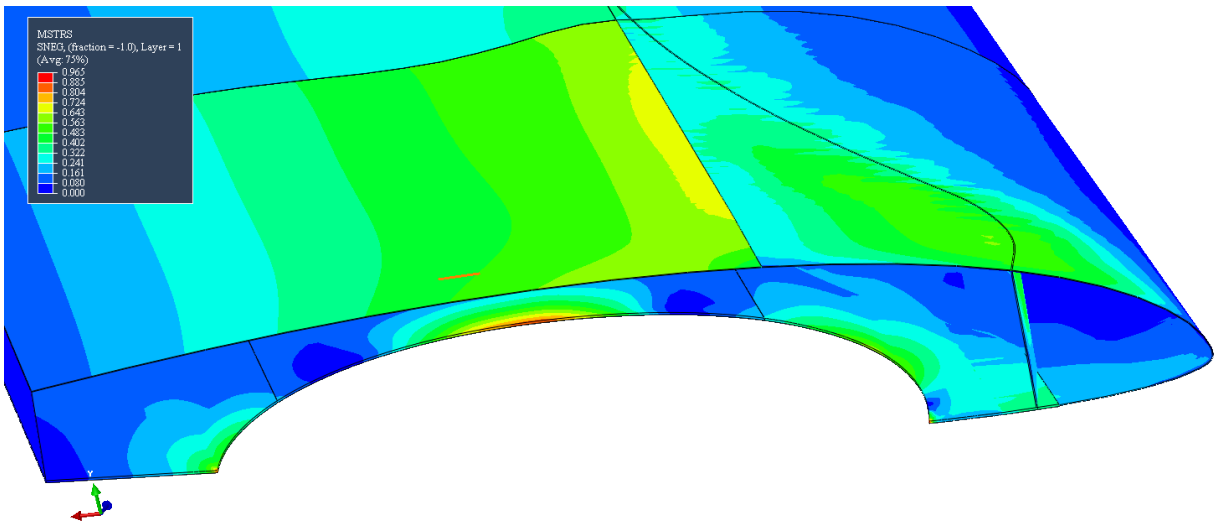

Figure 4.51: Developed stress to failure stress ratio at the cutout, load factor 3.84

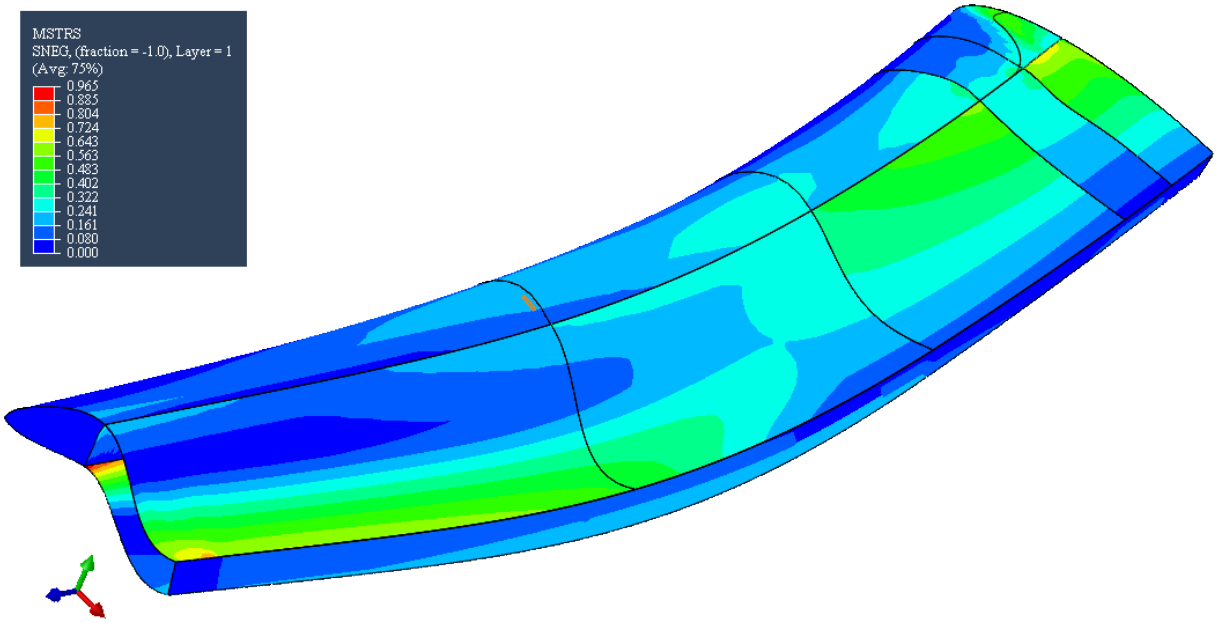

Figure 4.52: Developed stress to failure stress ratio, load factor 3.84

In Figure 4.52 the overall stress factor distribution is shown at the ultimate load. It is clear that the back spar and leading edge are still lightly loaded, which justifies the fact that the lightest possible laminates are used for them. The 5% to 10% span top panel shows lower stresses - this is due to the fact that the leading edge at this position is more reinforced.

Figure 4.53 shows the stress in the 0° direction in order to give an idea how each panel is loaded at the ultimate load conditions.

As expected the spars have low 0° stresses - they carry mostly shear loads. The leading edge also shows relatively small magnitudes - it is lightly loaded and it carries also predominantly shear loads due to the fact that it has low 0° stiffness compared to the rest of the structure. The top and bottom panels have the highest 0° stresses (positive stresses are tensile), meaning

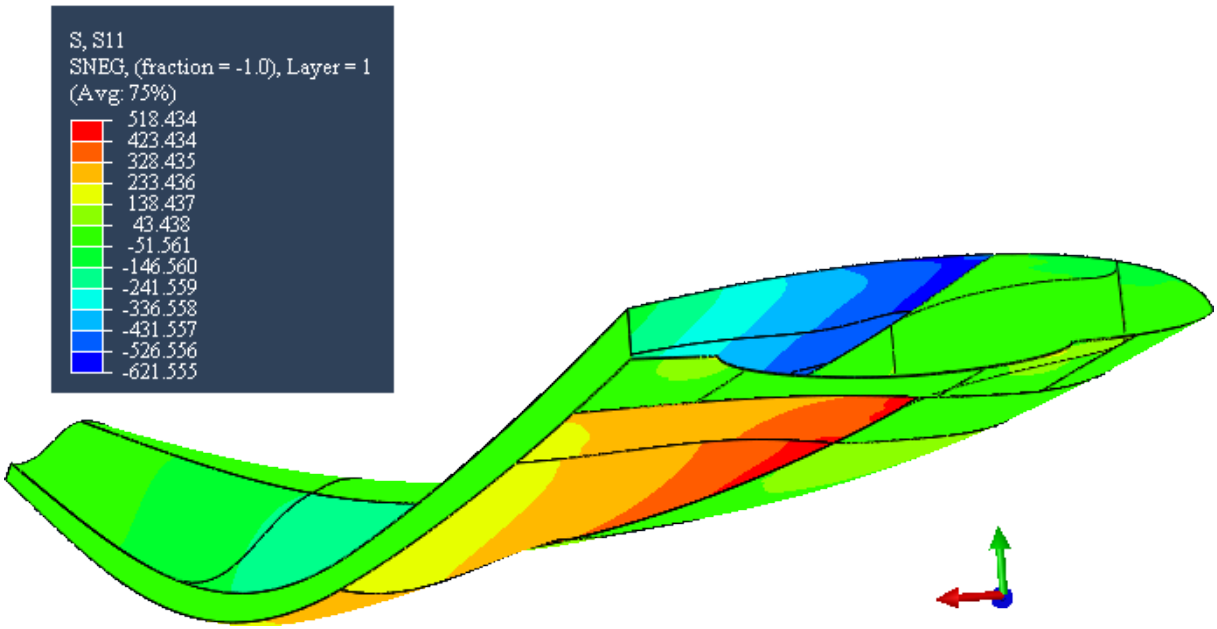

Figure 4.53: Stress in the 0° direction [MPa], load factor 3.84

they perform the role they are designed for. Finally the cutout section has lower tensile stresses, although it is essentially a bottom panel. This is attributed to the fact that this section is reinforced to achieve quasi-isotropic properties, therefore lowering its principal stiffness, as well as to its significantly higher thickness (4.25 mm compared to 2.3 mm for the next thickest panel).

Finally the deflections are presented in Figure 4.54 for the ultimate load factor.

As can be seen from the deflection distribution, the quarter chord sections have higher deflection than the leading edge at a certain spanwise location. This is used to achieve the negative twist angle required for aerodynamic performance (the twist angle is measured between the deformed and undeformed horizontal lines connecting the most upfront point to the front spar).

A summary of the results of the final design is presented:

- Total wingbox weight - 64.6 kg
- Maximum stress ratio in turns - 0.635
- Tip twist angle in cruise - 4.9°
- Tip twist angle in turns - 7.1°
- Tip deflection in cruise - 0.874 m
- Tip deflection in turns - 1.467 m
- Tip deflection at limit load factor - 2.86 m (13.5% of half span)
- Tip deflection at ultimate load factor - 3.48 m

4.9.4 Mechanical Fatigue

With the use of relative new materials as structural components a danger occurs in the form of fatigue, both thermally and mechanically. Fatigue is dangerous because it weakens the structure under cyclic loading, making it fail below the original Ultimate Tensile Strength (UTS) [100]. This is due to micro cracks that will occur in a material during loading and unloading. For polymers, also a thermal cycle life exist which can also induce strength reduction for repeated heating/cooling.
Different materials react in a different manner on fatigue but in general the number of cycles that can be achieved before failing depends greatly on the magnitude of the load. Decreasing the load factor will greatly increase the cycle life. In Figure 4.55 which is taken from [100] it can be seen that reducing the stress from 87% UTS to 72% UTS extends the fatigue cycles from around 3,000 to over 10,000 cycles.

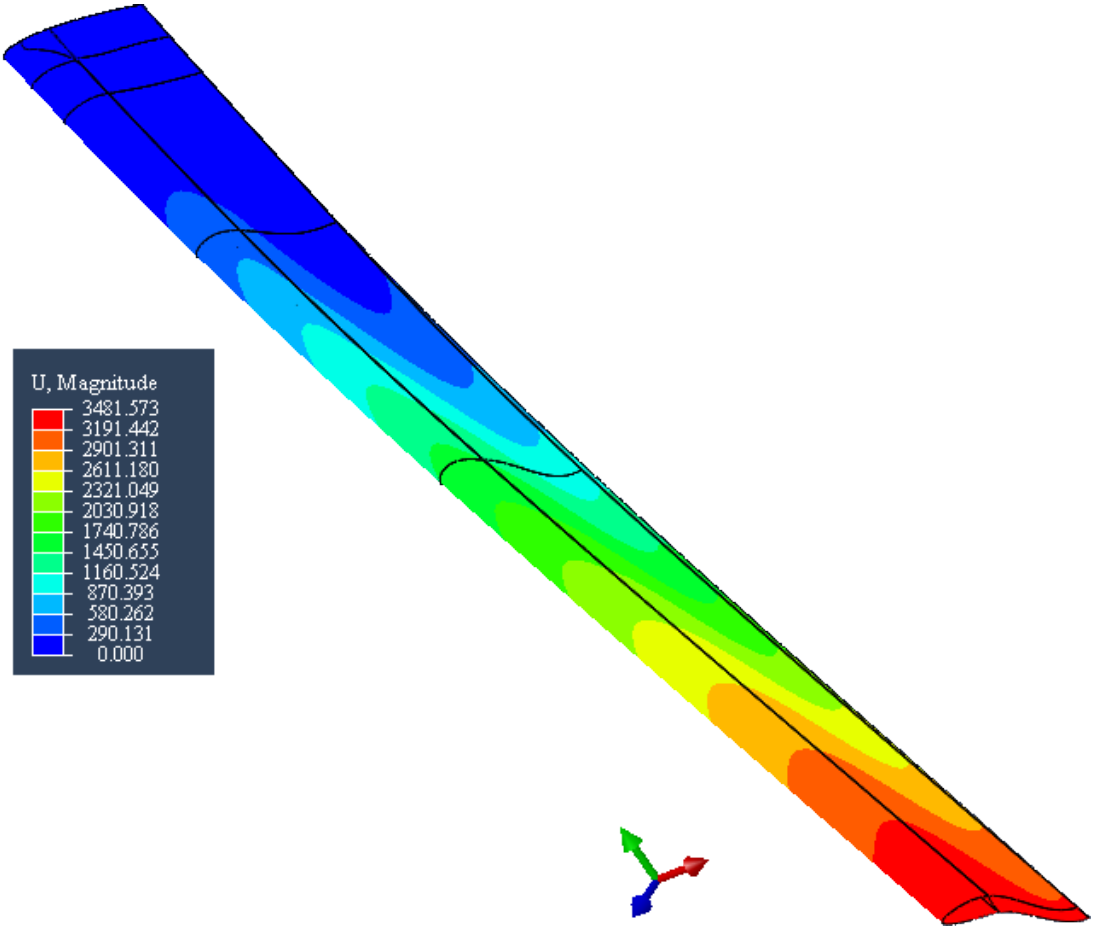

Figure 4.54: Deflection [mm], load factor 3.84

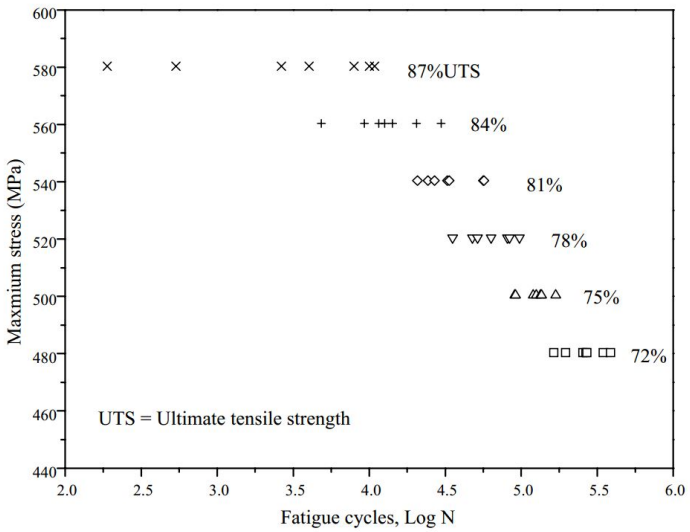

Figure 4.55: Fatigue cycles before failure versus maximum applied stress

4.9.5 Conclusion and Recommendations

The final design of the wingbox meets two of the most important requirements - it can sustain the ultimate load factor without structural failure, and it gives the optimal wing twist in cruise conditions which means that the necessary power efficiency is achievable. Also fatigue requirements are met, meaning that the wing should not need repairs during its lifetime unless unpredicted conditions occur (e.g. weather or impact damage).

At the limit load factor a tip deflection of 13.5% of the half span is predicted, which is higher than the required 10%. This requirement would be hard to meet without heavy weight penalties. A possible solution to the problem would be to implement active lift control. Lightweight piezoelectric sensors can be mounted in certain areas of the wing, to alarm for critical deflections; in such a scenario the elevons could be deflected or engine power setting lowered, in order to decrease lift and therefore wing loading, in heavy gust conditions. Another possible solution would be to move the batteries to the tip, increasing the moment relief. It should be noted that this would shift the center of gravity to the back and might be detrimental to the stability properties of the aircraft.

The most critical requirement that is not met is the wingbox weight. The resulting weight is 64.6 kg, almost 23% higher than what is budgeted. This results in the fact that a lower range of latitudes and time periods could be flown with the UAV. A number of improvements could be implemented in the design in order to decrease the weight:

- Consider removing the cutout, or moving it to a less critical position - this might require a redesign of the payload, but is likely to reduce the wingbox weight by more than 5%
- Consider splitting the wingbox in more sections containing different materials. This way a bigger part of the structure will be optimized to carry stresses close to its failure stresses. This might introduce higher manufacturing and assembly costs
- Consider a different design configuration for the wing. This would mean starting the structural analysis from scratch, but a more optimal layout could be found, since currently some panels carry a fraction of their failure loads, even at ultimate load conditions
- Consider improving the material database with more expensive or unpredictable state of the art materials, having higher specific properties. This is likely to increase material costs. Also materials testing would be required during the design if materials which do not have complete data sheets are chosen

Chapter 5
Final Design

This chapter focuses on the integration of the various subsystems into the preliminary design. Once this is done, the performance of the aircraft is analysed.

5.1 Subsystem Integration

With the subsystems designed in chapter 4, they are integrated into the final design in this section. Drawings will be shown of the individual systems, detailing all materials used. Additionally their place within the aircraft is shown. Finally the mass budget of the design is presented.

5.1.1 Design Integration

The starting point for integrating the design is the planform design generated in subsection 4.3.2. A top view of this planform can be seen in Figure 4.18. Yet individual systems have not been added. Subsystem integration will be the focus of this subsection.

Drive-train Integration

In subsection 4.4.3 the minimum motor distance is calculated as 13.56 m. Because the wing thickness decreases when moving towards the tip, the further the motor is placed away from the root, the more challenging it will be to integrate the motor into the wing without creating excessive drag. Therefore it was chosen to place the motor as close to the root as possible, while still maintaining the required yaw control. The motor placement on the planform can be seen in Figure 4.18 and is 6.78 m from the root.

Figure 5.1 shows the exploded view of the entire drive-train subsystem, while Table 5.1 shows the materials used for each part. Figure 5.1 shows the engine drive shaft to be unsupported. In reality this shaft will be supported by multiple bearings to avoid bending.

Table 5.1: Materials used in the drive-train subsystem

Part Number	Part Name	Material Used	Polymer %
1	Motor	Copper	0
2	Driveshaft	AS4-PEEK matrix composite	100
3	Hub	Polyamide 6/66	100
4	Propeller	Kevlar 49-Epoxy matrix composite	100
5	Planet Gear	Polyamide 6/66	100
6	Ring Gear	Polyamide 6/66	100
7	Sun Gear	Polyamide 6/66	100
8	Planet House	Polyamide 6/66	100

Payload Location and Communication system

The payload has been placed at the root of the wing for two reasons. The first reason is the payload has the largest dimensions of all subsystems, thus in order to reduce drag as much as possible it was chosen to fit the payload at the thickest part of the wing, which is at the root. Secondly, in order to benefit image quality it is beneficial to place the sensor on atleast one axis of rotation. With the current location of the payload, it is within two meters from the center of gravity and is located on the longitudinal axis. The communication system was integrated with the payload section to create a single, compact box. Therefore these systems share location.

Figure 5.2 shows the camera subsystem, while Table 5.2 details the materials used in this subsystem.

The communications system can be seen in Figure 5.3, with the accompanying materials in Table 5.3. The bolts used to join the various part are not listed, the material is Polyamide 6/66.

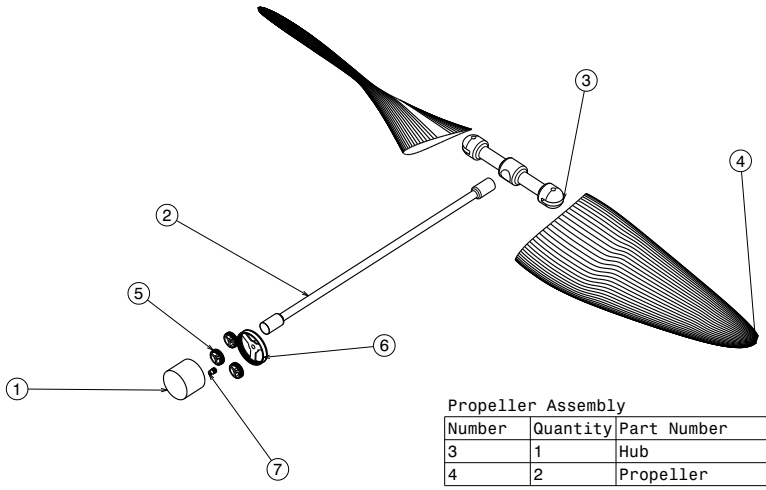

Propeller Assembly

Number	Quantity	Part Number
3	1	Hub
4	2	Propeller

Drivetrain

Number	Quantity	Part Number
	1	Propeller Assembly
1	1	Motor
2	1	DriveShaft
	1	Gearbox

Gearbox

Number	Quantity	Part Number
5	3	Planet Gear
6	1	Ring Gear
7	1	Sun Gear
8	1	Planet House

Figure 5.1: Overview of the drive-train subsystem

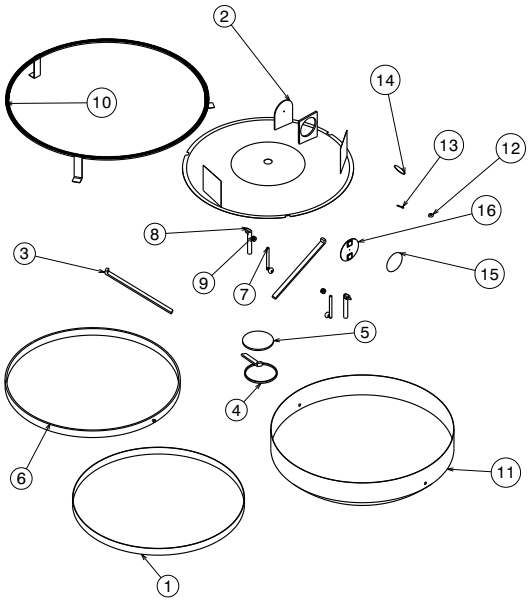

Camera

Number	Quantity	Part Number
1	1	Vibration Ring
2	1	Primary Mirror
3	3	Mirror Support
4	1	Sec. Mirror Holder
5	1	Secondary Mirror
6	1	Load Bearing Ring
7	2	Linear Actuator
8	2	Linear Actuator
9	2	Gear
10	1	Gear Ring
11	1	Dome
12	1	Ball Bearing
13	1	Ball Bearing
14	1	Focusing Mirror
15	1	Focus Lens
16	1	CMOS

Figure 5.2: Exploded view of the camera subsystem

Table 5.2: Materials used in the camera subsystem

Part Number	Part Name	Material Used	Polymer %
1	Vibration Ring	Rubber	100
2	Primary Mirror	Carbon Fiber and Aluminum Coating	80
3	Mirror Support	Carbon Fiber	100
4	Secondary Mirror Holder	Carbon Fiber	100
5	Secondary Mirror	Carbon Fiber and Aluminum Coating	50
6	Load Bearing Ring	Carbon Fiber	100
7	Linear Actuator	Carbon Fiber	100
8	Linear Actuator	Carbon Fiber	100
9	Gear	Carbon Fiber	100
10	Gear Ring	Carbon Fiber	100
11	Dome	Transparent Polymer	100
12	Ball Bearing	Carbon Fiber	100
13	Ball Bearing	Carbon Fiber	100
14	Focussing Mirror	Carbon Fiber and Aluminum Coating	100
15	Focus Lens	CaF_2	100
16	CMOS	-	0

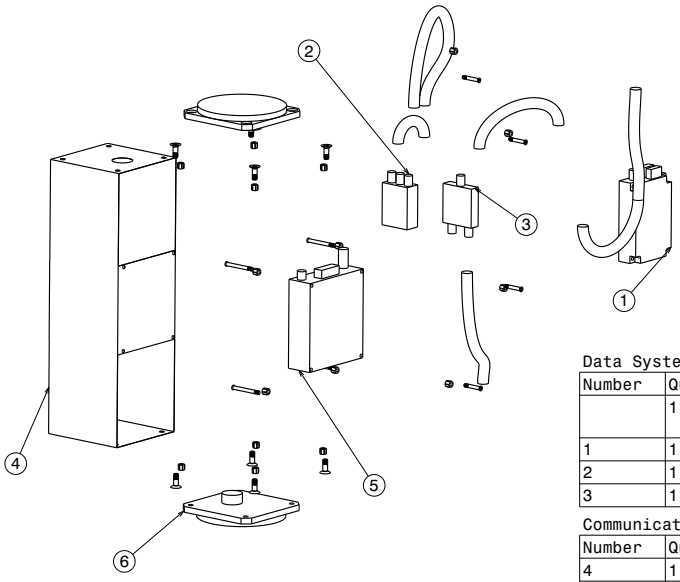

Data Systems

Number	Quantity	Part Number
	1	Communications Subsystems
1	1	S-Band Transmitter
2	1	RxTx switch
3	1	Combiner

Communications Subsystems

Number	Quantity	Part Number
4	1	Rack
5	1	Receiver
6	2	S-Band Antenna

Figure 5.3: Exploded view of the communication subsystem

Table 5.3: Materials used in the communication subsystem

Part Number	Part Name	Material Used	Polymer %
1	S-Band Transmitter	-	0
2	RxTx Switch	AS4-PEEK matrix composite	0
3	Combiner	Polyamide 6/66	100
4	Rack	Carbon Fiber	100
5	Receiver	-	0
6	S-Band Antenna	-	0

5.1.2 Elevons

Since the design is a flying wing, no elevator is used. For pitch control, the ailerons are combined with elevators to create elevons. These were sized in subsection 4.4.2. Figure 5.4 shows the exploded view of the elevon and servo control system, Table 5.4 shows the materials used in the design.

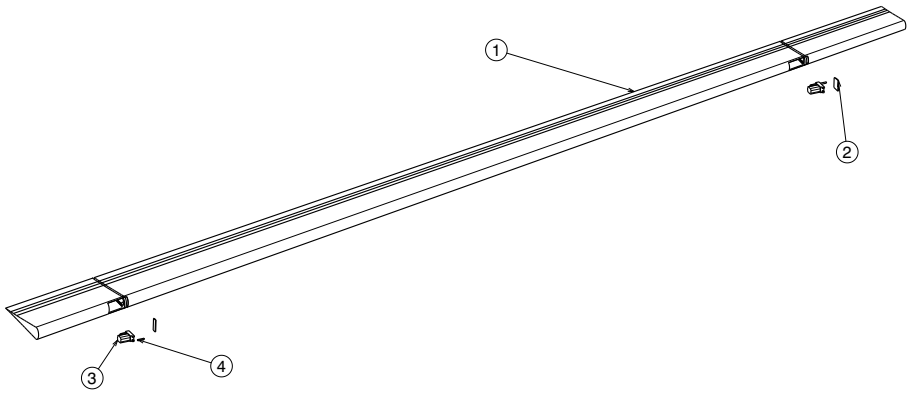

Elevon System

Number	Quantity	Part Number
1	1	Elevon
2	2	Flange
	2	MTC ERSA-0311

MTC ERSA-0311

Number	Quantity	Part Number
3	1	MTC ERSA-0311 engine
4	1	Shaft

Figure 5.4: Exploded view of the control subsystem

Table 5.4: Materials used in the control subsystem

Part Number	Part Name	Material Used	Polymer %
1	Elevon	Carbon Fiber - PEEK Matrix Composite	100
2	Flange	Nylon	100
3	MTC ERSA-0311 Engine	50% Nylon, 50% Copper	100
4	Shaft	Carbon Fiber	50

5.1.3 Maximum Power Point Tracker Location

The maximum power point trackers (MPPTs) have a relatively low size and mass, so in principle these can be placed anywhere in the wing. However, it makes most sense to locate them close to their specific solar panels. Thus the MPPTs will be evenly spread along the wingspan.

5.1.4 Battery Location

The main driver for placing the batteries is the center of gravity. With a total weight of almost 92 kg and a relative small size, the batteries are the perfect tool to regulate the center of gravity with. The required center of gravity location was determined in subsection 4.3.3 at 3.69 m from the front of the aircraft. Many subsystems have been placed in front of this location, requiring the batteries to be placed behind the required center of gravity. This result in a required location of 4.05 m behind the front of the aircraft. Since the root chord only has a length of 2.87 m, the batteries will have to be moved towards the wing tip to fulfill the requirements. This results in the batteries being placed at 13.8 m away from the root chord, 4.05 m behind the front of the aircraft. In an attempt to counteract flutter, the batteries were placed as far to the front of the wing box as possible.

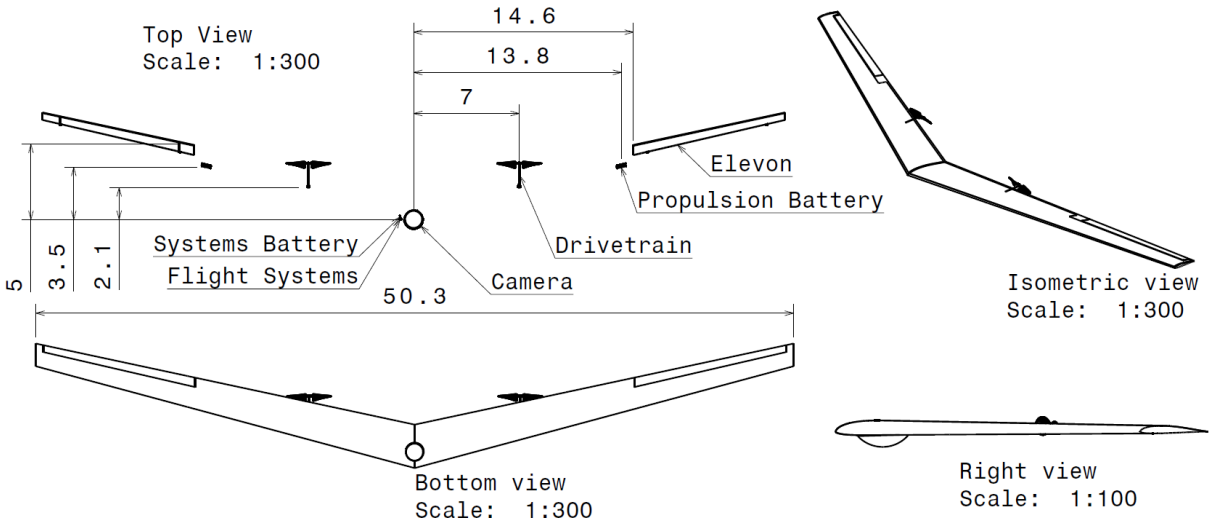

Figure 5.5: Overview of the aircraft including subsystem locations

5.1.5 Design Overview

Figure 5.5 shows the entire aircraft from different perspectives. Sizes are given in meters. The location of the different subsystems is given relative to the position of the payload. The location and sizing of the elevons has been discussed in subsection 4.4.2.

5.2 Technical Budget Overview

This section provides a brief summary of the mass and power budget. The data is calculated and discussed in previous sections.

5.2.1 Mass Budget

The mass budget is given in Table 5.5. The budgeted values are explained in subsection 4.3.2. The third column contains the actual values of each component as calculated by the specialist groups. The weight budget is thus exceeded by 10.7 kg. This has an impact for the feasibility of the design and will be discussed in section 6.5.

Table 5.5: Mass budget and actual values for the aircraft given in kg

	Budgeted Values	**Actual Values**
Wing	52.5	65
Batteries	87	92
Systems	7.2	7.2
Payload	3	1.5
Solar Panels	37	36.6
Propulsion	7	8.5
Power Point Trackers	5.1	5.2
Servos	0	3.5
Slack	10	-10.7
Total	208.8	219.5

5.2.2 Power Budget

The power budget is given in Table 5.6. The values given in this budget are derived from the explanation presented in section 4.2.

Table 5.6: Power usage budget for subsystems

Device	**Power [W]**
Payload Budget	
Daytime Sensor	0.5
Nighttime Sensor	0.13
Servos	20.8
Communication	
Computer	34.9
Transmitter	10
Receiver	4.8
Amplifier	0.163
Avionics	4.8
Total	76.093

5.3 Performance

The main purpose of the performance analysis is to justify the design. However, it was also necessary to obtain a first estimation of power required in different flight conditions to size the dependent subsystems. First of all, the climb and cruise requirements are evaluated as well as the take off and landing. Furthermore, the theoretical power required for each flight segment and situation is determined and the power delivered by either the solar panels or battery is verified. Finally, the aircraft is evaluated in terms of cruise range and range of gliding descend, in case of motor failure.

Critical for the design is the battery power (P_{br}) and power available (P_a). The difference between these is mainly determined by the component efficiencies, which are summarised in Table 5.7 for the propulsion system and are used in Equation 5.1.

$$P_a = P_{br} \cdot \eta_{motor} \cdot \eta_{gearbox} \cdot \eta_{propeller} \qquad \text{[W]} \tag{5.1}$$

Table 5.7: Component efficiencies of propulsion subsystem

Component	**Efficiency [%]**
Battery	98
Motor	90
Gear Box	97
Propeller	85

5.3.1 Climb

Figure 5.6 is generated with the assumption that power available is 1,187 W: 96% of maximum power the battery can deliver taking into account total drivetrain efficiency. An optimum climb can be performed by maximizing C_L^3/C_D^2, which is a function of altitude. Aerodynamic analysis showed a relation between this entity and altitude, given by Equation 5.2 and is achieved by flying the velocity computed by Equation 5.3. For every vertical 50 m these values were computed and power required and rate of climb were evaluated, of which the results are shown in Figure 5.6.

$$C_L^3/C_D^2 = 44.858 \cdot e^{-0.01H} \qquad \text{[-]} \tag{5.2}$$

$$V = 5.26434 \cdot e^{0.0736H} \qquad \text{[m/s]} \tag{5.3}$$

The rate of climb is almost 0.46 m/s at SL and about 0.11 m/s at 18 km altitude, which is therefore an achievable altitude. The theoretical ceiling is over 20 km. Finally, the bottom graph in Figure 5.6 indicates 16.9 hours are needed to reach loiter altitude. The battery can deliver the power assumed here for 17.8 hours, so the aircraft is capable of climbing even during the night.

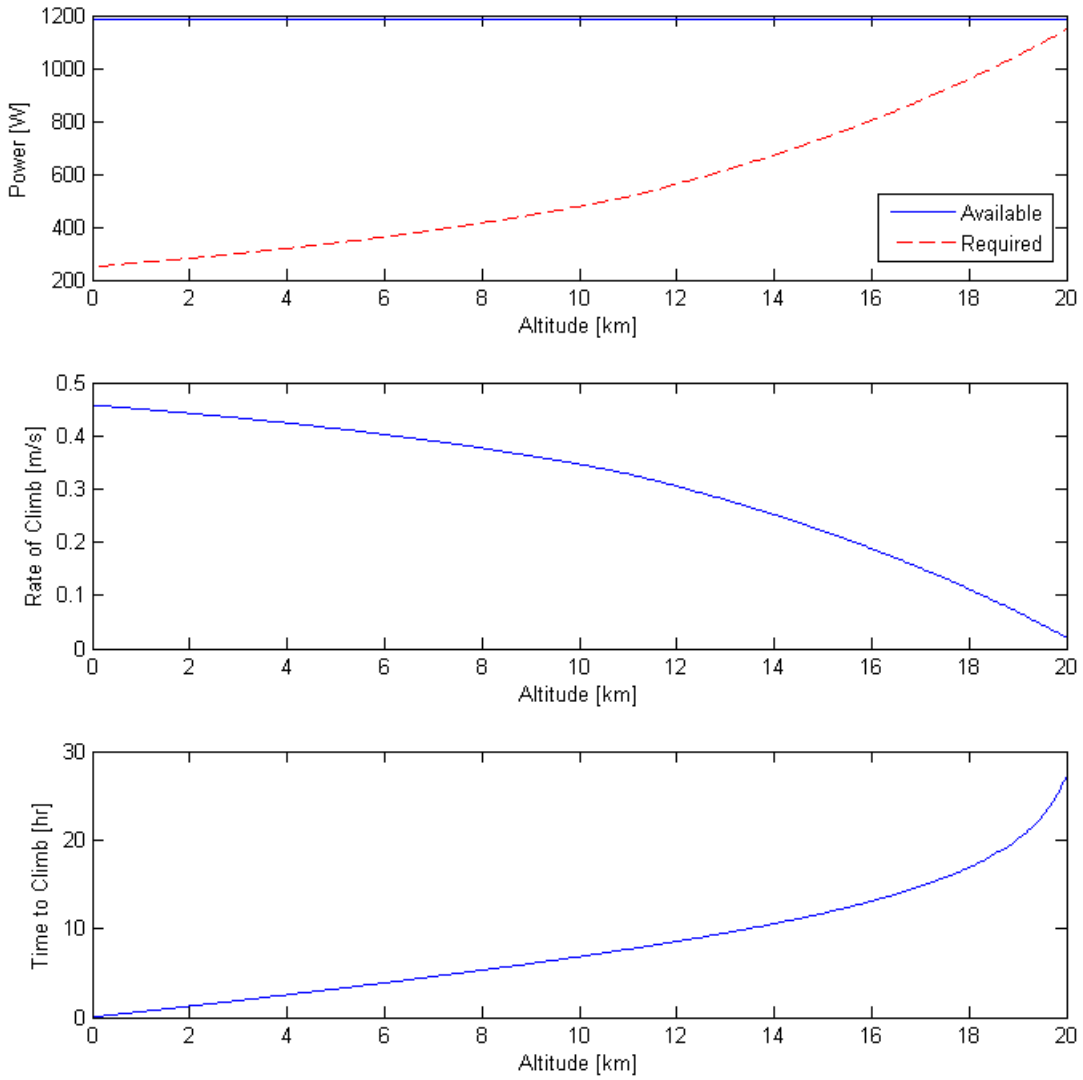

Figure 5.6: Climb performance

5.3.2 Cruise

With the cruise requirements from Figure 5.7 it can be computed that the power to be delivered by the propeller should be 922 W, which results in 1,242 W to be supplied to the motor. Both the batteries and solar array can deliver this power on the worst day, so this cruise performance is guaranteed. Range is in theory infinite for this specific aircraft, because no fuel is carried and power can be generated during an entire year. However, taking into account the cycle life of the battery and the range that can be flown during the worst day a rough estimation of the minimum total range achievable in a year can be calculated. The average daily power consumption is 1236 W and the battery is able to deliver 1162 W. Therefore, during daylight a velocity of 23 m/s can be flown for 6.9 hr and at night 22.5 m/s. Computing the day and night range and multiplying by the cycle-life of 323 gives a total yearly range of 631,840 km.

5.3.3 Level Turn

During nights, the UAV will fly turns with constant radius, determined by the obstacle angle as shown in Equation 5.4

$$R = H \tan(\alpha) \qquad [\text{km}] \tag{5.4}$$

where α is the obstacle angle. At 18 km this results in a turn radius of 564 m with a bank angle of 5 degrees. The power delivered by the propellers should be 974 W, so the battery needs to provide 1,312 W of power. The battery has been sized for this condition and thus is able to provide this. During days, a particular shape is flown with two dominant turns: with a bank angle of 5° and one of 40°. The power that should be supplied to the motors is respectively 1,341

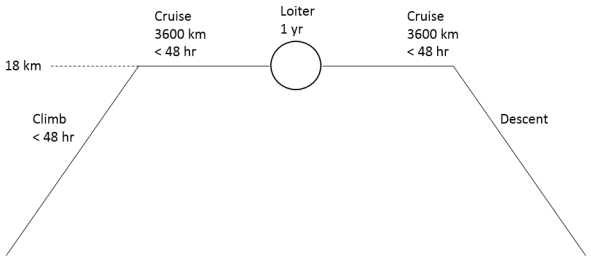

Figure 5.7: Mission Profile

W and 1,955 W. Also the solar panels can deliver the power stated here.

5.3.4 Descent

In an emergency case when both motors fail the aircraft should be able to return to base solely by gliding. A simple analysis was performed to compute the range the aircraft can glide from a certain altitude and is presented in Figure 5.8. The glide ratio depends on altitude and an approximation is given by Equation 5.5, obtained from aerodynamic analysis.

$$L/D = 56.914 \cdot e^{-0.01H} \qquad [-] \tag{5.5}$$

The results are shown in Figure 5.8. From 18 km the aircraft can glide for 23.7 hours and covers a ground distance of 940 km. This might just be enough to fly the aircraft to a safe place, but in more isolated areas this becomes a problem. Beneficial is that operators have a long window to respond to this and take the necessary precautions.

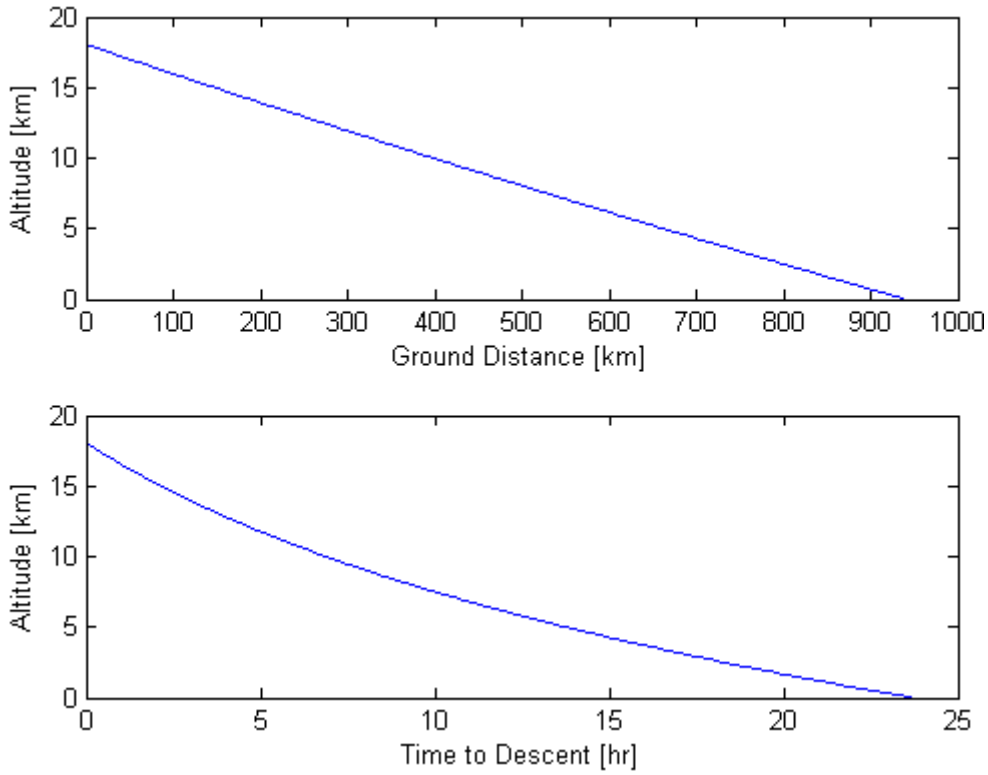

Figure 5.8: Glide range as function of altitude

5.3.5 Take Off and Landing

The aircraft can take off solely by itself for which it is assumed power available is the same as for climb: 1,187 W. The $C_{L_{max}}$ is 1.28 and C_{D_0} is 0.008 which result in a take-off field length of 29 m, well within the requirement.

Landing by only gliding would result in a landing field length of 679 m. However, the propellers can generate reverse thrust reducing this distance to only 96 m. This does not take into account ground effect.

Chapter 6

Final Design Analysis

With the designing finished and the performance and layout determined, the feasibility of the design can be analyzed. In this chapter several aspects regarding the design are therefore investigated. The operation and logistic is first described, followed by a costs analysis in section 6.2. The sensitivity of the design to changing parameters is discussed in section 6.3. The compliance of the design with the requirements is analyzed in section 6.4. The technical risks of the design are indicated in section 6.6. The sustainable analysis is done in section 6.7.

6.1 Operation and Logistics

In this section everything the vehicle requires for support is described from the moment it leaves the manufacturer. These supporting systems are of vital importance for the success of a mission. These supporting systems range from ground support and maintenance to communication.

For take-off and landing, a basic need for the vehicle is an airfield with sufficient space. Since the aircraft doesn't carry any landing gear it will touch down and take-off from the back of two cushioned flat-bed trucks, which will drive along with the aircraft. These trucks need room and a smooth surface to drive, therefore a concrete or asphalt runway will be necessary. The low take-off and landing velocity (6 m/s) makes this possible. To fly the safest way, weather developments must be known to avoid storms and highly turbulent areas.

Once airborne the vehicle can climb and fly autonomously towards cruise altitude and the target area. To achieve this the aircraft needs to determine it's position and altitude which is done via the GPS satellite system. Although it can fly and perform the mission autonomously communication with the vehicle is of vital importance. Data needs to be transmitted to the ground station and mission details towards the aircraft. Continuous communication is important if severe problems occur and manual control of the vehicle is necessary. To ensure this over all the required latitudes a global communication satellite network and ground antennas are used. An extra option is to also have mobile ground stations for communication.

High cost will come from mission control for the duration of a mission since continuous monitoring is required. This is a service that can possibly be provided in a centralised manner to reduce cost. This will exist of an office which takes care of the UAV's flight performance and relays the mission data to the costumer. This can also be done by the costumer itself, but can inflict a serious cost penalty. This mission control will require a satellite dish for receiving and transmitting. Operators to monitor the UAV's are needed 24/7 but can monitor more UAV's at the same time.

On completion of the mission or possibly if problems occur, the aircraft lands and maintenance is needed. Hangar space must be reserved and qualified staff hired for the replacement of parts like batteries and solar encapsulation. Inspection of the structure will be necessary to look for micro-cracks and other damage and require special tools. This can be done in a centralized manner like the mission control, again to reduce cost and complexity.

6.2 Costs Breakdown

The purpose of this section is to provide the customer with a detailed and low risk cost overview. The Costs breakdown not only focuses on the fixed costs. Taking maintenance, labour, replacements, variable prices, changing services and many more as much into account as possible. The breakdown will be divided in a structural section, payload & communication and other subsystems, power and propulsion, research and development, production and operations. Maintenance, price changes and services are included in the different categories rather then creating more categories. For every category some explanations are given such as the price prediction, material choices and more.
Price per unit at an order of 100 units is assumed with a 20% supplier discount where applicable. Maintenance and assembly are also assumed to be reduced by 20% for 100 units since this will result in a cost reduction on tools, employee experience and other services required.
Prices were first estimated in dollars and have been converted to euro's (1 U.S. \$ = 0.755 €).
Most prices are an Engineering estimates as most product prices are not available for the public.

If a source is available for a price this source is cited. The costs are listed in tables and most of these can be found in appendix C.

6.2.1 Costs Overview

In Table 6.1 an overview of the total costs is given. The costs are split in the previously mentioned categories and further elaborated upon in the rest of this section.

Table 6.1: Total costs

(a) Total Estimated Costs Overview

Department	**Unit Cost**	**Mission Cost**
Operations	€2,410,038.-	€485,038.-
Miscellaneous	€954,000.-	€133,250.-
R&D	€212,960.-	€26,620.-
Payload	€185,269.-	€25,237.-
Power	€272,764.-	€21,662.-
Structural	€79,600.-	€18,700.-
Communication	€199,391.-	€18,024.-
Propulsion	€27,106.-	€7,239.-
Data	€3,741.-	€1,557.-
Total	**Total unit cost €4,344,869.-**	**Total mission cost €737,327.-**

6.2.2 Operational Costs

Although the UAVs are autonomous they will require surveillance. For this purpose one operator per ten UAVs is estimated to be sufficient. In order to keep operational costs (Table C.1) to a minimum, the operators will make use of one control room. Operations will be delivered as a service to to the customer (Table C.1a). In this way the ground station can be shared as well as their communications and power.

6.2.3 Miscellaneous Costs

Additional costs are found in Table C.2 The costs for control actuation is an educated guess, since the UAV actuators used are tailored for specific clients and thus prices are also tailored to that. For the guess actuator are used that do not have the same torque, or temperature range[101, 102]. For this an extra margin is added.
Furthermore, in miscellaneous costs maintenance, assembly, end of life, costs of ownership and costs of certification are also included.

6.2.4 Research and Development Costs

Research and Development cost are shown in Table C.3. Since this particular UAV is designed by students these cost are considerably lower than would be expected at for example a large company like Boeing.

6.2.5 Payload Costs

The payload sensors costs (Table C.4a) includes a very expensive Far Infra Red sensor for visibility at night and coverage when flying over cloud. Since this is a Military grade sensor no prices are available. The sensor for the visible spectrum is relatively cheap and is overestimated here.
The prices for the mirrors (Table C.4c) are also engineering estimates with slack included.
The servos and actuators for the payload are manufactured by Transmotec and do not have prices listed. The estimation is based on price trends in the industry with a percentage of slack included.

6.2.6 Power Costs

The current price of the GaAs solar cells from AltaDevices is about $100 per Watt. Delivering about 230 W/m^2, results in $23,000 per square metre. However Alta Devices informed prices will go down to less than one tenth within 5 years. "We cannot quote exact prices but we expect to be in the dollars per watt range." [83]
Since certification is expected to be completed in 2019 it is assumed that the solar panels are bought in 2018 for a considerable lower price of $2,300.- per square metre. This results in a total price of €320,350.-. After 5 years they have degraded to 25%, which is the minimum required efficiency for the design. To make sure the efficiency doesn't drop below this value the solar panels will be replaced after 4 years. Price is expected not to drop below $2,300.- per square metre as there is a minimum material cost for the solar panels when they are made.

6.2.7 Structural Costs

Structure cost (Table C.6a) includes 65 kg structural wing weight and 5 extra kg for mounting material. The material prices were found in *CES EduPack 2012* by Professor Ashby. Structure part production was an engineering estimate at 10 times the material cost. The construction prices of the moulds are assumed included in this price and spread over 100 units. The structure is assumed assembled separately from the other components since all the components should be easy removable for maintenance and replacement. The impact on the costs for the assembly of the structure is therefore estimated to be low (Table C.6b). Maintenance would include monitoring of crack growth and concluding on it's safe life. It is the mechanics responsibility to order a entire new structure when necessary. There is the option to patch cracks but since this increase weight and most certainly does not increase strength this is not favourable.

6.2.8 Communication Costs

The communication cost is mostly formed by the satellite grade antenna (Table C.7a) and transmitter receiver splitter combiner and amplifier cost. (Table C.7b) Because combining of two antennas, a receiver and transmitter requires a custom solution this price estimate is rather high (Table C.7b). The navigation and flight control box, antenna, cabling and maintenance are all estimated to have a small impact on cost. (Table C.7b, Table C.7a and Table C.7c respectively)

6.2.9 Propulsion Costs

The propulsion systems contains 3,054 g carbon fibre and 1,100 g of nylon 6/66 in total. The costs of carbon fibre is assumed to be €100.- per kilogram [103] and €2.28.- per kilogram for nylon 6/66 [104]. The production costs are assumed to be hundred times the material costs [103]. Costs of bearings, servo-motors and integration are not included as they were not treated in the design process. The motors cost approximately €750.- each. The motors and gearing will be replaced after every mission as they contain moving parts and therefore wear off. The propellers require extensive checking after every mission. The propulsion cost can be found in Table C.8.

6.2.10 Data Handling Costs

Data handling in this instance requires computing power to handle and compress images whilst keeping power consumption at a minimum. Therefore a high performance low power CPU (Central Processing Unit) is chosen and a set of matching low Voltage RAM (Random Access Memory). (Table C.9a) The PCB (Printed Circuit Board) is solely selected on it's compatibility with the CPU. (Table C.9b) The storage provided is chosen to be a SSD (Solid State Drive) because of it's low power consumption and non-moving parts. (Table C.9b). The volume for storage was determined by being able to store a year of data and have backups for navigation data. Data cost has a minimal impact on the overall mission cost, it is therefore possible to expand to 2 CPU's and even more SSD's as long as the power budget allows it.

6.2.11 Conclusion on Costs

Although there is a slack of about €260,000.- per mission it is expected that due to lack of experience developing UAVs, unsure price estimates, unsure degradation values and further development and production risk this slack will probably be needed.
The expectance is therefore that cost will end up to be just on budget of €1M per mission.

6.3 Sensitivity Analysis

With the design finished, a sensitivity analysis has been performed to see how the feasibility of the mission is affected by design changes. Since every change affects the whole designs, while no full design iteration can be executed, the changes only show trends and will not show fully optimised values. The feasibility of the design in regard to payload, battery technology, latitude and height are analysed in this section.

For the customer it is of interest to see how the payload weight will affect the design. In Figure 6.1 shows the trends of the total weight and the surface area versus the payload weight. Doubling the payload weight from 3 to 6 kg will increase the surface area roughly 15% and the total weight 10%. However, by increasing the payload weight further, the total weight and surface area increase relatively more. Additional space might be required for payload operation, inducing more drag and a heavier wing, further enlarging the design. The design is therefore sensitive to adding extra payload, though these increases can be limited by optimisation.

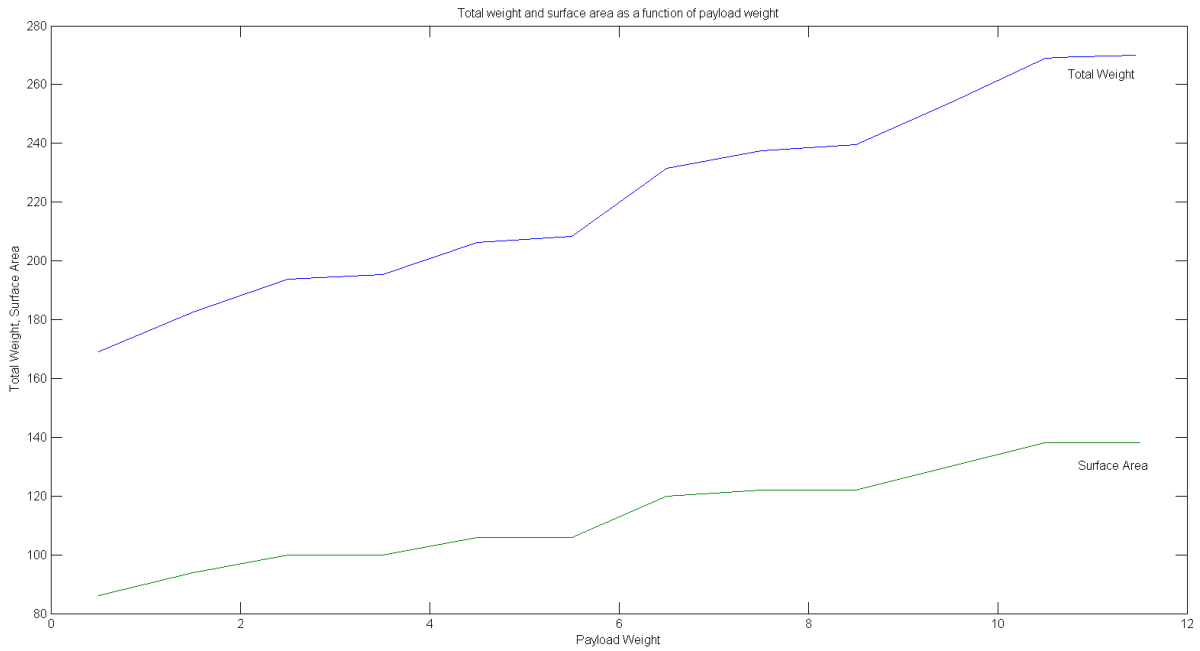

Figure 6.1: Total weight and surface area versus payload weight

One of the main design components concerning weight are the batteries. These depend mainly on the power density. Shown in Figure 6.2 are the changes in total weight and surface area when the power density changes. It can be observed that both the surface area decreases 30% and the total weight 40% when the power density doubles. The weight affected by the decrease in battery weight and also by the lower wing weight. This shows a large sensitivity on the design to battery performance. Since battery technology will improve the coming years, this will allow improvements to the design and can increase mission capabilities. A discrepancy is noticed in the total weight graph, this is due to the iterative nature of the program used and should smoothen out by increasing the number of iterations.

Since the mission is mainly limited by the critical conditions at high latitudes, it is advantageous to know how the design changes depending on the operating latitudes. Northern- and Southern-Hemisphere latitudes are considered identical in this analysis due to the symmetry of Earth. The surface area largely depends on the required power and thus latitude. Figure 6.3 shows the surface area required and the corresponding airspeed over the operating range of latitudes. Airspeed and surface area of the aircraft were varied during the analysis, keeping the ratios of lift over weight and power available over power required approximately at one. This figure clearly shows the exponential relationship between surface area and latitude due to the snowball effect. Figure 6.4 shows the total weight of the aircraft versus latitudes, which also increase significantly at the higher latitudes due to the increased surface area. The design is thus very sensitive to the operating range.

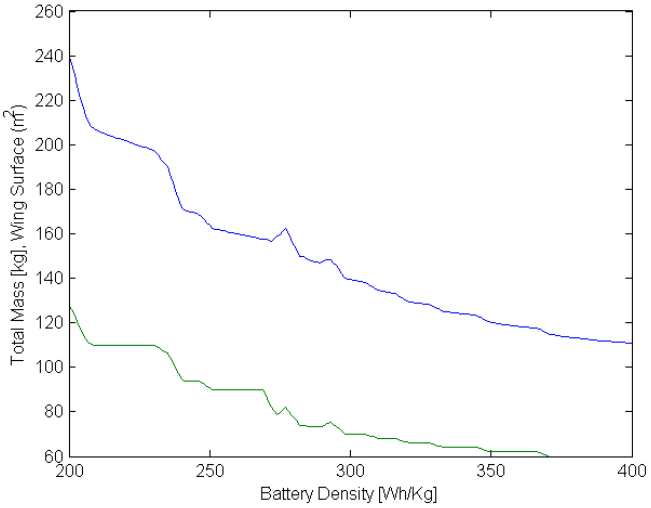

Figure 6.2: Total weight and surface area versus battery density

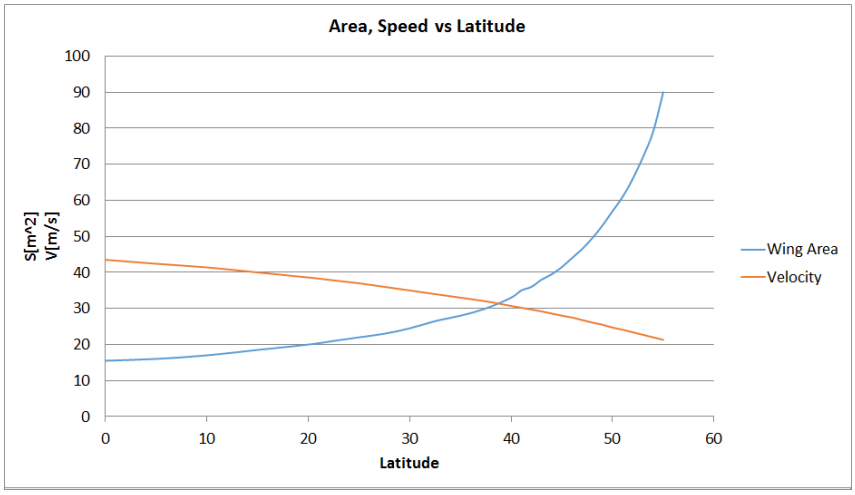

Figure 6.3: Surface area and airspeed versus latitude

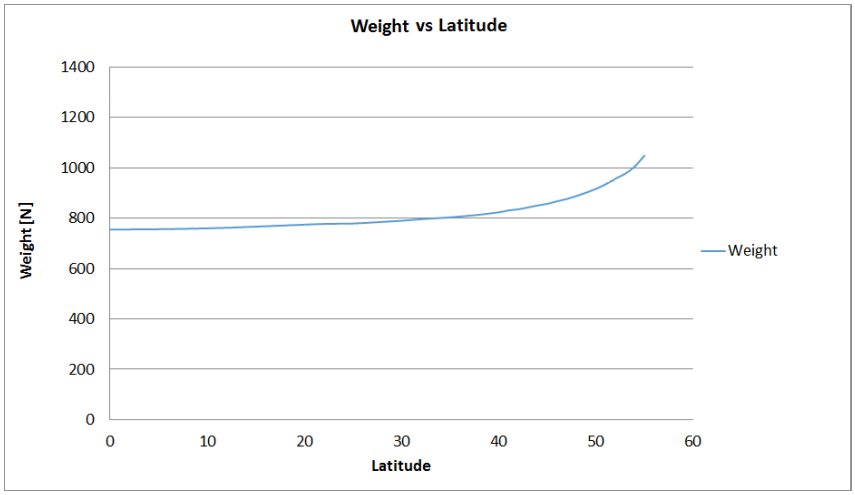

Figure 6.4: Weight versus latitude

Lastly, the influence of mission altitude is analyzed. The total weight and surface area as functions of cruise altitude are plotted in Figure 6.5. Since performance changes with air density

and thereby the optimal flying speed changes, this graph only shows the general trend. As can be seen, the design increases exponentially in weight and surface area with height. This is the basis for the design choice to fly at 18 km altitude, the lowest altitude where the wind speeds are sufficiently low. At altitudes over 22 km, the design feasibility becomes very critical while the wind speeds at those altitudes are higher as well, limiting the vehicle to 21 km altitude.

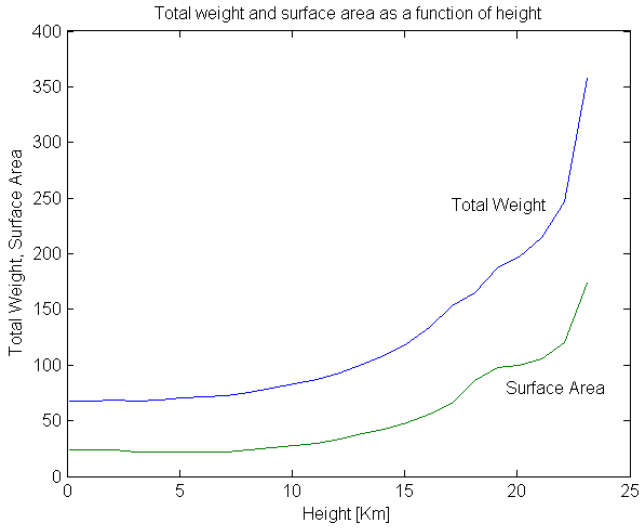

Figure 6.5: Total weight and surface area versus altitude

In conclusion, the design is very sensitive to changes. The payload might have a relatively mild effect but certainly not negligible. Battery technology, and in the same sense for example solar panel technology do affect the design a lot. Operating range in both latitude and height show large sensitivity of the design to its mission range.

6.4 Mission Compliance

Now that the final preliminary design has been completed, a check must be performed if all the requirements are met. The conclusion was certain requirements have not been met. Therefore a feasibility investigation is performed in section 6.5 to see what has to be changed for the design to fulfill all requirements.

6.4.1 Requirements Compliance Matrix

The following table, Table 6.2, contains the requirements where a tick mark verifies if they are met. An extra column is added with notes to the requirements. In the feasibility analysis the requirements which are not met are discussed and solutions are proposed to solve the issues.

Table 6.2: Compliance Matrix

Requirement	**Compliance**	**Note**
Top level requirements		
Cruise will take place between 0° and 55° latitude	✓	Up to -40° latitude on southern hemisphere
90% station keeping on cruise altitude guaranteed	✓	On some latitudes even 95%
Minimum cruise altitude of 15 km	✓	Cruise altitude will be 18 km
One year mission duration	✓	Able to stay airborne and keep station during one full year
Maximum payload mass of 3 kg	✓	The camera weighs three kg

Continued on next page

Continued from previous page

Requirement	Compliance	Note
Take-off and landing must be possible in wind force 3 conditions (Minimum landing speed must be 5.4 m/s)	✓	Landing speed of atleast 6.9 m/s is possible
Maximum cross wind during take off and landing of 5 kts	✓	There is sufficient yaw control to maintain crab angle and rotate the aircrat during landing
Resolution of the payload should be sufficient to track individuals on the ground from cruise altitude	✓	With a ground resolution of 0.57 x 0.57 cm individuals can be tracked
Night operation (Extra)	✓	With an extra infra-red sensor and a resolution 7 x 7 cm
Cost of one mission should be below one million Euro	✓	Mission cost is €... with mission life time of eight years
Total weight of the aircraft should not exceed 208.8 kg	✗	Total aircraft weight is 219.5 kg
Aircraft must be designed for cradle to cradle	✗	Aircraft is for about 80% cradle to cradle
Payload		
Payload should bank 10° for turning	✓	Banking up to 10° is possible
Minimum ground resolution 5x5 cm	✓	Only during daytime
Construction must fit within wing	✗	A dome beneath the wing is required, which sticks out 45 cm beneath the wing
Payload should be kept at operating temperature	✓	
Communication		
Communication coverage should be available on all required latitudes	✓	
Uplink of at least 40 Mb/s should be achieved	✓	
Downlink of at least 40 Mb/s should be achieved	✓	
Uplink should be continues for manual overwrite	✓	
Flight performance and propulsion		
Cruise speed of 22 m/s must be achieved	✓	Average cruise speed of 22 m/s during the critical conditions is possible. Higher cruise speed is possible when conditions improve
Maximum airspeed of 30 m/s to guarantee 90% station keeping	✓	Possible for a short period during the critical conditions
Station keeping must be done within an 1 km radius	✓	Normal operations are done within a radius of 563 m
Propulsion should deliver 46 N thrust during cruise conditions	✓	
Aircraft will be unmanned	✓	
Required runway length should be no more than 1500 m	✓	Take-off requires 30 m, Landing 96 m
Climb from take-off to cruise within 24 hours	✓	Climb is done within 16.9 hours
Energy collection and storage		

Continued on next page

Continued from previous page

Requirement	Compliance	Note
Solar panels must deliver 40.4 kWh on worst case scenario	✓	
Degradation of solar panels may not be more than 1% absolute loss in efficiency during four years	✓	Replacement every four years is necessary
Batteries must have an EOL capacity of 29.9 kWh	✓	
Batteries have lifetime of 320 cycles	✓	Replacement every year necessary
Batteries must be kept at operating temperature of at least -20° C	✓	
Structure		
Structure should allow storage of all systems	✓	Cut-out is made for the payload
Structure able to carry maximum load factor of 3.2	✓	
Structure should not degrade due to ozone and UV	✓	CF with PEEK has excellent resistance against degradation
Structure should not fail due to fatigue loading	✓	
Structure keeps the aerodynamic shape of the wing	✓	
Aerodynamics, Stability and Control		
Bank angle of 40° must be attainable	✓	Banks of atleast 60° are possible
Roll rate should be atleast 11°/s	✓	
Aircraft must be stable on all longitudinal eigenmodes	✓	
Aircraft must be stable on all lateral eigenmodes	✗	Marginally unstable during a spiral motion, $T_{\frac{1}{2}}$=43.728.
Aircraft must have acceptable aerodynamic performance at 30 m/s	✓	C_L/C_D at 30 m/s is 40.5

6.5 Feasibility Analysis

This section will discuss the requirements which have not been met in subsection 6.4.1. Possible solutions to fulfill these requirements will be presented and at the end a conclusion will be reached with respect to the feasibility of the design.

6.5.1 Weight problem

Exceeding the weight budget of 208.8 kg by 10.7 kg is the most important requirement which the current design has failed. All subsystems are designed with this weight in mind. The final weight of 219.5 kg will cause the engines to be under powered, the batteries unable to deliver enough power during the worst night and the solar panels unable to supply the required power during the day. A higher weight would make the design unable to fulfill a number of other requirements such as cruise speed and/or station keeping during the critical days. There are three potential solutions to this problem:

1. The least desirable solution is to accept the problem and the limitations it implies. This means the aircraft can perform year round station keeping between 0° and 54° latitude. Station keeping at 55° latitude is possible starting from the 6^{th} of January until the 4^{th} of December. Assuming the rest of year 100% station keeping is achieved, missing coverage for this period would still fulfill the 90% station keeping requirement.

2. Currently an area of 96.3 m^2 is being used by the solar panels, out of the 110 m^2 available. Increasing this area would provide the additional power needed to compensate for the

available weight. However, this will add solar panel weight and additional battery weight. This would start a snowball effect, increasing the required wing strength and thus mass, so it is uncertain if this approach would work.

3. Finally, the size of the entire aircraft can be increased which will increase the aerodynamic performance, allowing components such as the battery and solar panel to be a smaller fraction of the total aircraft weight. In addition to that, with a bigger wing the payload would protrude less, creating less drag. It is extremely likely this approach would work, but it would require a detailed recalculation of all of the aircraft parameters and subsystems. Unfortunately no time was available to perform this reiteration.

Thus three options are available to solve this problem. The first would require acceptance from the customer of the slightly reduce observation coverage. The second and third require a new engineering effort. Either way the order of magnitude in which the weight budget was exceeded should ensure the problem is solvable and thus the feasibility of the design is not under threat.

6.5.2 Sustainability

During an earlier phase of the project the desire was expressed to make the design fully cradle to cradle compliant. Unfortunately this has not been achieved by this design. The main reason is the fact the chosen solar panels cannot be recycled as explained in section 6.7. Fully recyclable solar panels are available, but their peak efficiency lies between 8-11% which is a factor two below what is required for the design, as was discussed in section 6.3. Therefore it must be concluded with the current state of technology it is impossible to make the current design fully cradle to cradle compliant. However the solar panels have a total expected lifetime of at least 15 years, reducing the environmental impact.

6.5.3 Payload Size

The requirement to fit the entire payload within the wing was introduced to avoid excessive aerodynamic drag and to prevent the payload from being damaged during landing. Both issues have been resolved: Payload drag is roughly 7.7% of the total drag and the aircraft has been designed for it. Damage to the dome during landing and take-off is avoided by vehicle assisted take-off. Therefore not complying with this requirement does not impact the designs feasibility.

6.5.4 Unstable Spiral

One stability issue the fact that the spiral eigenmode is slightly unstable. As discussed in subsection 4.3.3, this is not a major issue for the design. It is only slightly unstable and the flight management system will have loads of time to correct this maneuver.

6.6 Technical and Operational Risk

This section will give an estimate of the technical and operational of the project. First all the risks are identified and ordered in terms of severity, after wards some ways to reduce the most severe risks will be discussed.

6.6.1 Risk Analysis

For the final design a risk analysis is performed to identify problems that can occur during further development and the duration of a mission. The risk analysis is divided in two categories, a technical risk analysis and an operational risk analysis. Technical risk involves the probability in future design that requirements will not be met, where operational risk consist of risk that occur during operation. Table 6.3 shows the risks with an unique number and in Table 6.4 the numbers can be found in a risk map. In the risk map the probability of occurrence is linked with the consequence should the risk occur. Risks with a high probability and severe impact should be avoided or addressed.

TR1 One of the distinct advantages this project enjoys over satellite missions is the far lower costs. Exceeding the cost budget will make the project less competitive and directly impact the projects success.

TR3 The structure is currently designed assuming any shape can be fabricated. It also assumes a certain minimum skin thickness. Finally it is assumed appendages such as servos, engines

Table 6.3: Risks

Number	Risk	Number	Risk
	Technical risk		
TR1*	Cost budget exceeded	TR2	Insufficient camera resolution
TR3*	Structure impossible to construct	TR4*	Higher degradation components
TR5*	Insufficient battery power density	TR6	Higher component weight
TR7*	Landing configuration	TR8*	Extra systems inclusion
	Operational risk		
OR1	Payload failure	OR2*	Structural damage due to impact
OR3*	Battery failure (fire)	OR4	Communication loss
OR5	Motor failure	OR6	Solar eclipse
OR7*	Extreme gusts	OR8	Ozon degradation
OR9	One GPS failure	OR10	Both GPS failure
OR11*	Thunderstorms (TO & landing)	OR12*	Destruction (Military)
OR13*	Elevon servo failure (jammed)	OR14	Elevon servo failure (free)
OR15	CPU failure	OR16	Faulty landing

and the payload can be straightforwardly attached to the wing box. Any assumption which is invalid will lead to a higher structures weight.

TR4 The quality of a number of critical components such as batteries, solar cell area and the structure will decrease over time. Certain assumptions are made to account for the degradation. Should these prove to be false, the design will turn out heavier.

TR7 It has been chosen to have assisted take off and landing for the aircraft in order to avoid the weight of a landing gear. Using trucks to start and land from is a feasible option, but certainly introduces the risk of the aircraft being damaged during the somewhat unconventional ground handling.

TR8 While finalizing the design, it is possible some extra problems are encountered which will need an additional system to solve. Per definition this increases weight.

OR2 The wing was constructed to be as light weight as possible, which has led to low skin thicknesses at many parts of the wing. Impact from heavy or fast moving objects such as birds or hailstones is most likely to penetrate the skin and cause structural damage

OR3 Fire walls are present in the battery section, so a fire in one pack of cells will never take out the entire battery system. Capacity will be reduced, impacting the ability of the aircraft to fly at higher latitudes during winter

OR7 Gust of extreme magnitude, higher than specified by the CS-23 regulations. Another factor in terms of gusts is when flying into a gust, the angle of attack will increase to large values, possibly causing the aircraft to enter a stall. No analysis has been performed on how the aircraft will deal with these stall conditions.

OR11 Thunderstorms cause both extreme gusts as well as lightning strike impact. Lightning strike will most likely either destroy the structure by delamination due to extreme temperatures or cause the PEEK resin to smelt.

OR12 The aircraft can be used by the military as a silent and cheap observation platform. This results in the possibility of hostile action being taken against it. Since there was no design space available for damage mitigation, hostile fire will in all probability lead to a destroyed aircraft.

OR13 Servo's are moving components and can fail in two different ways. When failed but still free to move, the second elevon servo has to take all the load and the aircraft is still controllable, but unable perform the high required roll rates. If the servo fails and jams, the entire elevon is blocked and control of the aircraft is lost.

The actions to be undertaken for the different operational risks in Table 6.4 are as follows:

- Negligible: No impact with regards to the duration of the mission or the quality images

Table 6.4: Risk map

Probability ↑					
	High		TR(6)	TR(1,8)	
	Moderate		OR(1,8,9,14) TR(2)	OR(2,3) TR(3,4,7)	
	Low	OR(6)	OR(15)	OR(4,5,10) TR(5)	OR(7,11,12,13)
		Negligible	Marginal	Crictical	Catastrophic
			Consequence →		

- Marginal: Issue has sufficient impact to necessitate a return to base, no problems are expected during the return
- Critical: Immediate return to base is needed, the aircraft is expected to have trouble during descent and landing
- Catastrophic: The aircraft is lost

6.6.2 Risk Mitigation

The more risk can be avoided, the better. This section will briefly discuss some measures which can be taken to avoid the catastrophic and high probability critical risks.

Exceeding the cost budget can be very hard to avoid and may sometimes be inevitable. The best way to deal proactively is to make strict cost budgets for every subsystem and to fully implement systems engineering. The better the internal communication is, the faster issues are resolved, often at far less costs.

Inclusion of extra systems is another area where proper use of systems engineering is essential. The better this is implemented, the quicker the necessity of new systems is recognized and the cheaper it is to implement said system, because this will affect all previous existing systems as well.

Extreme gusts will only partially be able to be mitigated. The aircraft quickly becomes unfeasible to designd at higher load factors. Further effort can however be made to calculate how often these very extreme gusts will effect the aircraft and thus a more accurate estimation of this risk can be obtained. More detailed aerodynamic analysis can be performed to investigate the stall behavior and possible tweak the design to improve stall recovery.

Impact from thunder storms can best be minimized by totally avoiding them. Therefore active ground support with accurate meteorological forecasts must make sure the aircraft never risks performing take-off or landing during these condition.

Dealing with weapons fire is a direct consequence of the design choice. Due to the mission requirements the aircraft must be as light as it possibly can while limitations are also placed on the speed and maneuverability. These factors combined make it impossible to make the aircraft suited for combat in any way, shape or form without fundamentally altering the design.

A jammed elevon due to servo failure can be solved by designing some kind of break away system for the linkage between the servo and the elevon. Once the elevon is disconnected from the jammed servo, the impact goes down from catastrophic to marginal.

6.7 Sustainability

The UAV should be sustainable in several ways: sustainable manufacturing processes (of materials), no emissions and recycling or decomposition at EOL. This shortly comprises the Cradle-to-Cradle approach, which is illustrated in Figure 6.6. This section will elaborate on the sustainable aspects of the design presented in this report. Overall objectives were to minimize use of material (lightweight) and maximize operational life.

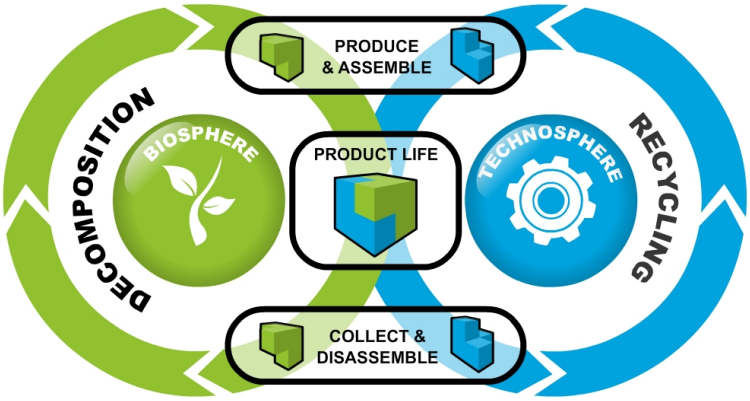

Figure 6.6: The cradle-to-cradle process

Mainly used is carbon fibre which is increasingly used in aerospace and automotive industries. Therefore legislations arise forcing manufacturers to increase the recyclability of this material, which is currently 70-75% with the use of pyrolysis [105]. Goals for coming years are to increase this to 90%. The structure and other carbon fibre components have been designed for the entire aircraft life so waste is relatively low.

Although the batteries used are being developed for use in the automotive industry and would therefore potentially have a sufficient cycle-life, it has been assumed this performance is not achieved when this aircraft should be produced. Therefore, the battery has to be replaced after each mission (of a year). Production of li-ion batteries typically require high temperatures, obtained by burning fossil fuels. However, by recycling the production energy can be reduced by 50%. Several recycling methods are developed and claim percentages of reusable material up to 93%. [106]

The solar panels are covered with a polycarbonate thin film sheet which has to be replaced each year due to UV radiation. Polycarbonate is hard to recycle, but can be re-used in less demanding applications. The solar cells are composed of mainly gallium and arsenide; both impose sustainability issues. Gallium is a very rare metal and is a by-product of zinc, bauxite, silver and tin mining. In 2010 the US Department of Energy stated that world gallium recycling capacity was around 42% [107]. Arsenic is a toxic material and has to be safely disposed of. However, although the solar panels on the UAV will be replaced after 4 years of operation, they can be sold for re-use since performance has only declined by about 1%.

All other electrical systems (motors, avionics) can be used for the entire aircraft life and optionally re-used in new aircraft. Otherwise, large amounts of material can be recovered from these systems (especially from the motors), but other parts (circuit boards) have the same environmental issues as the solar cells due to use of semiconductors.

Finally, the gearbox and hub are made from polyamide 6/66 which can not be recycled properly, but can be decomposed. The toxicity of products of this decomposition do not differ greatly from those of other polymeric materials and in general is quite low [108].

The UAV has been designed for 8 years of operational life which, taking into consideration the aforementioned, makes the design quite sustainable. The lightweight design requires little material and most systems that need to be replaced several times during the operational lifetime can be largely recycled or re-used. Mainly the solar panels impose a detrimental environmental impact, but can have a longer lifetime than the aircraft by re-using in other applications.

Besides the UAV the mission encompasses a ground station, which should also be sustainable. Therefore this station will be powered by solar panels and a wind turbine and store energy in batteries.

Chapter 7

Future Activities

A lot of development is still required to have a finished, working and certified product that can be sold to clients. This will take far more time than the design took up till now. Time will be spent on programming of the control software and the Verification and Validation of this software. The structure needs to be made and tested for all possible loadings. Full test flights will be performed. And for some elements which do not perform as expected a redesign needs to be conducted. Also the production and assembly of the aircraft needs to be structured. This chapter deals with all post DSE activities, including project planning, project design & development logic and recommendations.

7.1 Project Design and Development Logic

All activities required for a flying product can be seen in a logic diagram seen in Figure 7.1. The activities are required to get a certified product which is tested and works as it should. Testing of the structures, performing windtunnel tests and test al subsystems is an important step required before production is started.

Figure 7.1: Project Design & Development logic for post DSE activities

7.2 Project Planning and Gantt Chart

The planning of all post DSE activities presented in section 7.1 can be seen in the Gantt chart found in Figure 7.2. As can be seen a lot of time will be spend on testing of all systems and validating all results with structures tests and windtunnel tests. Certification is expected to be finished end of 2018 or begin 2019. Series production can start as soon as the certification is finished and is sceduled for begin 2019. During all operation of any customer support is provided and so the support continues until 2030.

7.3 Recommendations

Because the UAV is still in its preliminary design phase a lot more research has to be performed. In this chapter some recommendations will be given and what should be done before production of the UAV.

- Payload mirror detailed design
- Exact flight profiles for various wind speeds and directions
- 3D-solar irradiation
- Detailed design of the aircraft shape
- Detailed design of the solar modules
- Stall behaviour
- Aircraft optimization
- Detailed study on the aerodynamic inefficiency of the payload
- Electric wiring
- Casing design
- Design battery management system
- Bearings for moving parts
- Detailed mass budget calculation
- Fatigue studies
- Polymer degradation studies

As can be seen a lot of tasks still need to be done before the actual final design can be finished.

	Task Mode	Task Name	Duration	Start	Finish
1		**structure program**	**193 days**	**Fri 5-7-13**	**Tue 1-4-14**
2		Structure prototype manufacturing	60 days	Fri 5-7-13	Thu 26-9-13
3		load testing	30 days	Thu 26-9-13	Wed 6-11-13
4		Full mission load simulation	44 days	Thu 7-11-13	Tue 7-1-14
5		structure crack and damage analysis	30 days	Tue 7-1-14	Mon 17-2-14
6		limit load testing	1 day	Tue 18-2-14	Tue 18-2-14
7		structure certification	30 days	Wed 19-2-14	Tue 1-4-14
8		**Aerodynamic Program**	**193 days**	**Fri 5-7-13**	**Tue 1-4-14**
9		Detail CFD modelling	60 days	Fri 5-7-13	Thu 26-9-13
10		Windtunnel test design	60 days	Fri 5-7-13	Thu 26-9-13
11		Aerodynamic prototype manufacturing	10 days	Thu 12-9-13	Wed 25-9-13
12		Windtunnel testing	5 days	Thu 26-9-13	Wed 2-10-13
13		Windtunnel test evaluation	60 days	Wed 2-10-13	Tue 24-12-13
14		second aerodynamic prototype	10 days	Tue 24-12-13	Mon 6-1-14
15		windtunnel testing	5 days	Mon 6-1-14	Fri 10-1-14
16		aerodynamic certification	58 days	Fri 10-1-14	Tue 1-4-14
17		**Software program**	**193 days**	**Fri 5-7-13**	**Tue 1-4-14**
18		**software programming**	**74 days**	**Thu 15-8-13**	**Tue 26-11-13**
19		Verification	15 days	Thu 15-8-13	Wed 4-9-13
20		Validation	60 days	Wed 4-9-13	Tue 26-11-13
21		**Test program & certification**	**585 days**	**Fri 5-7-13**	**Thu 1-10-15**
22		individual subsystem testing	50 days	Fri 5-7-13	Thu 12-9-13
23		subsystem interaction testing	100 days	Mon 12-8-13	Fri 27-12-13
24		Low temperature testing	10 days	Wed 1-1-14	Tue 14-1-14
25		**Test flight program**	**1241 days**	**Tue 1-4-14**	**Tue 1-1-19**
26		Prototype building	60 days	Tue 1-4-14	Mon 23-6-14
27		First test flight	1 day	Mon 23-6-14	Mon 23-6-14
28		First test flight evaluation	15 days	Mon 23-6-14	Fri 11-7-14
29		test flights	191 days	Fri 11-7-14	Fri 3-4-15
30		Full mission test flight	262 days	Sun 5-4-15	Mon 4-4-16
31		Full mission test evaluation	284 days	Mon 4-4-16	Thu 4-5-17
32		Certification	1428 days	Fri 11-7-14	Tue 31-12-19
33		**Production**	**1827 days**	**Sun 1-1-17**	**Sun 31-12-23**
34		desing product line	262 days	Sun 1-1-17	Mon 1-1-18
35		producion line assembly	261 days	Mon 1-1-18	Mon 31-12-18
36		production of 100 units	1305 days	Tue 1-1-19	Sun 31-12-23
37		**support**	**4174 days**	**Tue 1-1-19**	**Fri 29-12-34**
38		Software support	4174 days	Tue 1-1-19	Fri 29-12-34

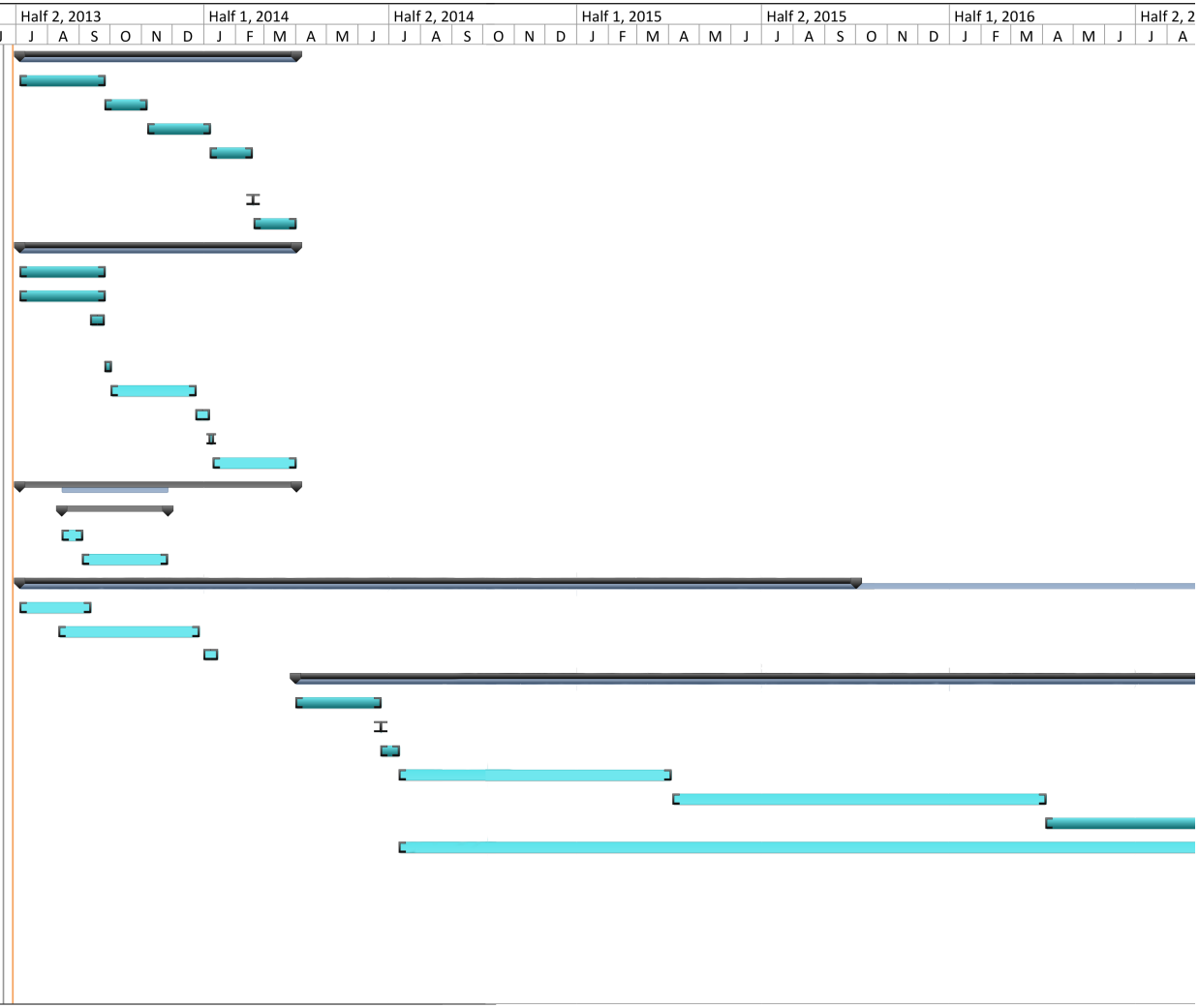

roject: Post DSE
ate: Fri 28-6-13

Task	External Milestone	Manual Summary Rollup	
Split	Inactive Task	Manual Summary	
Milestone	Inactive Milestone	Start-only	
Summary	Inactive Summary	Finish-only	
Project Summary	Manual Task	Deadline	

Chapter 8
Conclusion

The objective of this project was to develop a preliminary design of an all plastic, sustainable unmanned aerial vehicle capable of performing detailed ground observation during an entire year. An additional objective was to develop novel ways of using polymers in aeronautical applications. In order to reduce weight and the complexity of the design, it was attempted to use as many multi-purpose systems as possible. Finally it was envisioned to make the entire design cradle to cradle.

The most important and encouraging result of the project is the fact that the design is feasible. It is possible using current or very near future technology to create an aircraft capable of performing year round detailed earth observations up to moderate latitudes. This study has shown the exact range of latitude has a big impact on the size, design and costs. Above roughly 50° latitude the available power during the winter rapidly decreases. Going far beyond 55° latitude and into the polar regions is not possible with current technology, due to the near endless nights during the winter. Both battery and solar panel technology would need to improve significantly with respect to their weight and cost. A number of issues remain to be solved during the final design of this aircraft. The most important one of these is the fact that the aircraft has exceeded the weight budget by 5% with the most likely solution requiring the aircraft to increase in size and a subsequent redesign of the subsystems.

Nearly 85% of the total mass of the aircraft is made up of polymers. The structure though is fully made from polymers. The major areas where it is not possible to exclusively use polymers are the electrical motors and the solar panels. No feasible alternatives using more polymers were found. Electrical motors, which fundamentally require metals such as copper and magnets to work, are the only realistic propulsion device. Polymer solar panels exist, but their efficiency is an order of magnitude below what is required for this mission. Without near revolutionary technology improvements it is not possible to obtain a higher polymer level in this design.

A number of systems have multiple uses. The wing itself also acts as a fuselage, storing other systems such as the battery and payload. The engines are used for both yaw control and propulsion. Heat is recycled between different systems. Finally, the batteries are used both to ensure optimal centre of gravity positioning as well as bending relief for the wing.

Novel ways of applying polymers have been researched such as a flapping, morphing wings in order to increase the sun incidence angle. Morphing control surfaces to reduce trim drag were also investigated. Finally, a morphing airfoil was considered but not implemented because it would only be a benefit during climb and descend, which is a small part of the mission.

Given all the other technical design constraints a fully cradle to cradle design is not possible with current technology. The main issue are the solar panels which have a safe life of four years on the UAV and 15 years in total, but are not recyclable. Many other systems are fully or partially recyclable, such as the carbon fibre in the wings.

The most important objectives of the project have been met. A number of secondary objectives have also been met and the remainder has been partially fulfilled. Until the advent of improved technology, a fully cradle to cradle and polymer design meeting the technical objectives is not viable. This design is now ready to slot into the market as a low cost, more flexible alternative to observation satellites which can observe during both day and night.

Bibliography

[1] Boeing. *787 Dreamliner, program fact sheet.* http://www.boeing.com/boeing/commercial/787family/programfacts.page?. June 2013.

[2] J. RYHANEN. *Biocompatibility Evaluation of Nickel Titanium shape memory metal allot.* Oulun Yliopisto, 1999.

[3] E. Zhou J. Su Y. Wang C. Sun. "Deformation mechanisms of electrostrictive graft elastomer". In: *SMART MATERIALS AND STRUCTURES* 13.5 (Oct. 2004), pp. 1407–1413.

[4] Andrew J. Lovinger. "Ferroelectric Polymers". In: *Science* 220.4602 (1983), pp. 1115–1121. DOI: 10.1126/science.220.4602.1115. URL: http://www.sciencemag.org/content/220/4602/1115.abstract.

[5] Y. Koyama S.R. Hall Y. Chiang T.E. Chin U. Rhyner. "Lithium Rechargeable Batteries as Electromechanical Actuators". In: *Electrochemical and Solid-State Letters* 9.3 (2006), A134–A138. ISSN: 1521-4095. DOI: 10.1002/adma.201104795. URL: http://dx.doi.org/10.1002/adma.201104795.

[6] Lucintel. *Growth Opportunity in Global UAV Market.* http://www.lucintel.com/LucintelBrief/UAVMarketOpportunity.pdf. 2011.

[7] Z Sarris. *Survey of UAV applications in civil markets.* Tech. rep. Technical University of Crete, June 2001.

[8] A.H.Oort. *Global atmospheric circulation statistics.* 1958-1973. URL: http://iridl.ldeo.columbia.edu/SOURCES/.OORT/.

[9] Flemming et al. "Monthly Mean Global Climatology of Temperature, Wind, Geopotential Height and Pressure for 0-120 km". In: (Feb. 1988). URL: http://badc.nerc.ac.uk/data/cira/fleming.pdf.

[10] Ailsa Mhairi Fowler. *The contribution of small - scale wind and photovoltaic renewable energy sources to the scottish energy mix.* Apr. 2011. URL: https://openair.rgu.ac.uk/bitstream/10059/656/1/Ailsa\%20Fowler\%20PhD.pdf.

[11] Steven Crutchfield. *Java Applet on signals.* http://www.jhu.edu/signals/fourier2/index.html. Oct. 1996.

[12] J.A. Roney. "Statistical wind analysis for near-space applications". In: *Journal of Atmospheric and Solar-Terrestrial Physics* 69.13 (Sept. 2007), pp. 1485–1501. URL: http://www.sciencedirect.com/science/article/pii/S1364682607001290.

[13] R.B.Stull. *Meteorology for Scientists and Engineers.* Brookscole, 2000.

[14] EASA. *Certification Specifications for Normal, Utility, Aerobatic, and Commuter Category Aeroplanes CS-23.* EASA, July 2012.

[15] R. Steiner. "A review of NASA high-altitude clear air turbulence sampling programs". In: *AIAA* 65 (Jan. 1965).

[16] K.G. Pratt & W.G. Walker. "A revised gust-load formula and a re-evaluation of v-g data taken on civil transport airplanes from 1933 to 1950". In: *National Advisory Committee for Aeronautics* (1953), pp. 1149–1157.

[17] Measurement and Instrumentation Data Center (MIDC). *Compute the solar position and intensity from time and place.* http://www.nrel.gov/midc/solpos/solpos.html. 2013.

[18] Ecotect. *Solar Incidence.* http://wiki.naturalfrequency.com/wiki/Solar_Incidence. June 2013.

[19] Michael E. Ritter. *The Physical Environment: Global scale circulation.* 2008. URL: http://www4.uwsp.edu/geo/faculty/ritter/geog101/textbook/circulation/global_scale_circulation.html.

[20] V. Khavrus and I. Shelevytsky. *Introduction to solar motion geometry on the basis of a simple model.* http://iopscience.iop.org/0031-9120/45/6/010/. Nov. 2011.

[21] *Compact Telescope for Free Space Communications.* Tech. rep. Hamamatsu. URL: www.hamamatsu.com/eu/en/product/new/C11440-52U/index.html.

[22] *1/2-Inch Megapixel CMOS Digital Image Sensor.* Tech. rep. Micron. URL: download.micron.com/pdf/datasheets/.../mt9m001_1300_mono.pdf.

[23] *High Picture Quality Cellular Phone CMOS Image Sensors Feature Full HD Video.* Tech. rep. Sony. URL: www.sony.net/Products/SC-HP/cx_news/.../imx081_091_111pq.pdf.

[24] *KAI-16000 Image Sensor.* Tech. rep. Truesense. URL: www.truesenseimaging.com/all/download/file?fid=11.44.

[25] *KAI-29050 Image Sensor.* Tech. rep. Truesense. URL: www.truesenseimaging.com/all/download/file?fid=11.44.

[26] *Pico 1024E.* Tech. rep. ULIS. URL: www.ulis-ir.com/uploads/Products/Pico1024E-UL05251.pdf.

[27] *U8000*. Tech. rep. DRS Technologies. URL: www.drsinfrared.com/docs/datasheets/U8000.pdf.

[28] *U8000 LCC*. Tech. rep. DRS Technologies. URL: http://www.drsinfrared.com/docs/datasheets/U8000LCC_MR-2012-04-616_Rev02.pdf..

[29] *ASP-LWIR-640-480*. Tech. rep. Allied Scientific pro. URL: alliedscientificpro.com/wp-content/uploads/asp-lwir-640-480.pdf.

[30] W.J. Larson J.R. Wertz. *Space mission analysis and design*. 3rd ed. 2012.

[31] D.James D.Vladimir. *Compact Telescope for Free Space Communications*. Tech. rep. fSONA Communication Corporation.

[32] Transmotec. *Planetary Gear DC Motors*. www.transmotec.com/dc-motors/planetary-gear/PD32-Series.aspx. June 2013.

[33] Thomson. *Linear Actuator – S12-17A16-xx*. http://datasheets.globalspec.com/ds/729/Thomson/550D849B-F247-4D60-BCAD-9B32A70F6B68. 2013.

[34] Axis communication. *H.264 video compression standard*. Tech. rep. June 2013.

[35] Tweakers.net. *Tweakers pricewatch; AMD Opteron 4256 EE Tray*. http://tweakers.net/pricewatch/295828/amd-opteron-4256-ee-tray/specificaties//. June 2013.

[36] Tweakers.net. *Tweakers pricewatch; Kingston ValueRAM KVR13LR9D4K4/64*. http://tweakers.net/pricewatch/312021/kingston-valueram-kvr13lr9d4k4-64/specificaties/. June 2013.

[37] Crucial. *Crucial M500 960GB*. http://www.crucial.com/store/partspecs.aspx?IMODULE=CT960M500SSD1. June 2013.

[38] T. Ebrahimi C.Christopoulos A. Skodras. "The JPEG2000 still image coding system: an overview". In: *IEEE* 46.4 (Nov. 2000), pp. 1103–1127.

[39] L3 Communications. *ST-5000S S Band Multi-Mode Transmitter*. www.alldatasheet.com/view.jsp?Searchword=ST5000S&q=ST5000. June 2013.

[40] L3 Communications. *Compact Video/Data Receivers*. http://www2.l-3com.com/scm/pdf/datasheets/ML567_VR10_Compact%20Video%20Data%20Receivers_SCM_Rev%20D.pdf. June 2013.

[41] Surrey Satellite Technology US LLC. *S-Band Patch Antenna, Vibration Tested (2-Units)*. http://www.sst-us.com/shop/subsystems/telemetry-and-telecommand/s-band-patch-antenna,-vibration-tested--2-units-. June 2013.

[42] Geneva Aerospace. *flightTEK*. www.l-3com.com/uas/news/pr.htm. June 2013.

[43] K.W. Whites. *Lecture 34: Antenna Effective APerature. Friis equation*. Lecture. 2012.

[44] Andre Deperrois. *XFLR5 v6.09.01beta*. http://www.XFLR5.com. May 2013.

[45] R. Eppler. *Airfoil Design and Data*. Springer-Verlag, 1990.

[46] UIUC Applied Aerodynamics Group. *UIUC Airfoil Data site*. www.ae.illinois.edu/m-selig/ads/coord_database.html. June 2013.

[47] John McArthur. "Aerodynamics of Wings at Low Reynolds Numbers". PhD thesis. University of Southern California, 2007.

[48] D. Althaus. *Profile Polars for Model Flight, Wind-Tunnel Measurements on Profiles in Critical Reynolds Number Range*. Neckar-Verlag, 1980.

[49] G. S. Jones R. J. McGhee and R. Jouty. *Performance Characteristics from Wind-tunnel Tests of low-Reynolds-numbers Airfoils*. 1988.

[50] J. F. Donovan M. S. Selig and D.B. Fraser. *Airfoils at Low Speeds*. H. A. Stokely, 1989.

[51] A. P. Broeren M. S. Selig J.J. Guglielmo and P. Giguere. *Summary of Low-Speed Airfoil Data*. Vol. 1. SoarTech Publications, 1996.

[52] D. F. Volkers. "Preliminary Results of Windtunnel Measurements on Some Airfoil Sections at Reynolds Numbers Between $0.6*10^5$ and $5.0 * 10^6$". In: *Internal Memorandum* (1977).

[53] T. E. Noll et all. *Investigation of the Helis Prototype Mishap*. Tech. rep. NASA, Mar. 2004.

[54] G. La Rocca. *Wing Design, Systems Engineering Elements 2, part 2*. Dec. 2010.

[55] S.F. Hoerner. *Fluid Dynamic Drag*. Hoerner, 1956.

[56] M. Hepperle. *Basic Design of Flying Wing Models*. Tech. rep. Dec. 2002. URL: http://www.mh-aerotools.de/airfoils/flywing1.htm.

[57] K. Nickel & M. Wohlfahrt. *Schwanzlose Flugzeuge, available in English: Tailles aircraft in theory and practise*. Birkhuser Verlag, 1990.

[58] A.C in 't Veld et all. *Flight Dynamics*. Lecture Notes. TU Delft, 2013.

[59] G.J.J. Ruijgrok. *Elements of airplane performance*. 2nd ed. Delft University Press, 2009.

[60] R. T. Jones H. A. Pearson. "Theoretical Stability and Control Characteristics of Wings With Various Amounts of Taper and Twist". In: *National Advisory Committee for Aeronautics* 635 (1938).

[61] Harold Youngren Mark Drela. Tech. rep. MIT, Nov. 2003.

[62] Anthony Colozza. Tech. rep. Federal Data Systems, Mar. 1998.

[63] Mustafa Cavcar. Tech. rep. Anadolu University, School of Civil Aviation.
[64] D. H. Middleton. *Composite Materials in Aircraft Structures*. Longman, 1996.
[65] Gerard van Bussel. *Lecture Slides Wind*. www.blackboard.tudelft.nl. Mar. 2011.
[66] CPM. *Power Pack CPM90-22-1500-L (48V)*. June 2013.
[67] The Pennsylvania State University. 2010.
[68] MatWeb. *Wellman WellamidÂő GF60-66/6 XE-N 60% Glass Fibre Reinforced Nylon 66/6, Lubricated & Heat Stabilised*. http://www.matweb.com/search/datasheettext.aspx?matguid=ca970a6739b14fc28939ac08c8c69813. 2013.
[69] Woodgears USA CA. *Planetary gear ratio calculations*. woodgears.ca. June 2013.
[70] C. Kassapoglou. *AE2211-11*. Tech. rep. Technische Universiteit Delft, 2013. URL: blackboard.tudelft.nl.
[71] F. Tudron et al. *Lithium-Sulfur Rechargeable Batteries: Characteristics, State of Development, and Applicability to Powering Portable Electronics*. Tech. rep. Sion Power Corporation, 2013. URL: http://www.sionpower.com/pdf/articles/PowerSources2004.pdf.
[72] Battery University. *Comparison Table of Secondary Batteries*. Tech. rep. 2013. URL: http://batteryuniversity.com/learn/article/secondary_batteries.
[73] Steve W. Martin Inseok Seo. *Lithium Ion Batteries - New Developments*. Intech, 2012.
[74] EV World. *Sold-State, Lithium Air Batteries Development at Toyota*. Tech. rep. 2013. URL: http://evworld.com/news.cfm?newsid=29812#.
[75] Kan Huang, Yunfeng Li, and Yangchuan Xing. "Increasing round trip efficiency of hybrid Li-Air battery with bifunctional catalysts". In: *Electrochimica Acta* 103.0 (2013), pp. 44–49. ISSN: 0013-4686. DOI: 10.1016/j.electacta.2013.04.027. URL: http://www.sciencedirect.com/science/article/pii/S0013468613006683.
[76] V. Khavrus and I. Shelevytsky. *Introduction to solar motion geometry on the basis of a simple model*. Feb. 2011. URL: http://enviasystems.com/pdf/Press_Release_400WHK.pdf.
[77] Envia Systems. *Our technology enables Li-ion batteries to store previously unattainable levels of energy with the highest capacity in the world*. http://enviasystems.com/technology/. May 2013.
[78] B. J. Morrisey. "Multidisciplinary design optimisation of an extreme aspect ratio HALE UAV". diploma thesis. California Polytechnic State University, 2009. URL: http://digitalcommons.calpoly.edu/cgi/viewcontent.cgi?article=1123&context=theses.
[79] J. deBoisblanc. "Synthesis and Characterization of P3HT:PCBM Organic Solar Cells". diploma thesis. Pomona College, May 2010. URL: http://sces.phys.utk.edu/~dagotto/condensed/HW1_2009/osc.pdfz.
[80] G. Weihao. "An overview on P3HT:PCBM, the most efficien organic solar cell material so far". diploma thesis. University of Tennessee, 2009. URL: http://sces.phys.utk.edu/\~dagotto/condensed/HW1_2009/osc.pdf.
[81] E.A. Schiff X.Deng. *Handbook of Photovoltaic Science and Engineering*. John Wiley & Sons, Ltd, 2003. Chap. 12.
[82] AltaDevices. *Mobile Power Technology*. http://www.altadevices.com/technology-overview.php. June 2013.
[83] S. Cowley. *Personal Email contact with Alta Devices employee*. http://www.altadevices.com. June 2013.
[84] Ozone Solutions. *Material Compatibility with Ozone*. http://www.ozoneapplications.com/info/ozone_compatible_materials.htm. June 2013.
[85] James E. Mark. *Physical Properties of Polymers Handbook*. Springer Science+Business Media, LLC, 2007. Chap. 51.
[86] M.A. Lacasse and D.J. Vanier. *Durability of Building Materials and Components 8*. National Research Council Canada, 1999, pp. 884–898.
[87] drivetek ag. *The Series Champion by drivetek*. http://www.drivetek.ch/index.php?id=28&L=2. June 2013.
[88] PelicanRope. *Dyneema Fact Sheet*. http://www.pelicanrope.com/pdfs2010/DYNEEMA_factsheet_UHMWPE.pdf. June 2013.
[89] Torayca. *Torayca Summary Data Sheet*. http://www.toraycfa.com/pdfs/ToraycaSummaryDataSheet.pdf. June 2013.
[90] Hexcel. *Hexcel Summary Data Sheet*. http://www.hexcel.com/Resources/Cont-Carbon-Fiber-Data-Sheets. June 2013.
[91] EuroFibers. *High Performance Fibers Data Sheet*. http://eurofibers.com/en/fibers. June 2013.
[92] M. C. Y. Niu. *Composite Airframe Structures*. Conmilit Press LTD., 1993.
[93] Soller Composites. *Epoxy vs. Vinylester vs. Polyester Resins Comparison*. http://www.sollercomposites.com/epoxyresinchoice.html. June 2013.

[94] Hexcel Composites. *HexWeb Honeycomb Sandwich Design Technology*. Tech. rep. June 2013.
[95] J.M. Davies. *Lightweight Sandwich Construction*. Blackwell Science Ltd, 2001.
[96] Hexcel. *Hexcel Hexply 8552 epoxy datasheet*. http://www.hexcel.com/Resources/DataSheets/Prepreg-Data-Sheets/8552_eu.pdf. June 2013.
[97] Cytec. *Cytec APC-2 PEEK datasheet*. http://www.cemselectorguide.com/pdf/APC-2_PEEK_031912.pdf. June 2013.
[98] T.W. Clyne D. Hull. *An Introduction to Composite Materials*. 1996.
[99] Aerostudents. *Bending, shear and torsion summary*. http://aerostudents.com/files/aircraftStructuralAnalysis/bendingShearAndTorsion.pdf. June 2013.
[100] Chih-Ming Tseng Nyan-Hwa Tai Ming-Chuen Yip. "Influences of thermal cycling and low-energy impact on the fatigue behaviour of carbon/PEEK laminates". In: *Composites Part B: Engineering* 30.8 (1999), pp. 849 –865. ISSN: 1359-8368. DOI: http://dx.doi.org/10.1016/S1359-8368(99)00048-7. URL: http://www.sciencedirect.com/science/article/pii/S1359836899000487.
[101] HobbyClub. *Tonegawa-Seiko SSPS-105 Ultra High Torque Servo [TONESPS105]*. http://www.hobbyclub.com/product_info.php?cPath=24_81&products_id=361. June 2013.
[102] Tonegawa-Seiko. *SSPS105 Super Hi-Power servo for RC models*. http://www.tonegawaseiko.co.jp/pro/e_pro02.html. June 2013.
[103] Granta Design Material Inspiration Professor Ashby. *CES EduPack 2012*. http://www.grantadesign.com/education/overview.htm. June 2013.
[104] James Gubera. *Nylon-66 and Nylon-6 prices are up in the first quarter of 2011*. June 2013.
[105] "Recycling of composite materials". In: *Elsevier* (2011). URL: http://www.arn.nl/content/download/1125/7654/file/Recycling\%20of\%20composite\%20materials.pdf.
[106] "Life-Cycle Analysis for Lithium-Ion Battery Production and Recycling". In: (2011). URL: http://www.transportation.anl.gov/pdfs/B/855.PDF.
[107] T. Hayes C. Gibson. *Indium and gallium overview*. Tech. rep. Edison investment research, 2011. URL: http://www.edisoninvestmentresearch.com/sectorreports/IndiumGalliumOverview071011.pdf.
[108] B. C. Levin E. Braun. "Nylons: A review of the literature on products of combustion and toxicity". In: *Fire and Materials* (1987), pp. 71–88. URL: http://fire.nist.gov/bfrlpubs/fire86/PDF/f86013.pdf.
[109] Hexcel. *Hexcel HRH 36 Data Sheet*. http://www.hexcel.com/Resources/DataSheets/Honeycomb-Data-Sheets/HRH_36_eu.pdf. June 2013.
[110] ACP Composites. *ACP Composites Data Sheet*. http://www.acpsales.com/upload/Mechanical-Properties-of-Carbon-Fiber-Composite-Materials.pdf. June 2013.
[111] Windustry. *How much do wind turbines cost?* http://www.windustry.org/resources/how-much-do-wind-turbines-cost. June 2013.
[112] Transmotec. *Planetary Gear PD32-Series*. http://www.transmotec.com/dc-motors/planetary-gear/PD32-Series.aspx. June 2013.
[113] Tweakers.net. *Tweakers pricewatch; Supermicro H8SCM-F*. http://tweakers.net/pricewatch/279147/supermicro-h8scm-f/specificaties/. June 2013.

Appendix A
Seasonal Plots

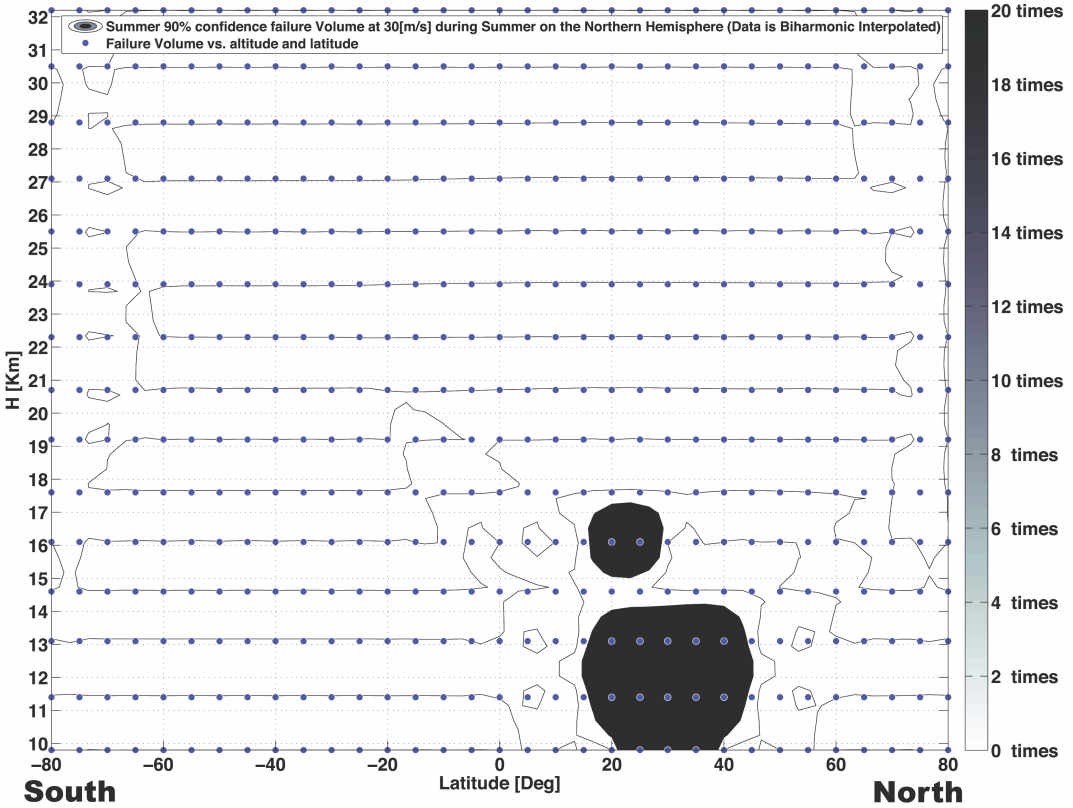

(a) Summer Failure Volume (Times Wind speed exceeds Max Design Wind speed)

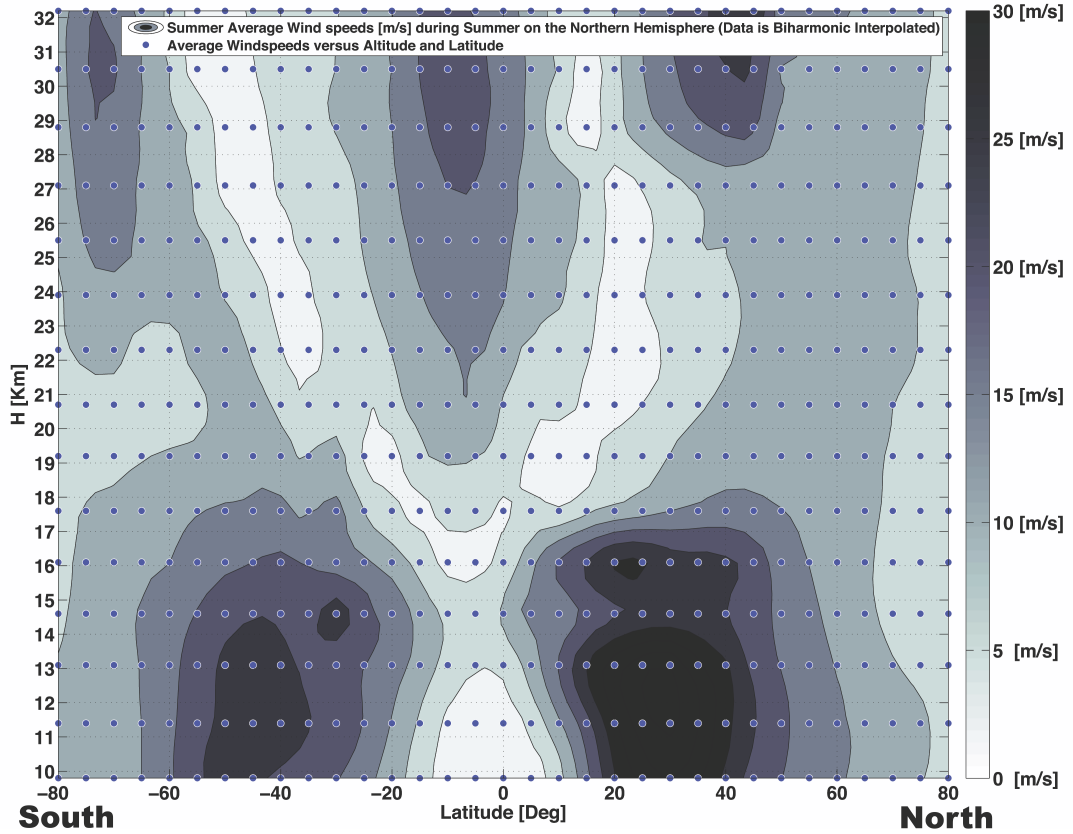

(b) Summer Average Wind speeds

Figure A.1: Summer Average and Failure Volume Wind data

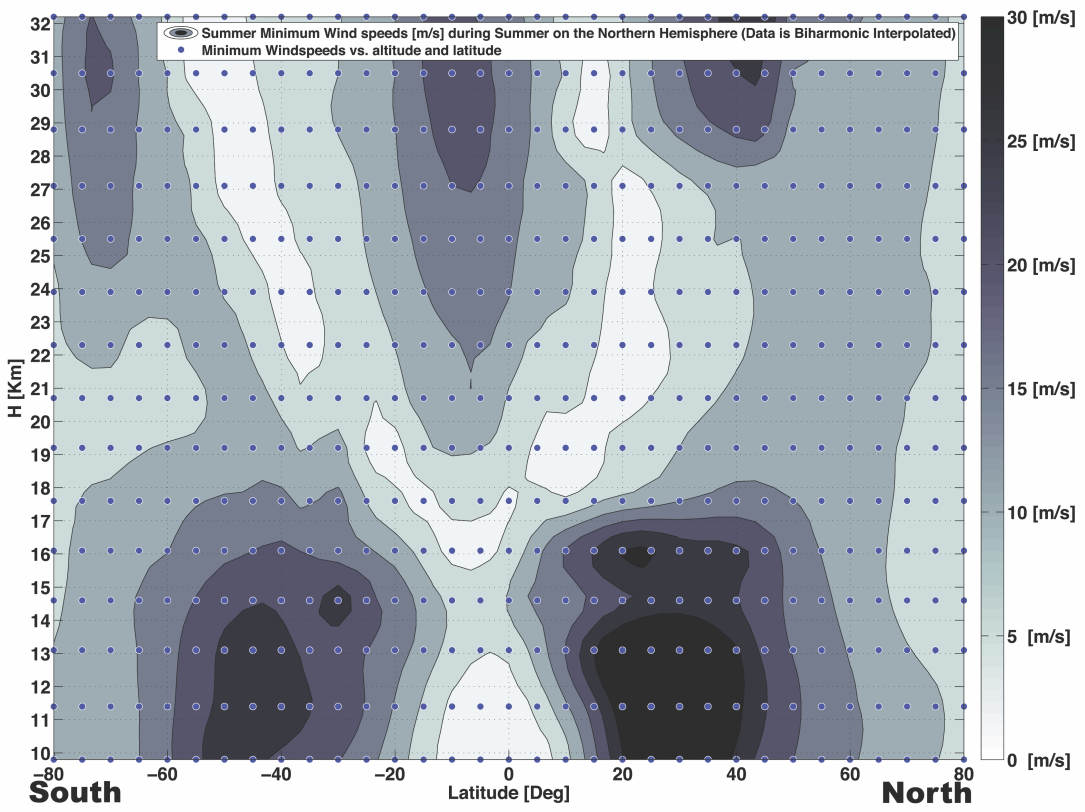

(a) Summer Minimum Wind speeds

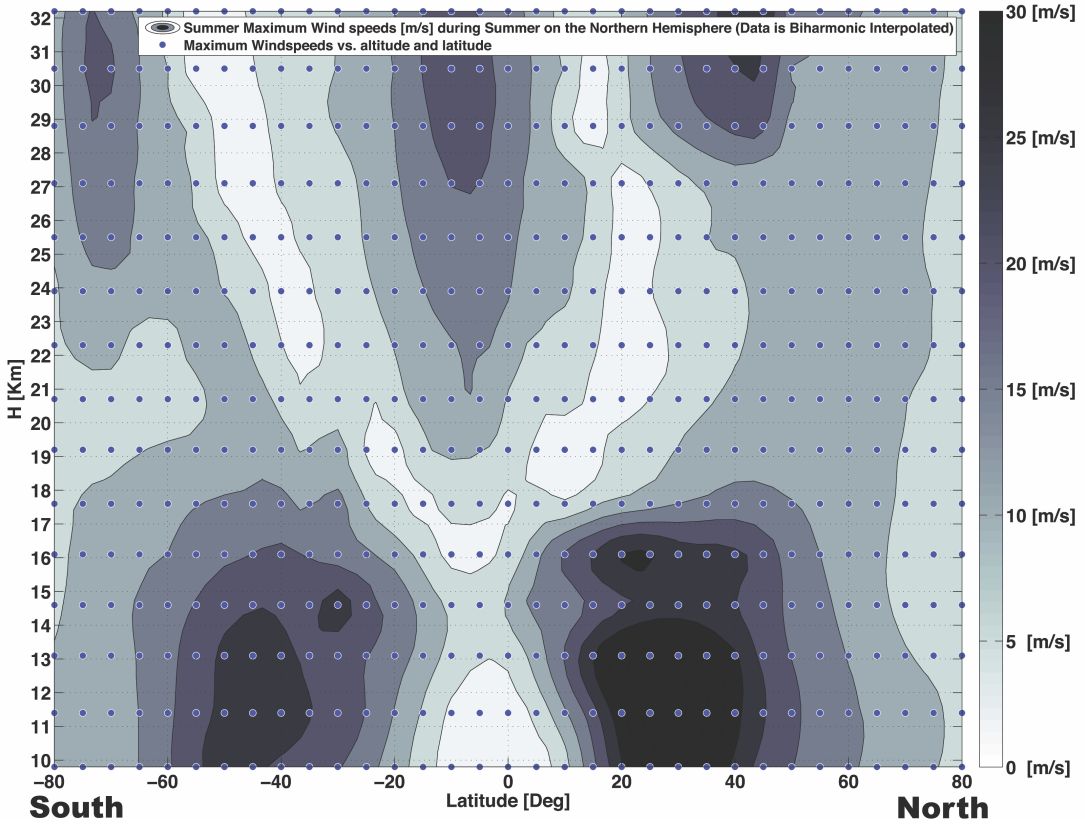

(b) Summer Maximum Wind speeds

Figure A.2: Summer Minimum and Maximum Wind data

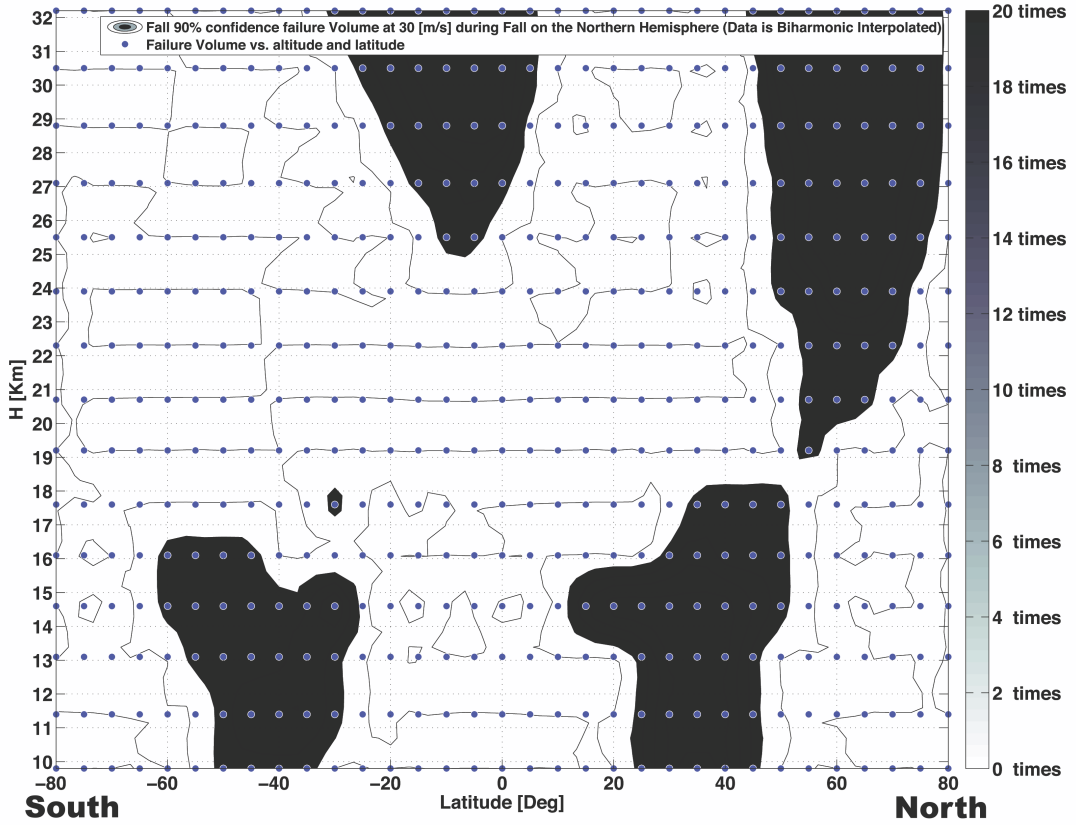

(a) Fall Failure Volume (Times Wind speed exceeds Max Design Wind speed)

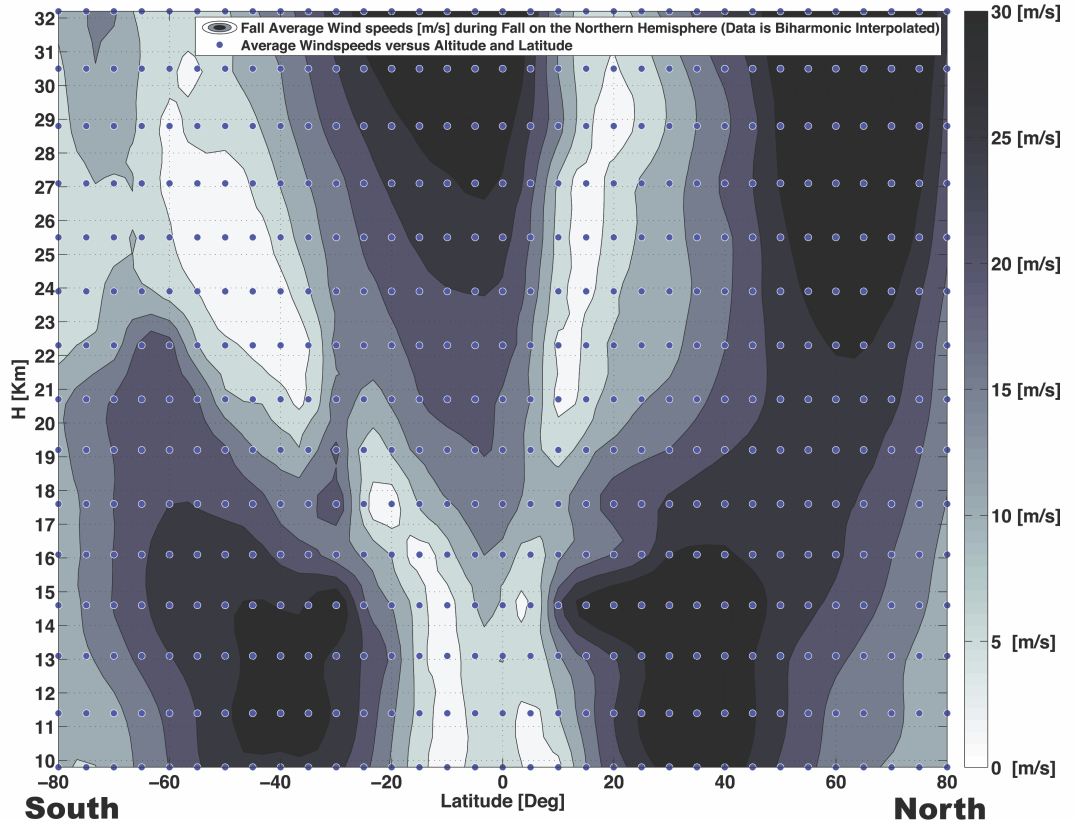

(b) Fall Average Wind speeds

Figure A.3: Fall Average and Failure Volume Wind data

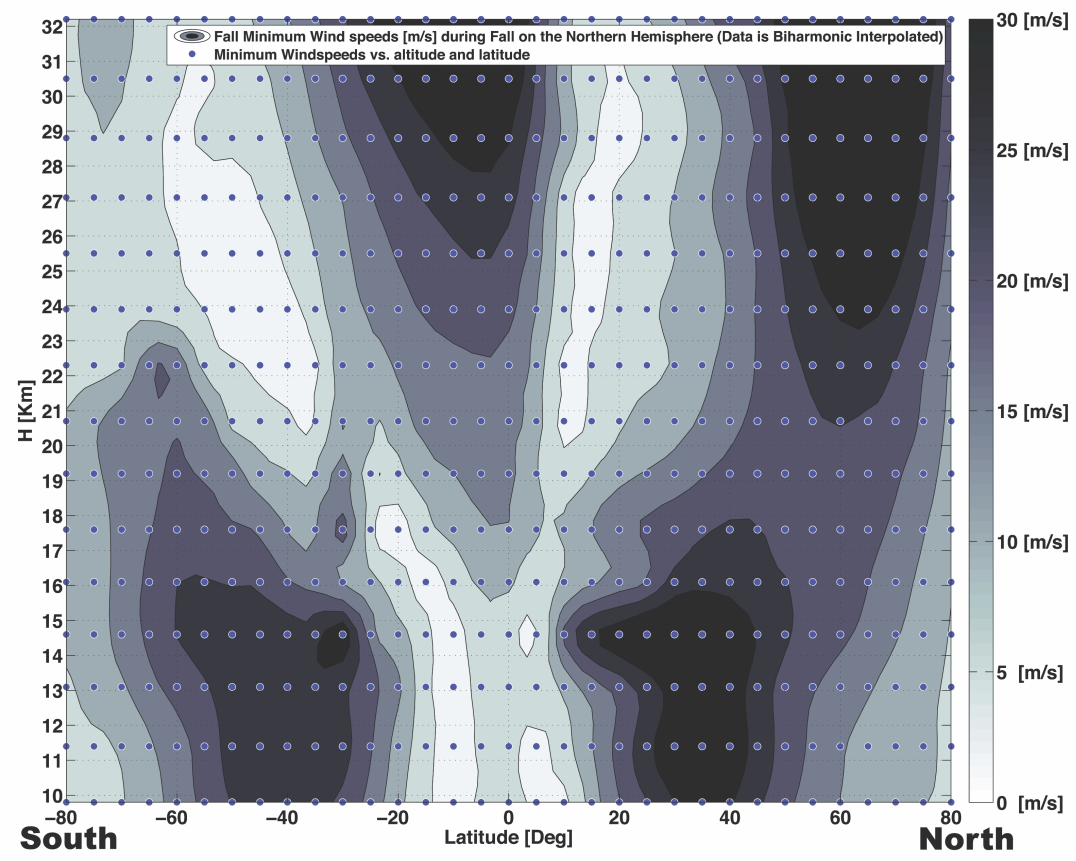

(a) Fall Minimum Wind speeds

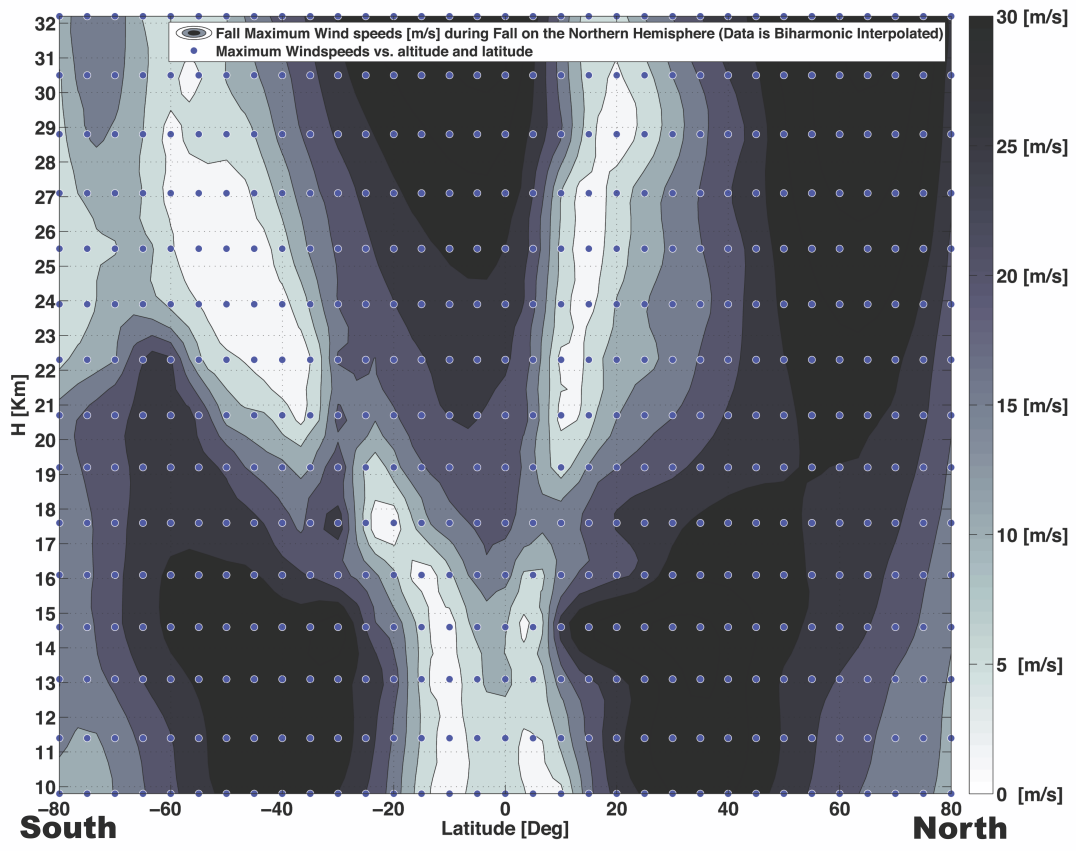

(b) Fall Maximum Wind speeds

Figure A.4: Fall Minimum and Maximum Wind data

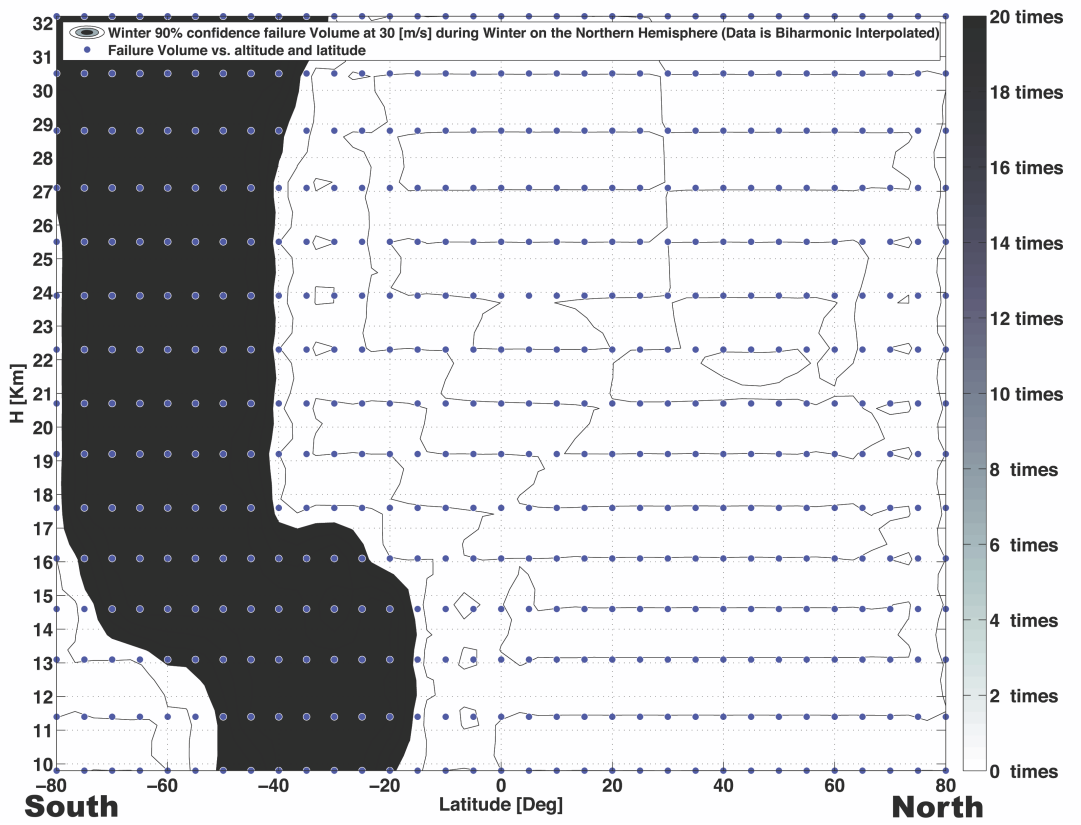

(a) Winter Failure Volume (Times Wind speed exceeds Max Design Wind speed)

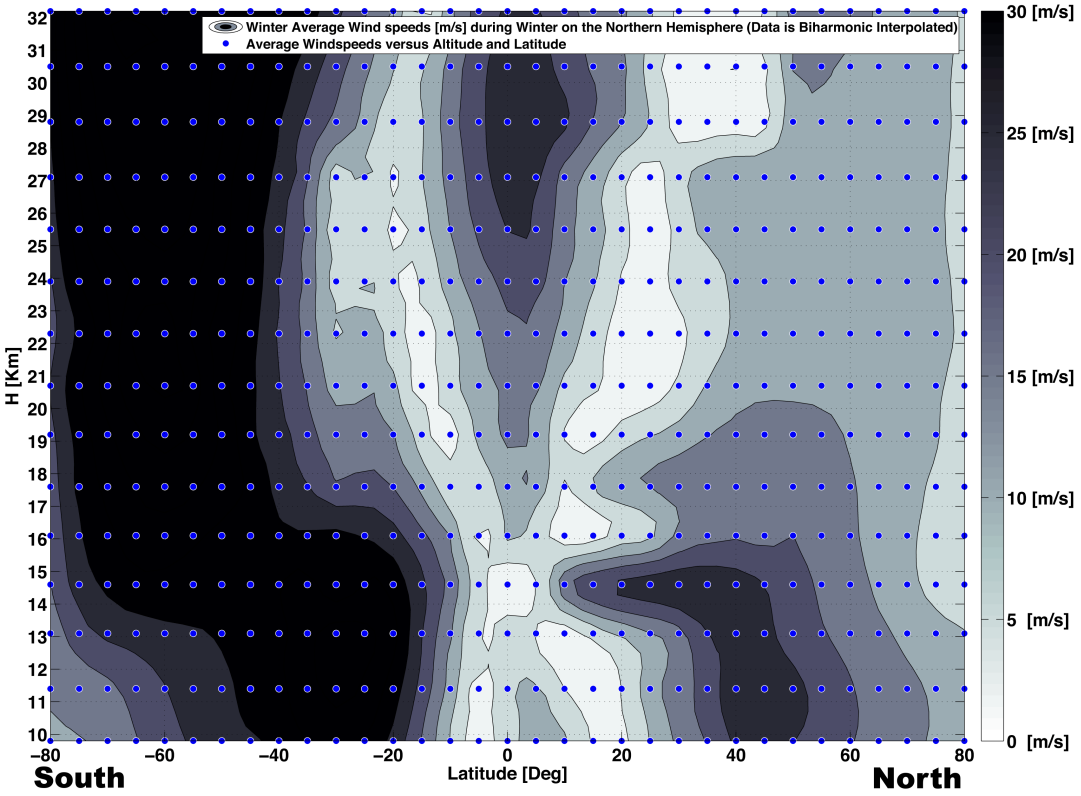

(b) Winter Average Wind speeds

Figure A.5: Winter Average and Failure Volume Wind data

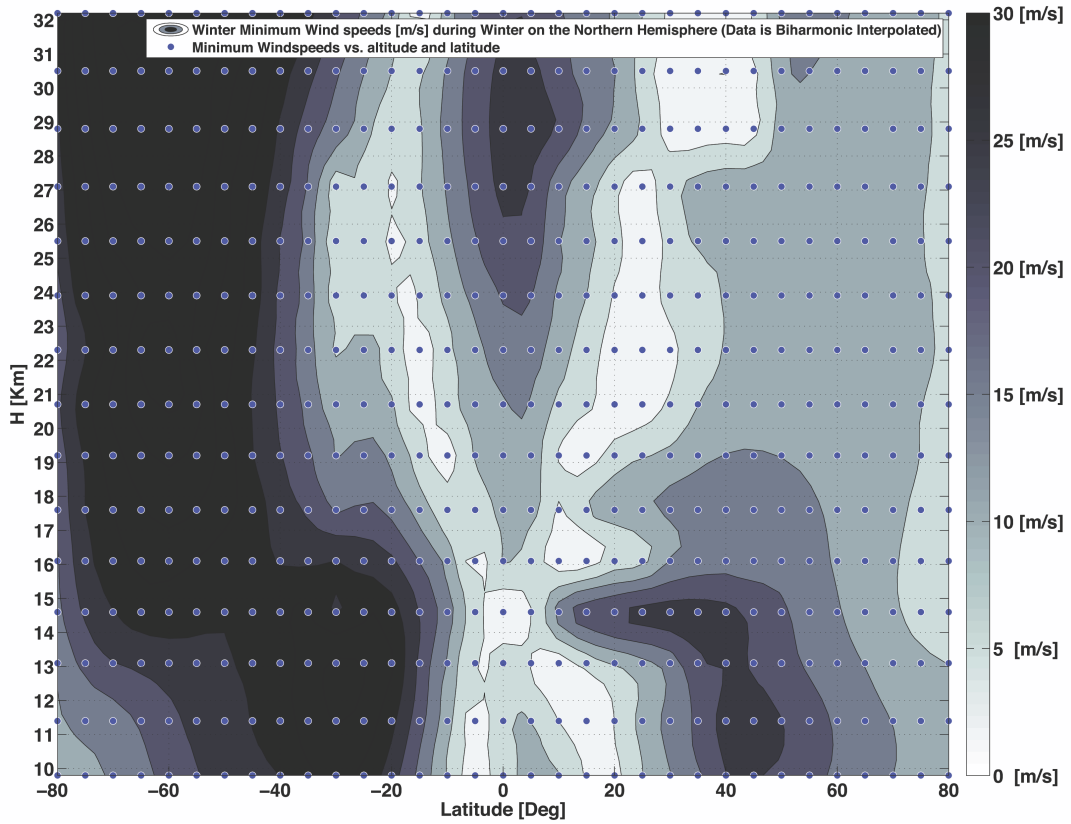

(a) Winter Minimum Wind speeds

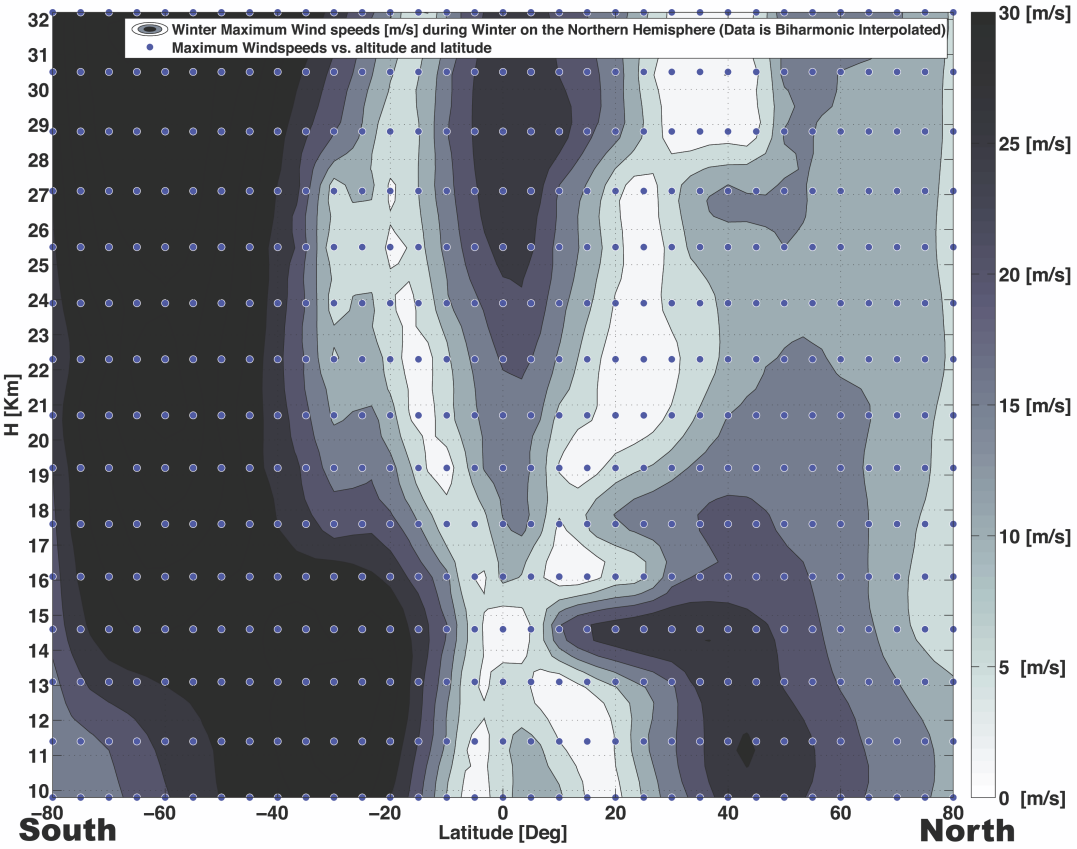

(b) Winter Maximum Wind speeds

Figure A.6: Winter Minimum and Maximum Wind data

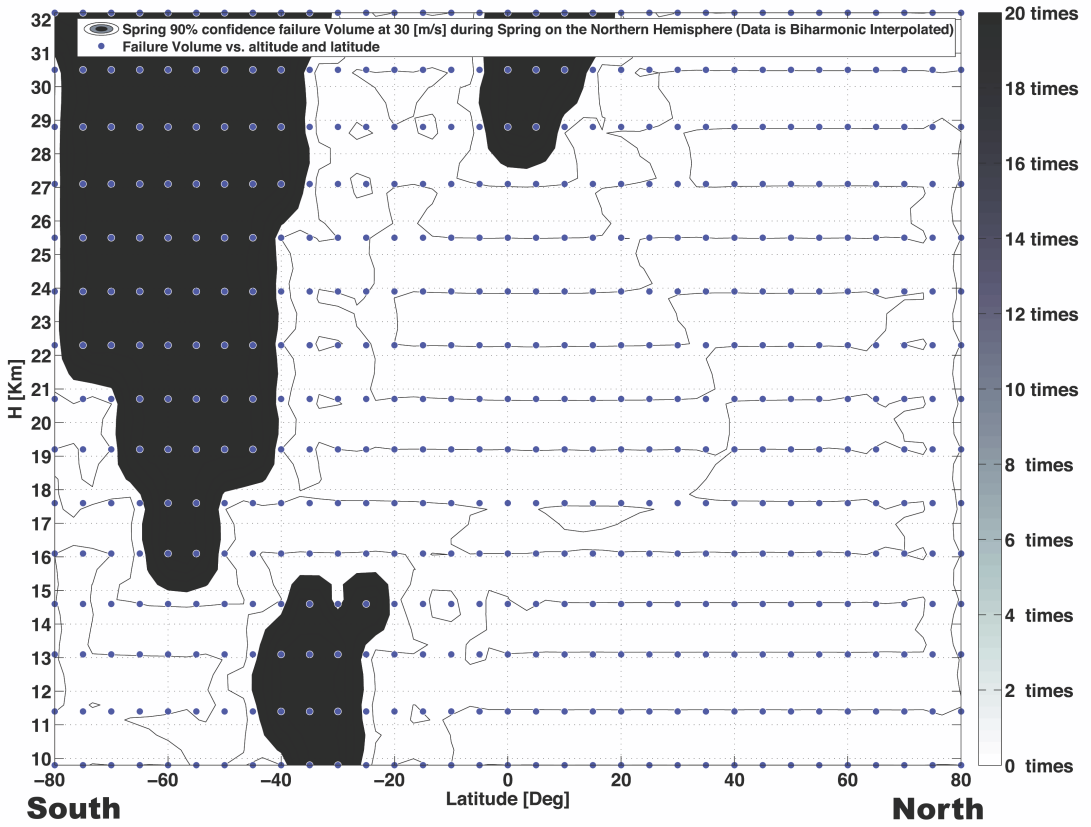

(a) Spring Failure Volume (Times Wind speed exceeds Max Design Wind speed)

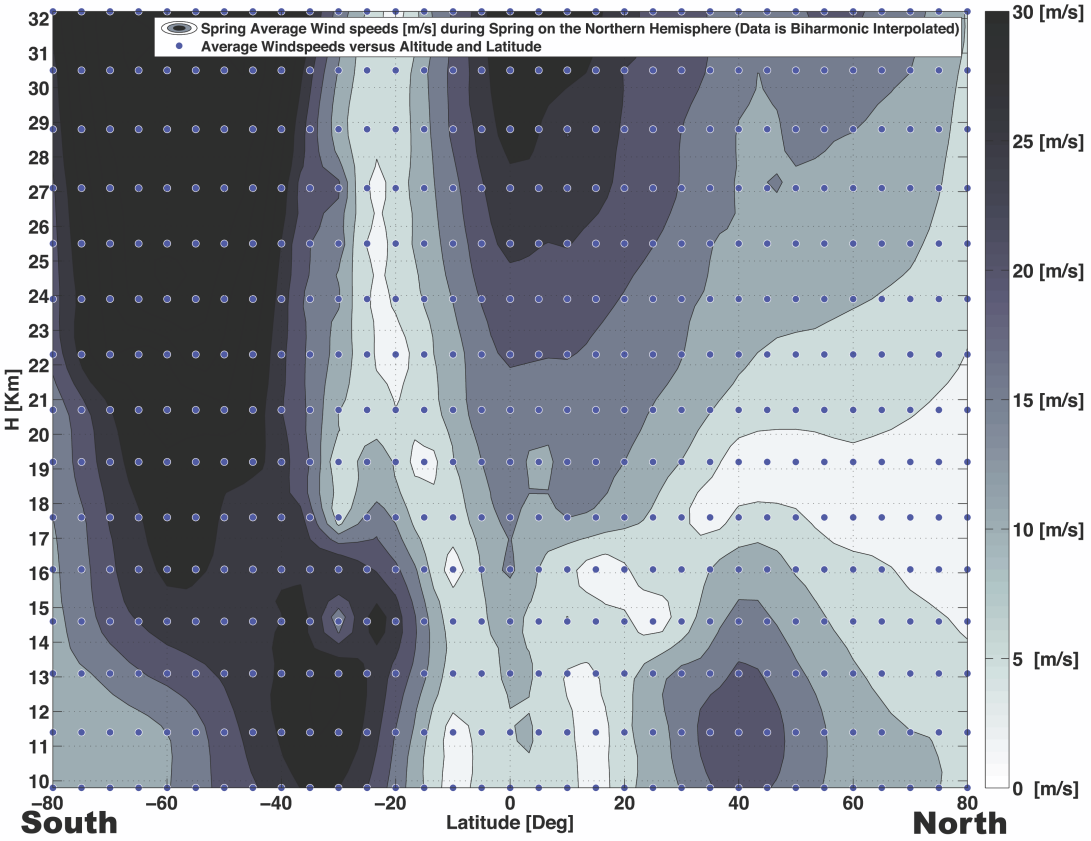

(b) Spring Average Wind speeds

Figure A.7: Spring Average and Failure Volume Wind data

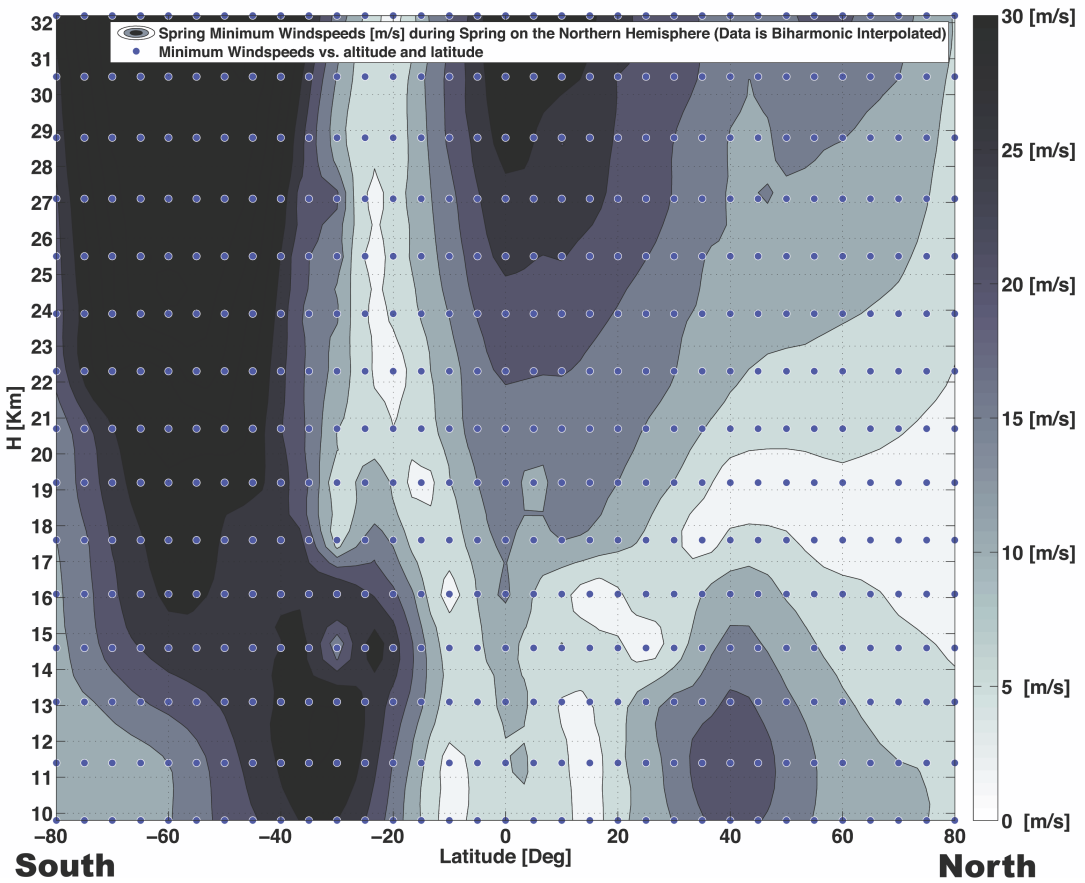

(a) Spring Minimum Wind speeds

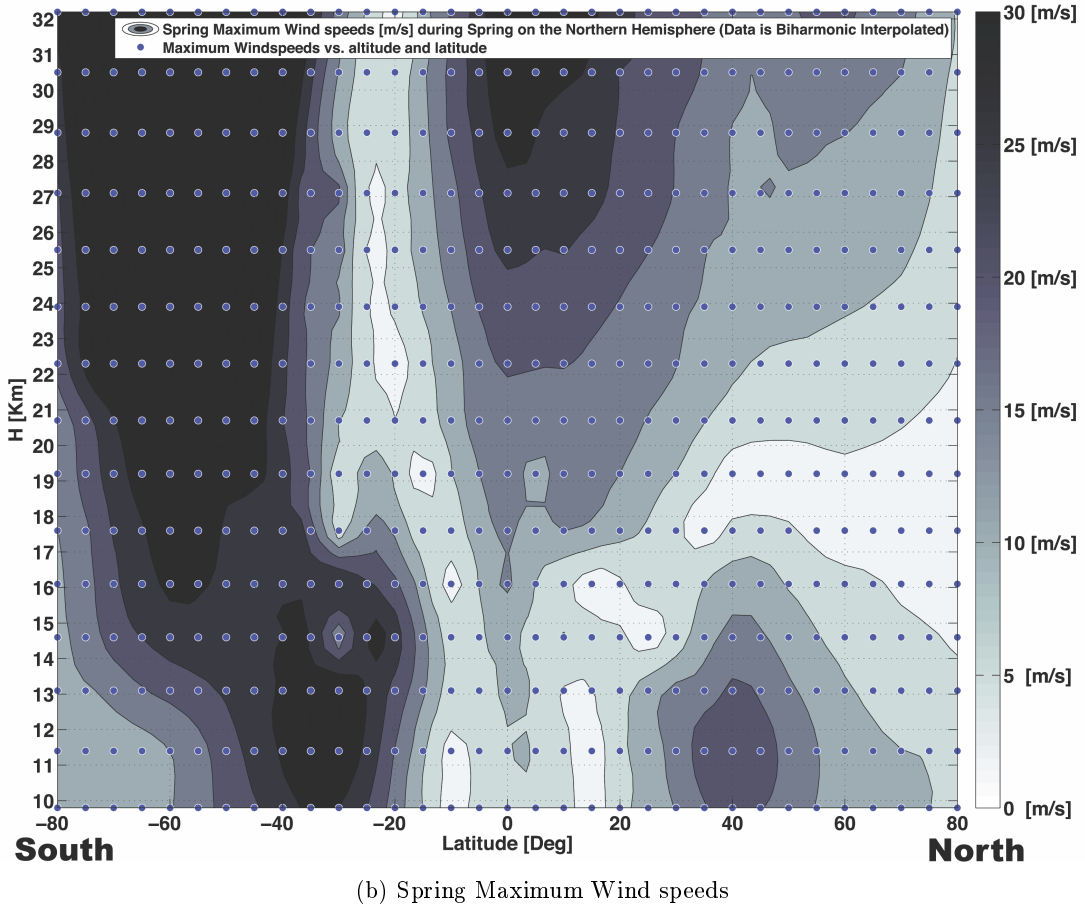

(b) Spring Maximum Wind speeds

Figure A.8: Spring Minimum and Maximum Wind data

Appendix B
Material Property Table

Table B.1: Honeycomb properties, [109]

Type	**Specific gravity [-]**	**Compressive strength [MPa]**	**L-direction Shear strength [MPa]**	**L-direction Shear modulus [MPa]**	**W-direction Shear strength [MPa]**	**W-direction Shear modulus [MPa]**
HRH-36-4.8-32	0.032	1.1	0.83	69	0.48	30
HRH-36-4.0-72	0.072	4.8	2.2	125	1.4	65

Table B.2: Selected plies' properties, [64, 110, 90]

Fiber Matrix Direction	Kevlar 149 Epoxy 0°/90°	HM CF Epoxy 0°/90°	IM6 Epoxy Unidirectional (UD)	M55J Cyanate UD	T300 Epoxy UD
Young's modulus 0° [MPa]	30	85	203	302	148
Young's modulus 90° [MPa]	30	85	11.2	6.2	9.65
Shear modulus [MPa]	5	4	8.4	3.7	4.55
Major Poisson's ratio [-]	0.2	0.2	0.32	0.3*	0.3
Tensile strength 0° [MPa]	480	350	3,500	2,027	1,314
Compressive strength 0° [MPa]	190	150	1,540	896	1,220
Tensile strength 90° [MPa]	480	350	56	35	43
Compressive strength 90° [MPa]	190	150	150	150*	168
Shear strength [MPa]	50	35	98	45	48
Specific gravity [-]	1.4	1.6	1.6	1.6	1.5
Thickness [mm]	0.08	0.125	0.125	0.125*	0.1

**values are estimated*

Appendix C
Cost Tables

C.1 Operational Cost Table

Table C.1: Total Operations Costs

(a) Estimated Salary and Ground Station Unit Costs

Subject	**Personnel Salary**	**Ground Station**
Description	Crew (Two Crews total) of: 10 Operators, 2 Mechanics, 1 IT specialist 1 Manager (One Operator per ten UAV's).	Mobile ground station.
Remarks	Estimated at 20 operators (slack or the option to have an extra mobile ground station).	Optional
Safe life missions	1	8
Cost	€100- per hour	€2,000,000.-
Quantity for 1 Unit	24 people 8,766 hours a year (Day and Night crew)	1
Cost for 1 Unit	€21,038.400.-	€2,000,000.-
Per Unit Cost for 100 Units	€210,038.-	€1,600,000.-
Mission Cost	€210,038.-	€200,000.-

(b) Estimated Ground station Communication and Power Costs

Subject	**Satellite Network**	**Ground Station Energy**
Description	Contract with Global Satellite Communication Firm	Estimated 2 MW required
Remarks	Data Budget influences Service price	Price includes estimate for a 2MW wind mill [111] batteries needed and small Solar Array to cover less windy days
Safe life missions	8	8
Cost	€50,000,000.-	€10,000,000.-
Quantity for 1 Unit	1	
Cost for 1 Unit	€50,000,000.-	€10,000,000.-
Per Unit Cost for 100 Units	€500,000.-	€100,000.-
Mission Cost	€62,500.-	€12,500.-
Operations	**Total unit cost** **€2,410,038.-**	**Total mission cost** **€485,038.-**

C.2 Miscellaneous Cost Table

Table C.2: Total Miscellaneous Costs

(a) Estimated Actuator and Assembly Costs

Subject	**Actuators**	**Assembly**
Description	Actuators for control surfaces	Team of 10 Mechanics for Assembly
Remarks		Includes Testing
Safe life missions	1	8
Cost	€4,000- per unit	€100.- per hour
Quantity for 1 Unit	2	2.080 hours
Cost for 1 Unit	€8,000.-	€208,000.-
Per Unit Cost for 100 Units	€6,400.-	€208,000.-
Mission Cost	€6,400.-	€26,000.-

(b) Estimated Certification Cost and Cost of Ownership

Subject	**Certification**	**Cost of Ownership**
Description	Certification procedure estimated start in 2018	Estimated 10% interest cost on total investment
Remarks	Once for all UAV's	Assume initial investment of €4M
Safe life missions	8	8
Cost	€25,000,000.- per certification	€400,000.- per U.A.V.
Quantity for 1 Unit	0.01	€400,000.- per unit
Cost for 1 Unit	€250,000.-	€400,000.-
Per Unit Cost for 100 Units	€250,000.-	€400,000.-
Mission Cost	€31,250.-	€50,000.-

(c) Estimated End of Life and Maintenance Costs

Subject	**End of Life**	**Maintenance**
Description	De-assembling and recycling	Miscellaneous costs and unexpected repairs
Remarks	High level of sustainability comes at an high price	
Safe life missions	8	1
Cost	€100,000.- per unit	€100.- per hour
Quantity for 1 Unit	1	120 hours
Cost for 1 Unit	€100,000.-	€12,000.-
Per Unit Cost for 100 Units	€80,000.-	€9,600.-
Mission Cost	€10,000.-	€9,600.-
Miscellaneous	**Total unit cost** **€954,000.-**	**Total mission cost** **€133,250.-**

C.3 Development Cost Table

Table C.3: Total R&D costs

(a) Estimated Research and Development Costs

Subject	**Research and Development**	**Avionics Software**
Description	10 students 10 weeks 40 hours a week	Custom software solution based on open source software to minimise development cost
Remarks	1 extra year required. Students are relatively cheap.	One year programming by ten programmers (not students)
Safe life missions	8	8
Cost	€20- per hour	€100.- per hour
Quantity for 1 Unit	10 people 400 hours plus 2.080 hours total	10 people 2.080 hours
Cost for 1 Unit	€496,000.-	€20,800.000.-
Per Unit Cost for 100 Units	€4,960.-	€208,000.-
Mission Cost	€620.-	€26,000.-
R&D	**Total unit cost €212,960.-**	**Total mission cost €26,620.-**

C.4 Payload Cost Table

Table C.4: Overview of Payload Costs

(a) Estimated sensors costs

Subject	**FIR sensor**	**ROYGBIV sensor**
Description	CMOS IR PiCo 124-E	KAI-29050
Remarks	Estimated price	Estimated price
Safe life missions	4	4
Cost	€3,031.22 per unit	€454.68 per unit
Quantity for 1 Unit	1	1
Cost for 1 Unit	€3,031.22	€454.68
Per Unit Cost for 100 Units	€2,425.-	€364.-
Mission Cost	€606.-	€91.-

(b) Estimated mirror costs

Subject	**Mirror**	**Maintenance**
Description	Imaging mirror	Mirror refurbishing
Remarks	1 Imaging mirror 4 deflection mirrors and 1 lens.	Scanning for deformation re-applying coating.
Safe life missions	8	1
Cost	€200,000.- per unit	€2,000.- per unit
Quantity for 1 Unit	1	1
Cost for 1 Unit	€200,000.-	€2,000.-
Per Unit Cost for 100 Units	€180,000.-	€1,600.-
Mission Cost	€22,500.-	€1,600.-

(c) Estimated stabelizer costs

Subject	**Servo's and Gears**	**Actuators and Supporting Structure**
Description	Angular Imaging Stability	Linear Imaging Stability
Remarks	Accuracy declines with increased lifetime.	Accuracy declines with increased lifetime.
Safe life missions	2	2
Cost	€149.- per servo [112]	€300.- per actuator
Quantity for 1 Unit	6	2
Cost for 1 Unit	€840.-	€120.-
Per Unit Cost for 100 Units	€780.-	€100.-
Mission Cost	€390.-	€50.-
Payload	**Total unit cost** **€185,269.-**	**Total mission cost** **€25,237.-**

C.5 Power Cost Table

Table C.5: Overview Power Costs

(a) Estimated solar array costs

Subject	**Solar Array**	**Solar Array Sale**
Description	Single Junction GaAs Thin Film	Single Junction GaAs Thin Film
Remarks	Estimated production start 2018	Reselling after 4 years at 10% original price
Safe life missions	4	4
Cost	€1,750.- per m^2 (2014)	€-175.- per m^2(2018)
Quantity for 1 Unit	$2 \cdot 91.5$ m^2	$2 \cdot 91.5$ m^2
Cost for 1 Unit	€320,250.-	€-3,203.-
Per Unit Cost for 100 Units	€256,200.-	€-2,562.-
Mission Cost	€2,562.-	€-26.-

(b) Estimated battery cost and profit

Subject	**Batteries**	**Recycling Batteries**
Description	Lithium-Ion high energy density batteries.	Recycling at 40% original price.
Remarks	Battery price decrease at 15% per year (45% over 5) price below is average per year.	High recycling cost estimated
Safe life missions	1	1
Cost	€400 per KWh (year 0) €256.13 per KWh (average)	€102.45 per KWh
Quantity for 1 Unit	30 KWh	30 KWh
Cost for 1 Unit	€7,683.90	€3,073.50
Per Unit Cost for 100 Units	€6.147.-	€2,459.-
Mission Cost	€6,147.-	€2,459.-

(c) Estimated protection and maintenance costs

Subject	**Solar Array Encapsulation**	**Maintenance**
Description	Poly Carbonate thin film	Battery and Encapsulation replacement
Remarks	Protects Solar Array against Ozone. High price due to thin sheets (micrometers)	Battery replacement is relatively easy due to small packs.
Safe life missions	1	1
Cost	€100.- per m^2	€100.- per hour
Quantity for 1 Unit	91.5 m^2	40 hours
Cost for 1 Unit	€9,150.-	€4,000.-
Per Unit Cost for 100 Units	€7,320.-	€3,200.-
Mission Cost	€7,320.-	€3,200.-
Power	**Total unit cost** **€272,764.-**	**Total mission cost** **€21,662.-**

C.6 Structural Cost Table

Table C.6: Overview of structural costs

(a) Estimated material and production costs

Subject	**Structure**	**Production**
Description	PEEK resin carbon fibre and aramid fibre composites	Structure Part Production
Remarks	Thermal cycles determine Safe Life	Estimated 10 times material
Safe life missions	8	8
Cost	€100.- per kg [103]	€1,000.- per kg
Quantity for 1 Unit	70 kg	70 kg
Cost for 1 Unit	€7,000.-	€70,000.-
Per Unit Cost for 100 Units	€5,600.-	€56,000.-
Mission Cost	€700.-	€7,000.-

(b) Estimated assembly and maintenance costs

Subject	**Assembly**	**Maintenance**
Description	Moving parts and cut outs	Crack growth monitoring and repairs
Remarks	Estimated low cost impact	Every mission
Safe life missions	8	1
Cost	€100.- per hour	€100.- per hour
Quantity for 1 Unit	100 hours	100 hours
Cost for 1 Unit	€10,000.-	€10,000.-
Per Unit Cost for 100 Units	€8,000.-	€10,000.-
Mission Cost	€1,000.-	€10,000.-
Structural	**Total unit cost** **€79,600.-**	**Total mission cost** **€18,700.-**

C.7 Communication Cost Table

Table C.7: Overview Communication Costs

(a) Estimated antenna costs

Subject	**S-band Antenna**	**NAV antenna**
Description	Air to air and Air to ground.	Navigation (NAV) and Control antenna
Remarks	Lifetime 7.5 years at LEO assumed 8 years at 18 km altitude.	Low cost. Price is an estimate
Safe life missions	8	2
Cost	€18.664.88 per unit [**ANTENNA2013**]	€1.000.- per unit
Quantity for 1 Unit	2	1
Cost for 1 Unit	€37,330.-	€1,000.-
Per Unit Cost for 100 Units	€29,864.-	€800.-
Mission Cost	€3,733.-	€400.-

(b) Estimated signal handling costs

Subject	**Tx, Rx, Switch, Splitter and Amplifier**	**Flight Control and GPS**
Description	Transmitter, Receiver, Switch and Splitter.	Navigation and control box off the shelf.
Remarks	High cost due to need for Custom solutions price is an estimate based on reference data [**ANTENNA2013**].	Backup unit required.
Safe life missions	8	8
Cost	€89,920.- per unit	€7,494.- per unit
Quantity for 1 Unit	1	2
Cost for 1 Unit	€90.-	€14,989.-
Per Unit Cost for 100 Units	€71,936.-	€11,991.-
Mission Cost	€8,992.-	€1,499.-

(c) Estimated Cabling and Maintenance Costs

Subject	**Cabling**	**Maintenance**
Description	Thick antenna cabling, data wiring and power supply cables.	Calibrating, cleaning, electronics measuring and repair where necessary.
Remarks	Includes data and payload cabling. Low cost estimated due to close placement of components.	Includes data and payload electronics maintenance.
Safe life missions	8	2
Cost	€2,000.- per unit	€100.- per hour
Quantity for 1 Unit	1	40 hours
Cost for 1 Unit	€2,000.-	€4,000.-
Per Unit Cost for 100 Units	€1,600.-	€3,200.-
Mission Cost	€200.-	€3,200.-
Communication	**Total unit cost** **€119,391.-**	**Total mission cost** **€18,024.-**

C.8 Propulsion Cost Table

Table C.8: Total Propulsion Costs

(a) Estimated Engine and Propellor Costs

Subject	**Electro-motors**	**Propellers**
Description	Compact Power Motors GmbH CPM90-22-1500L	Double Blade Carbon Fibre Composite Propellers
Remarks	Yearly Replacements required to reduce risk	Need maintenance
Safe life missions	1	8
Cost	€750- per unit	€13,938.- per unit
Quantity for 1 Unit	2	2
Cost for 1 Unit	€1,500.-	€27,876.-
Per Unit Cost for 100 Units	€1,200.-	€22,301.-
Mission Cost	€1,200.-	€2,788.-

(b) Estimated Gearbox and Maintenance Costs

Subject	**Gearbox**	**Maintenance**
Description	Polymer Gears	Gearbox
Remarks	Custom made hence high price	Replacements are relatively easy but propellers need extensive checking
Safe life missions	1	1
Cost	€253.3.- per unit	€100.- per hour
Quantity for 1 Unit	2	40 hours
Cost for 1 Unit	€506.6.-	€4,000.-
Per Unit Cost for 100 Units	€405.-	€3,200.-
Mission Cost	€51.-	€3,200.-
Propulsion	**Total unit cost** **€27,106.-**	**Total mission cost** **€7,239.-**

C.9 Data Handling Cost Table

Table C.9: Overview Data Handling Costs

(a) Estimated calculation power costs

Subject	**CPU**	**RAM**
Description	AMD Opteron 4256 EE Tray (8-core 1,6 GHz)	Kingston ValueRAM KVR13LR9D4K4/64
Remarks	Special Low Power CPU 32 Watts average	Special Low Voltage RAM 1.35 Volts. Value Pack includes 4x DDR3 RAM
Safe life missions	8	8
Cost	€364.- per unit [35]	€465.- per unit [**RAM2012**]
Quantity for 1 Unit	1	1
Cost for 1 Unit	€364.-	€465.-
Per Unit Cost for 100 Units	€291.-	€372.-
Mission Cost	€36.-	€47.-

(b) Estimated Data Storage and Infrastructure Costs

Subject	**SSD**	**PCB**
Description	Crucial M500 960GB 2.5-inch Internal SSD	Supermicro H8SCM-F (Motherboard)
Remarks	Data Storage for one year and Navigation backups	Single CPU PCB upgrade to 2 CPU PCB possible
Safe life missions	2	8
Cost	€453.62 per unit [37]	€218.45 per unit [113]
Quantity for 1 Unit	8	1
Cost for 1 Unit	€3,628.96	€218.45
Per Unit Cost for 100 Units	€2.903.-	€175.-
Mission Cost	€1.452.-	€22.-
Data Handling	**Total unit cost** **€3,741.-**	**Total mission cost** **€1,557.-**